School of Science

Department of Imaging and Applied Physics

$CaNi_5$-Based Alloys and Nanoconfined $NaAlH_4$ for Solid-State Hydrogen Storage

Somwan Chumphongphan

This thesis is presented for the Degree of

Doctor of Philosophy

of

Curtin University

October 2014

DECLARATION

To the best of my knowledge and belief this thesis contains no material previously published by any other person except where due acknowledgement has been made.

This thesis contains no material that has been accepted for the award of any other degree or diploma in any university.

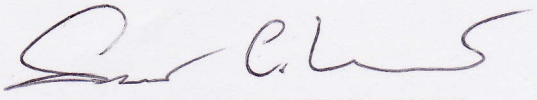

.....

October 20, 2014

To my wife and our lovely sons (Guar and Gunt) who hold my heart and soul

ACKNOWLEDGEMENT

Firstly I would like to express my gratitude to my Ph.D. supervisor Prof. Craig Buckley for his support, advice and providing first-class research facilities. Secondly, I wish to thank my associate supervisor Dr. Mark Paskevicius for his support and helpful discussions. Again, thanks to Mark, who certainly worked hard to educate me with his best scientific skills. I also enormously improved my writing skill from his feedback on both papers and thesis.

I would also like to thank:

Dr. Drew Sheppard for not only his help during working in the lab but also lots of useful suggestion on my work. Uffe Filsø who shared his experience on producing mesoporous material. Les Vickers and Dr. William Rickard for their help on SEM sample preparation. My former Ph.D. colleagues in the Hydrogen Storage Research Group, Anna-Lisa Chaudhary and Julie Murshidi, for their best friendship.

I would like to acknowledge Ministry of Science and Technology, Thai Government, and Mae Fah Luang University for full financial support of my Ph.D. program. I also acknowledge the facilities, scientific and technical assistance of the Curtin University Electron Microscope Laboratories, a facility partially funded by the University, State and Commonwealth Governments.

Finally but most importantly, to my wife Suchanya and our lovely sons Guar and Gunt, I would like to thank you with all my heart for their support and best wish.

Thanks to everyone else who has provided help and support during my Ph.D.

ABSTRACT

Hydrogen is considered as the primary energy carrier in near the future which is a solution to the energy related problems such as the eventual depletion of fossil fuels and the emission of green house gas. To become hydrogen-based society, however, many technical problems are needed to be resolved, especially on hydrogen storage system. At present, there is no outstanding hydrogen storage system that meets the requirements of hydrogen economy such as safety, low cost, fast kinetics and high storage capacity. In this research the hydrogen storage properties of $CaNi_5$-based intermetallic alloys and nanoconfined $NaAlH_4$ are investigated for a low-temperature hydrogen storage system.

To alter the hydrogen storage properties of $CaNi_5$, several metals (Zr, Cr, Al, and Mo) were added at a certain ratio. A simple mechanical milling and annealing process has been used to synthesise $CaNi_5$-based hydrogen storage alloys. Heat treatment at 800 ºC under vacuum results in the formation of a crystalline $CaNi_5$ phase. The abundance of $CaNi_5$ phase decreases for the substituted alloys with higher contents of additive metals. The remaining secondary phase is predominantly Ni for all samples, probably existing as a Ni-rich solid solution with additives. Other secondary phases, including Ca_2Ni_7 and Mo-Ni, are formed when substituting Mo for Ni. Replacement of Zr into the Ca site reduces the unit cell volume of $CaNi_5$ whilst replacement of Al and Mo into the Ni site significantly increases the unit cell volume.

The hydrogen storage capacity of all substituted alloys is decreased and the hydrogen sorption plateau regions are narrower compared to those of pure $CaNi_5$. Al and Mo substituted alloys show lower desorption plateau pressures corresponding to the larger unit cell volume of these alloys. Higher plateau pressures and larger hysteresis were observed for the substitution of Ca with Zr as a result of a smaller unit cell volume of its $CaNi_5$ phase. All substituted alloys, except $CaNi_{4.9}Mo_{0.1}$, show relatively fast and comparable kinetics to that of unsubstituted $CaNi_5$. The reaction enthalpy, ΔH, for both absorption and desorption are directly proportional to the unit cell volume of the alloys.

After 40 absorption-desorption cycles at 85 ºC, most of the synthesised alloys retain approximately 80 – 95% of their initial hydrogen storage capacity. The hydrogen absorption capacity of substituted alloys with Zr at the Ca site rapidly decreases for the first 50 cycles and then the rate of capacity loss slows beyond 100 cycle with ~70% of initial capacity at 200 cycles. $CaNi_{4.9}Al_{0.1}$ shows durability improvement by maintaining its initial hydrogen absorption capacity after 20 cycles performed at 85 ºC. After cycling, the $CaNi_5$ phase can be recovered by heat treatment with a comparable capacity and similar properties to the as-synthesised alloy.

To investigate the effect of particle size of $NaAlH_4$ on its hydrogen sorption properties, an ordered mesoporous carbon scaffold (CMK-1) has been synthesised and infiltrated with $NaAlH_4$ particles by solvent- and melt-infiltration techniques. The confined $NaAlH_4$ is expected to form nanoparticle with the size of 2 – 3 nm corresponding to the pore size of CMK-1. The hydrogen sorption properties of $NaAlH_4$ might improve because of the particle-size reduction.

The confined $NaAlH_4$ shows a significant improvement in the hydrogen decomposition temperature (with an onset below 100 ºC) and desorption kinetics compared to bulk $NaAlH_4$. Single step hydrogen desorption occurs for confined $NaAlH_4$ with the maximum release rate at a temperature lower than its melting point.

This study also focuses on some of the problems associated with nanoconfinement of hydrogen storage materials including scaffold contamination, residual solvent contamination, sample morphology changes after heating, and other factors that can be detrimental to the application of these systems. Careful thought must be given to the contamination from solvents during the solvent infiltration procedure, e.g. THF in this study, that has been used to dissolve and then infiltrate the hydrogen storage materials. Of particular interest is the expulsion of $NaAlH_4$ decomposition products from the scaffold after heating beyond its melting point under vacuum.

TABLE OF CONTENTS

LIST OF FIGURES

LIST OF TABLES

CHAPTER 1

INTRODUCTION

1.1 RESEARCH OVERVIEW

Fossil fuel, including coal, oil, and natural gas, has been considered as the main source of energy for centuries. Unfortunately, fossil fuels are not available in unlimited quantities. To meet the high level of the world's energy demand fossil fuels are being depleted rapidly. According to the International Energy Agency (IEA) [1], the world's proven reserves, including non-conventional oil, could be sustained at the current rate of extraction for approximately 40 years. Therefore, a short supply of fossil fuels exists and extreme prices could occur in the near future. To fill the gap between fossil fuel demand and supply, renewable energy has emerged as a solution to a sustainable energy future

This research aims to understand the hydrogen storage technique which might be the principal energy carrier in near future. The main purpose of this thesis is the study of hydrogen storage properties of $CaNi_5$-based intermetallic alloys and nanoconfined $NaAlH_4$ as low-temperature hydrides for a stationary energy generation. The motivation for studying $CaNi_5$-based alloy hydrides and $NaAlH_4$ is that they have partially favourable hydrogen storage properties for stationary and distributed energy generation applications. These hydrides also have potential for low-temperature hydrides or secondary hydrides in concentrating solar thermal (CST) system [2, 3]. In this research, the hydrogen storage properties of $CaNi_5$ will be altered by substitution of metals, e.g. Zr, Cr, Al, and Mo at certain ratios. To enhance the hydrogen sorption properties of $NaAlH_4$, this research will be attempted to infiltrate the $NaAlH_4$ into the porous scaffold to reduce the particle size.

Calcium is cheap (~ $5 US/kg) and abundant (4.15 *wt.*% of elements in the earth's crust) compared to certain rare earth metals such as lanthanum) [4-6]. Thus, the average price of La from 2008 – 2013 is ~32 US/kg [7]. The price of elements is affected not only by their abundance and purity but also by demand patterns that [2] vary with time. For instance, the price of a rare earth oxide (REO), ≥ 99% purity, of lanthanum has increased rapidly from $7.75 US/kg to $66.5 US/kg in 2008 and the

4th quarter of 2011, respectively [6]. Therefore, the production cost of $CaNi_5$-based alloys will be less expensive than for the well-known hydrogen storage alloy, $LaNi_5$. Furthermore, $CaNi_5$ shows favourable sorption kinetics at near ambient pressure and temperature, which is suitable to supply hydrogen to a low-temperature fuel cell and a CST system. However, the critical limitation of $CaNi_5$ is its poor cyclic stability due to the disproportionation of Ca from the alloy [8, 9]. Accordingly, this research is directed towards adding third and fourth metal elements to this alloy to enhance its cyclic stability.

Studying $NaAlH_4$ is not only for CST applications, but also particularly relevant for vehicular applications because of its high gravimetric hydrogen capacity of 7.4 wt.% H [10]. In addition, it has been studied for decades and its properties are reasonably well understood [11-14]. This makes $NaAlH_4$ a perfect candidate to assess the impact of nanoconfinement on its hydrogen storage properties. In this research, infiltration of $NaAlH_4$ into an ordered mesoporous carbon CMK-1 scaffold will be studied systematically. This promising technique can reduce the particle size of $NaAlH_4$ to approximately 2 – 3 nm with the consequence of kinetic improvement and lowering the hydrogen release temperature of this complex hydride.

1.2 WORLD ENERGY CRISIS AND CLIMATE CHANGE

The demand for oil is increasing continuously, which is generally related to the growth of world population and economics [15]. The increase of oil consumption leads to an extended gap between oil demand and production. Consequently, this results in a rapid escalation of the oil price. As shown in Figure 1-1, the average price for crude oil was below $40 per barrel for decades before 1990, but it has dramatically increased from $50 per barrel in 2005 to $100 and $110 per barrel in 2008 and 2011, respectively [16].

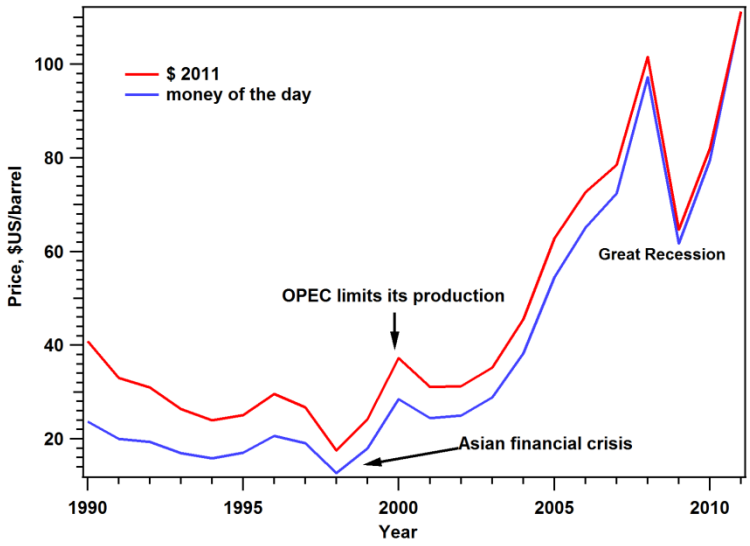

Figure 1-1: Crude oil average prices during 1990 – 2011, data from ref. [16].

The concern of using fossil fuels is not only due to the limited amount and increasing cost but also due to environmental concerns. The combustion of fossil based fuels causes an emission of carbon dioxide, CO_2, which is the main greenhouse gas (GHG) [15]. In fact, GHG also includes other gases such as methane (CH_4), nitrous oxide (N_2O), hydrofluorocarbons (HFCs), perfluorocarbons (PFCs) and sulphur hexafluoride (SF_6). As shown in Figure 1-2, carbon dioxide is the highest portion of the world greenhouse gas (77%) followed by methane (15%) and N_2O (7%) [17]. Energy production and use (including transportation) sectors represent the largest portion of GHG emission, approximately 80% of total world CO_2 emission [17]. An increase in GHG, especially carbon dioxide, leads to an increase in the greenhouse effect that, in turn, causes climate change. Carbon dioxide emissions are increasing faster in some parts of the world than in others (see Figure 1-3), especially in Asia

Pacific. This is probably a result of the rapid economic growth in this region, especially in China and India [18].

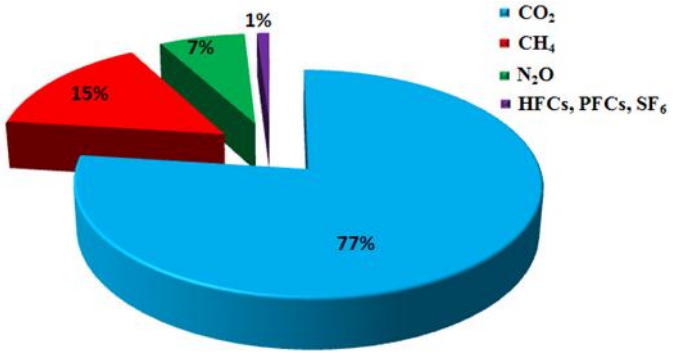

Figure 1-2: World greenhouse gas portion in 2005 based on 44,153 MtCO_2 equivalent [17].

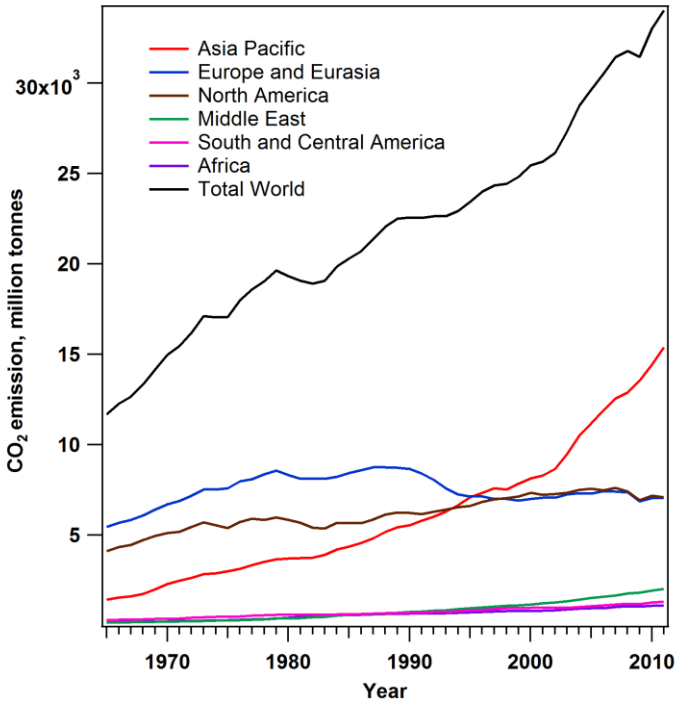

Figure 1-3: Carbon dioxide emission by regions across the world since 1965 [16].

Among the greenhouse gases, carbon dioxide is considered as the most important of the greenhouse gases because of both its concentration in the atmosphere and the strength of its absorption of long-wavelength or infrared radiation [15]. Briefly, the mechanism of the greenhouse effect begins when visible radiation from the sun passes almost unimpeded through the atmosphere and is absorbed by the planet. Then, the thermal radiation emits back from the earth's surface to atmosphere, where

it may be absorbed by GHG, and re-emitted back to the planet. Thus, the GHG thus acts like a blanket surrounding the earth, keeping it warm. However, an increase of GHG causes imbalance between incoming and outgoing thermal radiation, and enhances the '*global warming*' phenomena.

Overall, it has been reported that the temperature of the earth's surface has increased by about 0.7 ºC since the beginning of the 20^{th} century [19]. The estimation of future global warming based on GHG emission is approximately 1 – 5 ºC by 2100, relative to 1990 [20]. Accordingly, the global CO_2 concentration has been targeted to be reduced by 60 – 80% by 2050 compared to the 1990 emission level [21]. The key solution to protect the planet from a global warming effect is to substitute or improve current technologies (especially in the energy sector) with other alternatives that provide a comparable or better performance without GHG emission. Several initial steps have been launched such as the European Union (EU) leaders signed an agreement committing to cut GHG emissions to 20% below the 1990 level by 2020 as well as to promote the use of renewable energy sources [22, 23].

1.3 HYDROGEN ENERGY: OPPORTUNITIES AND APPLICATIONS

Among the various options of alternative energy options, hydrogen seems to be an especially promising technology to satisfy the global energy requirements. Hydrogen offers a potential solution for the world energy crisis by its extremely high specific energy (142 kJ/g) compared to gasoline (46.5 kJ/g) [15]. Moreover, the only emission is water, instead of carbon dioxide and other greenhouse gases, as a result of electrochemical reaction of hydrogen and oxygen. These are the main reasons that have inspired automotive companies and other fuel cell developers to start developing fuel cell technology. Based on energy usage history, it is estimated that the global energy system will be completely supplied by hydrogen by the end of 21st century [24]. In Fiscal Year (FY) 2012, Japan invested approximately US$ 240 million in fuel cell and hydrogen energy programs including subsidies for residential micro-CHP systems, hydrogen infrastructure and vehicle demonstration projects, and fuel cell-hydrogen energy research and development projects [25]. Furthermore, the U.S. National Research Council (NRC) and the National Academy of Engineering (NAE) projected that fuel cell vehicles (FCVs) in the U.S. would make up 12% and 40% of new light duty vehicles sold in 2020 and 2030, respectively [26].

1.3.1 Fuel Cell

The first fuel cell was demonstrated in 1839 by Sir William Grove, which was able to generate electricity from hydrogen and oxygen by reversing the electrolysis process [27]. It has taken over a century to develop a mature process for this technology. Therefore, more intensive research on fuel cells has emerged since 1968 when an alkaline fuel cell system was introduced for the Apollo lunar mission by the National Aeronautics and Space Administration (NASA) [28]. Recently, in 2011, the worldwide supply of fuel cells shipped to the market including stationary, portable and auxiliary power has been reported to be approximately 24,600 units, which grew by 39% compared to 2010 [29].

Figure 1-4 shows a schematic diagram of a Proton-Exchange-Membrane (PEM) fuel cell. To generate electricity, hydrogen gas is supplied to the negative electrode (anode) where electrons are stripped from H_2 molecules, called an oxidation reaction, resulting in the formation of positively charged hydrogen ions, H^+. Typically, the splitting of H_2 can be accelerated by the presence of catalysts such as noble metals,

which can also be used as the electrode. Meanwhile, the electrons are directed to the cathode through a conductor wire where the electric current is generated.

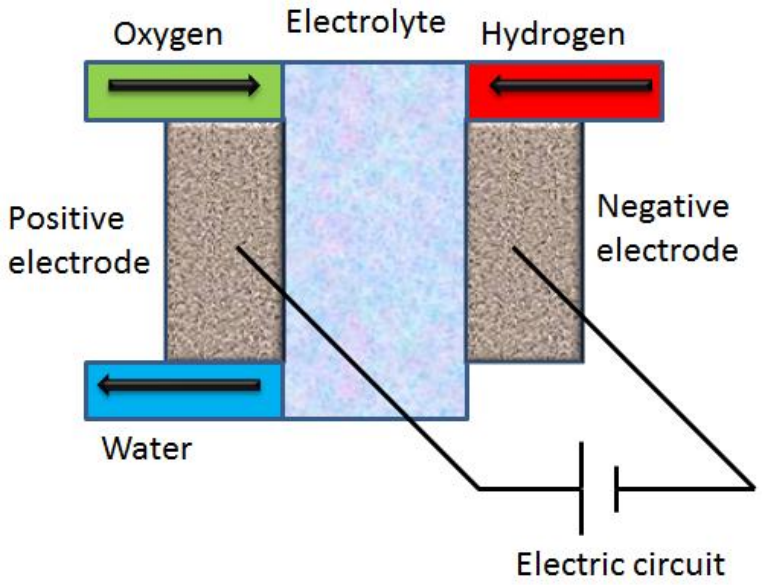

Figure 1-4: Schematic diagram of main components of PEM fuel cell.

At the cathode, O^{2-} ions (O_2 reduced by a reaction with released electrons) associate with H^+ ions, which have diffused through the electrolyte to form water. This seems to be a simple reaction; however, a more complex process has taken place at the cathode than at the anode. Over all, the basic reaction equations of a fuel cell are shown below;

At the anode:

$$H_2 \rightarrow 2H^+ + 2e^- \qquad (1.1)$$

At the Cathode:

$$\frac{1}{2}O_2 + 2H^+ + 2e^- \rightarrow H_2O \qquad (1.2)$$

Total reaction:

$$H_2 + \frac{1}{2}O_2 \rightarrow H_2O \qquad (1.3)$$

The overall reaction is an exothermic process where energy (heat) is released from the process. The higher-heating value (HHV) and lower-heating value (LHV) are defined corresponding to the released heat when water is formed as liquid and steam, respectively [30]. Thus, the difference in the HHV and LHV is the heat required to vaporize the water product. At 25 ºC and atmospheric pressure, the heat or enthalpies

of this reaction (1.3) are 286.02 kJ/mol and 241.98 kJ/mol for the HHV and LHV, respectively, see Table 1-1. In fact, a portion of the HHV, for example, cannot be converted into useful work (electricity) due to an entropy loss. The portion of the reaction enthalpy of HHV that can be converted to electricity in a fuel cell corresponds to Gibbs free energy and is given by the following equation:

$$\Delta G = \Delta H - T\Delta S \qquad (1.4)$$

Therefore, 237.34 kJ/mol out of 286.02 kJ/mol of the HHV can be converted into electricity whilst the remaining 48.68 kJ/mol is converted into heat.

Table 1-1: Enthalpies and entropies of formation for fuel cell reactants and products at 25 ºC and atmospheric pressure [30].

Reactant/product	ΔH (kJ/mol)	ΔS (J/(mol·K)
Hydrogen, H_2	0	130.66
Oxygen, O_2	0	205.17
Water (liquid), H_2O (*l*) : HHV	-286.02	69.96
Water (vapour), H_2O (*g*) : LHV	-241.98	188.84

Assuming that all of the Gibbs free energy can be converted into electrical energy, the maximum possible (theoretical) efficiency of a fuel cell is:

$$\eta = \frac{\Delta G}{\Delta H} \qquad (1.5)$$

Therefore, the theoretical efficiency of a fuel cell at standard temperature and pressure (25 ºC and atmospheric pressure) is (237.34/286.02) ×100 ≈ 83%.

The theoretical voltage of a hydrogen fuel cell can be calculated from:

$$V = \frac{-\Delta G}{nF} \qquad (1.6)$$

where:

n is number of electrons per molecule of H_2 = 2 electrons per molecule

F is Faraday's constant = 96,485 coulomb/electron-mol.

At 25 ºC, the theoretical voltage is then calculated as:

$$V = \frac{237{,}340 \text{ J } mol^{-1}}{2 \cdot 96{,}485 \text{ As } mol^{-1}} = 1.23 \; Volts \qquad (1.7)$$

However, the actual efficiency of fuel cell is around 60%, which means the practical voltage of each cell is about 0.74 V. Higher voltages can be achieved when individual cells are connected together as a fuel cell stack. For example, 1 kW power output can be generated from a 40-cell stack connected in series where each cell operates at 0.6 V and 1 A/cm^2, with a total current of 42 amperes at 24 volts. Furthermore, the efficiency of the entire fuel cell system is lower than that of the stack itself due to energy loss and also energy requirements in the system, as shown in Figure 1-5. Thus, the total efficiency of the system is approximately 51% based on a fuel cell stack with an efficiency of 60% at LHV.

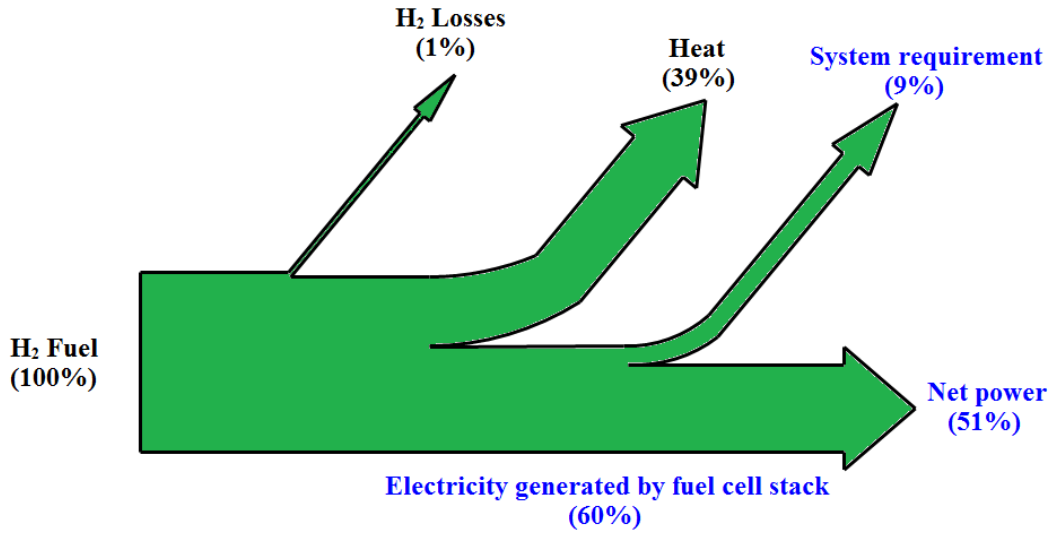

Figure 1-5: The estimated main portions of energy from tank to load of a 60%-efficiency fuel cell stack at LHV.

There are various different types of fuel cell that differ in terms of their electrolyte, chemical reactions and also operating temperature range. The principal types of fuel cell are listed in Table 1-2. Based on their working temperature, the fuel cells can be classified into three categories, i.e., low temperature (50 – 150 ºC), medium temperature (~200 ºC) and high temperature (600 – 1000 ºC) [31].

Table 1-2: Principal types of fuel cells [31-33].

Type	Electrolyte	Charge carrier	Temperature range (°C)	Fuel	Range of efficiency[a] (%)
Proton-exchange-membrane fuel cell (**PEMFC**)	Proton-conducting polymer	H^+	50 – 90	H_2	40 – 60
Alkaline fuel cell (**AFC**)	KOH	OH^-	60 – 150	H_2	45 – 60
Phosphoric-acid fuel cell (**PAFC**)	H_3PO_4	H^+	150 – 220	H_2	35 – 45
Direct-methanol fuel cell (**DMFC**)	Proton-conducting polymer	H^+	60 – 100	CH_3OH	35 – 40
Molten-carbonate fuel cell (**MCFC**)	Li_2CO_3, K_2CO_3	CO_3^{2-}	600 – 700	H_2	45 – 60
Solid-oxide fuel cell (**SOFC**)	Oxygen-ion conductor	O^{2-}	700 – 1000	H_2	45 – 55

[a] The efficiency of fuel cells vary widely depending on the calculation methods, i.e. using the higher heating value (HHV) or the lower heating value (LHV) expression.

1.3.2 Applications for Fuel Cells

There are many potential applications for fuel cells that vary depending on its wide range of possible output power. The output power can be in the range 1 – 50 W, which is suitable for small electronic appliances such as mobile phones, digital cameras and laptop computers. At larger power ranges (kW – MW), hydrogen fuel cells can potentially be applied to vehicles and electricity power plants. Accordingly, the applications are mainly classified into three sectors as follows.

1.3.2.1 Portable Power Sources

The advantage of small fuel cells that can be used as battery replacements is their long operating time without recharging. Recently, many companies across the world have been developing fuel cell solutions for portable products. In 2008, Medis Technologies Ltd (USA) launched a portable charger, Medis 24-7 Power Pack, for small electronic devices such as a mobile phone or an iPod, which is capable of charging a mobile phone for about five or six full charges [34]. The price of a starter kit of this charger with adapter is about $US 40 and a replacement pack is about $US 20. Horizon Fuel Cell Technologies have also developed small portable generators called the MiniPak and HydroPak with cartridge weights of 210 g and 3.0 kg, respectively [35]. The hydrogen cartridge used in the MiniPak, for example, called

HydroStik contains a metal alloy that allows hydrogen to be stored in a solid-state form. The cartridge is able to be refilled approximately 100 times from a pressurized hydrogen gas bottle.

Several governments, e.g. the USA, Germany and UK, have funded many programmes that are developing fuel cell products for military applications [36]. These programmes are specifically looking at how the future military personal power requirements can be met. Prototype fuel cell systems, designed to act as an equivalent to portable battery packs for the infantry, are reaching advanced stages of technical readiness. For instance, the UltraCell XX25 is a portable fuel cell designed to meet the power requirements of mobile electronic devices such as satellite communication terminals, rugged computers and radios used by military and public safety personnel on remote missions as a light weight, long duration power solutions (70% weight savings for a 72-hour mission, compared to batteries) [37]. Some other examples of early military fuel cell products or prototypes include [38]

- Unmanned Aerial Vehicles (UAV)
- Unmanned Ground Vehicles (UGV)
- Soldier portable power
- Silent camp/Silent watch capabilities
- Submarines/Warships
- Trucks/Cars
- Forklifts for defence depots
- Clean base operations

Research and development of fuel cell systems for powering portable electronic devices and micropower systems have emerged from large electronics companies including Fujitsu, Hitachi, IBM, LG, Sanyo, Sony, Samsung, NEC, Sharp and Toshiba [39]. However, it is still difficult to predict when fuel cell powered electronic devices will mature and be available in mass commercial production.

1.3.2.2 Hydrogen Fuel Cell Vehicles

Fuel cells promise a high practical energy efficiency (35 – 60 %) and a CO_2-free-emission engine, which could become a key part in the solution to the energy and environmental crisis [32]. Compared to a battery system, major automotive manufactures have considered fuel cell technology because of its advantages in terms

of the longer driving range and faster refilling rate [40]. The five main parts of a fuel cell vehicle system are illustrated in Figure 1-6.

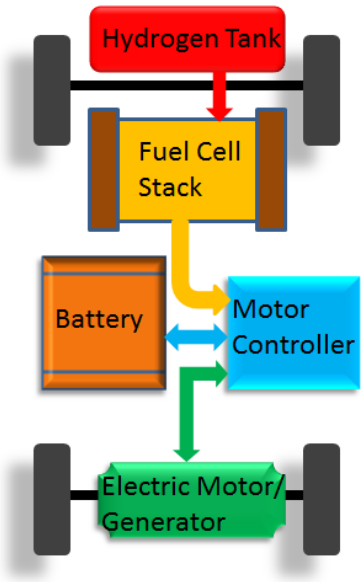

Figure 1-6: Schematic of main parts of a fuel cell vehicle.

The race to develop commercial fuel cell electric vehicles (FCEVs) began during the 1990s and continues in the first decades of the 21st century. As shown in Figure 1-7, the number of hydrogen fuel cell vehicles used in the U.S. significantly increased from 9 units in 2003 to 421 units in 2010 [1]. As a result, the demand for hydrogen as a vehicle fuel has increased dramatically from ~2 to 152 thousand gasoline-equivalent gallons (energy of one gallon of gasoline = 33.4 kWh of electricity ≈ energy of 1 kg H_2) in 2003 and 2010, respectively [1]. The analysis based on major vehicle/fuel scenarios over the 21st century showed that hydrogen-powered FCEV will reach 50% market share by mid-century [40].

Many car production companies have revealed their key progress on FCEV projects during the last two decades. Daimler-Benz launched a project on a fuel cell car named the New Electric Car Number 1 (NECAR 1) in 1994, and announced as the world's first passenger fuel cell vehicle [41]. The sixth version of NECAR concept cars, NECAR 5, was presented in November 2000, claimed as the world's most advanced FCV. The top speed of NECAR 5 is over 145 km/h and it can cover more than 400 kilometres before refuelling.

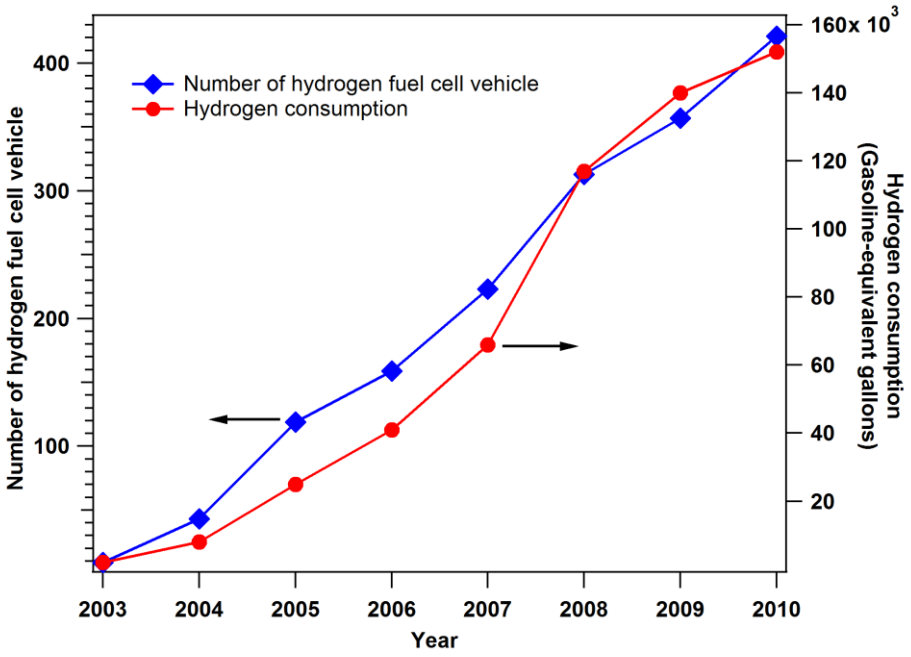

Figure 1-7: Estimated number of hydrogen fuel cell vehicles and their related hydrogen consumption in the U.S. between 2006 and 2010, data from ref. [1].

In July 2002, Honda's FCX Clarity was certified by the U.S. Environmental Protection Agency (EPA) and the California Air Resources Board (CARB) becoming the first FCV for commercial use [42]. The technical specifications of FCX Clarity are given in Table 1-3. Honda also plans for a mass production of 200 units of the FCX Clarity by 2015. In 2012, Toyota and BMW announced a collaboration to share their fuel cell technologies and jointly develop a fundamental fuel cell vehicle platform [43]. Toyota also plans to produce tens of thousands of hydrogen FCEVs annually by the 2020s. Currently, the production cost of a fuel-cell vehicle is about $140,000, but the cost should drop to about $50,000 in next few years due to the economy of scale in mass production [44]. However, it is not only FCEV technology but also hydrogen refuelling infrastructure that needs to be improved. Accordingly, more than 5,200 hydrogen fuelling stations for FCEVs will be operating worldwide by 2020, a significant increase from just 200 stations in 2010 [45]. A large focus on this technology is in Japan where it expects to open 1000 and then 5000 fuelling stations by 2020 and 2030, respectively [46].

Table 1-3: Specifications of Honda fuel cell vehicle FCX Clarity, data from ref. [47].

Vehicle weight	1625 kg
Number of occupants	4
Maximum speed	160 km/h
Driving range	400 km
Maximum power output	100 kW
Fuel cell stack type	PEMFC
Fuel	Compressed H_2 (35 MPa in a 171 L high-pressure tank)

1.3.2.3 Stationary Power Generation

A generation system designed for stationary power generation is similar, in principle, to the automobile application. However, there are some different requirements between these two systems. For example, a compact size and low weight are essential requirements for automotive applications but not so significant in stationary applications. Automobile systems are expected to start up rapidly in an the order of a minute, whereas start-up time at ambient temperature could be approximately 20 – 30 minutes for a stationary system [30]. Finally, a stationary fuel cell power system is expected to be operated with longer operating hours at 40,000 to 80,000 hours compared to 3,000 to 5,000 hours for an automotive system [30]. Stationary applications can be classified with respect to their power output as shown below.

- 1 – 10 kW system supplying electricity for individual houses.
- 10 – 50 kW system supplying electricity for larger homes, groups of homes, and small commercial uses such as small businesses, restaurants, warehouses, and shops.
- 50 – 250 kW system supplying electricity for small communities, office buildings, hospitals, hotels, and military bases.

A proton-exchange-membrane fuel cell (PEMFC) is likely the best candidate system for small stationary power generation, which is limited to about 200 kW. For a larger scale several MW system, Molten-carbonate fuel cell (MCFC) and Solid-oxide fuel cell (SOFC) systems are more attractive than PEMFC because of their internal-reforming function and combined heat and power (CHP) capability [15].

In 2011, FuelCell Energy Inc., founded in the U.S., plans to operate fuel cell power plants in more than 50 locations worldwide [48]. These plants are expected to generate more than one billion kilowatt hours (kWh) of electricity, which can supply more than 90,000 average size U.S. homes for one year. FuelCell Energy's product, the DFC3000 system, can generate power up to 2.8 MW with 47% electrical efficiency [48]. The DFC3000 can be used for on-site power generation and also utilises a combined heat and power (CHP) system. The DFC3000 system also has the potential to supply electricity for larger load requirements such as hospitals, manufacturing facilities, wastewater treatment plants, and utility grid support.

In 1999, MTU CFC Solutions GmbH, a Tognum Group company in Germany, installed a HotModule molten-carbonate fuel cell (MCFC) running with natural gas as fuel [49]. Currently, HotModule type fuel cell plants can generate approximately 250 kW electrical and 170 kW thermal energy. Up until 2008, more than 20 HotModules were installed across Europe. The electricity is fed into a grid distribution system, whilst hot and cold water can be produced from the thermal energy by using an absorption refrigeration unit [49].

Hybrid power system combining a high-temperature fuel cell (HTFC), e.g. molten carbonate fuel cell (MCFC) or the solid oxide fuel fell (SOFC), with a gas turbine (GT) have been introduced as the next generation of power generation systems [50]. This system benefits from the combination of performance advantages and, consequently, exhibits an unusually high fuel-to-electrical efficiency compared to that of either system alone. The hybrid systems are classified in various scales, e.g. 15 kW to 50 MW with an electrical efficiency of 60 to 70% depending on the capacity of the fuel cell modules [50, 51].

Ceramic Fuel Cells (CFC), headquartered in Australia, has developed a small SOFC module, Gennex, which is designed for integration inside future appliances with 60% electrical efficiency at the optimum output of 1.5 kW [52]. Gennex is ideally suited for micro-combined heat and power (micro-CHP) appliances such as high efficiency condensing boilers. Gennex can also supply power to stand-alone, air circulation, electric vehicle re-charging systems.

Grid-independent operation, especially for remote locations, is another promising application for stationary fuel cells [53]. The cost of extending the electricity grid to

these areas is not economically viable when compared to a stand-alone remote-area power supply (RAPS). The photovoltaic (PV) metal-hydride-fuel-cell system, shown in Figure 1-8, is currently considered as a practical application for RAPS. This system is based on solar photovoltaic electricity generation in which the excess power will be used to produce hydrogen via electrolysis. The hydrogen is stored in a metal hydride until required. When the primary energy input is unavailable such as at night and in periods of dull or rainy weather, hydrogen will be released and supplied to the fuel cell to generate electricity.

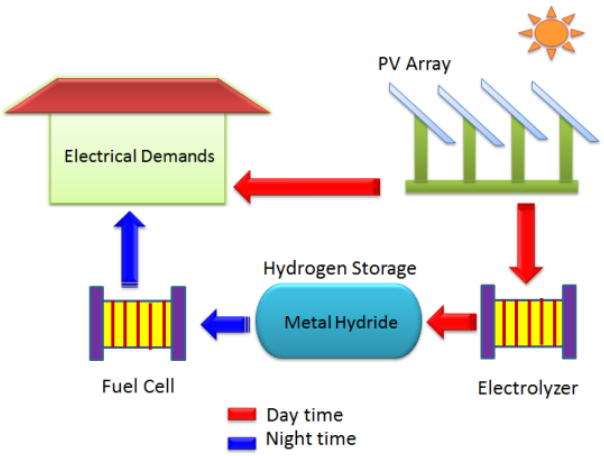

Figure 1-8: Solar-Hydrogen power generation as stand-alone remote-area power supply.

Currently, concentrating solar power is considered as the most efficient use of sunlight to generate power [54]. At the concentrating solar power plant, series of mirrors focus sunlight onto a fluid such as oil or molten salts. Consequently, the hot fluid flows through a heat exchanger producing steam to drive a turbine that generates electricity. However, this system alone cannot provide power at night or during sunless hours. Presently, concentrated solar thermal (CST) systems coupled with heat storage using the heat capacity (sensible heat) of binary liquid molten salt mixtures (40% $NaNO_3$; 60% KNO_3) to produce electricity during sunless hours [55]. However, this system comes with some problems, e.g. requirements of a large quantity, volume and cost of the molten salts to store sufficient heat to operate the plant for several hours. To minimize the problems, it was suggested to use higher energy density storage materials to reduce the volume and mass of material, and to use higher energy storage temperatures to increase overall solar to electricity conversion efficiencies [2].

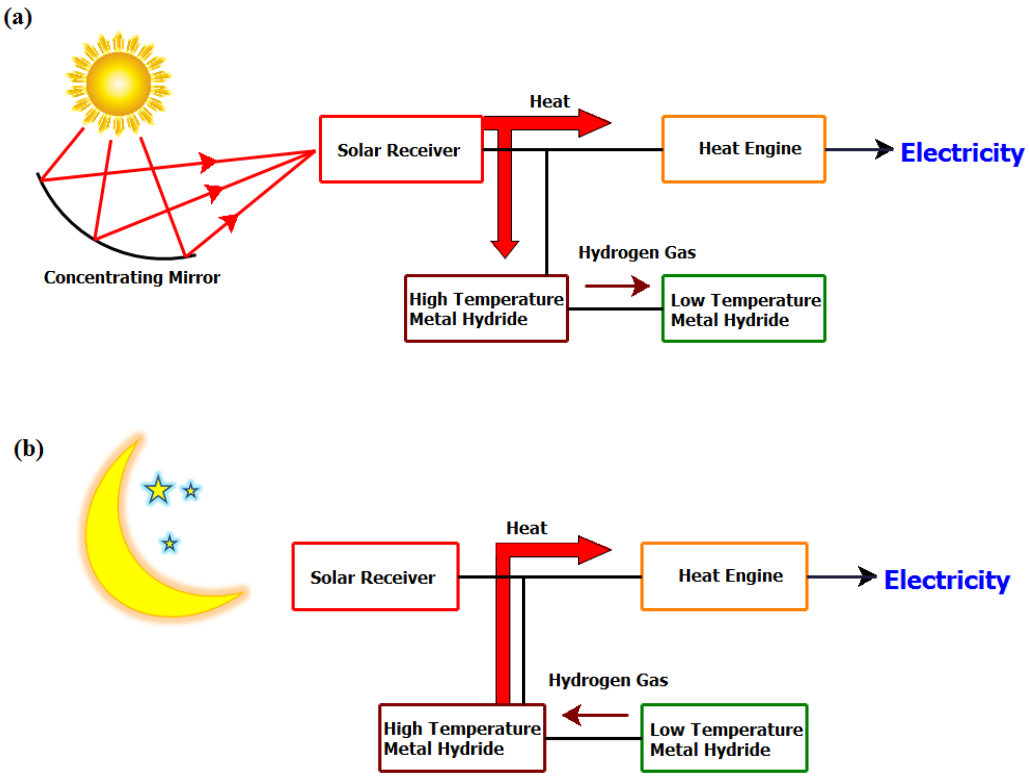

Figure 1-9: Concentrating solar thermal system equipped with metal hydrides as a thermal storage medium during (a) daytime and (b) nighttime operation.

Reversible thermochemical reactions of metal hydrides have been introduced with higher heat storage capacities compared to sensible heat or phase change materials [2]. Figure 1-9 shows the operation of CST system equipped with reversible metal hydride systems (high and low temperature hydrides). There are some candidates of high temperature hydrides for this application such as MgH_2, $MgFeH_6$ and $NaMgH_3$ [54]. On the other side, the low temperature hydrides can be TiFe, $LaNi_5$, $CaNi_5$, $TiMn_{1.5}$ and $NaAlH_4$. Traditionally, heat from solar receiver is primarily used to operate the heat engine (i.e. steam turbine) to generate electricity as shown in Figure 1-9 (a). Excess heat energy can be stored chemically by driving an endothermic chemical reaction at high temperature hydride material to release hydrogen. Consequently, this hydrogen moves to the low temperature hydride material and forms hydride phase. At nighttime, for example, the pressure in this vessel falls as it is cooling down. Then, hydrogen moves back into the high temperature hydride vessel (reactor) forming high temperature hydride (Figure 1-9 (b). This exothermic reaction can supply heat to the reactor to generate electricity at night or sunless period.

1.4 CHALLENGES IN HYDROGEN AS ENERGY CARRIER

1.4.1 Hydrogen Production

Although hydrogen offers benefits as a clean energy carrier, it is noted thatt hydrogen is not an energy source but an energy carrier. Thus, hydrogen can be produced from other energy sources such as natural gas, coal, and petroleum. Accordingly, the advantage of hydrogen as an energy carrier depends on the process of hydrogen production. The key challenge on this issue is how to reduce or avoid the emission of CO_2 during the hydrogen production.

There are several ways of producing hydrogen including steam reforming of natural gas, partial oxidation of hydrocarbons and coal gasification [56]. Therefore hydrogen is predominantly produced from fossil fuels. To produce a kilogram of hydrogen by steam reforming, for example, approximately 13.7 kg of CO_2 is emitted [57]. To avoid CO_2 emission, a special method is proposed to produce hydrogen by water electrolysis using renewable energy such as wind and solar energy [56]**.** Thus, water is split into hydrogen and oxygen through the application of electrical energy, as in equation

$$H_2O + \text{Electricity} \rightarrow H_2 + 1/2O_2 \qquad (1.8)$$

However, only a small amount, approximately 3% worldwide, of the world's hydrogen production is produced via electrolysis [58]. Other challenges in hydrogen production are reducing the capital costs of the equipment, improving the energy efficiency of the electrolyser, and producing at larger scale [59].

1.4.2 Hydrogen Storage

Storing hydrogen is one of the most challenging steps for the transition into a hydrogen-based society as well as issues with hydrogen production and transportation. Ideally, hydrogen should be stored with a high storage capacity under near ambient conditions, safely, economically and only producing environmentally friendly byproducts. Furthermore, the hydrogen storage system should perform with a rapid and reversible hydrogenation and dehydrogenation process for practical applications. Currently, there are several different hydrogen storage techniques including conventional methods (compressed gas and liquid hydrogen) and other

alternative methods (physically and chemically bound hydrogen) [60]. According to the U.S. Department of Energy (DOE), the revised 2015 targets for vehicular hydrogen storage systems are shown in Table 1-4 [61]. Meanwhile, the research on hydrogen storage systems is not only focused on achieving the volumetric and gravimetric capacity targets but also meeting the kinetic and economic requirements.

Table 1-4: U.S. Department of Energy (DOE) revised 2015 targets for light-duty vehicles [61].

Target	2015 (old)	2015 (revised)
System Gravimetric Density (wt.% H_2)	9.0	5.5
System Volumetric Density ($g \cdot H_2/L$)	81	40
Usable specific energy (kWh/kg)	3.0	1.8
Refuelling Rate ($kg \cdot H_2$/minute)	2.0	1.5
System Fill Time for 5-kg fill (minute)	2.5	3.3
Storage System Cost (US$/kg H_2)	67	To be determined

1.4.2.1 *Compressed gas*

Pressurized gas cylinders are currently the most common method to store the hydrogen. Small quantities of hydrogen, as used on a laboratory scale, can be conveniently stored in simple steel pressure cylinders, usually up to 150 bar. For fuel cell vehicles (FCVs), the hydrogen pressure of container may be up to 700 bar to store the necessary fuel for a 500 km driving range, which requires approximately 5 kg of hydrogen [40]. Accordingly, storing hydrogen as a compressed gas requires high-strength containers to support such high pressure. For a given compressed gas container, a major quantity of interest is the maximum gravimetric percentage, *wt.*%, which is defined as the maximum amount of hydrogen stored in the tank divided by the mass of the tank (M_{tank}) including the hydrogen present in the tank. The maximum amount of gas corresponds to the gas content at just under the burst

pressure of the tank, P_{burst}. The performance factor (*PF*) of the tank is then proportional to:

$$PF \equiv \frac{P_{burst}V}{M_{tank}} \quad (1.9)$$

Methods to improve the *PF* involve using better materials and technologies in the tank construction that allow storing higher pressures with lower weights. Vehicular light-weight hydrogen storage tanks made from composite materials are now available, lighter than regular metallic vessels [62]. The vessel consists of an ultra-thin polymeric liner (but can be steel or aluminum), which is over wrapped with carbon fibers set in a resin matrix. The outer layer also protects the vessel from considerable levels of mechanical damage.

For adiabatic hydrogen compression from atmospheric pressure to 200 and 800 bar, the energy required for the compression of 1 kg of hydrogen is around 14 and 23 MJ, respectively [63]. This is between 10 and 16% of the higher-heating value (HHV) energy content of hydrogen. Typically, a multi-stage compression technique can lower energy waste in the process, i.e. between 7 and 13% of the HHV energy. However, including other energy losses, e.g. mechanical and electrical losses, for the entire system, approximately 20% of the HHV energy is required to compress hydrogen from atmospheric pressure to 200 – 800 bar [63].

1.4.2.2 *Liquefied hydrogen*

Liquefied hydrogen (LH_2) has a higher hydrogen storage density (70.8 kg/m^3) than compressed H_2 at 700 bar (39 kg/m^3) [64]. Theoretically, the amount of energy required to cool hydrogen gas from 298 K (25 ºC) to its boiling point of ~20 K and to condense the gas at this temperature under atmospheric pressure is about 14.2 MJ/kg [63]. However, this value is calculated by a simple exergetic analysis which excludes electrical, mechanical, thermal, or flow-related energy losses of complex processes [65]. For instance, the best large plant in the U.S. requires an energy consumption of about 54 MJ/kg to liquefy hydrogen [66]. The most undesirable property of LH_2 is the wasteful loss of hydrogen by boil-off during storage, although cryogenic systems have been designed to minimize this problem. The loss of hydrogen would be significant for a relatively small tank that is used in a vehicle, and may amount to 2 –

3 % a day [64]. The latest tank design for LH_2 using a double-wall and vacuum insulator can store LH_2 up to 2 weeks with minor hydrogen loss [15].

1.4.2.3 *Solid-state hydrogen storage*

Storing hydrogen as a solid with a high volumetric capacity (amount of hydrogen per unit volume) may offer the best solution to store hydrogen, especially for the transportation sector. Figure 1-10 shows a comparison of relative hydrogen tank sizes using various systems to store 5 kg of hydrogen for a mid-SUV car. Thus, the solid-state hydrogen storage systems can provide not only a compact tank size but also improved safety aspects in practical applications [67]. Ideally, hydrogen carrier materials should have the ability to absorb and release hydrogen rapidly as well as reversibly. Moreover, the materials should be inexpensive and be able to be operated at near-ambient conditions.

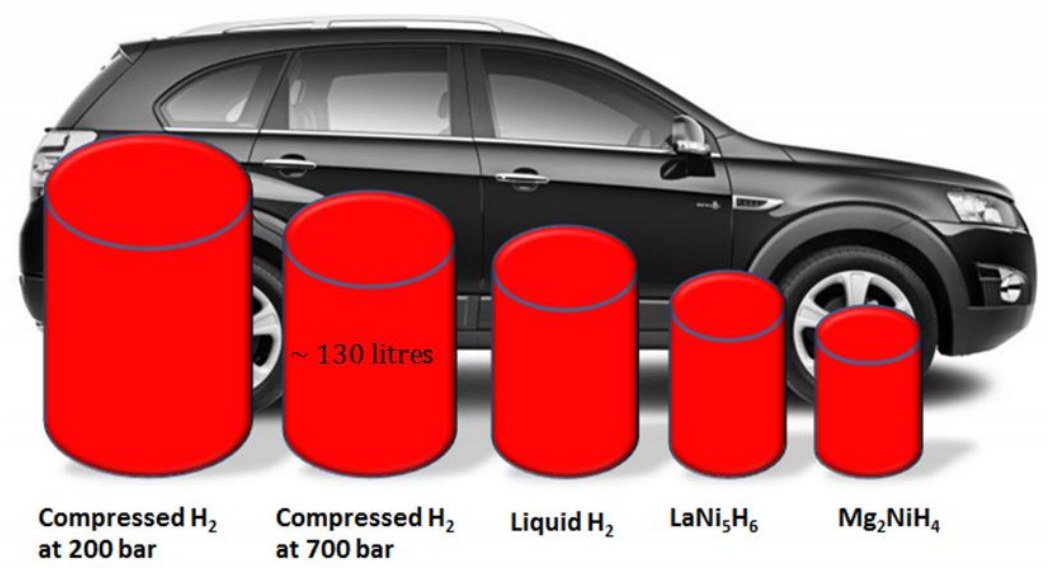

Figure 1-10: Comparison of 5-kg hydrogen tank size of different systems related to an SUV- car size, adapted from ref. [67].

Hydrogen atoms can be bonded in a carrier material by the following mechanisms:
Chemisorption involves the dissociation of hydrogen molecules into hydrogen atoms and subsequent chemical bonding of hydrogen by integration in the lattice of a metal, alloys or chemical compounds [68]. In this case, classically, the metals or alloys (*M*) will react with hydrogen forming a hydride, which is usually considered as a reversible reaction;

$$2M + xH_2 \rightleftarrows 2MH_X + heat \quad (1.10)$$

More details of metal hydrides will be discussed in section 1.4.

Another mechanism for storing hydrogen is *physisorption*, which implies the adsorption of molecular hydrogen by weak van der Waals forces at the surface of highly porous materials such as carbon nanotubes (CNTs), zeolites, porous carbons and metal-organic frameworks (MOFs). The hydrogen storage capacity of these materials is proportional to their specific surface area, surface area per unit mass [69]. The characteristics and hydrogen storage properties of typical porous materials are presented in Table 1-5. Physisorption, a surface phenomenon, normally requires low temperature, usually 77 K (due to its convenience), to lower the thermal energy of hydrogen molecules; otherwise they will easily overcome the van der Waals interactions [70].

Table 1-5: Characteristics and hydrogen storage properties of typical porous materials.

Material	Surface area (m^2/g)	Adsorption capacity (wt.%)	Adsorption pressure at 77 K (bar)	Ref.
Single-wall nanotubes (SWNTs)	854	2.20	10	[71]
Zeolites (NaY)	725	1.80	15	[72]
MOF-5 ($[OZn_4]^{6+}$)	2500 – 3000	4.50	20	[73]
Carbon aerogel (CA)	2206	4.88	46	[74]

1.5 METAL HYDRIDES FOR HYDROGEN STORAGE

The formation of metal hydrides includes the dissociative chemisorption of H_2 on the metal surface and then hydrogen atom diffusion into the crystal lattice [75]. The hydrogen is incorporated in the metal by covalent, ionic or metallic bond for an elemental hydride [76]. Thus, there are a number of elements can form elemental hydrides such as magnesium, calcium, sodium, titanium, zirconium, iron, yttrium, lanthanum, and palladium. Hydrides of elemental metals are called binary hydrides, or simple hydrides, e.g. MgH_2, CaH_2, NaH, TiH_2 and ZrH_2 [76].

Hydrides can also be formed in intermetallic alloys as ternary, quaternary hydrides and other higher degrees depending on the alloy system. In this case, the hydrogen atom resides interstitially in the alloy. It should be noted that a ternary hydride is defined as a hydride formed by a combination of hydrogen with a binary compound or alloy. Figure 1-11 shows typical orders of alloys formed by partial substitution of third and fourth elements into A and/or B sites of an AB_5-type alloy.

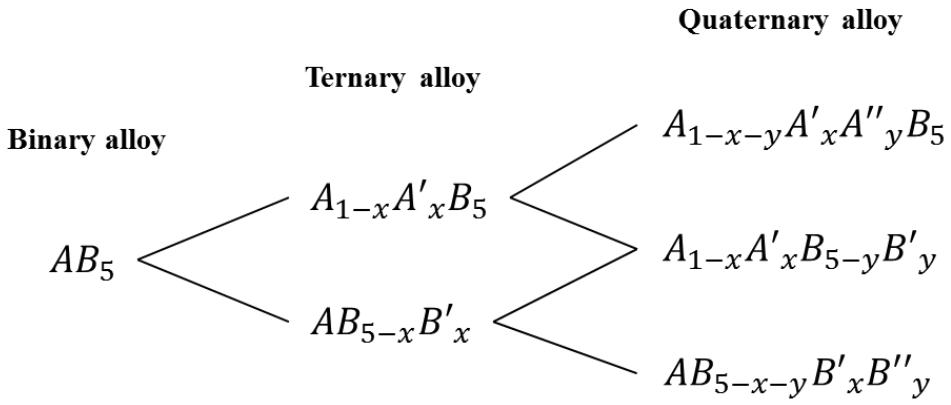

Figure 1-11: Composition formulae of AB_5-type alloy by partial substitution (A', A'' and B', B'' elements substituted at A and B sites, respectively).

Group 1, 2 and 3 salts of $[BH_4]^-$ (borohydride) and $[AlH_4]^-$ (alanate) are especially interesting as potential hydrogen storage materials, known as complex hydrides. The hydrogen forms a covalent bond in the complex hydrides, and is often located at the corners of a tetrahedron with Al or B in the center. These materials have high gravimetric storage capacity, *wt.*%, because of their light weight elements. For instance, the capacity of $NaAlH_4$ and $LiAlH_4$ is 7.4 and 10.5 wt.%, respectively [77]. However, hydrogen decomposition of these complex hydrides usually only occurs at

a temperature above their melting point. Catalysis of hydrogen sorption from $NaAlH_4$ has been successful [11], but there is no catalyst to date that is effective for borohydrides.

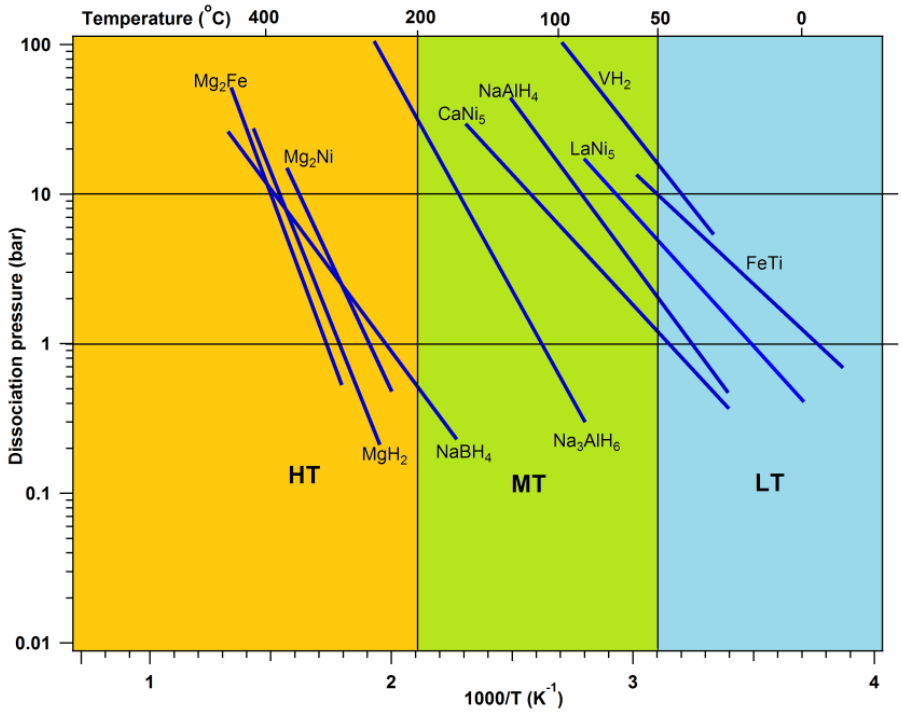

Figure 1-12: Comparison of van't Hoff plots of typical elemental, intermetallic and complex hydrides, data from ref. [77, 78].

Figure 1-12 illustrates the van't Hoff plots of various hydrides as a relationship between equilibrium pressure (P) and the absolute temperature (T) as expressed in the van't Hoff equation:

$$\ln P = \frac{\Delta H}{RT} - \frac{\Delta S}{R} \qquad (1.11)$$

where ΔH is the enthalpy of reaction, R is the universal gas constant and ΔS is the entropy of reaction. Basically, the hydrides can be categorised into three groups based on their operating temperature range [77], i.e. low-temperature (LT), medium-temperature (MT) and high-temperature (HT) hydrides as shown in Figure 1-12. In an ideal scenario for vehicular applications, the desorption pressure of a hydride should operate from 1 to 10 bar at near-ambient temperature [67]. Other hydrogen sorption properties of the storage materials requiring consideration include sorption kinetics and cyclic stability.

CHAPTER 2

EXPERIMENTAL

2.1 SYNTHESIS

All sample preparation procedures were undertaken in an argon atmosphere to protect the materials from moisture and oxygen contamination. Furthermore, many hydrogen storage grade materials can be flammable on contact with moisture or oxygen. Thus, the working chamber of the Ar-filled glove box (Unilab-mBraun, Germany) was equipped with a real-time monitor showing oxygen and water levels, normally, $O_2 < 5$ ppm and $H_2O < 1$ ppm.

2.1.1 Synthesis of Intermetallics by Mechanical Alloying

Mechanical alloying (MA) has been widely used to synthesise new intermetallic compounds. The fundamental of this technique is to modify the microstructures of a mixture of two (or more) individual metal powders, normally, by using high energetic ball milling [79]. The kinetic energy of the balls can be transferred to the powder particles by several mechanisms including ball-powder-wall impacts, ball-powder-ball collisions and ball-powder-ball shearing as shown in Figure 2-1. Accordingly, solid-state chemical reactions can also be induced at room temperature. This method can be used to produce alloys and compounds that are difficult or impossible to obtain by conventional melting and casting techniques. For example, synthesis of alloys from the Al-Ta binary system are difficult due to a significant difference between the melting points of Al (660 ºC) and Ta (3020 ºC), however, the amorphous phase of this compound has been observed after MA for 48 h [80].

The reaction products during the milling process may be formed as different phases, e.g. solid solutions, intermediate and amorphous alloys, respectively [81]. A crystalline phase can be formed from a non-crystalline product by heat treatment or annealing. The annealing of mechanically alloyed powders causes grain growth, the release of microstrain and changes to the phase structure in the material [82]. Buschow [83] mentioned that the annealing temperature should be lower than the *peritectic* temperature where a solid phase and liquid phase exist and form a second solid phase. The proper conditions of annealing (temperature and time) are required

for a particular mixture to reach a satisfactory alloy homogeneity [84]. For instance, an amorphous ball-milled mixture of Ca and Ni (at a desired composition) forms crystalline $CaNi_5$ after annealing at 640 ºC for 2 h [85].

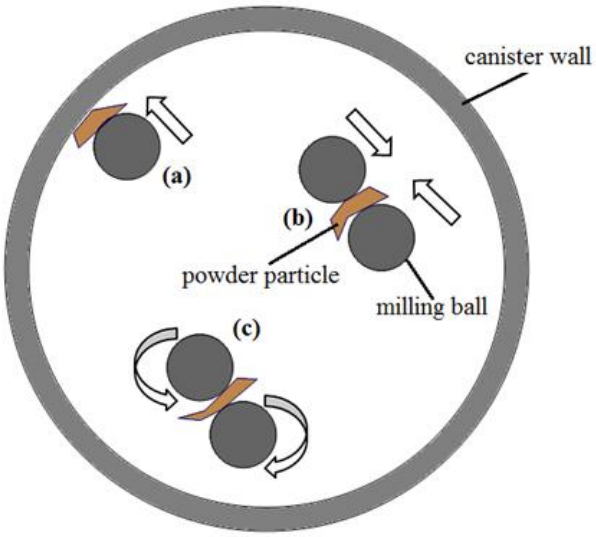

Figure 2-1: Schematic of ball milling mechanisms; (a) ball-powder-wall impact, (b) ball-powder-ball collision and (c) ball-powder-ball shearing, the arrows indicate the ball direction.

During ball milling, the microstructure of powder particles can be affected by both fracturing and cold welding processes, which can be divided into four stages, i.e. initial stage, intermediate stage, final stage and complete stage [86]. At the *initial stage*, the particles are flattened by the impact of the balls and create a composite layer. The particle size of the composite is distributed across a wide range from a few micrometers to a few hundred micrometers. The *intermediate stage* is significantly dominated by fracturing and cold welding, leading to microstructural refinement with randomly orientated lamellae. The temperature of the powder may increase due to the transfer of kinetic energy from the balls to the powder. Dissolution of solute elements and the formation of solid solution regions may occur at this stage but the chemical composition of the alloyed powder is inhomogeneous. The refinement and reduction in particle size continues in the *final stage* with the production of finer lamellae. The uniform alloy is likely formed at this stage and the microstructure of the particles is more homogenous than that of the previous stage. Homogeneity of the particles implies an equilibrium between cold welding and fracturing [87]. At the *completion stage*, the powder particles have been deformed to a metastable structure containing a uniform distribution of dispersoids, considered as stable insoluble

phases in the alloy matrix. Further milling will not physically improve the microstructure as it has reached a limiting equilibrium. The uniform alloy has thus been achieved with a uniform composition equivalent to the starting mixture.

In this research, all $CaNi_5$-based alloys were prepared by ball milling, performed with a custom made ball milling canister (650 cm^3 internal volume) (see Figure 2-2) attached to a Glen Mills Turbula T2C shaker mixer operated at 160 rpm. The ball milling canister was made from stainless steel (316) and was sealed with an o-ring on both ends. The milling balls were also made from the same material (316 SS) as the canister to minimise sample contamination due to the degradation of both the canister and balls. The milling equipment was made from 316-grade stainless steel because of its high corrosion and pitting resistance.

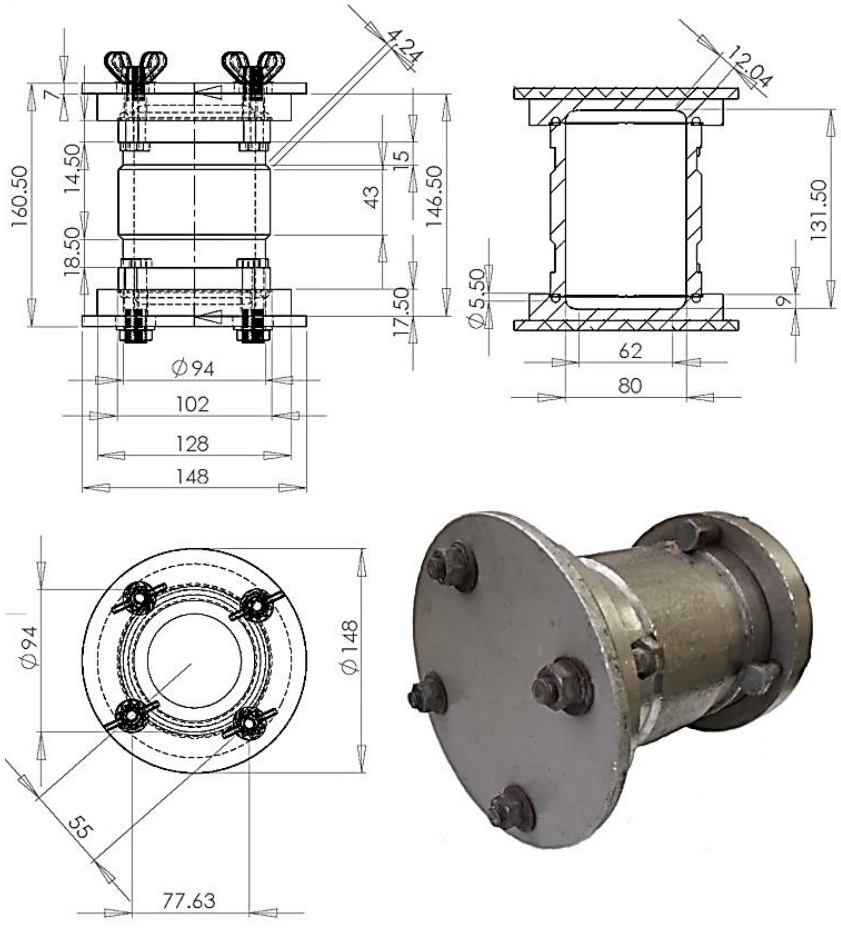

Figure 2-2: Schematics and photo of custom-made 316 SS ball-milling canister used at Curtin University on a Glen Mills Turbula T2C Shaker-Mixer. All measurements are given in mm. Top and bottom plates are sealed by the rubber o-rings, adapted from [88].

To prevent oxidation and contamination during milling, all sample mixtures were milled under an argon atmosphere at room temperature. However, the actual temperature, both local and overall temperatures, in the canister during milling might be higher than room temperature due to the high-energy ball impacts and also exothermic mechanochemical reactions among the powder particles. The ball to powder ratio (BPR) is another controlled milling parameter. A wide range of BPRs have been used in a variety of investigations, e.g. from 1:1 to 220:1 [89]. In this research, all samples were milled with a BPR of 12:1 using an equal number of 12.7 mm and 7.938 mm 316 SS balls. As suggested by Suryanarayana [89], the combination of different ball sizes results in the random motion of the milling balls, thus, the highest collision energy can be obtained. Finally, the milling time was also varied from 20 to 40 h to investigate the effect of this parameter on alloy phase formation.

2.1.2 Alloy Annealing Procedure

After ball milling, the mixture of metals is most often transformed into an amorphous phase. Crystallization of the amorphous compound can be obtained by annealing, a heat treatment process at a certain temperature. Annealing of the powder results in strain relief and leads to an increase in crystallite size [90]. The formation of crystalline structure is affected by not only the annealing temperature, but also annealing time and atmosphere [82]. To investigate the effects of these parameters, the as-milled powder was subjected to annealing at various temperatures (500 – 800 ^{o}C) and durations (3 – 48 h) under vacuum or an argon atmosphere.

2.1.3 Nanoscaffold and Nanoconfinement Synthesis

The idea of nanoconfined $NaAlH_4$ is proposed to limit the $NaAlH_4$ particle size to the nanoscale. This concept of nanoconfined $NaAlH_4$ in an ordered mesoporous carbon scaffold (CMK-1) is shown schematically in Figure 2-3. The $NaAlH_4$ particles are formed and held within the CMK-1 scaffold with a pore size of 2 – 3 nm [91]. As a result of nanoscopic particle size, the hydrogen sorption kinetics and/or thermodynamic properties of this complex hydride may be altered [92]. Furthermore, the presence of the scaffold also prevents long-range phase segregation as Al and NaH during the hydrogen desorption process. Thus, reversibility of this hydride is also enhanced and can occur at mild conditions.

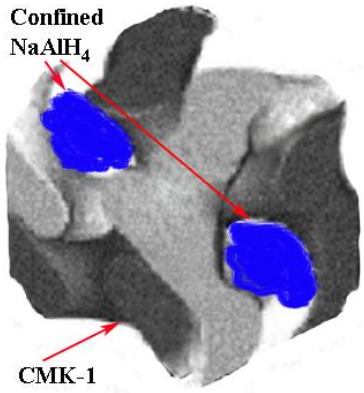

Figure 2-3: Nanoconfinement of $NaAlH_4$ in a mesoporous CMK-1 scaffold, adapted from [91].

The mesoporous carbon, CMK-1, was prepared using an MCM-48 silica template that was impregnated with sucrose in the presence of sulphuric acid, followed by carbonization and then removal of the silica template by a NaOH solution as shown in Figure 2-4. The ordered mesoporous silica, MCM-48, was firstly synthesised according to [93] by dissolving 10 g of cetyltrimethylammonium bromide (CTAB, Sigma-Aldrich) and 1.1 g of sodium hydroxide (NaOH, ≥ 99 %, Merck) in 56.6 g of deionized water at 35 ºC, and then 11.9 g of tetraethylorthosilicate (TEOS, ≥ 99.0 %, Fluka Chemika) was added dropwise. The mixture was heated in a water bath at 100 ºC for 24 h. After cooling to room temperature, the pH of the mixture was adjusted to 7 using 1 M HCl solution, followed by heating at 100 ºC for a further 24 h. The product was filtrated, rinsed with distilled water, and dried in air at 100 ºC. It was then calcined by thermal treatment in air at 550 ºC for 6 h, resulting in ~3 g of MCM-48.

Ordered mesoporous carbon CMK-1 was synthesised according to [94] by adding 1.25 g of sucrose (≥ 99.5 %, Sigma-Aldrich) into a solution of 0.14 g of sulphuric acid (H_2SO_4) and 5 g of deionized water. Then 1 g of MCM-48 was added into the above solution. The mixture was then heated in air at 100 ºC for 6 h, and subsequently at 150 ºC for 6 h in air. The mixture was then reheated at 100 and 150 ºC for 6 h, respectively, after a second batch of 0.80 g of sucrose, 0.09 g of H_2SO_4 and 5.0 g deionized water was added. The product was treated at 900 ºC for 6 h under vacuum for carbonization of the sucrose to form the templated scaffold. To remove the silica template from the carbon template, the product was washed with excess 1 M NaOH solution in deionized water (50 vol%) and ethanol (50 vol%) just below its boiling point. It was then filtered, rinsed with ethanol and rewashed with

deionized water (50 vol%)–ethanol (50 vol%) solution three times just below its boiling point. Finally, the product was dried at 100 ºC for 2 h in air and finally at 250 ºC for 3 h under vacuum to remove moisture and adsorbed gases before transferring the carbon scaffold into a glovebox under an Ar atmosphere.

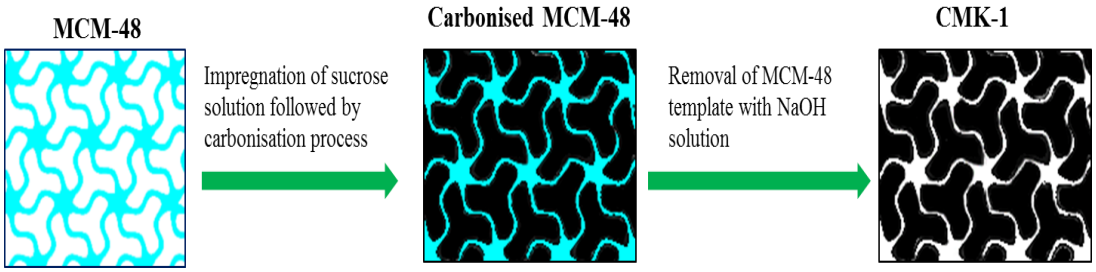

Figure 2-4: Preparation process of ordered mesoporous carbon, CMK-1, from an MCM-48 silica template.

$NaAlH_4$ was infiltrated into the pores of the CMK-1 scaffold either by a solvent or melt infiltration method. For solvent infiltration, the precursor solutions were prepared under an Ar atmosphere by using 1.2 g of $NaAlH_4$ (95 % purity, Sigma–Aldrich) and 23.1 ml of anhydrous tetrahydrofuran (THF, ≥ 99.9 %, Sigma–Aldrich) to make a 1 M $NaAlH_4$ solution. A catalysed sample was also prepared in the same manner with the addition of 0.07 g of titanium trichloride ($TiCl_3$, 99.995 %, Sigma-Aldrich) to the $NaAlH_4$ solution to yield 2 mol% Ti-doped $NaAlH_4$. CMK-1 (1 g) was added to this solution, magnetically stirred for 15 h and then centrifuged for 30 minutes to separate the loaded scaffold from excess solvent. This was followed by decanting the excess solvent off. Surface deposits were removed by washing the CMK-1 surface with pure THF followed by centrifuging for 20 minutes and then decanting once more. Finally, the samples were dried in a glove box under an argon atmosphere for several days followed by 2 h under vacuum at room temperature before hydrogen desorption measurements were conducted.

For the melt infiltration, $NaAlH_4$ and CMK-1, with a certain weight ratio of $NaAlH_4$/CMK-1, i.e. 20, 33 and 50 wt.%, was mixed manually by hand-grinding using an agate mortar in an Ar-filled glovebox and loaded into a stainless steel cell. The sealed cell was evacuated and filled with hydrogen to 110 bar at room temperature. It was then heated to 185 ºC, which is just above the melting point of $NaAlH_4$, and kept at this temperature for 15 minutes with the final hydrogen pressure of 125 bar before cooling to room temperature.

2.2 CHARACTERISATION

The as-synthesised samples were characterised in regard to their morphology, crystalline structure, elemental and phase composition. Thus, several techniques were performed in this research including powder X-ray diffraction (XRD), small angle X-ray scattering (SAXS), scanning electron microscopy (SEM) and energy dispersive X-ray spectroscopy (EDS).

2.2.1 X-ray Diffraction

An X-ray diffractometer is a key instrument for both phase identification and crystal structure determination of materials. The XRD method can reveal details of internal microstructure of matters in the order of 10^{-10} m in size. The information that may be obtained from XRD analysis includes phase composition, crystallite size, lattice parameters, atom positions in the unit cell and site occupancies, etc. In this study, all samples were synthesised in powder form, thus, the *X-ray diffraction* (XRD) in this case is also known as the *powder X-ray diffraction* (PXD) method.

In conventional laboratory based X-ray diffraction experiments, X-rays are produced when electrons with sufficient kinetic energy are rapidly decelerated by bombarding a metal target such as Cu, Mo, Cr, Fe, Co, Ag and W. When the voltage used for accelerating electrons is raised above a certain threshold value, characteristic radiation of the target metal appear as sharp peaks at certain wavelengths, superimposed on the continuous spectrum. The energy (and wavelength) of these peaks is characteristic of the target metal, called characteristic lines. These lines fall into several sets, referred to as *K*, *L*, *M*, etc., as a result of electrons transferring from a particular higher energy level to a vacant level with the consequence of X-ray emission, see Figure 2-5.

A typical voltage for accelerating electrons to generate X-rays from a Cu target, for example, is 25 – 40 kV. Only two characteristic lines, K_α (1.54 Å) and K_β (1.39 Å), are observed at low energy resolution. In practice, a Ni filter is often used to attenuate Cu K_β radiation. In fact, the K_α line can be seen as a doublet ($K_{\alpha1}$ and $K_{\alpha2}$) due to the splitting of 2*p* orbitals in Cu, and leads to slightly different wavelengths of $K_{\alpha1}$ (1.540598 Å) and $K_{\alpha2}$ (1.544426 Å) [95]. The intensity ratio of $K_{\alpha1}$ to $K_{\alpha2}$ is approximately 2 to 1.

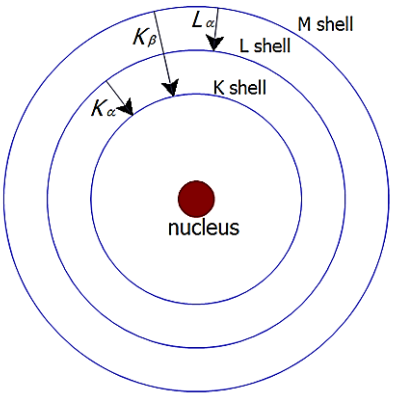

Figure 2-5: Schematic of electronic transition in an atom.

The ideal XRD sample is homogeneous and the crystallites are randomly distributed. Thus, only crystallites having reflecting planes (*h*, *k*, *l*) parallel to the specimen surface will contribute to the reflected intensities. If the sample is in a truly random orientation, each possible reflection from a given set of *h*, *k*, *l* planes will have an equal number of crystallites contributing to the reflected intensities. Figure 2-6 illustrates a schematic of the diffraction of X-rays by a pair of parallel planes, P_1 and P_2, with the interplanar spacing of *d*. The parallel incident rays, *A* and *B*, make an angle (θ) with these planes, and then scatter from the crystal by periodic atoms located on the planes. The angle between the incident and reflected beams (2θ) is known as the diffraction angle.

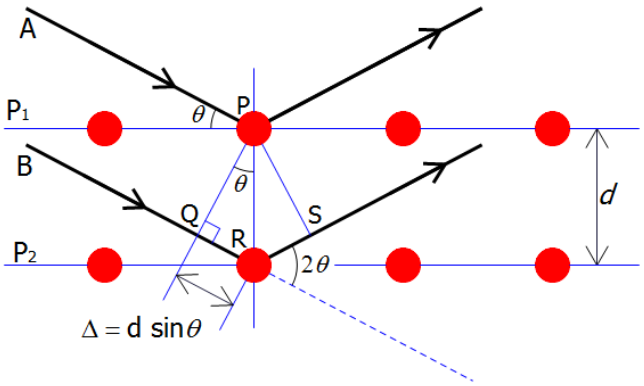

Figure 2-6: Diffraction of X-rays by a crystal.

A diffraction pattern is formed from the interference of the scattered waves. The traveling distance of ray *B* through the crystal is greater than ray *A* by the length

$\Delta = QR + RS$. Constructive interference occurs when two waves are in phase with their traveling paths separated by an integer number of wavelengths (λ), i.e.

$$\Delta = n\lambda \qquad : n = 0, \pm 1, \pm 2, \ldots \qquad (2.1)$$

This results in the formation of a new wave with larger amplitude. As can be easily seen from Figure 2-5, geometrically,

$$\Delta = 2dsin\theta \qquad (2.2)$$

Combining equations (2.1) and (2.2), thus

$$n\lambda = 2dsin\theta \qquad (2.3)$$

Equation (2.3) is known as *Bragg's law*.

In this research, a Bruker D8 Advance diffractometer at Curtin University was utilised to collect XRD data. This diffractometer is configured in Bragg-Brentano geometry with a θ:θ (or 2θ) setup as shown in Figure 2-7. Slits are used to control the divergence of the incident and reflected X-rays. According to this setup, the sample position is fixed while the X-ray tube and the detector move simultaneously at the same rate over the angle θ with respect to the sample surface plane.

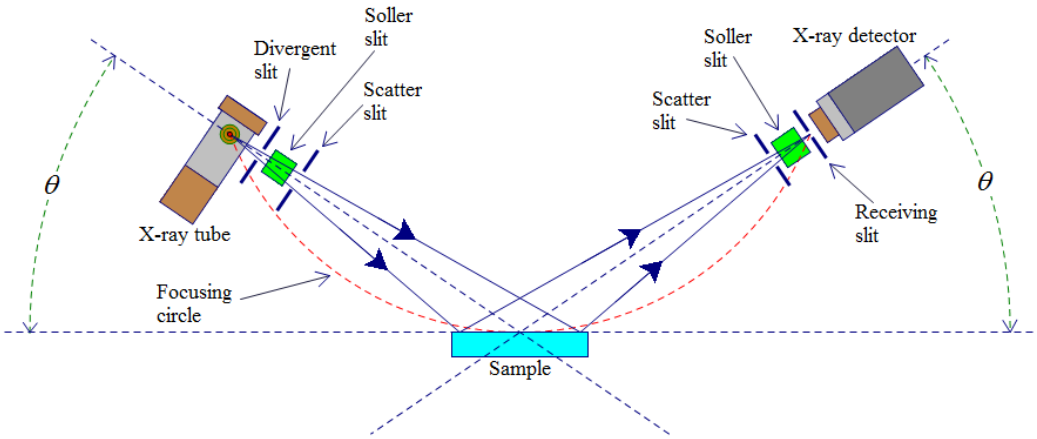

Figure 2-7: X-ray diffractometer schematic in Bragg-Brentano geometry.

To collect data, the diffractometer was operated with the instrument parameters given in Table 2-1. Samples were loaded into an air-tight dome sample holder in an argon glovebox, which proved very successful in maintaining an air-free

environment for samples during data collection. The holder consists of two parts, e.g. base and dome, made from poly(methylmethacrylate) (PMMA), which is joined and sealed with a rubber o-ring. This holder type, generally, attenuates the diffracted X-ray intensity by a factor of 3 when the sample was loaded in Ar-atmosphere [88]. In addition, amorphous humps from PMMA at ~ 10º and 20º 2θ are present in the background, see Figure 2-8.

Table 2-1: X-Ray diffraction instrumental parameters for the Bruker D8 Advance diffractometer at Curtin X-ray Laboratory (CXL), Curtin University.

Parameter	
Radiation source	Cu (λ = 1.5418 Å)
Operating voltage	40 kV
Operating current	40 mA
Detector	3º Linear PSD (LynxEye)
Goniometer radius	250 mm
Sample length	25 mm
Receiving slit length	17 mm
Fixed divergence slit angle	0.3º
Primary Soller slit angle	2.5º
Secondary Soller slit angle	2.5º

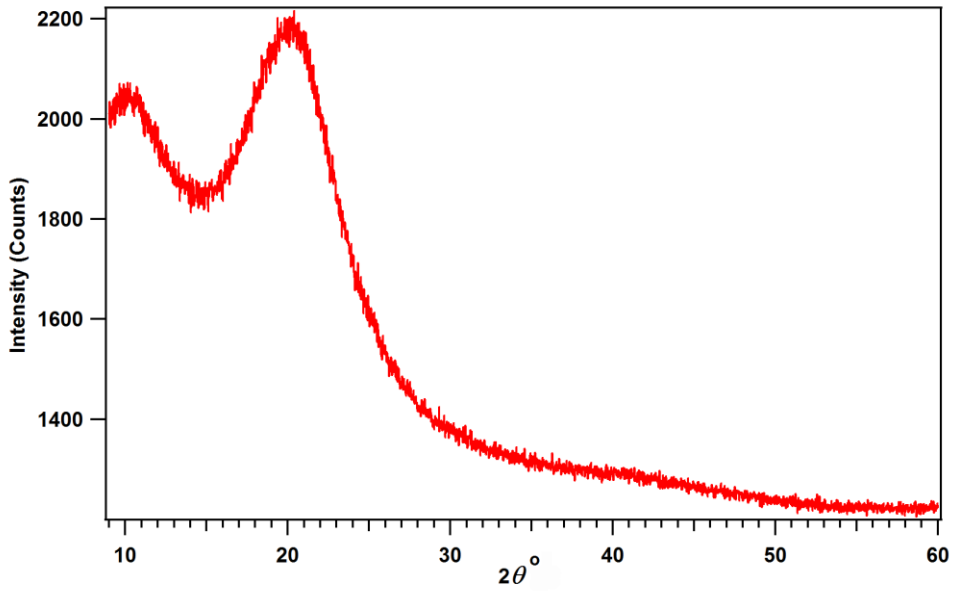

Figure 2-8: XRD pattern of poly(methylmethacrylate) (PMMA) dome sample holder filled with Ar gas.

As mentioned above, the diffraction pattern provides information such as relative phase abundance in a sample, unit cell parameters and site occupation of atoms in a unit cell. Rietveld analysis is a comprehensive method performed on the collected XRD pattern by least squares fitting a calculated pattern(s) to the raw data [96]. The success of Rietveld refinement can be indicated by key figures-of-merit (FOM), e.g. agreement indices (*R* values) and the goodness-of-fit (*GOF*) factors. The common *R* values include profile *R* (R_p), weighted profile *R* (R_{wp}), Bragg *R* (R_B) and expected profile *R* (R_{exp}). Accordingly, the refinement is usually acceptable when the *GOF* is less than 4, R_B for each phase is less than 4% and R_{wp} is less than 20% for the XRD pattern [96, 97]. Figure 2-9 shows an example of a Rietveld refinement plot for a $CaNi_5$ alloy using the Topas v.4.2 (Bruker, Germany) software package.

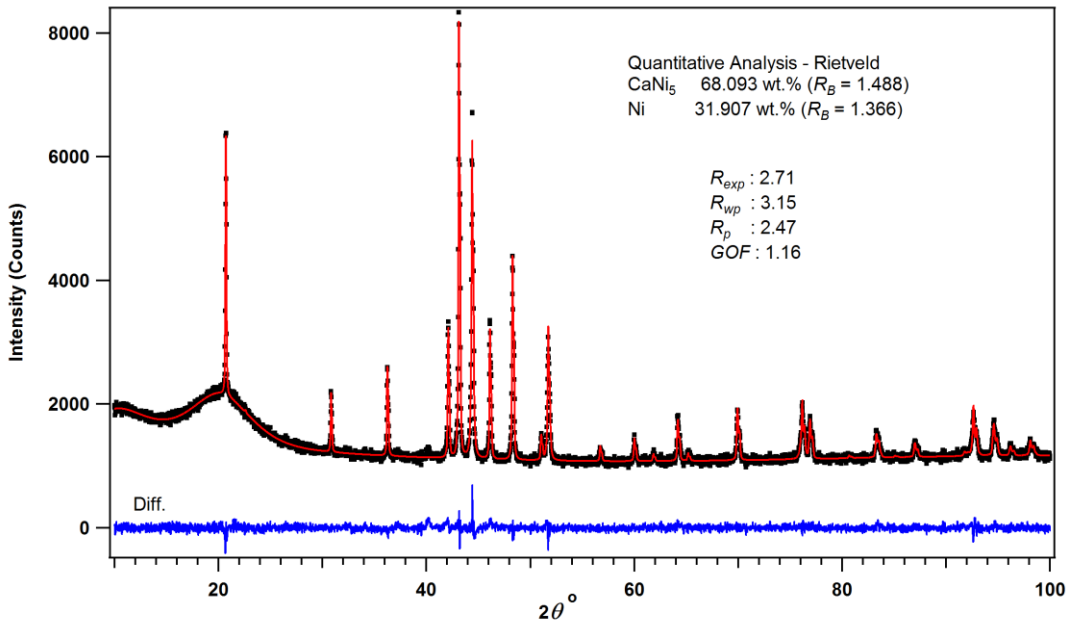

Figure 2-9: Rietveld refinement for a synthesised $CaNi_5$ alloy. The collected XRD and calculated patterns are represented by black dots and a red line, respectively. The blue line below the plot is the difference profile.

2.2.2 Small-Angle X-ray Scattering

Small-angle X-ray scattering (SAXS) can resolve microstructural features as well as crystallographic features with a dimension between tens and several thousand angstrom [98]. Thus, the information from SAXS analysis reveals structural and ordering information on the nanometer to submicrometer scale. In contrast to XRD, which detects the diffraction of X-rays from the crystal lattice with diffraction angles (2θ) of ~0.5 – 170º, SAXS occurs from particles or fluctuations in electron density at

angles $2\theta < 5^{o}$. The SAXS technique can analyse samples regardless of whether they are crystalline or amorphous. A typical small-angle X-ray scattering setup is shown in Figure 2-10. The scattered beam makes a scattering angle, 2θ, with the direction of the incident X-ray.

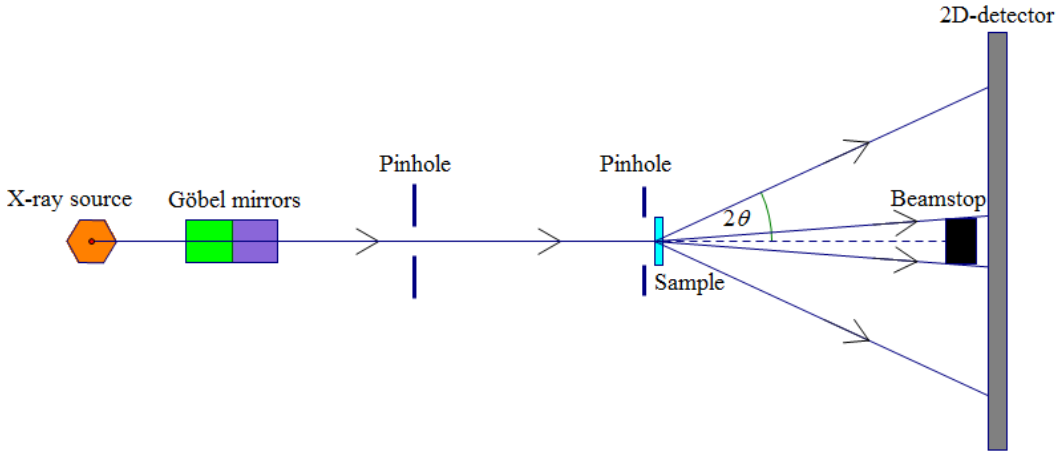

Figure 2-10: Schematic of the main parts of a small-angle X-ray scattering (SAXS) setup.

Figure 2-11 illustrates the scattering of X-rays from a sample. Two scatterers (electrons) located at points O and P are small enough to consider as points of scattering. $\vec{S}_0$ and $\vec{S}$ are represented unit vectors in the direction of the incident and scattered X-rays, respectively, and $\vec{r}$ is a position vector pointing from O to P.

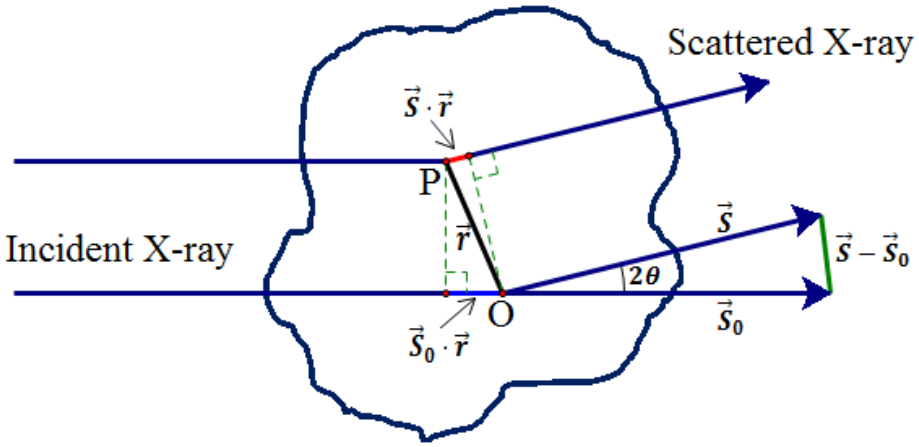

Figure 2-11: Schematic of X-ray scattering from a particle.

The path difference of the upper beam against the lower beam is $\left|\vec{\boldsymbol{S}} \cdot \vec{\boldsymbol{r}} - \vec{\boldsymbol{S}}_{\boldsymbol{0}} \cdot \vec{\boldsymbol{r}}\right|$. The phase difference (in radian) of these two waves is

$$\frac{2\pi}{\lambda}\left|\vec{\boldsymbol{S}} \cdot \vec{\boldsymbol{r}} - \vec{\boldsymbol{S}}_{\boldsymbol{0}} \cdot \vec{\boldsymbol{r}}\right| = \vec{\boldsymbol{q}} \cdot \vec{\boldsymbol{r}} \qquad (2.4)$$

Thus,

$$\vec{\boldsymbol{q}} = \frac{2\pi}{\lambda}\left(\vec{\boldsymbol{S}} - \vec{\boldsymbol{S}}_{\boldsymbol{0}}\right) \qquad (2.5)$$

Vector $\vec{\boldsymbol{q}}$ is also known as scattering vector. The magnitude of vector $\vec{\boldsymbol{S}} - \vec{\boldsymbol{S}}_{\boldsymbol{0}}$ can be calculated, i.e.

$$\begin{aligned}\left|\vec{\boldsymbol{S}} - \vec{\boldsymbol{S}}_{\boldsymbol{0}}\right|^{\boldsymbol{2}} &= \left|\vec{\boldsymbol{S}}\right|^{\boldsymbol{2}} + \left|\vec{\boldsymbol{S}}_{\boldsymbol{0}}\right|^{\boldsymbol{2}} - 2\left|\vec{\boldsymbol{S}}\right|\left|\vec{\boldsymbol{S}}_{\boldsymbol{0}}\right| cos2\theta \\ &= 1 + 1 - 2(1)(1)cos2\theta \\ &= 2 - 2cos2\theta \\ &= 2(1 - cos2\theta) \\ &= 2(2sin^2\theta) \\ &= 4sin^2\theta \qquad (2.6)\end{aligned}$$

Hence,

$$\left|\vec{\boldsymbol{S}} - \vec{\boldsymbol{S}}_{\boldsymbol{0}}\right| = \sqrt{4sin^2\theta} = 2sin\theta \qquad (2.7)$$

From equation (2.5) and (2.7), the magnitude of scattering vector, q, can be determined, i.e.

$$q = \frac{4\pi sin\theta}{\lambda} \qquad (2.8)$$

From Bragg's law, $\lambda = 2dsin\theta$, equation (2.8) can be rewritten as

$$q = \frac{2\pi}{d} \qquad (2.9)$$

The scattering intensity, $I(\vec{\boldsymbol{q}})$, is determined from the product of the scattering amplitude, $A(\vec{\boldsymbol{q}})$, and its complex conjugate, $A^*(\vec{\boldsymbol{q}})$, i.e.

$$I(\vec{\boldsymbol{q}}) = A(\vec{\boldsymbol{q}}) \cdot A^*(\vec{\boldsymbol{q}}) = |A(\vec{\boldsymbol{q}})|^2 \qquad (2.10)$$

For a continuous scatterer, amplitude of the entire scattered volume *V* is given by

$$A(\vec{\boldsymbol{q}}) = \iiint \rho(\vec{\boldsymbol{r}}) \cdot e^{-i\vec{q}\cdot\vec{r}}\, dV \qquad (2.11)$$

where $\rho(\vec{\boldsymbol{r}})$ is electron density.

Consider scattering from a solid sphere (a centro-symmetric object) as the simplest system, the scattering amplitude, $A(\vec{\boldsymbol{q}})$, does not depend on the orientation of scattering vector ($\vec{\boldsymbol{q}}$) then it can be given by

$$A(q) = 4\pi \int_0^\infty \rho(r) \frac{\sin(qr)}{qr} r^2 dr \qquad (2.12)$$

For a uniform solid sphere with a radius of *R*, the electron density is expressed by

$$\rho(r) = \begin{cases} 1, & r \le R \\ 0, & r > R \end{cases} \qquad (2.13)$$

Thus,

$$\begin{aligned} A(q) &= 4\pi \int_0^R \frac{\sin(qr)}{qr} r^2 dr \\ &= \frac{4}{3}\pi R^3 \frac{3[\sin(qR) - qR\cos(qR)]}{(qR)^3} \end{aligned} \qquad (2.14)$$

From equation (2.14), the scattering amplitude at q = 0 is equal to the volume of the sphere. The scattering amplitude is then normalised so that a consequent intensity $I(q=0) = |A(q=0)|^2 = 1$. Thus, the normalised function of $|A(q)|^2$ is then written as

$$P(q) = \left|\frac{1}{V} A(q)\right|^2 \qquad (2.15)$$

$P(q)$ is also called the form factor. Therefore, the form factor of a sphere with radius *R* is

$$P(q) = \left(\frac{3[\sin(qR) - qR\cos(qR)]}{(qR)^3}\right)^2 \qquad (2.16)$$

This function is directly proportional to the scattering intensity, *I*(*q*), i.e.

$$I(q) \equiv P(q) \qquad (2.17)$$

The form factor depends on the product qR and therefore a large particle has a narrow curve in q (and in scattering angle) and a small particle has a broader curve as shown in Figure 2-12.

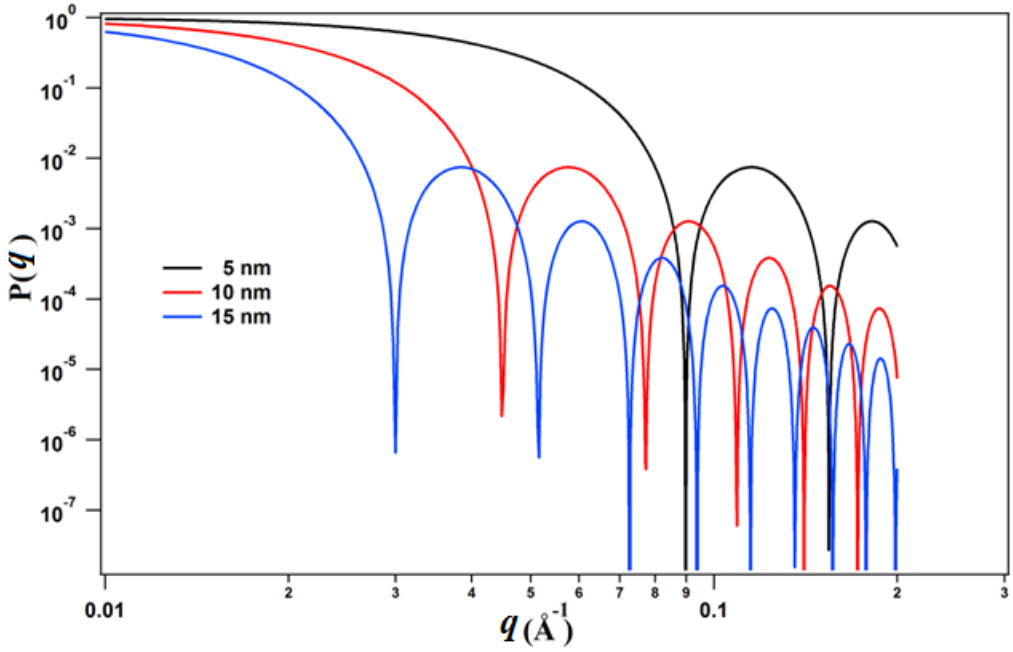

Figure 2-12: Form factor of ideal monodisperse spheres with different radii.

There are two important regions that can present in SAXS data for many applications, *Guinier* and *Porod* regions [99] as shown in Figure 2-13. The scattering data, typically at low q, called the Guinier region reveals, especially, the estimation of the overall size of the particle. The Guinier approximation is given by:

$$I(q) = I(q=0)e^{\left(-\frac{q^2R_g^2}{3}\right)} \qquad (2.18)$$

where R_g is the radius of gyration defined as the mean square distance from the center-of-mass of the particle. In practice, the Guinier plot, i.e. the ln $I(q)$ vs q^2 is generally used to determine the radius of gyration, R_g. The Guinier region is, normally, limited to $qR_g < 1$. Typically at higher values of q, the Porod region, scattering intensity decay is proportional to q^{-4} for globular particles with smooth surface and uniform density. The scattering intensity in this region is expressed by the *Porod law*, i.e.

$$I(q) = 2\pi\Delta\rho^2 S q^{-4} \qquad (2.19)$$

where $\Delta\rho$ is the electron density difference and S is the particle surface area per unit volume., Thus, the slope of the plot ln $I(q)$ vs ln q (Porod plot) represents the surface morphology of the scattering particles. According to Porod plot, a slope of -4 represents a smooth surface particle, whilst slopes between -3 and -4 describe a surface fractal or rough surface [100].

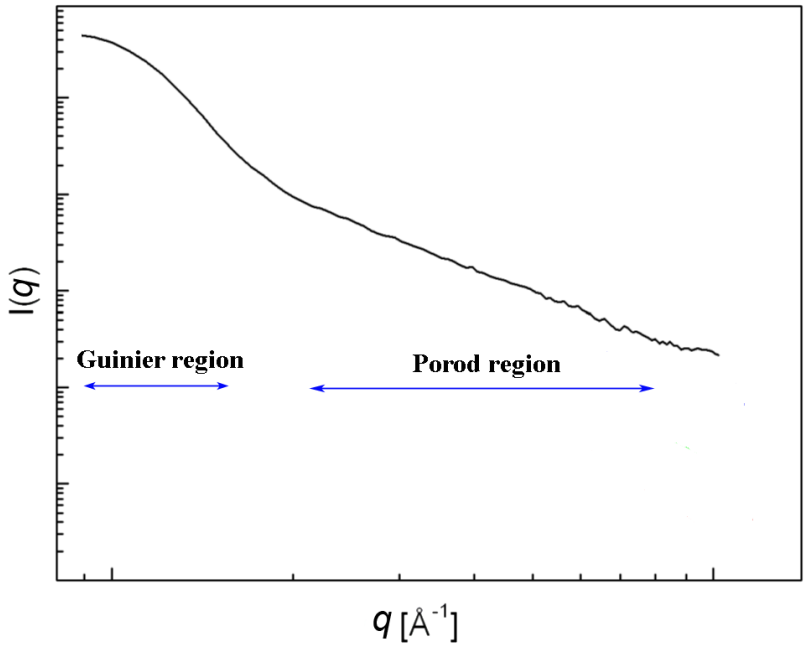

Figure 2-13: A typical plot of SAXS data including Guinier and Porod regions.

In practical application, SAXS absolute or scaled intensity, $I_{abs}(q)$, with a unit of cm^{-1} is required for determining the pore volume fraction and specific surface area of samples. Intensity data generated by the NanoSTAR SAXS instrument at Curtin University can be made absolute by the following equation [88].

$$I_{abs}(q) = I_{abs,st}\frac{I_c(q)}{I_{st}}\frac{t_{st}}{t_s}\frac{d_{st}}{d_{sp}}\frac{\tau_{st}}{\tau_s} \qquad (2.20)$$

where $I_{abs,st}$ and I_{st} are the differential scattering cross section per unit volume and the number of detected photon in time t_{st} of the standard (i.e. S-2907 from Oak Ridge National Laboratories), respectively. These parameters were measured at q = 0.0227 $Å^{-1}$. The thickness of the sample and S-2907 standard are denoted by d_{sp} and d_{st}, respectively. The transmission coefficient of the sample and standard are represented by τ_s and τ_{st}, respectively. I_c is a corrected intensity which removes the effects from the sample holder or from any air present in the vacuum chamber, and is equal to:

$$I_c = I_m - \tau_s I_b - (1 - \tau_s) I_{noise} \qquad (2.21)$$

where I_m = intensity from the sample in a sample holder in time t_s

I_b = intensity from empty sample holder

I_{noise} = detector noise (collecting data without sample and X-ray generator off)

2.2.3 Scanning Electron Microscopy

Scanning electron microscopy (SEM) is most widely used for characterising materials for surface topography and also chemical composition at the near surface. The SEM can operate with an extensive magnification range (100X – 300,000X) and high resolution (a few nanometers). Figure 2-14 schematically illustrates the main parts of a typical electron microscope. It should be noted that all focusing lenses are electromagnetic lenses.

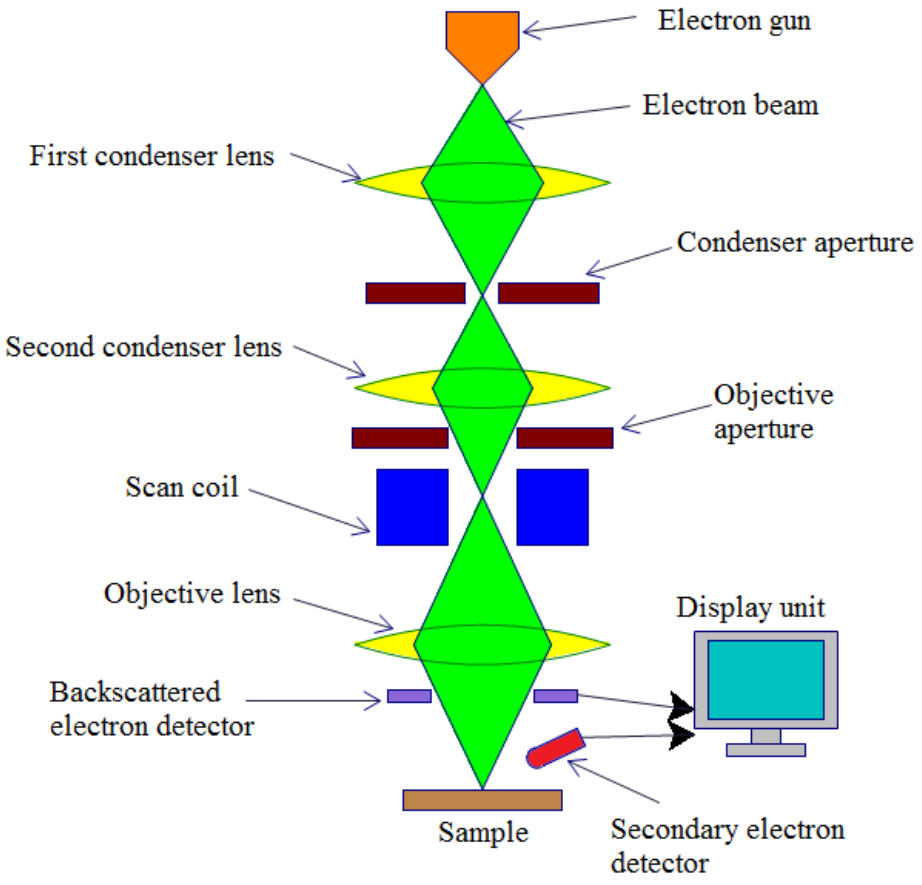

Figure 2-14: Schematic drawing of a scanning electron microscope (SEM).

In principle, when an electron beam interacts with a target sample, a variety of electron, photon, phonon, and other signals can be produced. Thus, there are three types of electrons that can be emitted from the sample, i.e. Auger electrons,

secondary electrons and back scatter electrons. Auger electrons are produced by the decay of the excited atoms in the sample, and can be used for chemical analysis. Secondary electrons (SE) are produced from the ejection of the valence electrons of the constituent atoms in the sample by inelastic scattering. Therefore, the primary electron transfers part of its energy to the other electron. With a sufficient transferred energy, the energised electron can be emitted from the sample with energy of E_{SE} < 50 eV. The secondary electron can convey structural information from the near surface (5 – 10 nm). Backscattered electrons (BSE) have high energy, 100 – 1000 eV, which is close to that of the primary or incident electron. The emission of BSE is a result of elastic scattering of the primary electron by atoms in the sample. The probability of electron backscattering is direct proportional to the mean atomic number of the specimen and primary beam energy. Accordingly, BSE images convey compositional information by contrasting the regions in the sample related to the atomic number (Z) of elements. Therefore, brighter regions in a BSE image likely correspond to heavier elements (higher Z). However, the BSE signal cannot be used for elemental identification. Figure 2-15 shows the SEM images of a $CaNi_5$ alloy collected from SE and BSE signals, respectively. The bright spot in the SE image is a result of sample charging whilst the BSE image indicates the distribution of the heavier element, i.e. Ni, in this alloy is signified by bright regions.

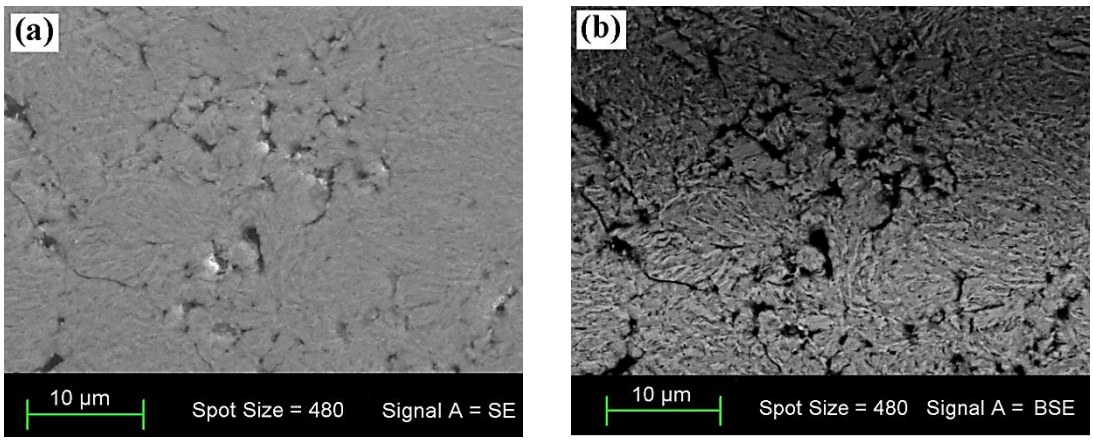

Figure 2-15: Scanning electron micrographs of a $CaNi_5$ alloy collected from (a) secondary electron (SE) and (b) backscattered electron (BSE) signals.

Scanning Electron Microscopy (SEM) was performed on a Zeiss Evo 40XVPan at Curtin University operating at 15 kV. All samples were coated with platinum (Pt) prior to the SEM imaging processes to reduce charging. The microscope was coupled

with an Oxford Instruments energy dispersive X-Ray spectrometer (EDS) for qualitative elemental analysis. More details on EDS will be discussed in the next section.

2.2.4 Energy Dispersive X-ray Spectroscopy

As discussed in section 2.2.3, various different interactions may take place between an incident electron and atoms in the sample when performing SEM. There are not only various electrons but also electromagnetic waves emitted from the sample. When an electron in the inner shell of an atom is ejected by a collision of an incident electron, this vacant orbital will then be filled with outer-shell electrons with a consequent X-ray emission. The energy of the emitted X-ray corresponds to the energy difference of electrons in the outer-shell and inner-shell. This X-ray is called a characteristic X-ray as it is characteristic of an individual element as shown in Table 2-2. For K-line spectra, the relative intensities of the principal lines, e.g. $K_{\alpha 1}$, $K_{\alpha 2}$ and $K_{\beta 1}$, are given by 100, ~50 and ~20 %, respectively [99].

Table 2-2: Characteristic X-ray energies of relevant elements [101].

Element	Characteristic X-ray energies (keV)			
	$K_{\alpha 1}$	$K_{\alpha 2}$	$K_{\beta 1}$	$L_{\alpha 1}$
C	0.277			
O	0.5249			
Na	1.04098	1.04098	1.0711	
Al	1.48670	1.48627	1.55745	
Si	1.73998	1.73938	1.83594	
Ca	3.69168	3.68809	4.0127	0.3413
Fe	6.40384	6.39084	7.05798	0.7050
Ni	7.47815	7.46089	8.26466	0.8515
Mo	17.47934	17.3743	19.6083	2.29316

By detecting and analysing the characteristic X-rays, each element contained in the sample can be identified (qualitative analysis). The weight concentration of a certain element in the sample (quantitative analysis) can be evaluated since the intensity of a characteristic X-ray is proportional to the concentration of the corresponding element. In practice, a relative intensity (I_r) of a certain element is determined from

the ratio of characteristic X-ray intensities from a sample to that of a standard specimen, i.e. the relative intensity of element *M* in the sample is given by

$$I_{rM} = \frac{I_{spM}}{I_{stM}} \tag{2.22}$$

where I_{spM} and I_{stM} are the X-ray intensities from element *M* of the test sample and standard specimen, respectively. However, the X-ray generated in the sample may undergo absorption and also excite other atoms with a consequence of fluorescent X-ray emission. Therefore, quantitative correction is required mainly from the atom number correction (*Z*), absorption correction (*A*) and the fluorescent correction (*F*) [102]. This whole procedure is known as the *ZAF* correction. The estimated weight concentration of element *M* in the sample can be expressed by

$$C_M = \frac{I_{spM}}{I_{stM}} \cdot [ZAF]_M \cdot C_{stM} \tag{2.23}$$

where C_M and C_{stM} are the concentrations of element *M* in the sample and standard specimen, respectively. In practice, the *ZAF* factor correction is carried out by running a *ZAF* program on the computer. Some prerequisites are required for this technique to obtain a satisfactory result, e.g. a uniform distribution of elements at the X-ray emission area, a flat sample surface and a perpendicular incident electron beam with respect to the sample surface.

2.3 HYDROGEN SORPTION MEASUREMENTS

2.3.1 Sieverts Apparatus

In this research, a Sieverts apparatus was used to study the hydrogen absorption and desorption properties of as-synthesised hydrogen storage materials. The instrument can provide information about the sorption kinetics, pressure composition isotherms (PCIs) and circle life of a sample. In the Sieverts (manometric) technique, a calibrated reference-side volume is filled with hydrogen gas at a certain pressure and then opened to a known-volume sample side. The volumes must be known so that the moles of hydrogen in the system can be calculated. After the system reaches thermal equilibrium, the amount of hydrogen absorbed by the sample can be calculated from the change in the hydrogen pressure in the system for a certain experimental temperature.

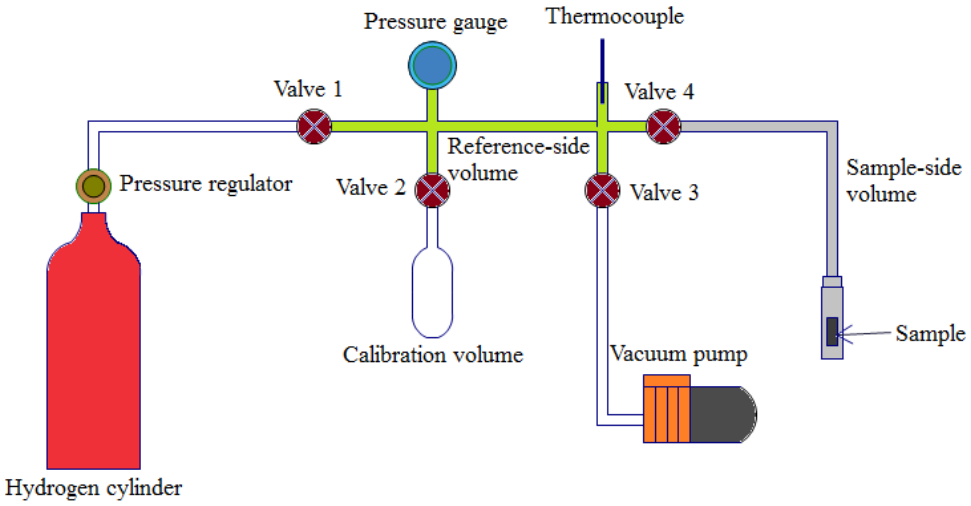

Figure 2-16: Components of a typical Sieverts apparatus for hydrogen sorption measurements, light-green and gray regions represent reference-side and sample-side volumes, respectively.

The components of a typical Sieverts apparatus are shown in Figure 2-16. All parts of the custom built Sieverts apparatus at Curtin University, e.g. tubes, VCR metal gasket face seal fittings and sample vessel, are made from 316 stainless steel. However, the calibration volume is made from 304L stainless steel. All connection points between VCR faces are joined by silver-coated stainless steel washers whilst the calibration volume is sealed by NPT (National Pipe Thread) fittings. The system is operated manually through diaphragm valves. Accordingly, this apparatus

successfully enables very low internal leak rates, which are necessary for the manometric method. The pressure and temperature are measured by a high precision pressure gauge (model 3051S_T Ultra from Rosemount, Emerson Process Management, Australia) and a K-type thermocouple (Hinco Instruments, Australia).

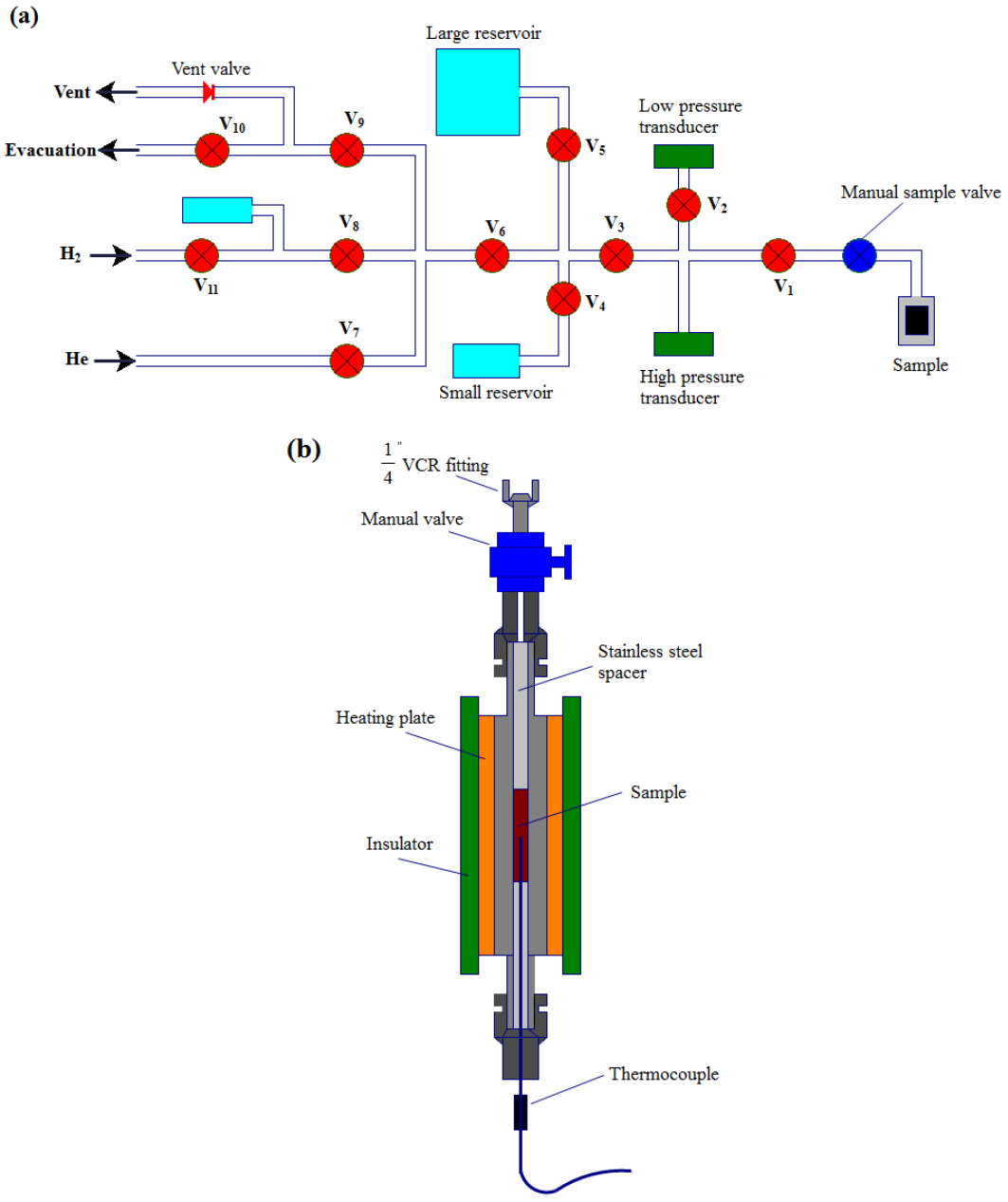

Figure 2-17: Schematic diagrams of (a) PCTPro E&E gas sorption analyser and (b) a standard sample holder.

A PCTPro E&E gas sorption analyser (Setaram) is a fully automated Sieverts instrument that is designed to operate for a wide range of sample temperature (-260 to 500 ºC), pressure (vacuum to 200 bar) and sample size (a few mg to ~100 kg). The

computer control interface has been developed using LabView®-based software. A diagram of the working volumes of this instrument is illustrated in Figure 2-17 (a).

The system exhibits a number of advanced features including proportional-integral-derivative (PID) controlled gas pressure and temperature regulated gas handling systems. The inert gas line, i.e. He line, is available for the volume calibration process. The instrument provides five calibrated reference volumes corresponding to the operation of automatic valves (V_1, V_3, V_4, V_5 and V_6), e.g. approximate ranges of these volumes are 3, 20, 150, 1000, and 1150 cm^3. Two transducers are available for measuring at high-pressure (up to 200 bar) and low-pressure (< 5 bar). Figure 2-17 (b) shows a standard stainless steel sample holder for operating up to 200 bar and 400 ºC, equipped with a temperature monitoring system.

2.3.2 Hydrogen Sorption Calculations

In the Sieverts (manometric) technique, the moles of hydrogen absorbed/desorbed by the sample (n_{ads}) can be calculated from the difference of hydrogen content in the system (reference and sample volumes) at initial and final thermal equilibriums. Therefore, the moles of hydrogen uptake of a sample can be expressed as,

$$n_{ads} = n_r + n_s - n_e \qquad (2.24)$$

where n_r and n_s are initial moles of hydrogen in the reference-side volume (V_r) and sample-side volume (V_s) respectively, and n_e is the final number of moles of hydrogen in the entire system (both reference- and sample-side volumes) after equilibrium. For an ambient temperature experiment, n_r and n_s can be calculated by using a real gas equation of state, i.e.

$$n_r = \frac{P_r V_r}{Z_r R T_r} \qquad (2.25)$$

and

$$n_s = \frac{P_s (V_s - V_{sample})}{Z_r R T_r} \qquad (2.26)$$

where P_r is initial pressures of reference side.

P_s is initial pressures of sample side.

T_r is initial temperature of reference side.

T_s is initial temperature of sample side.

Z_r is the compressibility of hydrogen associated with pressure P_r.

Z_s is the compressibility of hydrogen associated with pressure P_r.

V_{sample} is the sample volume calculated from the sample mass and density

R is the gas constant (= 8.314472 $JK^{-1}mol^{-1}$ in S.I. unit)

After the system reaches final equilibrium, the number of moles of hydrogen can be given by

$$n_e = \frac{P_e(V_r+V_s-V_{sample})}{Z_e R T_e} \quad (2.27)$$

where P_e, T_e and Z_e are equilibrium pressure, temperature and hydrogen compressibility of the system at the final equilibrium measurements, respectively. As can be seen, real gas equation of state, contained in a volume V at a pressure P, is connected with the compressibility of hydrogen, Z, which is given by:

$$Z = \frac{V_m}{V_i} \quad (2.28)$$

where V_i is the molar volume given by the ideal gas law, i.e. $V_i = RT/P$, and V_m is the corrected molar volume of H_2 calculated from an equation of state (EOS) for hydrogen [103, 104] which is given as

$$\left(P + \frac{a(P)}{V_m^{\alpha(T)}}\right)(V_m - b(P)) = RT \quad (2.29)$$

where

$$a(P) = \exp[a_1 + a_2 \ln(P) + \exp(a_3 + a_4 \ln(P))],\ P > 1 \text{ bar} \quad (2.30)$$

$$b(P) = \begin{cases} \sum_{i=0}^{8} b_i \ln(P)^i & (P \geq 100\ bar) \\ b(100\ bar) & (P < 100\ bar) \end{cases} \quad (2.31)$$

and

$$\alpha(T) = \begin{cases} \alpha_0 + \alpha_1 T + \alpha_2 T^2 & (T \leq 300\ K) \\ \alpha(300\ K) & (T > 300\ K) \end{cases} \quad (2.32)$$

The coefficients for equations (2.30) − (2.32) are given in Table 2-3. Consequently, the EOS given by equation (2.29) can be solved numerically [88] to determine the molar volume, V_m. Then the compressibility is calculated according to Equation (2.28). Figure 2-18 shows the hydrogen compressibility at typical temperatures, 273.15, 298.15 and 373.15 K.

Table 2-3: Coefficients *α*, *a*, and *b* for equations (2.29) – (2.32), for pressure expressed in bar, molar volume in cm^3 mol^{-1} and temperature in Kelvin [103, 104].

α_0	2.9315	b_0	20.285
α_1	-1.531×10^{-3}	b_1	-7.44171
α_2	4.154×10^{-6}	b_2	7.318565
		b_3	-3.463717
a_1	19.599	b_4	0.87372903
a_2	-0.8946	b_5	-0.12385414
a_3	-18.608	b_6	9.8570583×10^{-3}
a_4	2.6013	b_7	$-4.1153723 \times 10^{-4}$
		b_8	7.02499×10^{-6}

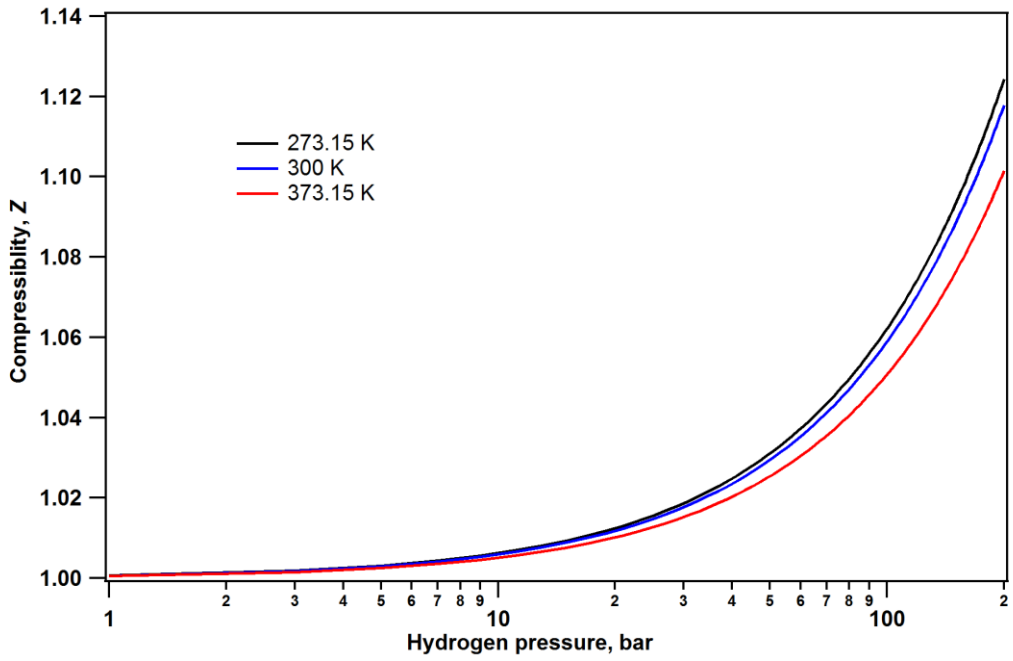

Figure 2-18: Compressibility of hydrogen at 273.15, 298.15 and 373.15 K.

For a non-ambient temperature (T_{na}) experiment, the number of moles of hydrogen in the sample-side volume (n_s) and in the total system at equilibrium (n_e) has been modified from equations (2.26) and (2.27), respectively, i.e.

$$n_s = \frac{P_s(V_s - V_{na})}{Z_s R T_s} + \frac{P_s(V_{na} - V_{sample})}{Z_{na} R T_{na}} \qquad (2.33)$$

and

$$n_e = \frac{P_e V_r}{Z_e R T_e} + \frac{P_e(V_s - V_{na})}{Z_e R T_e} + \frac{P_e(V_{na} - V_{sample})}{Z_{ena} R T_{na}} \qquad (2.34)$$

where V_{na} is the non-ambient sample side volume

Z_{na} is the compressibility at the initial sample side for non-ambient temperature

Z_e is the compressibility at the final equilibrium for ambient temperature

Z_{ena} is the compressibility at the final equilibrium for non-ambient temperature.

2.3.3 Temperature Programmed Desorption Mass Spectrometry

Temperature-programmed desorption (TPD) technique is an important method for the evaluation of kinetic and thermodynamic parameters of the hydrogen desorption process of a sample. The TPD method involves heating a sample with a constant heating rates $\beta = dT/dt$ (with the temperature T usually being a linear function of the time t), while under vacuum and simultaneously detecting the released hydrogen (and also other residual gases) using a residual gas analysis mass spectrometer (RGA-MS). As the temperature increases, certain absorbed gases will have enough energy to escape the sample and will then be detected and discriminated by the mass spectrometer. The amount of a certain released gas corresponds to its partial pressure and results in a peak in the plot of partial pressure of the gas versus time (or temperature of the sample). The temperature programmed desorption mass spectroscopy (TPD-MS) at Curtin University is performed using a Stanford Research Systems (SRS) Residual Gas Analyzer (RGA 300) Quadrupole Mass Spectrometer

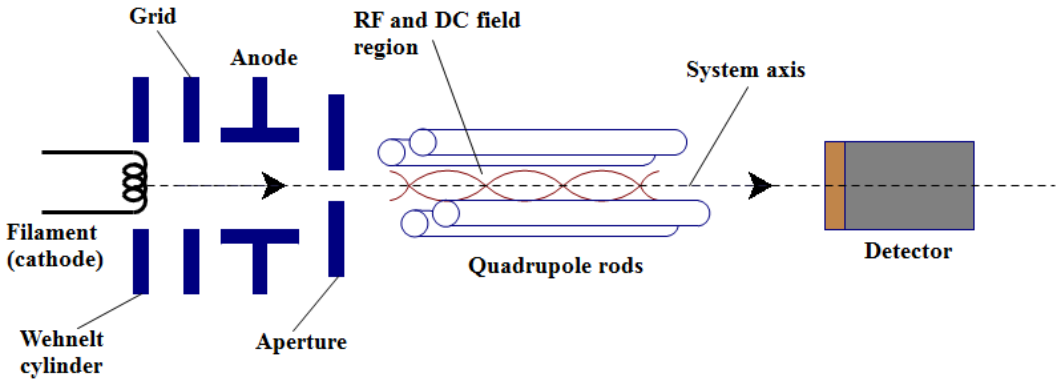

Figure 2-19: Schematic diagram of a quadrupole mass spectrometer.

Figure 2-19 illustrates the main parts of a quadrupole mass spectrometer (QMS). During analysis, positive ions are formed by the impact of electrons and the released residual gas molecules within the ionising chamber. Thus, free electrons are

generated by thermal emission from an electrically heated tungsten filament. The emitted electrons are accelerated by a potential difference between the filament and the grid. The ions are then directed towards the quadrupole analyser, which consists of four cylindrical conducting rods arranged symmetrically around *z*-axis of the system. The ions that reach the detector are determined from the mass-to-charge ratio, *m/Z*, by an analysis of the ion trajectories in the radio frequency (RF) and direct current (DC) fields. The mass-to-charge ratio is defined as the ratio of the mass number (*m*) of the ion to its charge (*Z*) in units of electron charge. For example, the singly charged ions of hydrogen (H_2^+) and water (H_2O^+) have *m*/*Z* of 2 and 18, respectively. Therefore, the *m*/*Z* of a singly charged ion corresponds to the mass of the ion, generally equivalent to its molecular mass. However, for doubly ionised molecules (*Z* = 2), their *m/Z* possibly appears in the spectrum at half of their ion mass, triply charged ions (*Z* = 3) at one third, etc. As a result, a mass spectrum of a particular gas is the products of not only the gas isotope patterns but also the ion fragmentation processes as shown in Table 2-4.

Table 2-4: Mass spectra of typical gases.

Gas		Mass Spectra					
Nitrogen	*m/Z*	28	14	29			
	Relative intensity (%)	100.0	7.2	0.8			
Oxygen	*m/Z*	32	16	34	33		
	Relative intensity (%)	100.0	11.4	0.4	0.1		
Water	*m/Z*	18	17	16	20	19	
	Relative intensity (%)	100.0	23.0	11.0	0.3	0.1	
Argon	*m/Z*	40	20	36	38	18	
	Relative intensity (%)	100.0	10.0	0.3	0.1	0.1	
Carbon dioxide	*m/Z*	44	28	16	12	45	46
	Relative intensity (%)	100.0	11.0	9.0	6.0	1.0	0.5

CHAPTER 3

HYDROGEN STORAGE AND THERMODYNAMIC PROPERTIES OF INTERMETALLIC HYDRIDES

3.1 INTERMETALLIC HYDRIDE SYSTEMS

Intermetallics, multicomponent compounds and ordered alloys can be formed from combinations of metals whose original crystal structures are different from their combined structures [105]. An intermetallic bond is formed with an ordered distribution of metal atoms, which tend to have strong interactions between unlike atoms, stronger than that between like atoms [106]. Figure 3-1 (a) and (b) illustrate the crystalline structure of the common binary intermetallics $LaNi_5$ ($CaCu_5$-type, *P*6/*mmm*) and TiFe (CsCl-type, *Pm*-3*m*). The formation of hydrides in intermetallics, known as intermetallic hydrides, occurs when hydrogen occupies octahedral and/or tetrahedral interstitial lattice sites and forms a hydrogen bond with metals within the intermetallic compounds or alloys, see Figure 3-1 (c) and (d).

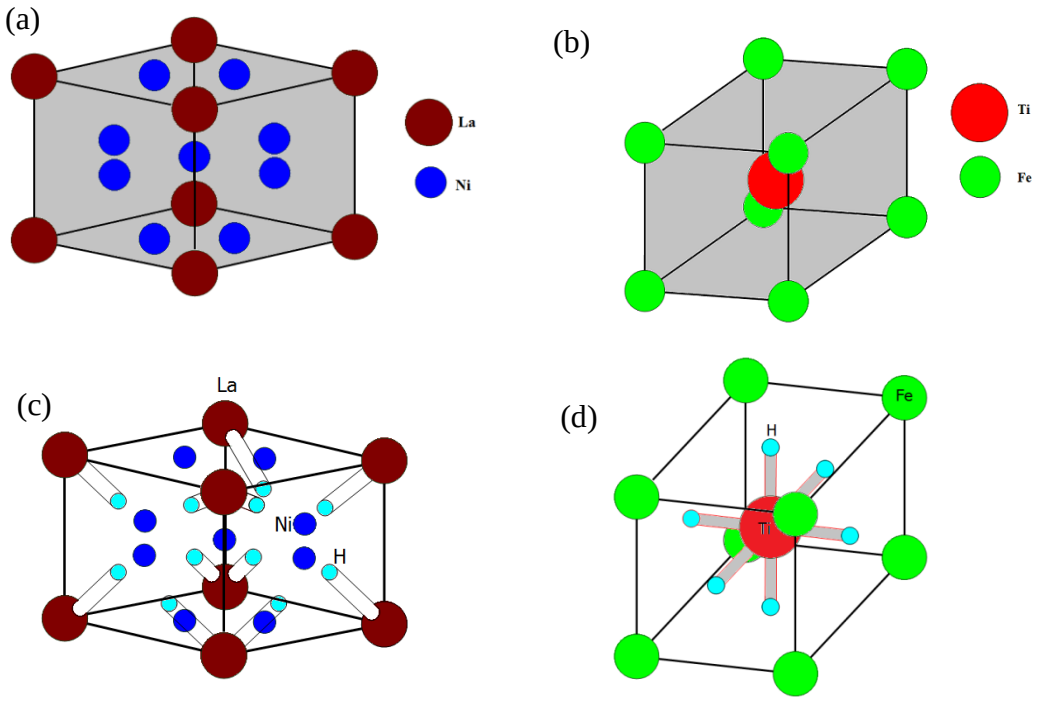

Figure 3-1: Crystalline structures of (a-b) intermetallics ($LaNi_5$ and TiFe) and (c-d) their hydrides.

Figure 3-2 shows the one-dimensional Lennard-Jones potential energy combined with a schematic of the hydride formation process. Firstly, hydrogen molecules at the intermetallic surface interact with metal atoms of the solid via the Van der Waals force, see Figure 3-2 (a). Thus, hydrogen molecules are attracted leading to a physisorption energy, $E_{phys,}$ of approximately 5 kJ/mol H_2. The dissociation of hydrogen then occurs at the solid surface (Figure 3-2 (b)). To dissociate, hydrogen molecules have to overcome an activation barrier, which depends on the metal elements found on the intermetallic surface. Finally, hydrogen atoms occupy the interstitial sites in the subsurface and share their electron with the metal atoms, which is called chemisorption (Figure 3-2 (c)). Generally, the hydrogen absorption process is exothermic with a chemisorption energy level, E_{chem}, ranging from 20 – 150 kJ/mol H [107]. Consequently, the hydrogen can diffuse further into the bulk lattice sites of the intermetallics to form a hydride phase.

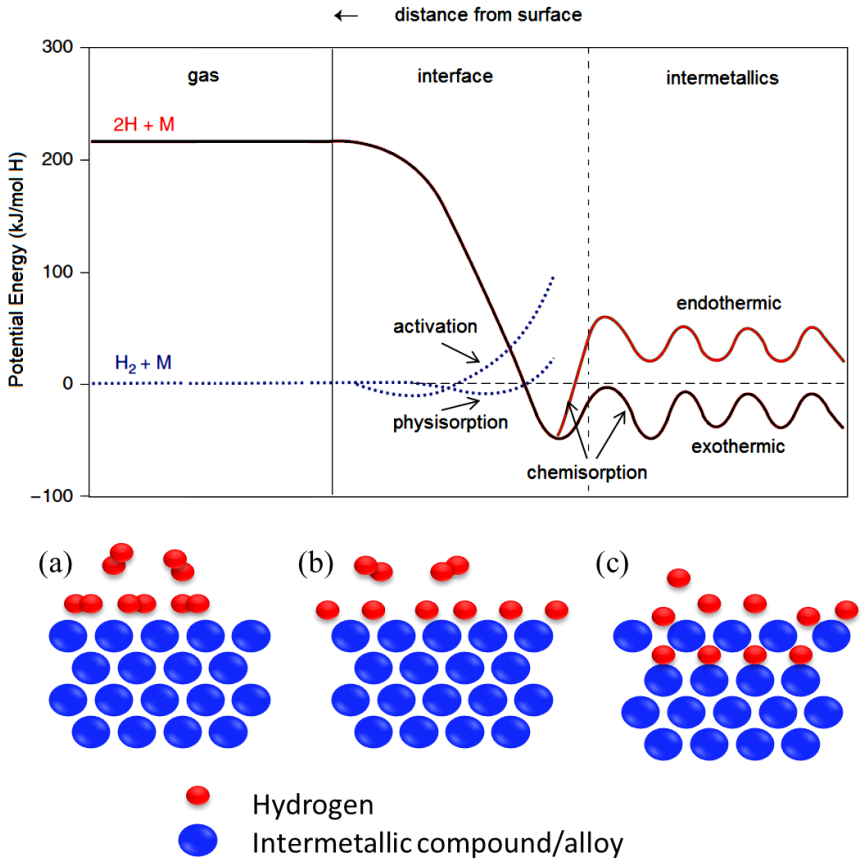

Figure 3-2: Lennard–Jones potential and schematics of a hydrogen intermetallic system during absorption; (a) H_2 physisorption (b) hydrogen dissociation and (c) hydrogen-metal bonding, adapted from [108].

The presence of hydrogen in an interstitial site generally causes an expansion of the intermetallic lattice by ~ 2 – 3 $Å^3$ per hydrogen atom [109]. In the case of $LaNi_5$, for instance, its cell volume expands by 24% during hydride formation at 25 ºC [110]. The expansion during absorption and contraction during desorption cause a driving force acting to pulverize the intermetallic and break it into a fine powder. For instance, a typical metal hydride with a grain size of 50 – 100 µm reaches an equilibrium grain size of about 1 µm after approximately 10 to 100 hydriding/dehydriding cycles [111].

Considering binary alloys (A_xB_y), generally, the element *A* is usually a rare earth or an alkaline earth metal that can form a stable hydride, whilst *B* is an unstable or non-forming hydride element in its pure state [108]. Therefore, the typical *A* elements are Mg, Ca, Ce, Y, Zr and La, and typical *B* elements are V, Cr, Mn, Fe, Co, and Ni. For instance, CaH_2, MgH_2, YH_3 and LaH_2 are very stable hydrides where decomposition of hydrogen is observed at a high very temperature (≥ 350 ºC) [112]. On the other side, Ni, for example, only forms a hydride ($NiH_{x<1}$) at very extreme conditions, i.e. the absorption pressure is in order of 3000 to 3600 atm [113].

When an alloy is first synthesised, it will not usually react directly with hydrogen, likely due to an oxide layer on its surface, especially for air-exposed samples [114]. Accordingly, most alloys require a hydrogen activation process for at least one and possibly several cycles prior to a stabilisation of its hydrogen sorption properties. In addition, Kisi et al. [115] mentioned that irreversible change in the fundamental lattice parameters of the alloy occurred during activation process. The process typically involves heat treatment under high vacuum for outgassing, and high purity hydrogen exposure at a certain pressure and temperature depending on alloy type. For instance, $LaNi_5$ can be activated at 30 ºC with the hydrogen pressure of 10 bar [115] whilst TiFe requires a higher temperature and pressure, at 400 ºC and 60 bar for activation [116].

3. 2 HYDROGEN SORPTION PROPERTIES OF INTERMETALLICS

Reversibility of hydrogen storage materials is termed as a materials ability to undertake multiple hydrogen sorption cycles. The term *sorption* includes two processes, *absorption* and *desorption*. Hydrogen absorption or hydrogenation is the process of hydrogen filling and occupying an interstitial site. Hydrogen desorption or dehydrogenation is the process of hydrogen release. Generally, the hydrogen concentration of metal hydrides, MH_x, is presented in term of gravimetric concentration (*wt.*%), stoichiometric index (*x*) or hydrogen/metal ratio (*H/M*). The gravimetric concentration is the ratio of the mass of hydrogen to the total mass of the metal hydride material, which is presented as weight percentage, *wt.*%, as shown in Equation (3.1).

$$wt.\% = \frac{m_H}{m_H + m_M} \times 100 \qquad (3.1)$$

where m_H and m_M are the total mass of hydrogen and the storage material, respectively. The hydrogen/metal ratio, *H/M*, can be calculated from the number ratio of hydrogen atoms (*x*) to metal atoms of an intermetallic (N_M) i.e.,

$$H/M = \frac{x}{N_M} \qquad (3.2)$$

For example, ternary hydride $FeTiH_{0.5}$ consists of two metal atoms per formula unit (Fe and Ti), and the stoichiometric hydrogen index at this stage is $x = 0.5$, therefore;

$$H/M = \frac{0.5}{1+1} = \frac{0.5}{2} = 0.25 \qquad (3.3)$$

In another case, the *H/M* of a substituted alloy $Fe_{0.8}Ni_{0.2}TiH_{1.4}$ can be calculated;

$$H/M = \frac{1.4}{0.8+0.2+1} = \frac{1.4}{2} = 0.7 \qquad (3.4)$$

In other words, each mole of metal stores 0.7 mole of H (~ 0.7 g) at the given composition.

3.2.1 Pressure-Composition Isotherms

The sorption characteristics can be examined from Pressure-Composition Isotherms (PCIs), which depict a relationship between hydrogen pressure and hydrogen

concentration at a certain temperature. Figure 3-4 shows ideal PCIs where hydrogen concentration, *wt.*% or *H/M*, is plotted versus the equilibrium pressure, (P_{eq}), with schematics of hydride formation in the different regions. The formation of a hydride in intermetallics can be considered in three states (or phases).

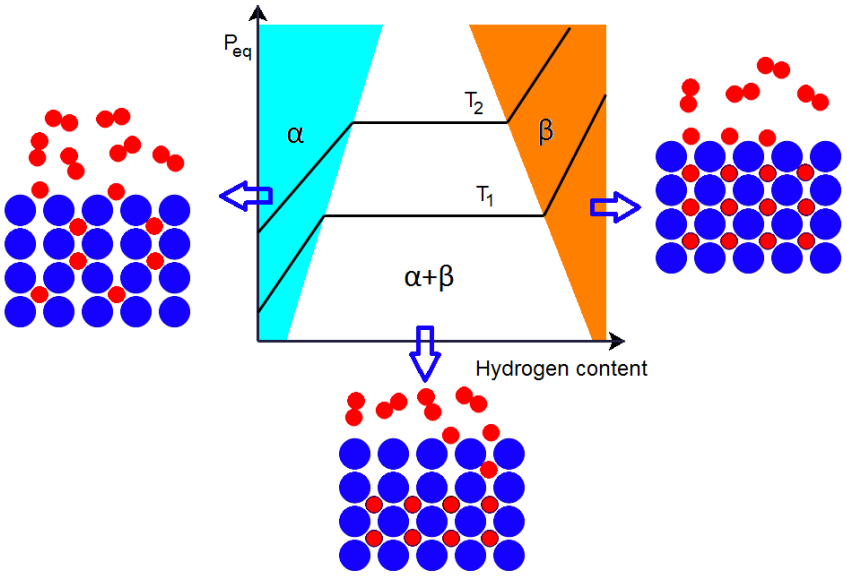

Figure 3-3: Pressure-Composition Isotherms (PCIs) of hydride formation in intermetallics ($T_2 > T_1$).

From Figure 3-3, the first state is called the α-phase, which indicates a low-hydrogen concentration phase. In this stage, hydrogen atoms either occupy some interstitial sites or dissolve in the alloy without changing the chemical composition. The hydrogen equilibrium pressure depends strongly on the amount of hydrogen stored in the alloy. The α-phase region on the PCI is also called a *solid-solution* or *depleted region*. As the hydrogen concentration increases beyond a certain point, a *plateau region* is introduced where the equilibrium pressure is almost independent of hydrogen concentration and the second hydride phase, β-phase, begins to form. At this state, the plateau region represents a coexistence of α- and β-phases. The plateau region continues until the alloy lattice is saturated with hydrogen atoms, i.e., the alloy is completely formed β-phase hydride. Further increase the hydrogen content results in a rapid rising of equilibrium pressure due to the excess hydrogen atoms dissolved in the β-phase. The corresponding region in the PCI diagram is called the *saturated region*. Consequently, γ-phase is formed and a second plateau may be

observed at still higher equilibrium pressures. For instance, the γ-phase of $CaNi_5$ exists for approximately $CaNi_5H_x$ (x = 4.5 – 5.5) at the equilibrium pressure of ~30 bar at 25 ºC [9].

In practice, the PCIs of metal hydrides often depart from the ideal shape. For example, the plateau pressure during absorption may be higher than during desorption (called sorption hysteresis) and the PCIs may exhibit a sloping plateau. These characteristics can be due to microstructure such as localized defects, surface and/or grain inhomogeneity, and lattice expansion/contraction [117]. The PCI characteristics of relevant alloys including plateau pressure, plateau slope and hysteresis are shown in Table 3-1.

Table 3-1: PCI characteristics of relevant binary alloys.

Alloy	Desorption plateau pressure at 25 °C (bar)	Plateau slope $\frac{d \ln P}{d(H/M)}$	Hysteresis parameter P_a/P_d	Ref.
TiFe*	4.10	0.00	0.64	[114]
$CaNi_5$	0.47	0.19	1.17	[118]
$LaNi_5$	1.77	0.11	1.41	this work
$LaNi_5$	1.65	0.09	1.21	[118]
$TiMn_{1.5}$	8.40	-	-	[119]
Mg_2Ni	0.00001	-	-	[119]

*Determined from lower plateau.

The degree of sorption hysteresis is determined from the ratio of the absorption plateau pressure, P_a, to the desorption plateau pressure, P_d, generally measured at 25 ºC and at H/M = 0.5. The plateau slope (or slope parameter) is defined as;

$$plateau\ slope = \frac{d \ln P}{d(H/M)} \qquad (3.5)$$

where P is the plateau pressure of the PCI.

From Figure 3-4, the degree of hydrogen sorption hysteresis in $LaNi_5$ is P_a/P_d = 2.49/1.77 = 1.41. The plateau pressure of this alloy at point A is 1.91 bar and point B

is 1.67 bar with the *H/M* of 0.0 and 1.2, respectively. Then the desorption plateau slope of $LaNi_5$ at 25 ºC can be determined as follows:

$$plateau\ slope = \frac{d \ln P}{d(H/M)}$$

$$= \frac{\ln 1.91 - \ln 1.67}{1.2 - 0.0}$$

$$= 0.11$$

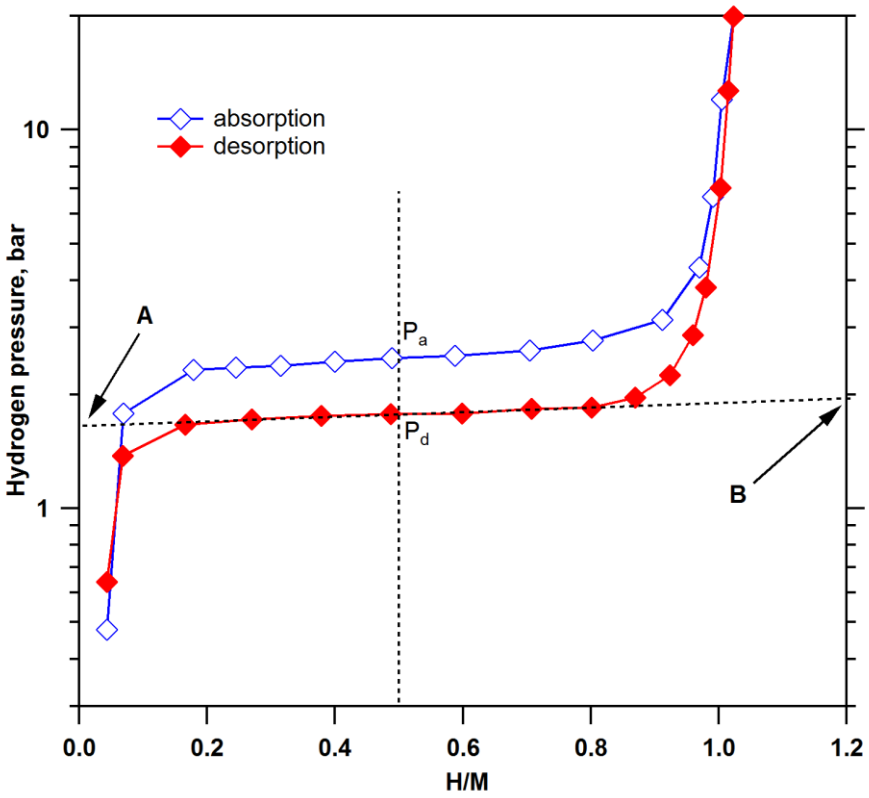

Figure 3-4: Absorption-desorption PCIs of $LaNi_5$ measured at 25 ºC.

3.2.2 Hydrogen Sorption Kinetics

The rate of hydrogen absorption-desorption is known as *kinetics* and is generally measured as the hydrogen evolution as a function of time. The kinetics of hydrogen sorption of metal hydrides can be limited by the rate of molecular hydrogen dissociation and hydrogen diffusion proceeding through the surface or bulk, and from the α- to β-phase transformation [120]. Therefore, the reaction rate is an interrelation between the intrinsic kinetics of materials and the heat transfer of the

reactor system [121]. $LaNi_5$ alloy, for example, has extremely fast kinetics at 25 °C, thus this alloy's performance, in practice, is probably limited by the heat transfer system [122, 123].

The hydrogen evolution can be observed by hydrogen pressure changes in a closed system, allowing hydrogen content to also be determined. Therefore, the kinetic characteristics can be presented as a function of hydrogen pressure or hydrogen content versus time at a given temperature as shown in Figure 3-5. According to the United States Department of Energy (DOE) targets for an ideal hydrogen storage material for vehicles, fast hydrogen absorption kinetics are required, i.e., a complete hydrogen refuelling time should be less than 3 minutes [124]. In a related application, a minimum hydrogen release rate of 1.2 g/s is required, based on the DOE target of 0.02 g/s/kW, is required to supply a 60 kW fuel cell system. In addition, a heat removal system is necessary for a hydrogen storage material with fast kinetics because of the highly exothermic reaction during hydriding [125]. For example, a metal hydride with an enthalpy of -30 kJ/mol H_2 will generate ~ 400 kW of heat to refuel 5 kg of hydrogen within 3 minutes.

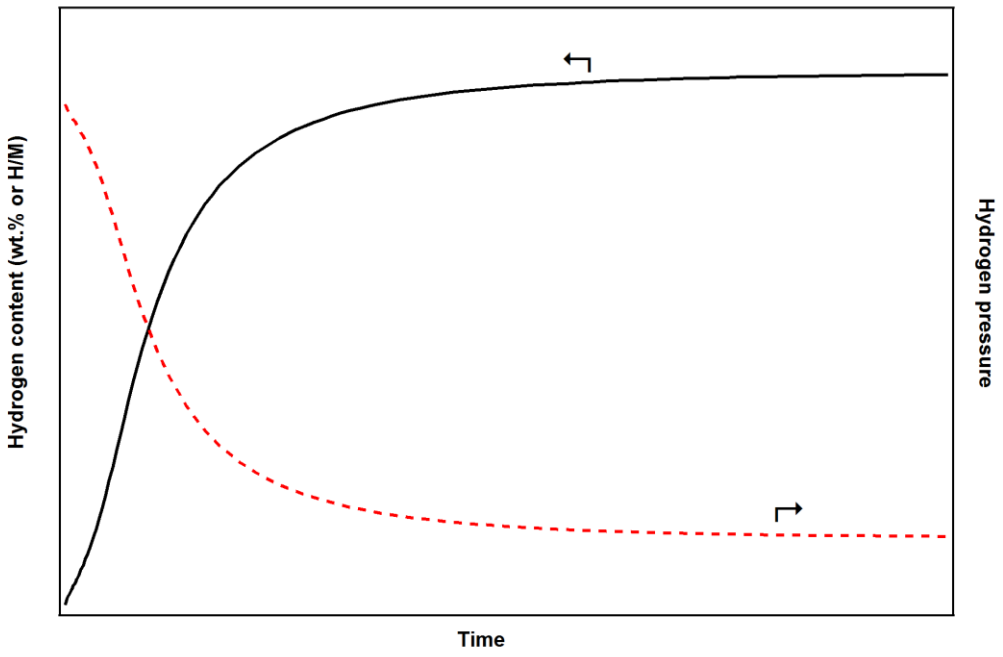

Figure 3-5: Hydrogen absorption kinetics as the plots of time vs. hydrogen content (——) and time vs. hydrogen gas pressure (-------).

3.3 THERMODYNAMIC THEORY OF METAL HYDRIDES

The pressure-composition isotherms, PCIs, of metal hydrides are temperature dependent. For example, Figure 3-6 illustrates desorption PCIs measured at various temperatures of $CaNi_5$ including the hydride phase regions. This effect is considered as a function of the thermodynamic properties of a material. A higher temperature results in a higher plateau pressure but a narrower plateau region. The plateau region disappears after heating beyond the critical temperature, T_c, where the α-phase converts to β-phase continuously, see Figure 3-7 (a). When the hydride is formed, the Gibbs free energy of formation per mole of hydride at constant temperature, T, is

$$\Delta G = \Delta H - T\Delta S \qquad (3.6)$$

where ΔH is the formation enthalpy of the hydride and ΔS is the change in entropy of the system.

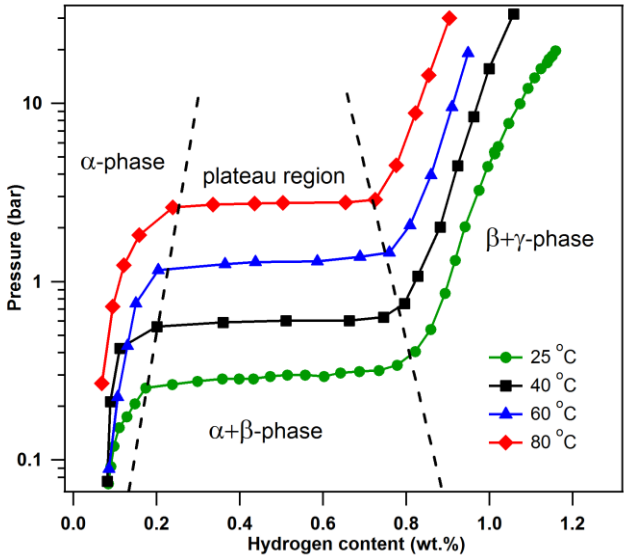

Figure 3-6: PCIs of $CaNi_5$ measured at various temperatures.

When considered as an ideal gas (at low pressure), hydrogen gas is in equilibrium with the hydride over pressure, P, at temperature T, and the Gibbs free energy can then be expressed in the form [12];

$$\Delta G = RT \ln \frac{P}{P_0} \qquad (3.7)$$

where R is the gas constant and P_o is the pressure at standard conditions, 1 atm. If the hydrogen pressure is measured in atmospheric unit (atm.), then equation (3.7) can be rewritten as;

$$\Delta G = RT \ln P \qquad (3.8)$$

So,

$$\Delta G = \Delta H - T\Delta S = RT \ln P \qquad (3.9)$$

Thus,

$$\ln P = \frac{\Delta H}{RT} - \frac{\Delta S}{R} \qquad (3.10)$$

For hydrogen desorption, equation (3.8) is rewritten as,

$$\ln P = -\frac{\Delta H}{RT} + \frac{\Delta S}{R} \qquad (3.11)$$

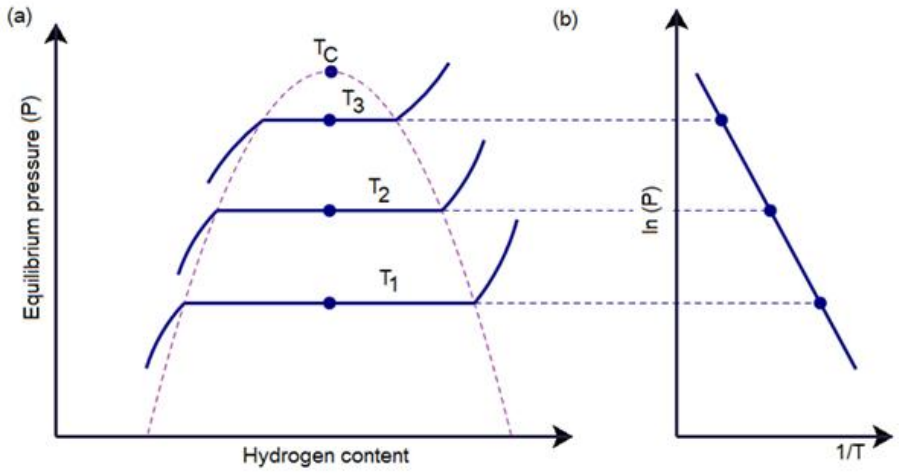

Figure 3-7: (a) Plots of PCIs with (b) a corresponding van't Hoff plot.

The enthalpy, ΔH, is expressed as the formation energy per mole of hydrogen. The enthalpy change is negative for the case of absorption, since absorption is an exothermic reaction. On the other hand, hydrogen desorption is endothermic resulting in a positive ΔH. A larger ΔH is indicative of a more stable hydride, which has a lower equilibrium pressure for a given temperature. The entropy change is also negative in the case of absorption because hydrogen is in a more ordered state in the hydride than in the gas. The entropy change (ΔS) is roughly the same for most metal

hydrides, which primarily corresponds to the loss of the standard entropy of hydrogen gas, approximately 130 J/(K·mol H_2) for a perfectly ordered hydride [126]. Figure 3-7 (b) shows the linear plot of *ln (P)* vs. 1*/T* for a metal hydride, known as the *van't Hoff* plot. Graphically for absorption the slope of this line is $\frac{\Delta H}{R}$, and the intercept is $\frac{-\Delta S}{R}$. For desorption the slope is $\frac{-\Delta H}{R}$, and the intercept is $\frac{\Delta S}{R}$.

It should be noted that in equations (3.10) and (3.11) it is assumed that ΔH and ΔS are temperature independent. It is also assumed that the sorption characteristics exhibit ideal PCIs, i.e., a zero plateau slope and the absence of hysteresis. However, these conditions do not often occur in most hydrides, thus, the equations are used as a best estimate for the hydride properties. The enthalpy and entropy of hydride formation of some relevant binary alloys are listed in Table 3-2.

Table 3-2: Enthalpy and entropy of hydride formation of relevant binary alloys.

Alloy	Capacity, wt.% H	ΔH (kJ/mol H_2)	ΔS (J/(K·mol H_2))	Ref.
$CaNi_5$	1.87	-31.9	-101	[114]
$LaNi_5$	1.51	-31.8	-109	[127]
$ZrCr_2$	1.96	-46.0	-	[128]
$TiCr_2$	2.32	-23.0	-	[83]
$CeNi_5$	1.67	-14.6	-111	[129]
$ZrMn_2$	1.77	-53.2	-121	[119, 130]
TiFe	1.86	-28.1	-106	[119, 131]

The PCIs of $LaNi_5$ measured at 25, 40 and 60 ºC are shown in Figure 3-8 (a). The absorption plateau pressures at these temperatures were found at 2.50, 5.10 and 9.46 bar, respectively; whilst desorption plateau pressures were at 1.72, 3.81 and 7.21 bar, respectively. The van't Hoff plot of both absorption and desorption is presented in Figure 3-8 (b) with slopes of -3550 and -3820, respectively. Accordingly, the enthalpy can be determined by using equation (3.10) and (3.11) with R = 8.314 J/(K·mol).

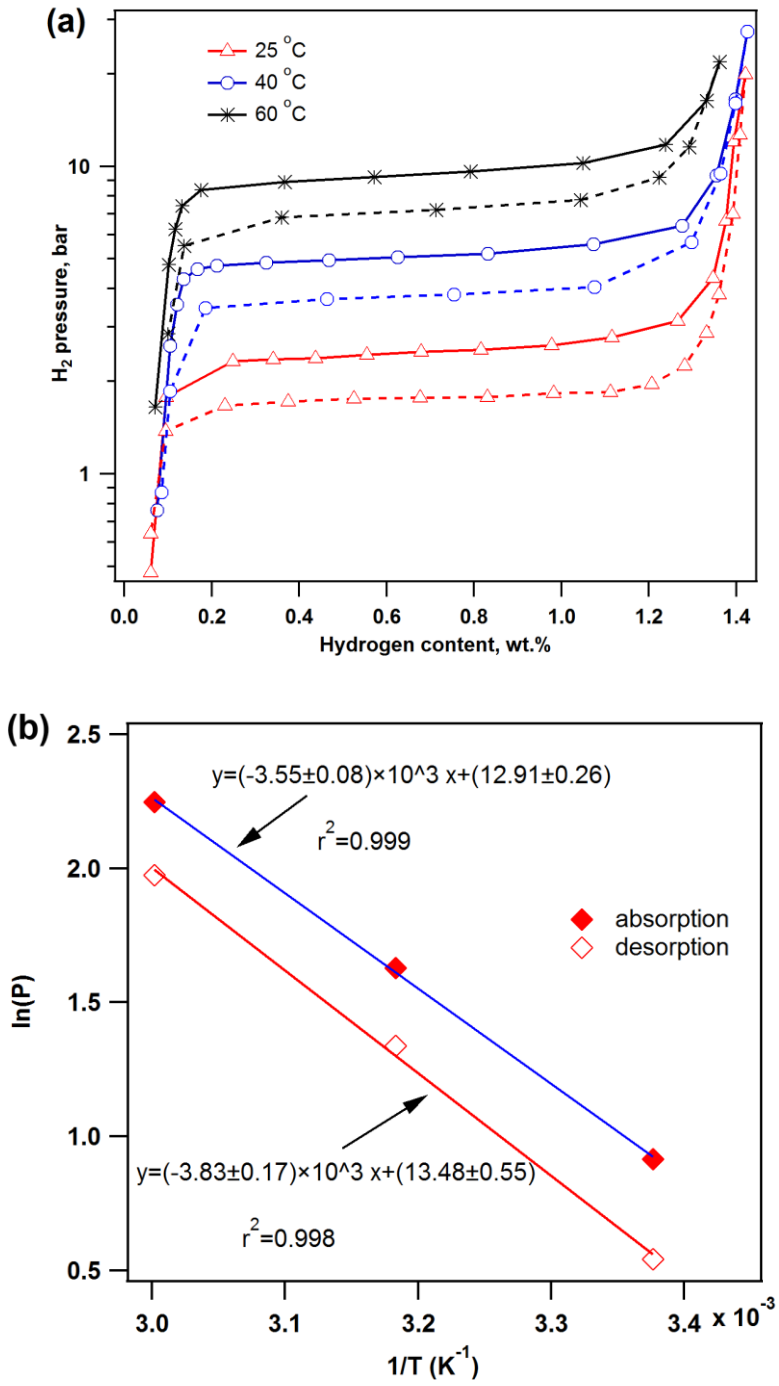

Figure 3-8: (a) PCIs of $LaNi_5$ including absorption (solid lines) and desorption (dash lines) at 25, 40, and 60 ºC, and (b) van't Hoff plots.

Thus, for absorption;

$$\Delta H = 8.314 \cdot slope = 8.314 \cdot (-3.55 \pm 0.08) \times 10^3 = -29.5 \pm 0.7\ kJ/mol\ H_2$$

The enthalpy of desorption is

$$\Delta H = 8.314 \cdot (-slope) = 8.314 \cdot (3.82 \pm 0.17) \times 10^3 = 31.8 \pm 1.4\ kJ/mol\ H_2$$

The entropy can also be calculated as -107 ± 3 and 112 ± 5 *J/(K·mol H_2)* for absorption and desorption, respectively. The enthalpy (heat of formation) of a metal hydride implies its stability [132], where the higher the $|\Delta H|$ the more stable the hydride. The ΔH of formation of a ternary hydride, AB_nH_{x+y}, can be predicted by a simple empirical model known as *Miedema's rule* [133] where ΔH is calculated from three parts, i.e.,

$$\Delta H(AB_nH_{2x}) = \Delta H(AH_x) + \Delta H(B_nH_x) - \Delta H(AB_n) \qquad (3.12)$$

where n is greater than 1, $\Delta H(AH_x)$ is the heat of formation of the hydride of metal A, $\Delta H(B_nH_x)$ is the heat of formation of the hydride of metal B, and $\Delta H(AB_n)$ is the heat of formation of the AB_n alloy.

According to equation (3.12), the heat of formation of ternary hydride $LaNi_5H_6$ can be estimated by;

$$\Delta H(LaNi_5H_6) = \Delta H(LaH_3) + \Delta H(Ni_5H_3) - \Delta H(LaNi_5) \qquad (3.13)$$

The heat of formation (ΔH) of LaH_3, Ni_5H_3 and $LaNi_5$ are reported as -247, 21 and -141 kJ/mol, respectively [134]. Thus, the heat of hydride formation of the process;

$$LaNi_5 + 3H_2 \rightarrow LaNi_5H_6 \qquad (3.14)$$

is calculated to be -247 + 21 – (-141) = -85 kJ/mol metal or ~ -28 kJ/mol H_2 which is comparable to the experimental result (~ -30 kJ/mol H_2) as shown above.

3.4 IMPROVEMENT OF HYDROGEN STORAGE MATERIALS

The ideal properties of a metal hydride used as a hydrogen storage material are high hydrogen capacity, fast kinetics, reversibility with a long cycle life, low dissociation temperature a moderate dissociation pressure, and a low cost material [135, 136]. However, there is no material that can satisfy all of these performance categories due to the thermodynamic and kinetic constraints of known materials. For example, some metal hydrides have a high hydrogen capacity but do not have favourable kinetic and PCI properties. Some intermetallics show satisfactory desorption temperatures and plateau pressures for practical applications but usually have either low hydrogen capacities or poor cyclic durability. The performance of a solid-state hydrogen storage material may be improved by various techniques including micro- and nanostructure modifications.

The sorption kinetics are strongly affected by the microstructure of a material, i.e., the particle, grain or crystallite size of the material [137]. Smaller grain size provides faster diffusion pathways for hydrogen in a bulk material. Furthermore, fine microstructure also generates a high surface area, which increases the rate of reaction between the material surface and hydrogen. It has been reported that a material with particle diameters of 10 nm only has 30% of all atoms within the grain boundaries whilst the number increases to 50 – 60% for particles with a diameter of 5 nm [138]. Thus, the reaction rate of nanoscale materials is likely to be influenced by the numbers of atoms located along the grain boundaries. Nanostructured and nanoscale materials show promise of not only improving kinetic properties but also influencing the material thermodynamics [139].

There are several methods to prepare nanostructured materials including inert gas condensation, rapid solidification, electrodeposition, sputtering, crystallization of amorphous phases, chemical reactions, plasma processing, and mechanical alloying [140, 141]. Among these techniques, the mechanical alloying method (MA) has been widely used and considered the most powerful tool for nanostructured materials because of its simplicity, relatively inexpensive equipment, and the possibility of large scale production [81]. Usually, mechanical alloying is undertaken by mechanical ball-milling and/or rod-milling [80].

The energetic ball milling of magnesium hydride, MgH_2, results in small particle size and an increase in specific surface area by an order of magnitude compared to that of an unmilled sample [142]. As a result, milled MgH_2 shows faster kinetics and a lower desorption activation energy than unmilled MgH_2. However, the thermodynamic properties of MgH_2 are not changed under these experimental conditions. In an extreme case, it has been shown that a reduction in MgH_2 particle size to less than 10 nm can affect the thermodynamics of the hydride phase [92, 143].

For intermetallic hydrides, the equilibrium pressure and stability of the material can be improved by adding a small quantity of other elements. For instance, the hydriding performance of binary alloys such as $LaNi_5$, Mg_2Ni and FeTi have been altered by adding a third element (*M*) [144-146] to form ternary hydrides $LaNi_{5-x}M_x$, $Mg_{2-x}M_xNi$ and $FeTi_{1-x}M_x$, respectively. Stability of the hydride can be empirically related to size of the interstitial site available to hydrogen or the unit cell volume [147]. The larger the interstitial site (or the unit cell volume), the more stable the hydride. As a result, a lower equilibrium pressure is required to release hydrogen from a more stable hydride at a particular temperature. For example, $LaNi_5$ (unit cell volume of 86.90 $Å^3$) relates to a more stable hydride at room temperature than YNi_5 (unit cell volume of 80.24 $Å^3$) where their absorption equilibrium pressures are approximately 2 and 300 bar, respectively. However, this empirical rule is invalid in some cases. For example, $CaNi_5$ has unit cell volume of 83.5 $Å^3$ [85] but its absorption equilibrium pressure at room temperature is ~0.5 bar [118], which is lower than $LaNi_5$.

There have been many studies on the effects of partial substitution of elements at *A* and/or *B* sites of binary alloys, A_nB_m, to improve their hydrogen sorption properties. The addition of metals into the mother alloy causes a change in chemical interaction between atoms in the alloy; consequently, the hydride stability can also be modified [148]. Substitution of Ni by Zn or Al in $LaNi_5$, forming $LaNi_{5-x}(Zn \text{ or } Al)_x$, shows a decrease of plateau pressure and an increase of the unit cell volume, whilst hydrogen capacity is slightly decreased with increasing Zn content [149]. In fact, the Zn and Al atoms are significantly larger than Ni. As a result, substitution of larger atomic-size metals in an alloy tends to increase the unit cell volume and also increase the stability of the hydride phase. It was reported that aluminium replaces nickel on the 3g site (mid-plane) rather than the 2c site of the $LaNi_5$ lattice [150] as in Figure 3-9.

Particularly, an Al-substituted alloy, e.g. $LaNi_{4.7}Al_{0.3}$, exhibited a performance improvement with no disproportionation damage and almost no change in sorption capacity during cycling tests of 1500 cycles at 85 ºC [8]. Moreover, partial substitution of Al in $LaNi_5$ can also enhance of the alloys durability against impurities such as O_2 and H_2O found in hydrogen gas [151].

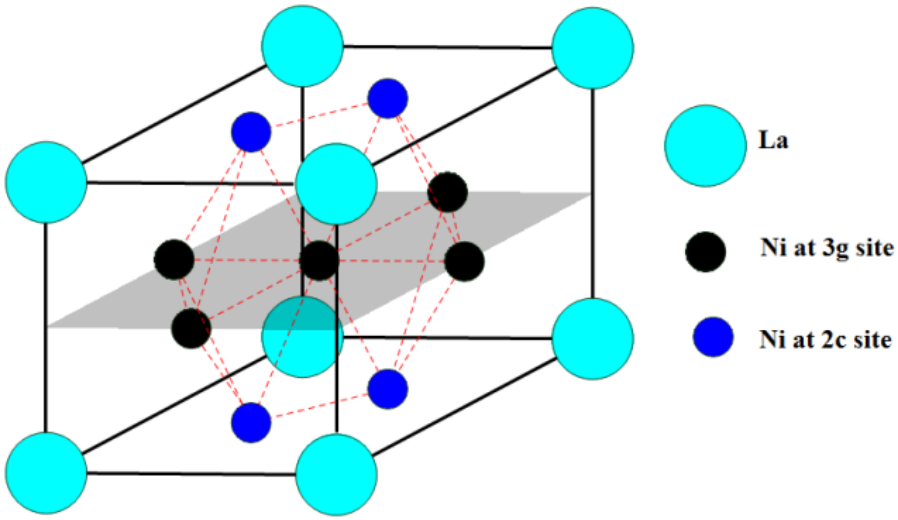

Figure 3-9: Metal lattice of $LaNi_5$, adapted from [109].

CHAPTER 4

$CaNi_5$-BASED ALLOYS FOR SOLID-STATE HYDROGEN STORAGE

4.1 BACKGROUND

Although AB_5-type alloys, with theoretical capacities of ~2 wt.% H, cannot meet hydrogen storage capacity targets for transport vehicle applications, they possess excellent properties for use as an energy storage for both stationary and distributed energy generation applications [135]. The AB_5-type alloys are also considered as one of the most suitable hydrogen storage materials for use in solar-hydrogen power generation systems, which are candidates for remote-area power supply (RAPS) applications [53]. These systems can operate as residential and/or industrial power supplies located in regions far from grid energy networks. As a prototype, it was shown that AB_5-type alloys have potential as the hydrogen storage material for a 3 kW polymer electrolyte membrane (PEM) fuel cell operating around 60 – 70 ºC, which also successfully connected to the electrical grid network [152]. Furthermore, some short-range automotive applications for low gravimetric-capacity material include materials handling equipment (MHE) and ground support equipment (GSE), such as forklifts, tow tractors, and specialty vehicles such as golf carts, lawn mowers and wheel chairs [153]. Commercial metal hydride storage systems have been successfully developed by several companies such as Ergenics, Inc., Wyckoff, NJ, U.S.A., Hydrogen Consultants, Inc. (HCI), Littleton CO, U.S.A., Hydrid-Wasserstofftechnik (HWT), Mulheim/Ruhr, F.R.G., and Japan Metals and Chemicals Co. Ltd., Tokyo, Japan [154].

$CaNi_5$, an AB_5-type alloy, has a hydrogen content up to 1.9 wt.% [9], which is comparable to promising AB_2 alloys [155]. The β-phase of the hydride, $CaNi_5H_x$, typically exists in a range of hydrogen contents ~ x = 0.75 – 4.5 [156]. The crystal structure of the hydrided $CaNi_5$ alloy in the β-phase has been reported to be different from the unhydrided alloy [157]. Therefore, the crystalline space group is changed from *P*6/*mmm* (hexagonal) to *Im*2*m* (orthorhombic) after hydriding to the β-phase [158], as shown in Figure 4-1. Further hydriding results in the γ-phase ($x \approx 4.5 – 5.5$) [9].

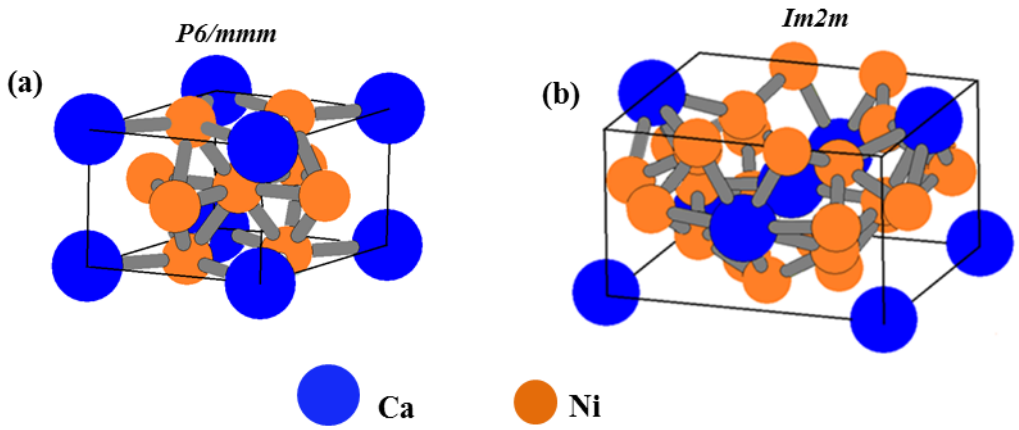

Figure 4-1: Schematic illustration of crystal structure of $CaNi_5$ alloy, (a) α-phase and (b) β-phase.

The $CaNi_5$ alloy has been studied widely as a moderate-cost hydrogen storage material in comparison to other low hydrogen-to-metal atom ratio [H]/[M] materials that operate near room temperature, such as mischmetal (Mm)- or La-based alloys. In August 2013, the average market price in China for Freight On Board (FOB) of Ca was approximately $4 US per kg [159], whilst the FOB price of La, and Ni was approximately $10 and $13 US per kg, respectively [160, 161]. Assuming the usable capacity of $LaNi_5$ and $CaNi_5$ is 1.4 and 1.05 wt.% of hydrogen, respectively. Although the maximum storage capacity of $CaNi_5$ is 1.9 wt.%, this intermetallic hydride has three plateau pressures, e.g. 0.03, 0.4 and 25 bar for hydrogen desorption at 25 ºC [9]. Thus, the usable capacity at near ambient is determined from the middle plateau. Based on the simple calculation for raw material cost, it means that to store 1 kg of hydrogen would cost approximately $900 US for $LaNi_5$ and $1100 US for $CaNi_5$. Thus, it is expected that the cost of storing hydrogen in $CaNi_5$ is slightly higher than in $LaNi_5$. Furthermore, the real cost of hydrogen storage materials must include the processing cost. Currently, the conventional casting process is preferred for industrial scale to produce the intermetallic alloys whereas the mechanical ball milling is another method with some advantages that will be discussed in section 4.2.

It should be noted that the world's major supplier of rare earth metals, China, imposes a 25% tariff on exports, a value that is not included in the stock market price [162]. The market price for Freight On Board (FOB) rare earth and Ni metals, the full price including packaging and shipping, is typically higher than the stock market price. The wide range of high-tech applications for rare earth metals and the limited

number of high-concentration rare earth ore bodies suggests ongoing pressure for the cost of rare earth metals such as lanthanum and mischmetal. Wide scale deployment of lanthanum or mischmetal based hydrogen storage systems would further add to this price pressure. As such, $CaNi_5$ presents a potentially cheaper option for long-term, wide scale deployment as a hydrogen storage material.

$CaNi_5$ shows favorable properties for practical applications with fast hydrogen absorption/desorption kinetics and a relatively flat plateau pressure at near ambient temperature, approximately 1 bar at 60 ºC for hydrogen desorption [163]. Moreover, the cyclic capacity degradation of this alloy is not as severe at lower operated temperatures, i.e. 78% of initial capacity was maintained after 5000 cycles in 30 – 55 ºC range [164]. However, its poor cycle-life property is considered as the most serious barrier for its implementation as a hydrogen storage material when performed at a higher temperature [8, 163]. For instance, the hydrogen storage capacity of $CaNi_5$ decreased to less than 50% of the initial capacity in one study after absorption/desorption for 200 cycles at 85 ºC [8]. As a result, the poor cyclic durability of $CaNi_5$ is caused by the disproportionation of Ca from the alloy as CaH_2 [165, 166]. Accordingly, many studies have been attempted to improve the hydrogen storage properties of this alloy, including its capacity and stability [85, 167-169].

In the past decade much research has been undertaken to improve the hydrogen storage properties of $CaNi_5$ by partial substitution of rare earth or transition metals at Ca and Ni sites. It was determined that the hydrogen storage capacity could be improved when the host metals of AB_5 alloys were partially replaced by larger metal atoms, as this would create larger unit cell volume after the substitutions [170]. Replacement of Ca by Ce and Ni by Zn changed the unit cell volume and consequently the plateau pressure and the thermodynamics of hydrogenation [85]. The hydrogen storage capacity of these substituted alloys was decreased and the plateau region was narrowed. Another study showed that adding a small amount of Mg into $CaNi_5$ destroyed the AB_5 structure and formed AB_3 and Ni phases [82]. Although Sn and Al can improve the stability of $LaNi_5$- and $MmNi_5$-based alloys, they are not effective for $CaNi_5$ based alloys [8, 171, 172]. Furthermore, an attempt to replace Ni by Sn did not result in the formation of the $CaNi_5$ phase by mechanical alloying followed by heat treatment [85]. In other research, the cycling stability of Ca-Mg-Ni and La-Mg-Ni alloys as battery electrodes could be significantly

improved by the substitution of Cr [173, 174] but it led to a decrease in the discharge capacity.

It was suggested that substitution for Ca in $CaNi_5$ is the likely option to improve cyclic stability [167]. Accordingly, substitution of the Ca site by rare earth or alkaline earth elements such as La and Ce can dramatically improve the cycle life of $CaNi_5$-based alloys during electrochemical charging and discharging [169] . In addition, La-substituted $CaNi_5$-type alloys annealed at a higher temperature and for a longer time show better electrochemical durability [175]. The incorporation of Zr in the Mg-Ni system causes a considerable increase in the stability of the alloy [176]. Furthermore, it was also reported that Zr formed a high strength metallic bond with Ni as found in substituted $LaNi_5$ [177]. Consequently, partial substitution of Zr at the Ca site may enhance the stability of the $CaNi_5$ alloy.

4.2 SYNTHESIS

A $CaNi_5$ alloy was initially undertaken by a conventional induction melting technique [8, 9, 169]. However, the investigation of the phase relationship of the Ca-Ni system is seriously limited by the low boiling point of calcium (1484 ºC) [178], which is similar to the melting point of nickel (1455 ºC). As a result, the Ca metal can possibly be lost from the system by evaporation during the melting process [179]. Furthermore, this technique is likely to undergo further difficulties in producing a ternary $CaNi_5$-based alloy by adding a third transition metal such as Zr, Cr and Mo that melt at 1852, 1890 and 2610 ºC, respectively. The melting temperatures of these metals are higher than the boiling temperature of Ca [180]. Another disadvantage of this method has been reported by Yasuda [181], detecting metal segregation as a secondary phase in the alloy. In contrast, a mechanical alloying technique benefits by the alloy synthesis of low and high melting-temperature metals with a reaction at room temperature. In addition, homogeneous particles of the alloy can be achieved by using this method [182] . Thus, all $CaNi_5$-based alloys in this study were synthesised by mechanical ball-milling method. The raw elemental metals, listed in Table 4-1, were prepared under an argon atmosphere by mixing at a desired composition followed by ball milling.

Table 4-1: Specifications of raw elemental metals.

Metal	Purity	Metal form	Supplier
Ca	99%	Granule	Sigma-Aldrich
Ni	99.999%	Powder with particle size < 150 µm	Sigma-Aldrich
Al	99.99%	Flake with particle size 1 mm	Sigma-Aldrich
Cr	99+%	Powder, -325 mesh	Sigma-Aldrich
Zr	97%	Powder	Riedel-de Haën
Mo	99.99%	Powder with particle size 1 – 2 µm	Sigma-Aldrich

Binary alloys of Ca-Ni are formed in different compositions as shown in the Ca-Ni phase diagram (Figure 4-2). To synthesise the $CaNi_5$ binary alloy, a mixture of Ca granules (12.02 wt.%) and Ni powder (87.98 wt.%) were first hand mixed. Mechanical ball-milling was performed in a 316-stainless steel (SS) canister (650 cm^3 internal volume) attached to a Glen Mills Turbula T2C shaker mixer with the

ball to powder mass ratio (B:P) of 12:1 using equal numbers of 12.7 mm and 7.938 mm 316 SS balls. A small amount of hexane, approximately 2 ml, was added to the mixture as a process control agent (PCA) to prevent cold welding.

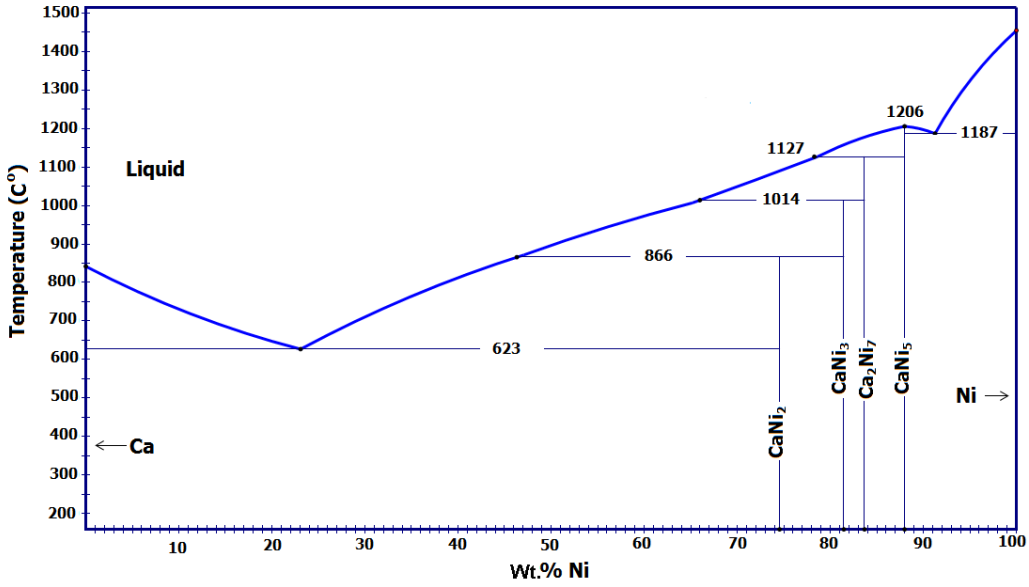

Figure 4-2: Alloy phase diagram of Ca-Ni system, adapted from [183].

Ternary and quaternary $CaNi_5$-based alloys can be synthesised by partial substitution of metallic elements at both the Ca and Ni sites. In this work, Cr, Al and Mo are expected to be incorporated at the Ni site whilst Zr should be substituted at Ca site, see Figure 4-3. Small quantities of these additive metals, approximately 1 – 5 wt.%, were used for each desired composition. The mixtures of metals were subjected to mechanical ball-milling under an Ar atmosphere with a ball to powder mass ratio of 12:1. The milled powders were then followed by heat treatment under a vacuum $< 10^{-3}$ torr (1.33×10^{-3} mbar).

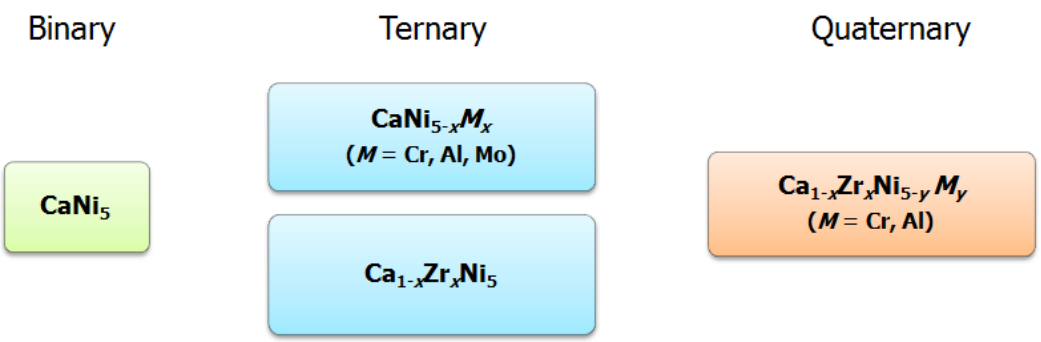

Figure 4-3: Schematic diagram of partial substitution of $CaNi_5$-based alloys.

4.3 BINARY $CaNi_5$ ALLOY

After milling for 20 or 40 h, the mixture of Ca granules (12.02 wt.%) and Ni powder (87.98 wt.%) formed into a fine powder. As shown in Figure 4-4, the XRD pattern of 40 h as-milled powder does not show the $CaNi_5$ phase. The strong diffraction peaks for Ni are present for this as-milled sample, but the peaks from Ca are not observable due to its low weight fraction and small crystallite size. In addition, ball milling may lead to Ca becoming amorphous or nanocrystalline i.e., Ni peaks are broad but clearly crystalline whereas the Ca peaks and/or its intermediate phases with Ni are masked by the background [85]. Although the $CaNi_5$ phase does not form directly at this stage, the formation of a partially amorphous phase has probably taken place mixed with the nanocrystalline Ni phase [82]. However, different milling parameters including impact energy and milling time can possibly lead to the direct formation of the $CaNi_5$ phase as found in some substituted alloys [85].

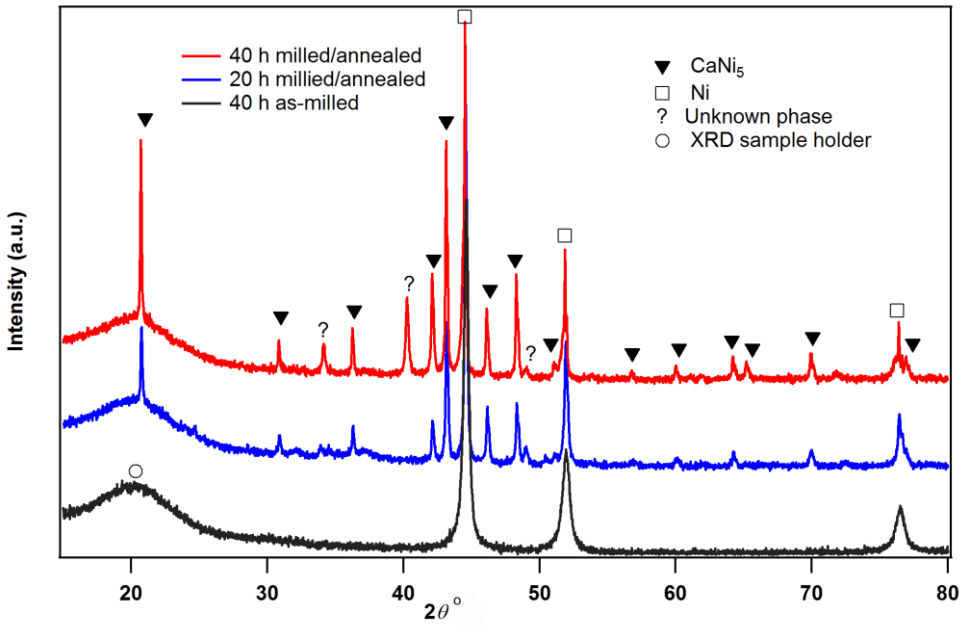

Figure 4-4: XRD patterns of as-milled and annealed powder under vacuum at 550 ºC for 24 h.

The $CaNi_5$ structure was formed after heat treatment at 550 ºC under vacuum for 24 h. Rietveld analysis revealed that a higher abundance of the $CaNi_5$ phase was formed for the 40 h milled sample as compared to the 20 h milled sample as shown in Table 4-2. Thus, it can be inferred that the longer milling time possibly increases the

homogeneity of the mixture. An unknown phase exists while annealing under vacuum. More details on the formation of this phase will be discussed below.

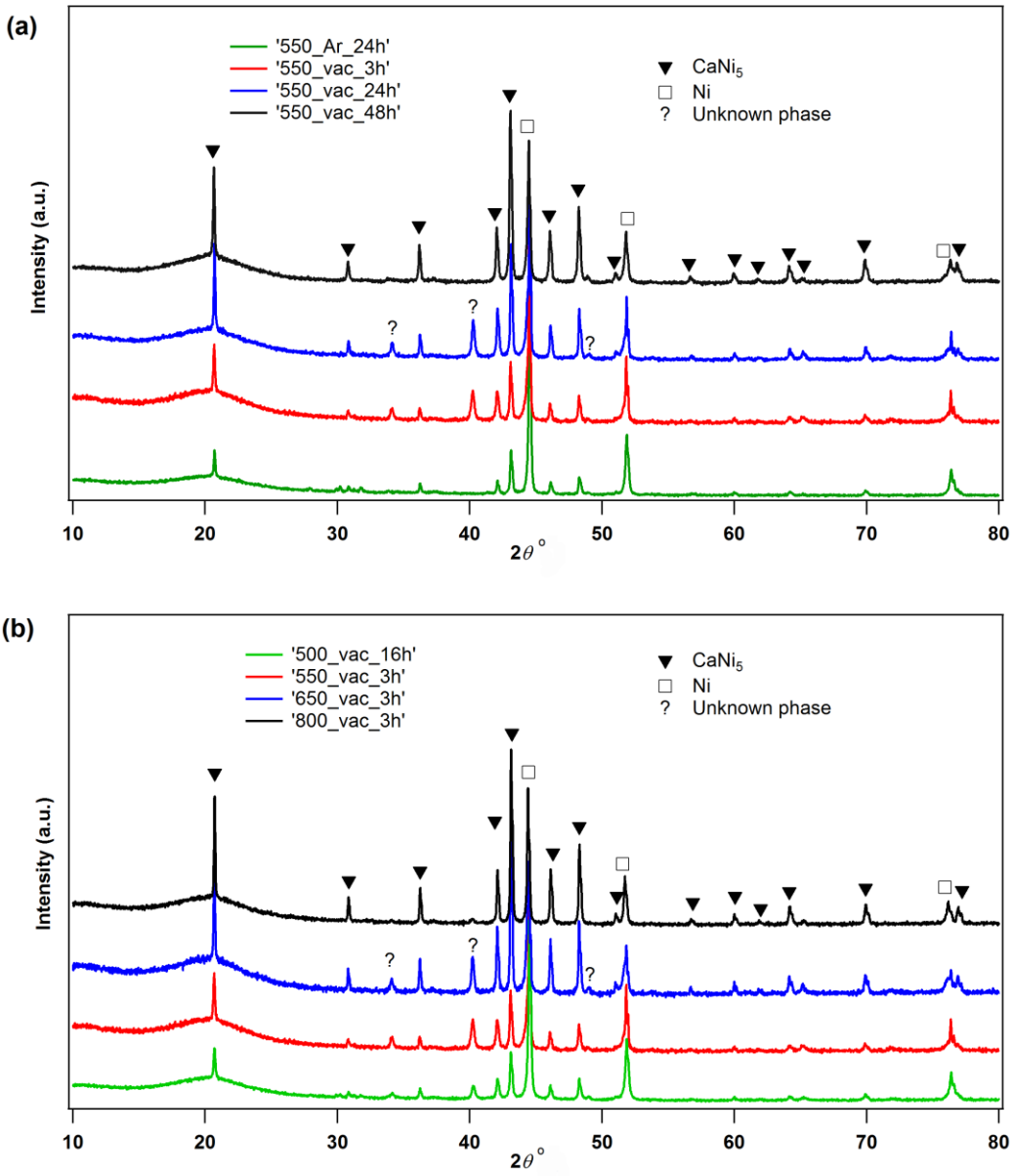

Figure 4-5: Effect of annealing conditions, (a) atmosphere and duration and (b) temperature, on the formation of $CaNi_5$ phase for the 40 h milled powder.

To optimize the annealing conditions, the 40 h as-milled powder was annealed under either vacuum or an argon atmosphere at various annealing temperatures and durations. Figure 4-5 (a) shows the formation of the $CaNi_5$ alloy from 40 h milled-samples after annealing at 550 ºC for various annealing times. As shown in Table 4-2 the longer the annealing time, the higher the proportion of $CaNi_5$ that is formed. For 24 h annealing, a higher abundance of the $CaNi_5$ phase is observed when annealed under vacuum compared to that under an Ar atmosphere. The presence of the $CaNi_5$

phase after annealing at 550 ºC under vacuum and Ar are approximately 55 and 29 wt.%, respectively. There is a remnant secondary Ni phase in all samples. There was possibly some loss of Ca metal during mechanical milling as calcium is a ductile metal, which adheres easily to the surface of the milling canister and balls. Thus, the Ca-poor system leads to the incomplete formation of the desired $CaNi_5$ alloy system and excess Ni metal persists in the powder.

The unknown diffraction peaks are clearly observed when the mixtures were annealed at 550 ºC under vacuum for 3 and 24 h. In contrast, these peaks are not found for the sample annealed under Ar for 24 h. These unidentified phases are likely an intermediate Ca-Ni compound. It was previously reported that intermediate phases could form due to inadequate annealing times [82]. As a result, further annealing for 48 h at 550 ºC not only increases the quantity of $CaNi_5$ phase but also reduces these intermediate phases.

Table 4-2: Rietveld analysis of $CaNi_5$ phase formation at various annealing conditions for 40 h milled powder.

Annealing conditions			Abundance of $CaNi_5$ phase (wt.%)
Temperature (ºC)	Atmosphere	Time (h)	
550	Ar	24	28.94
500	Vacuum	16	31.56
550	Vacuum	3	41.14
550*	Vacuum	24	40.06
550	Vacuum	24	54.75
550	Vacuum	48	66.95
650	Vacuum	3	61.88
800	Vacuum	3	68.10

*Ball milling for 20 h.

Figure 4-5 (b) displays the effect of temperature on the formation of the $CaNi_5$ alloy under vacuum. Although the annealing time is longer than for other samples, annealing at 500 ºC for 16 h under vacuum forms a very low abundance of the $CaNi_5$ phase, ~31.56 wt.%, incorporated with an unknown phase. Annealing at higher temperatures, 550 and 650 ºC, for 3 h increases the $CaNi_5$ content to 41.14 and 61.88

wt.%, respectively. However, the unknown phase still shows strong peaks in the XRD patterns when annealing under these conditions. Annealing at 800 ºC for 3 h shows not only an increase of the $CaNi_5$ alloy (68.10 wt.%) but also a reduction of the unknown phase. As can be seen, this quantity of $CaNi_5$ is comparable to that obtained from annealing at 550 ºC for 48 h. Accordingly, the longer annealing time is required for a lower annealing temperature to promote the formation of $CaNi_5$ and eliminate the intermediate phases. In other words, higher temperatures can shorten the annealing time. However, high annealing temperatures have an additional limitation due to the evaporation of Ca at high annealing temperatures.

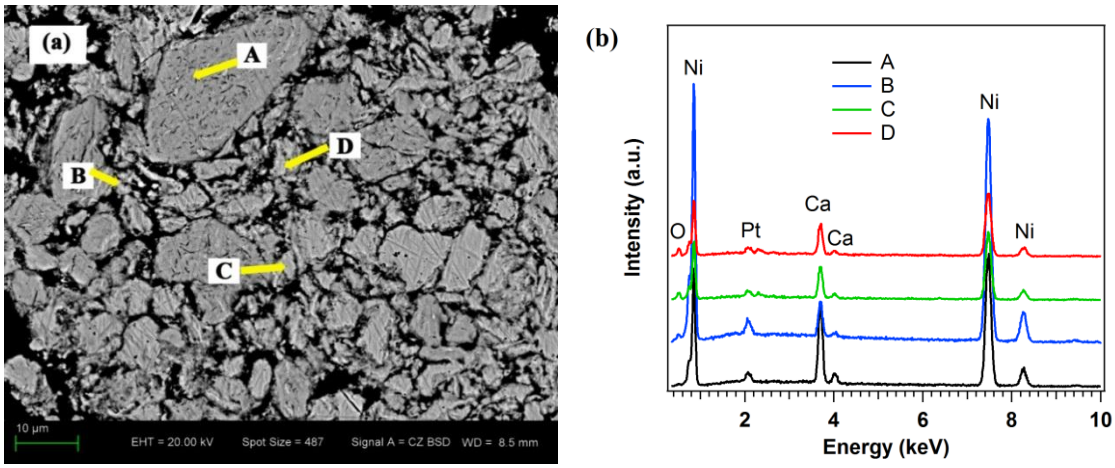

Figure 4-6: (a) BSE-SEM image (b) EDS spectra at selected areas of $CaNi_5$ after annealing under vacuum at 800 ºC for 3 h.

Figure 4-6 (a) is a backscattered electron SEM (BSE-SEM) micrograph of the $CaNi_5$ distribution after annealing under vacuum at 800 ºC for 3 h. The alloy is relatively homogeneous with a particle average size ranging from 1 – 50 µm. The Ni-rich phase observed from XRD has been identified as the brighter regions because atomic mass of Ni is greater than that of Ca, causing increased electron scattering. EDS spectra at four selected areas are shown in Figure 4-6 (b). All initially milled elements, Ca and Ni, are present including a small quantity of Pt due to the SEM sample coating process. The quantitative EDS analysis results are shown in Table 4-3. The Ca-rich $CaNi_5$ alloy is observed in larger particles (area A), whilst Ca-poor regions appear in a smaller particles (area B). Particles with average sizes such as those in regions C and D show Ca and Ni ratios close to those expected from a pure $CaNi_5$ phase. The minor inhomogeneity appears to be due to an artefact of milling large Ca granules (1 – 2 mm) and small Ni powder (< 150 µm), which leaves some

powder grains with excess Ca. Accordingly, this also leads to the presence of the excess Ni in other regions of the sample. To promote the formation of $CaNi_5$ phase, it is suggested to compact the milled powder into a firm pellet before annealing, thus providing adequate diffusion paths for the elements [184]. In addition, optimization of ball milling and annealing conditions can also improve the homogeneity of the alloys [82].

Table 4-3: Quantitative EDS analysis of the element composition of $CaNi_5$.

Area	Elemental composition, wt.%		Atomic ratio (Ca : Ni)
	Ca	Ni	
A	18.46	81.54	1 : 3.0
B	5.76	94.24	1 : 11.2
C	11.37	88.63	1 : 5.3
D	13.87	86.13	1 : 4.2

4.4 Cr-, Al- AND Mo-SUBSTITUTED $CaNi_5$-BASED ALLOYS

The elemental metals Cr, Al and Mo were added to mixtures of Ca and Ni to synthesise the desired ternary alloys $CaNi_{5-x}$(Cr, Al or Mo)$_x$ as listed in Table 4-4. After ball milling a fine powder was achieved. Morphology, crystalline structure and phase composition of the samples were investigated after thermal annealing.

Table 4-4: Metal compositions of synthesised alloys by partial substitution of Cr, Al and Mo.

Composition	Metal (wt.%)				
	Ca	Ni	Cr	Al	Mo
$CaNi_5$*	12.02	87.98	-	-	-
$CaNi_{4.9}Cr_{0.1}$*	12.04	86.40	1.56	-	-
$CaNi_{4.8}Cr_{0.2}$*	12.06	84.81	3.13	-	-
$CaNi_{4.9}Al_{0.1}$	12.13	87.05	-	0.82	-
$CaNi_{4.8}Al_{0.2}$	12.25	86.10	-	1.65	-
$CaNi_{4.9}Mo_{0.1}$	11.88	85.27	-	-	2.85
$CaNi_{4.8}Mo_{0.2}$	11.75	82.62	-	-	5.63

*Hexane was used as PCA during ball milling.

Figure 4-7 shows the XRD spectra of the substituted alloys, including pure $CaNi_5$ after annealing at 800 ºC for 3 h under vacuum. The $CaNi_5$ phase was identified for all alloys except $CaNi_{4.8}Mo_{0.2}$, which primarily formed a Ca_2Ni_7 phase, Er_2Co_7 structure, space group *R*-3*m*. Secondary phases of Ca-Ni compounds such as $CaNi_2$, $CaNi_3$ and Ca_2Ni_7 have been formed previously instead of $CaNi_5$ when using a high content of Cr, Mn, Fe and Co as additives [167]. It was reported that the A_2B_7 phase usually formed coexisting with the AB_5 phase for $Ca_{1-x}La_xNi_{4.7}Al_{0.3}$ alloys, however, the appropriate annealing conditions can reduce this A_2B_7 phase [175]. The mixed results in other similar systems reveal that each composition attempted herein is probably not completely homogeneous due to a strong dependence on the conditions of annealing. The Cr- and Mo-substituted alloys form an unidentified phase which is probably an intermediate phase of Ca-Ni or Ni-Cr/Mo. As can be seen, the high content of the additive Cr tends to increase the formation of this intermediate phase. Pure elemental Ni is still present after annealing, with strong diffraction peaks, and it is likely present due to the evaporation or loss of Ca during the milling and annealing processes as mentioned in section 4.3. Excessive Ni was also previously observed as an effect of Ca evaporation while annealing under an Ar atmosphere [175]. The Ca-

poor system leads to the incomplete formation of the desired $CaNi_5$ alloy system and excess Ni metal persists in the powder. Interestingly, the excessive Ni phase in the annealed $CaNi_{5-x}$(Al or Mo)$_x$ systems displays Ni peak positions that are shifted to lower angle (higher *d*-spacing). This is likely a result of Al and Mo dissolving into the pure Ni and forming nickel rich solid solutions of Ni-Al and Ni-Mo, respectively [167]. This phenomenon results in the expansion of the Ni unit cell because the metallic radii of Al (1.43 Å) and Mo (1.39 Å) are larger than that of Ni (1.24 Å), see Figure 4-8. Similarly, this behaviour was observed in another alloy such as Ti–Cr–V substituted by Nb or Fe [185].

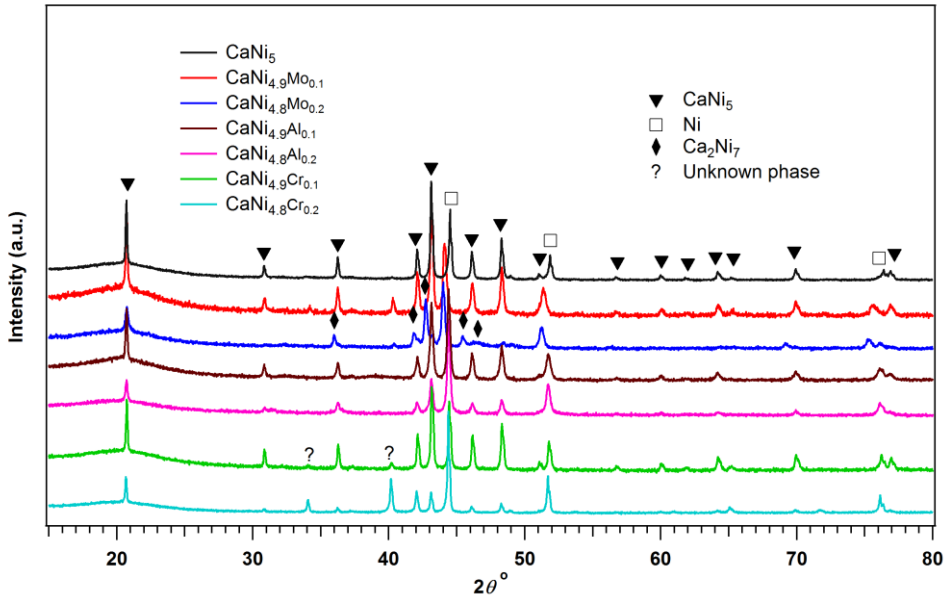

Figure 4-7: XRD patterns of Cr-, Al- and Mo-substituted $CaNi_5$-based alloys after heat treatment.

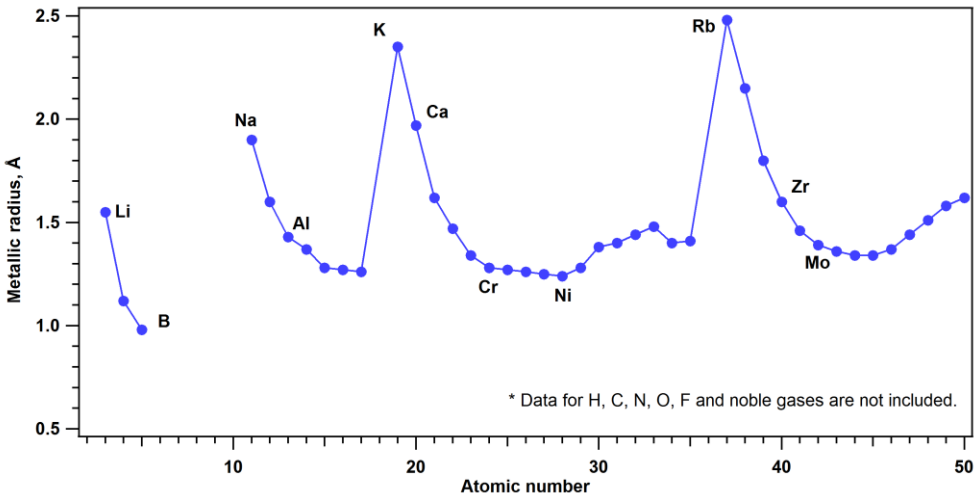

Figure 4-8: Plots of metallic radius of elements, data from ref.[186].

As shown in Table 4-5, the calculated lattice parameters of pure $CaNi_5$ from XRD are a = 4.956 and c = 3.935 Å, with a unit cell volume of 83.700 $Å^3$. The unit cell volume of $CaNi_5$ increases for all substituted alloys. For a low content of additives, the unit cell volume of $CaNi_{4.9}Al_{0.1}$ > $CaNi_{4.9}Mo_{0.1}$ > $CaNi_{4.9}Cr_{0.1}$ corresponding to the fact that the atomic radii of Al > Mo > Cr. The formation of an unidentified phase possibly causes the nonlinear variation of the unit cell volume with additive loading of the substituted alloys. Due to additional segregation or poor mixing, the abundance of the $CaNi_5$ phase in substituted alloys, $CaNi_{5-x}M_x$, has been reduced with increasing x, except for the $CaNi_{4.9}Mo_{0.1}$ and $CaNi_{4.9}Cr_{0.1}$ composition.

Table 4-5: Phase analysis and crystalline structures of Cr-, Al- and Mo-substituted $CaNi_5$-based alloys.

Alloy	Phase	Phase abundance (wt.%)	Lattice parameters		
			a (Å)	c (Å)	V ($Å^3$)
$CaNi_5$	$CaNi_5$	68.10	4.9557	3.9354	83.700
	Ni	31.90	3.5334		44.115
$CaNi_{4.9}Cr_{0.1}$	$CaNi_5$	72.58	4.9562	3.9348	83.706
	Ni	27.42	3.5317		44.050
$CaNi_{4.8}Cr_{0.2}$	$CaNi_5$	32.33	4.9568	3.9348	83.723
	Ni	67.67	3.5333		44.112
$CaNi_{4.9}Al_{0.1}$	$CaNi_5$	62.72	4.9604	3.9377	83.907
	Ni	37.28	3.5365		44.231
$CaNi_{4.8}Al_{0.2}$	$CaNi_5$	41.43	4.9602	3.9363	83.872
	Ni	58.57	3.5360		44.213
$CaNi_{4.9}Mo_{0.1}$	$CaNi_5$	69.88	4.9587	3.9364	83.822
	Ca_2Ni_7	7.77	4.9600	36.0933	768.994
	Ni	21.32	3.5580		45.044
	Mo	1.04	3.1661		31.738
$CaNi_{4.8}Mo_{0.2}$	$CaNi_5$	3.70	4.9596	3.9416	83.963
	Ca_2Ni_7	63.31	5.0046	35.9980	780.808
	Ni	32.61	3.5719		45.572
	Mo	0.38	3.1649		31.701

It is of interest that the Ca_2Ni_7 phase is only observed for the Mo loaded samples, however a solid solution phase between excess Ni and Al/Cr/Mo is observed in all substituted systems. Liang and Schulz [82] pointed out that intermediate phases involving Ni and additives may be present when using a low temperature and short period for annealing. Furthermore, alloys with a higher content of a substituted metal also require heat treatment at a higher temperature and longer time to be completely homogenised [175]. This unwanted solid solution with free Ni results in the reduction of the ideal additive ratio and supports the formation of the Ca_2Ni_7 phase instead of the desired $CaNi_5$ phase. The unit cell volume of the Al- and Mo-substituted Ni increases to 44.230 – 45.572 $Å^3$ compared to 44.115 $Å^3$ for pure Ni. On the other hand, substitution of Cr does not show a significant change in unit cell volume of either $CaNi_5$ or Ni phases because of the comparable atomic radius (R_{at}) of Cr (R_{at} = 1.28 Å) and Ni (R_{at} = 1.24 Å), as shown in Figure 4-8.

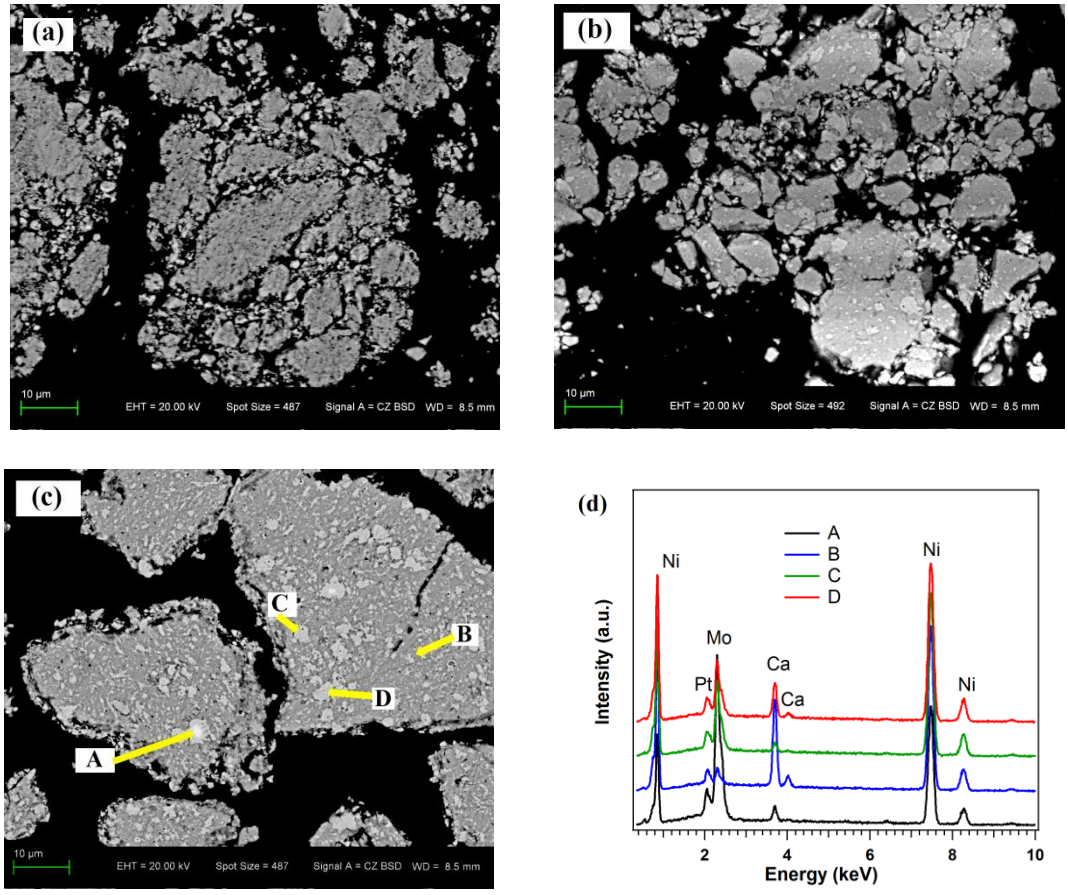

Figure 4-9: BSE-SEM images of (a) $CaNi_{4.9}Al_{0.1}$ (b) $CaNi_{4.9}Mo_{0.1}$ (c) $CaNi_{4.8}Mo_{0.2}$ and (d) EDS spectra at selected areas of $CaNi_{4.8}Mo_{0.2}$.

Backscattered electron SEM micrographs of partially substituted $CaNi_5$ by Al and Mo are shown in Figure 4-9 (a – c). The $CaNi_{4.9}Al_{0.1}$ alloy, Figure 4-9 (a), shows relative homogeneity of the as formed phases, similar to the result of pure $CaNi_5$ (see Figure 4-6 (a)). Partial substitution of Mo, ~2 – 5 wt.%, increases inhomogeneity, which is proportional to the content of this additive metal as shown in Figure 4-9 (b) and (c). Therefore, more segregation appears in $CaNi_{4.8}Mo_{0.2}$ compared to that of $CaNi_{4.9}Mo_{0.1}$. From the quantitative EDS measurement, Figure 4-9 (d) and Table 4-6, a Ni–Mo alloy is observed in Ni-rich regions of $CaNi_{4.8}Mo_{0.2}$ shown in areas C and D of Figure 4-9 (c). This result confirms the expansion of the Ni unit cell by Mo incorporation observed by XRD. Other regions of this sample resemble a pure Ca_2Ni_7 phase i.e. area B of Figure 4-9 (c). From Table 4-6, the atomic ratio of Ca:Ni at this area is 1:3.4 and comparable to 1:3.5 for Ca_2Ni_7.

Table 4-6: Quantitative EDS analysis of the element composition of $CaNi_{4.8}Mo_{0.2}$.

Area	Elemental composition, wt.%			Atomic ratio (Ca:Ni:Mo)
	Ca	Ni	Mo	
A	2.15	42.30	55.55	1:13.4:10.8
B	15.47	76.10	8.43	1:3.4:0.2
C	1.51	67.16	31.33	1:30.3:8.7
D	5.97	68.61	25.42	1:7.8:1.8

4.5 TERNARY AND QUATERNARY ALLOYS $Ca_{1-x}Zr_xNi_{5-y}$(Cr or Al)$_y$

In this section, $CaNi_5$-based ternary alloys were investigated by substitution of Zr at the Ca site. Furthermore, substitution of both the Ca and Ni site, forming quaternary alloys, was also studied. Thus, the stoichiometric formula of the alloys is $Ca_{1-x}Zr_xNi_{5-y}$(Cr or Al)$_y$ with x = 0.05, 0.1 and 0.2, y = 0 and 0.1. The mixtures of metals, with compositions shown in Table 4-7, were ball milled with hexane as the process control agent (PCA), followed by heat treatment.

Table 4-7: Metal compositions of substituted alloys $Ca_{1-x}Zr_xNi_{5-y}$(Cr or Al)$_y$.

Composition	Metal (wt.%)				
	Ca	Ni	Zr	Cr	Al
$Ca_{0.95}Zr_{0.05}Ni_5$	11.33	87.31	1.36	-	-
$Ca_{0.9}Zr_{0.1}Ni_5$	10.65	86.66	2.69	-	-
$Ca_{0.8}Zr_{0.2}Ni_5$	9.33	85.37	5.30	-	-
$Ca_{0.95}Zr_{0.05}Ni_{4.9}Cr_{0.1}$	11.35	85.74	1.36	1.55	-
$Ca_{0.95}Zr_{0.05}Ni_{4.9}Al_{0.1}$	11.44	86.38	1.37	-	1.67

Figure 4-10 depicts the XRD spectra of the $Ca_{1-x}Zr_xNi_{5-y}$ (Cr or Al)$_y$ alloys after annealing under vacuum at 800 ºC for 3 h. The abundance of the $CaNi_5$ phase in the alloys was calculated by the Rietveld method and varies in each composition ranging from approximately 50 to 70 wt.% (see Table 4-8) with the remaining proportion being predominantly Ni. Secondary phase $ZrNi_5$ (space group $F4$-$m3$, $AuBe_5$-type structure) was indexed in all samples. An unidentified phase is also observed in both quaternary alloys, $Ca_{0.95}Zr_{0.05}Ni_{4.9}Cr_{0.1}$ and $Ca_{0.95}Zr_{0.05}Ni_{4.9}Al_{0.1}$, with its strongest diffraction peaks at 2θ ~ 34.05º and 40.20º, respectively. This phase could not be indexed to any known Ca-Ni-Cr (or Al)-Zr alloy. Neither could it be attributed to any known Ca-Ni-Cr (or Al)-Zr oxide or carbide phase, nor to any Fe phases that may be present due to contamination from the milling media. As discussed above (in section 4.3), this phase was also observed in either pure or substituted $CaNi_5$ alloys. Thus, it appears that the unknown phase is an intermediate Ca-Ni alloy, which increases proportionally to the content of additive metals. Optimization of the annealing conditions for each alloy can reduce this intermediate phase as reported previously in section 4.3.

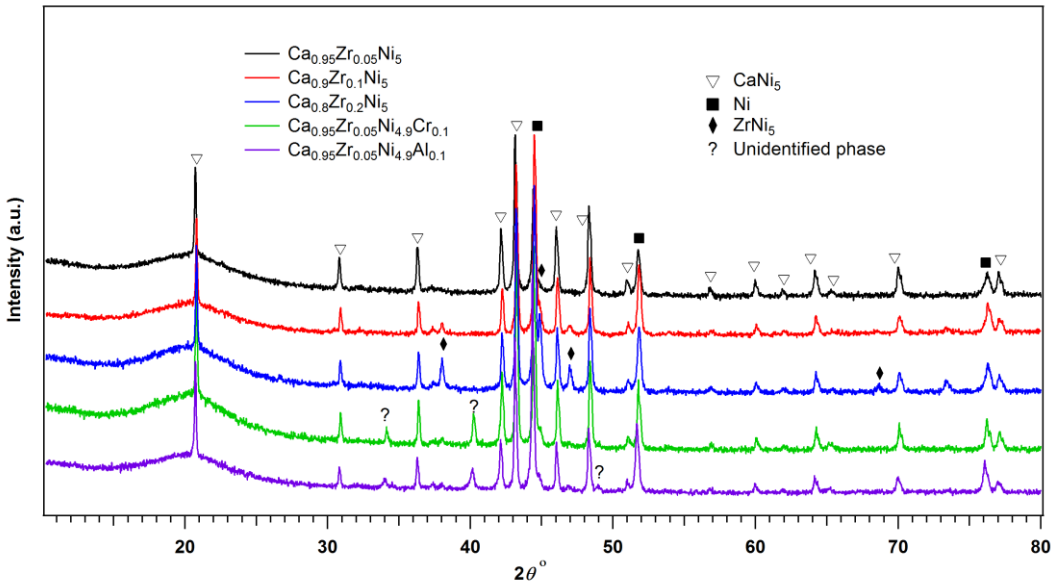

Figure 4-10: XRD patterns of $Ca_{1-x}Zr_xNi_{5-y}$ (Cr or Al)$_y$ alloys after annealed under vacuum at 800 ºC for 3 h.

Substitution of Zr into the Ca site causes a decrease in the unit cell volume compared to pure $CaNi_5$. In fact, the atomic radius (r_{at}) of Zr is less than that of Ca as shown in Figure 4-8. Thus, this result is in agreement with the replacement of Ca (r_{at} = 1.97 Å) by Zr (r_{at} = 1.60 Å) and confirms that the expected substitution has taken place. This substitution results in an increase in the *a*-lattice parameter and decrease in the *c*-lattice parameter. Previously, a similar result has been reported when smaller atoms were replaced at the A site of another AB_5-type alloy such as $LaNi_5$ [187]. The unit cell volume of the $CaNi_5$ phase in quaternary alloys is increased for $Ca_{0.95}Zr_{0.05}Ni_{4.9}Al_{0.1}$ but slightly decreased for $Ca_{0.95}Zr_{0.05}Ni_{4.9}Cr_{0.1}$. In fact, the atomic radius of Cr is comparable to Ni (1.25 Å), but significantly smaller than Al (1.43 Å). Accordingly, substitution of Al at the Ni site results in an increase of the unit cell volume. However, the unit cell volume of the $CaNi_5$ phase in these quaternary alloys is smaller than that of ternary alloys ($CaNi_{4.9}Cr_{0.1}$ and $CaNi_{4.9}Al_{0.1}$) due to the additional effect of Zr substitution at the Ca site.

Table 4-8: Phase analysis and crystalline structures of $Ca_{1-x}Zr_xNi_{5-y}$(Cr or Al)$_y$ alloys .

Alloy	Phase	Phase abundance (wt.%)	Lattice parameters		
			a (Å)	*c* (Å)	*V* (Å^3)
$Ca_{0.95}Zr_{0.05}Ni_5$	$CaNi_5$	71.56	4.9486	3.9420	83.601
	$ZrNi_5$	3.66	6.7445		302.01
	Ni	24.78	3.5307		44.012
$Ca_{0.9}Zr_{0.1}Ni_5$	$CaNi_5$	52.80	4.9492	3.9416	83.610
	$ZrNi_5$	6.01	6.7101		302.12
	Ni	41.19	3.5313		44.037
$Ca_{0.}Zr_{0.2}$ Ni_5	$CaNi_5$	51.15	4.9484	3.9420	83.592
	$ZrNi_5$	13.33	6.7064		301.62
	Ni	35.52	3.5315		44.044
$Ca_{0.95}Zr_{0.05}Ni_{4.9}Al_{0.1}$	$CaNi_5$	53.33	4.9525	3.9420	83.734
	$ZrNi_5$	2.87	6.7056		301.52
	Ni	43.80	3.5371		44.254
$Ca_{0.95}Zr_{0.05}Ni_{4.9}Cr_{0.1}$	$CaNi_5$	64.20	4.9488	3.9402	83.572
	$ZrNi_5$	3.33	6.7058		301.55
	Ni	32.47	3.5332		44.109

4.6 HYDROGEN SORPTION PROPERTIES OF $CaNi_5$-BASED ALLOYS

All alloys (after annealing) were first 'activated' by performing three cycles of hydrogen absorption and desorption before hydrogen sorption measurements were undertaken. Each cycle of the activation process includes evacuation for 1 h and hydrogen absorption under a starting pressure of ~ 60 bars at room temperature for 1 h. Figure 4-11 shows the hydrogen absorption of pure $CaNi_5$ during its activation procedure. As can be seen, the first absorption curve shows an incubation period that lasts about 5 minutes. Thus, only ~2% of full capacity has been reached at this stage. Full absorption of the 1st cycle is reached after ~50 minutes. The hydrogen absorption rate is initially very slow due to the formation of an oxide layer on the alloy surface and also the difficulty of lattice expansion of the fresh alloy during hydride formation [188]. However, this incubation time disappears in the second and third cycles with a significant faster absorption rate.

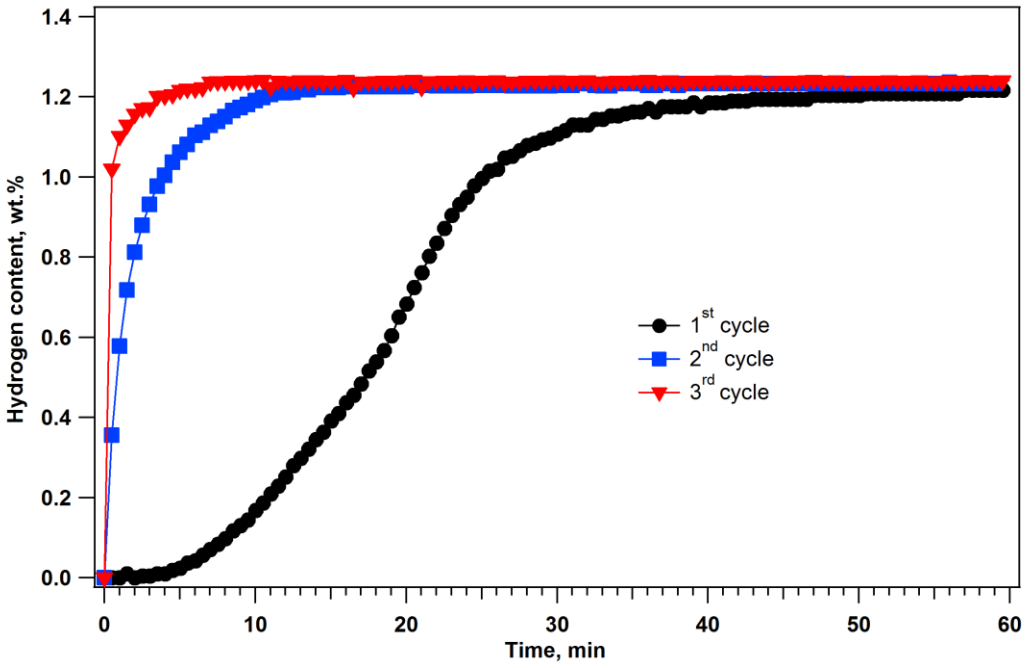

Figure 4-11: Activation curves of $CaNi_5$.

4.6.1 Pressure-Composition-Isotherms (PCI) measurements

The PCI measurements of pure $CaNi_5$ and ternary alloys $CaNi_{4.9}$(Cr, Al or Mo)$_{0.1}$ at four temperatures were evaluated by a PCTPro-E&E (Hy-Energy) gas sorption analyser shown in Figure 4-12. The hydrogen storage capacity is reduced by approximately 20% for all substituted alloys compared to pure $CaNi_5$. Accordingly,

the plateau regions of these alloys are narrowed. The decrease of hydrogen storage capacity is likely caused by a reduction of sites in the lattice that may be occupied by hydrogen, as reported in the $LaNi_{5-x}Fe_x$ system [189].

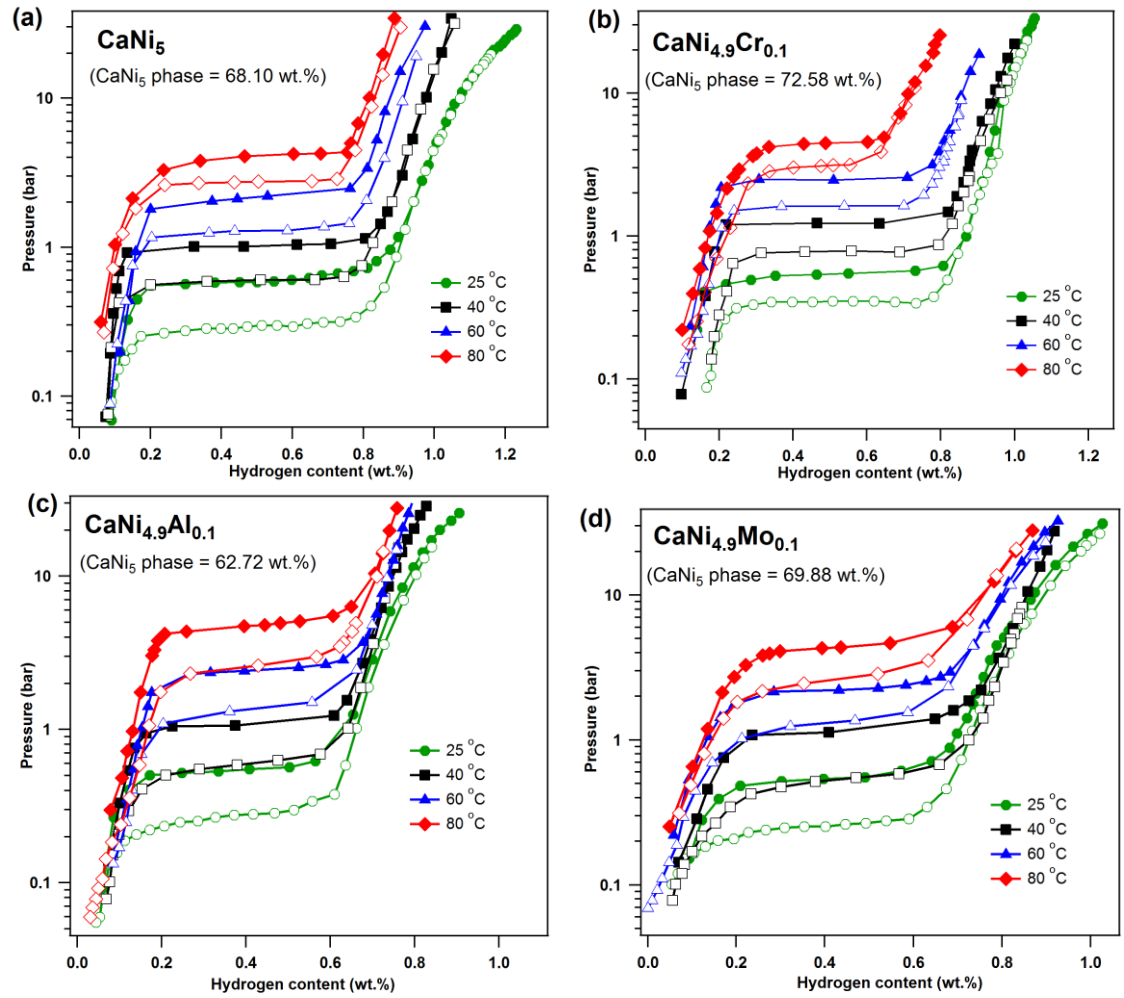

Figure 4-12: PCI's of (a) $CaNi_5$, (b) $CaNi_{4.9}Cr_{0.1}$, (c) $CaNi_{4.9}Al_{0.1}$and (d) $CaNi_{4.9}Mo_{0.1}$ with the hydrogen content calculated from the weight of the entire sample measured at 25, 40, 60 and 80 ºC, respectively.

The measured hydrogen capacity presented in Figure 4-12 is correlated to the weight of the entire sample. There is excessive Ni in all samples equating to ~ 30 wt.%. However, the formation of nickel hydride (NiH_x) only occurs under very high hydrogen pressure, approximately 3000 bar at 25 ºC [113]. Thus, the Ni phase will not absorb hydrogen under these experimental conditions, and can be considered as 'dead-weight'. As shown in Table 4-9, the hydrogen content of unsubstituted $CaNi_5$ alloy is 1.76 wt.% H when normalized to the $CaNi_5$-phase content (based on Rietveld results). This capacity is comparable to other studies where 1.5 – 1.9 wt.% H capacities have been obtained [9, 85]. Consequently, the hydrogen content of

$CaNi_{4.9}$(Cr, Al or Mo)$_{0.1}$ alloys is ~ 1.5 wt.% H when normalised. The hydrogen storage capacity of $CaNi_5$-based alloys does not significantly increase by substitution of Al or Mo as found in another AB_5-type alloy, *Lm*(Ni, Mn, Co, Al)$_{5-x}$Mo$_x$, where *Lm* is La-rich mischmetal [170, 190].

Table 4-9: PCIs properties and hydrogen storage capacity of $CaNi_{4.9}$(Cr, Al or Mo)$_{0.1}$ alloys.

Alloy	[a]Plateau Pressure (bar)		[a]Plateau slope	[a]Hysteresis ($P_{abs.}/P_{des.}$)	[b]Abs. capacity (wt.% H)	
	Abs.	Des.			[1]wt.% H	[2]wt.% H
$CaNi_5$	0.59	0.33	0.22	1.79	1.25	1.83
$CaNi_{4.9}Cr_{0.1}$	0.55	0.35	0.05	1.72	1.05	1.45
$CaNi_{4.9}Al_{0.1}$	0.54	0.28	0.65	1.93	0.93	1.49
$CaNi_{4.9}Mo_{0.1}$	0.54	0.26	0.48	2.07	1.03	1.47

[a] Determined from 25 ºC plateau.

[b] Maximum absorption capacity measured at 25 ºC and 30 bar of hydrogen pressure where [1]wt.% H and [2]wt.% H are calculated from the weight of the entire sample and only the $CaNi_5$ phase, respectively.

The absorption and desorption plateau pressures at 25 ºC for $CaNi_5$ are observed at ~ 0.6 and 0.3 bar, respectively, with relatively flat plateaux. Replacement of Ni in the $CaNi_5$ alloy by a small content of Al and Mo results in a lower pressure desorption plateau, which indicates a higher stability of the hydride in the substituted alloys. Al and Mo atoms are significantly larger than Ni and Cr. Incorporation of Al or Mo at the Ni site of $CaNi_5$ significantly increases the unit cell volume as seen in Table 4-5. Thus, higher stability hydrides form in the alloys with larger unit cell volumes, as mentioned previously, resulting in lower desorption plateau pressures. The sorption hysteresis ($P_{abs.}\backslash P_{des.}$) of all alloys ranges between 1.7 and 2.1. The hysteresis is detrimental to practical applications but tends to decrease with temperature, likely due to a thermally activated stress relaxation processes [191].

The Al and Mo substituted alloys show a slight increase in the slope of the plateau. It is possible that the chemical bond strength of Al/Mo-Ni and Ca-Al/Mo may be greater than those of Ni-Ni and Ca-Ni, respectively. Similarly, the increase of metal-metal bond order of Ni-substituted $LaNi_5$ alloy has been reported [177]. The stronger bond leads to a greater difficulty in expanding the crystal lattice during absorption. In

addition, replacement of Ni by a larger atom could possibly deform the crystal lattice, which affects the hydrogen diffusion path during the hydrogen sorption process. For each step of PCIs measurement (at a certain applied pressure), a longer time is required to form the hydride in these lattices compared to the unmodified alloy. This can result in the increase of plateau slope for the Al and Mo substituted alloys if the PCIs are measured with an inadequate time interval for each step.

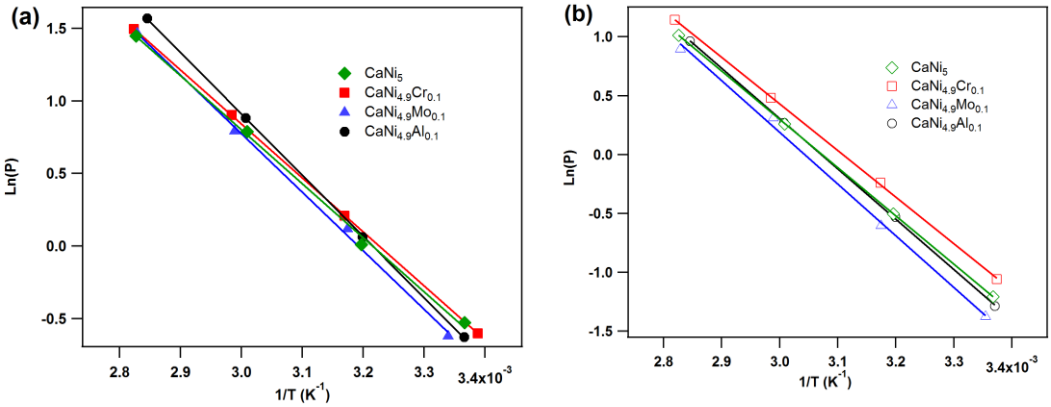

Figure 4-13: van't Hoff plots of hydrogen (a) absorption and (b) desorption of the synthesised alloys.

The reaction enthalpy (ΔH) and entropy (ΔS) of the hydrogen sorption mechanisms were determined from the least-squares linear fit to van't Hoff plots (Figure 4-13) by using equations 3.8 and 3.9. These values are also given in Table 4-10. The ΔH of absorption of pure $CaNi_5$ is -31.0 ± 0.2 kJ/mol H_2, which is comparable to an earlier study, -33.5 kJ/mol H_2 [9] .

Table 4-10: Thermodynamic data for $CaNi_{4.9}$(Cr, Al or Mo)$_{0.1}$ alloys.

Alloy	ΔH (kJ/mol H_2)		ΔS (J/mol H_2 K)	
	$\Delta H_{abs.}$	$\Delta H_{des.}$	$\Delta S_{abs.}$	$\Delta S_{des.}$
$CaNi_5$	-31.0 ± 1.2	34.1 ± 0.2	-99.7 ± 2.3	105.0 ± 0.4
$CaNi_{4.9}Cr_{0.1}$	-30.9 ± 0.1	32.9 ± 0.3	-99.8 ± 0.2	102.4 ± 1.0
$CaNi_{4.9}Al_{0.1}$	-35.2 ± 0.2	35.6 ± 0.3	-113.1 ± 0.6	109.2 ± 0.9
$CaNi_{4.9}Mo_{0.1}$	-33.6 ± 0.9	36.6 ± 1.4	-107.3 ± 2.8	111.2 ± 4.2

The results provided in Table 4-10 for substituted alloys also agree with an earlier report [192], which shows that the magnitude of ΔH for both absorption and

desorption is directly proportional to the unit cell volume. In fact, ΔH is related to the bonding strength of hydrogen in the alloys. Therefore, larger unit cell alloys, especially $CaNi_{4.9}Al_{0.1}$ and $CaNi_{4.9}Mo_{0.1}$ compositions, show greater metal-hydrogen (M-H) interactions, reflected by more negative reaction enthalpies for the hydride formation. In other words, more stable hydrides have been formed in these alloys with a consequence of lower desorption plateau pressures. As can be seen, the absolute value of the reaction entropy (ΔS) ranges between 100 and 115 J/(K·mol H_2), which is comparable to 130 J/(K·mol H_2) for a perfectly ordered hydride [126].

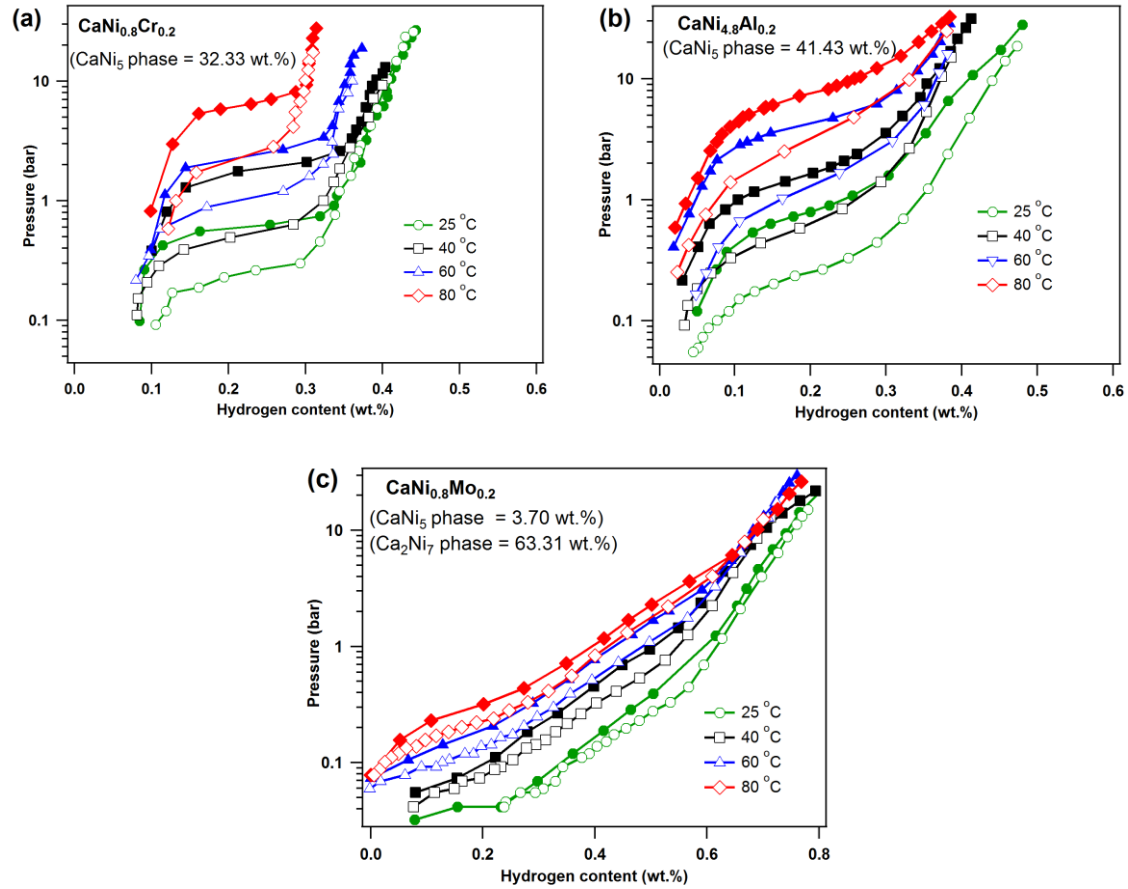

Figure 4-14: PCI's of (a) $CaNi_{4.8}Cr_{0.2}$, (b) $CaNi_{4.8}Al_{0.2}$ and (c) $CaNi_{4.8}Mo_{0.2}$ measured at 25 , 40 , 60 and 80 °C, respectively.

Figure 4-14 illustrates the PCIs of $CaNi_{4.8}$ (Cr, Al or Mo)$_{0.2}$ at near ambient temperature (25 – 80 °C). The plateaux exist with a high slope and wide hysteresis for the PCIs of $CaNi_{4.8}Cr_{0.2}$ and $CaNi_{4.8}Al_{0.2}$ alloys. The desorption plateau slopes at 25 °C for $CaNi_{4.8}Cr_{0.2}$ and $CaNi_{4.8}Al_{0.2}$ are 3.8 and 5.5, respectively, compared to 0.22 for $CaNi_5$. The hydrogen storage capacity for the entire sample of these alloys is reduced because of the low abundance of the $CaNi_5$ phase in these substituted

samples. In contrast to other alloys, a plateau does not exist for the $CaNi_{4.8}Mo_{0.2}$ composition due to the presence of Ca_2Ni_7 as the main phase. Ca_2Ni_7 forms a very stable hydride and full desorption can only be undertaken at a very low pressure. A similar result is found by Si et al. [193] where a $(Ca,Mg)_2Ni_7$ alloy was found to have no plateau for hydrogen pressures above 0.1 bar at 45 ºC.

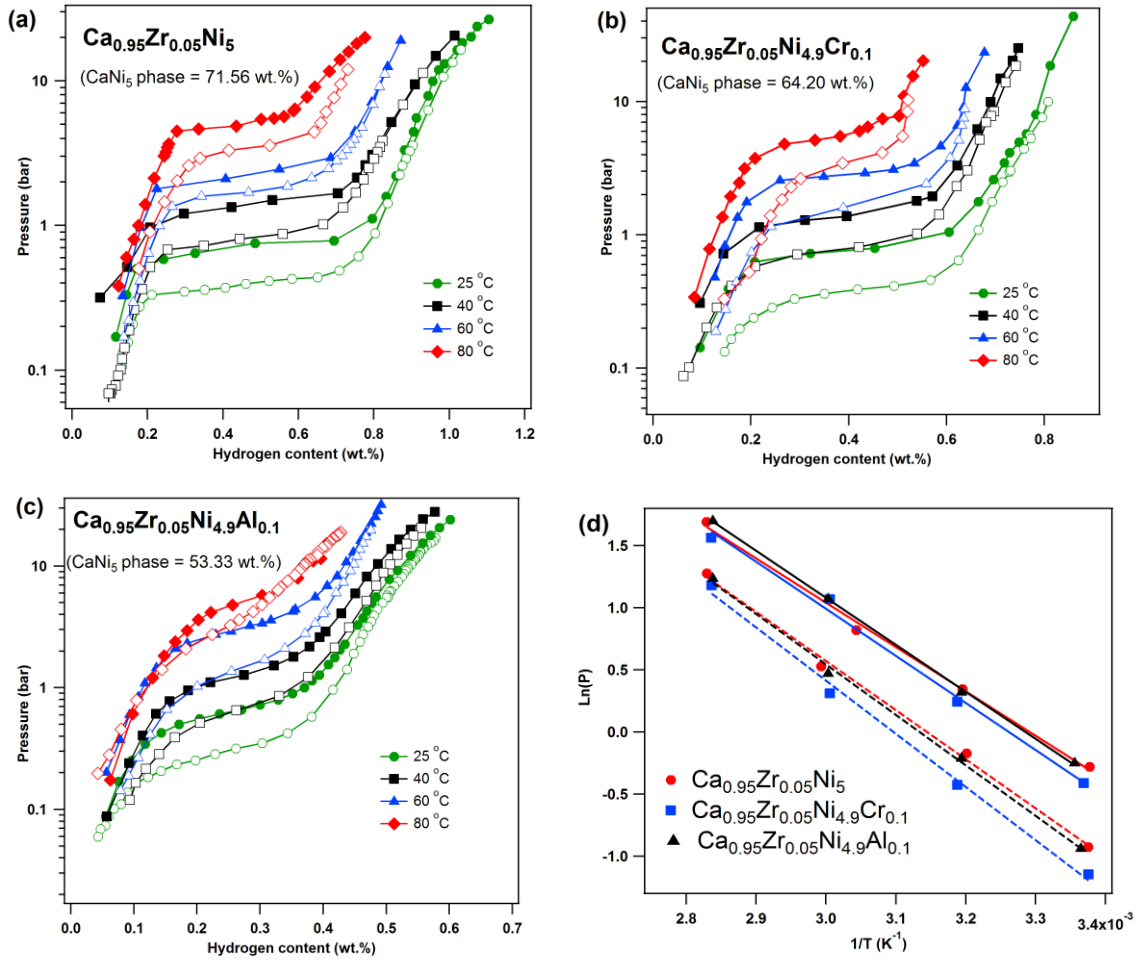

Figure 4-15: PCI's at 25 ºC of (a) $Ca_{0.95}Zr_{0.05}Ni_5$, (b-c) $Ca_{0.95}Zr_{0.05}Ni_{4.9}$(Cr or Al)$_{0.1}$ alloys and (d) van't Hoff plots of hydrogen absorption (dash lines) and desorption (solid lines) of the alloys.

The plateau pressures of $Ca_{0.95}Zr_{0.05}Ni_5$ and $Ca_{0.95}Zr_{0.05}Ni_{4.9}$(Cr or Al)$_{0.1}$ shown in Figure 4-15 (a – c), are clearly higher than those of pure $CaNi_5$ and $CaNi_{4.9}$(Cr or Al)$_{0.1}$ ternary alloys. Absorption and desorption plateau pressures of these quaternary alloys, at 25 ºC, are observed at ~ 0.75 and 0.40 bar, respectively. Thus, partial replacement of Zr at the Ca site is effective in increasing the plateau pressure. This can be a function of the atomic radius (R_{at}) of Zr, which is significantly smaller than that of Ca and will directly influence the unit cell volume of the substituted alloys.

As such, the plateau pressure tends to be higher for alloys with a smaller unit cell. In contrast to the results of pure $CaNi_5$ PCIs, sloping plateaux are observed for all of these alloys. Thus, replacement of Zr at the Ca site does not exhibit a flat plateau as is found for pure $CaNi_5$ likely due to the greater strength of the Zr-Ni metallic bond [177] compared to Ca-Ni and Ni-Ni. This is because the stronger Zr-Ni bond leads to difficulties in expanding the crystal lattice during hydrogen absorption.

The maximum hydrogen storage capacity of $Ca_{0.95}Zr_{0.05}Ni_{4.9}Al_{0.1}$, at 25 ºC, is much lower than for the other two compositions because of the lower abundance of the $CaNi_5$ phase (~50 wt.%) in this sample. It should be noted that a low abundance of $ZrNi_5$ has also been indexed in these alloys. Minor hydrogen absorption into $ZrNi_5$, H/M < 0.2, was reported under approximately 100 bar of hydrogen pressure at 25 ºC [187]. Therefore, it can be assumed that the $ZrNi_5$ phases do not influence the hydrogen absorption/desorption process for this low pressure study.

Table 4-11: Hydrogen sorption and thermodynamic data for $Ca_{0.95}Zr_{0.05}Ni_5$ and $Ca_{0.95}Zr_{0.05}Ni_{4.9}$(Cr or Al)$_{0.1}$ alloys.

Alloy	Plateau pressure[a] (bar)	Absorption capacity[b] (wt.%)	ΔH (kJ/mol H_2)	
			$\Delta H_{abs.}$	$\Delta H_{des.}$
$Ca_{0.95}Zr_{0.05}Ni_5$	0.40	1.10	-29.7 ± 1.2	32.9 ± 1.3
$Ca_{0.95}Zr_{0.05}Ni_{4.9}Cr_{0.1}$	0.39	0.84	-31.5 ± 0.5	33.8 ± 1.1
$Ca_{0.95}Zr_{0.05}Ni_{4.9}Al_{0.1}$	0.32	0.61	-31.6 ± 1.7	35.6 ± 1.7

[a] Measure from desorption PCIs at 25 ºC.
[b] Maximum absorption capacity calculated from the weight of the entire sample measured at 25 ºC and 30 bar of hydrogen pressure.

As shown in Table 4-11, the magnitude of the enthalpy ($|\Delta H|$), calculated from the least-squares linear fit of van't Hoff plots (Figure 4-15 (d)), of the substituted alloy $Ca_{0.95}Zr_{0.05}Ni_5$ is smaller than that of unsubstituted $CaNi_5$. In fact, the unit cell volume of $Ca_{0.95}Zr_{0.05}Ni_5$ is smaller than pure $CaNi_5$. Thus, the smaller unit cell volume causes a less stable hydride in the alloy. As can be seen, the desorption ΔH of the $Ca_{0.95}Zr_{0.05}Ni_{4.9}Al_{0.1}$ alloy is clearly greater than those for $Ca_{0.95}Zr_{0.05}Ni_5$ and $Ca_{0.95}Zr_{0.05}Ni_{4.9}Cr_{0.1}$. Accordingly, addition of Al results in a high stability hydride

with a lower desorption plateau pressure. Similarly, this effect has also been observed previously for the ternary alloy $CaNi_{4.9}Al_{0.1}$ as discussed above.

4.6.2 Hydrogen Sorption Kinetics

Figure 4-16 shows the hydrogen absorption and desorption kinetics of selected alloys, performed at 25 and 60 ºC with the final equilibrium pressures (P_{eq}) of 10 ± 1 and 0.15 ± 0.04 bar for absorption and desorption, respectively. The hydrogen content is calculated with respect to the entire weight of the alloys. As a result, the full absorption capacity of the alloys is variable depending on the abundance of the hydrogen active phase. The sorption kinetics of the alloys is a temperature dependent property, i.e. the higher temperatures result in the faster kinetics.

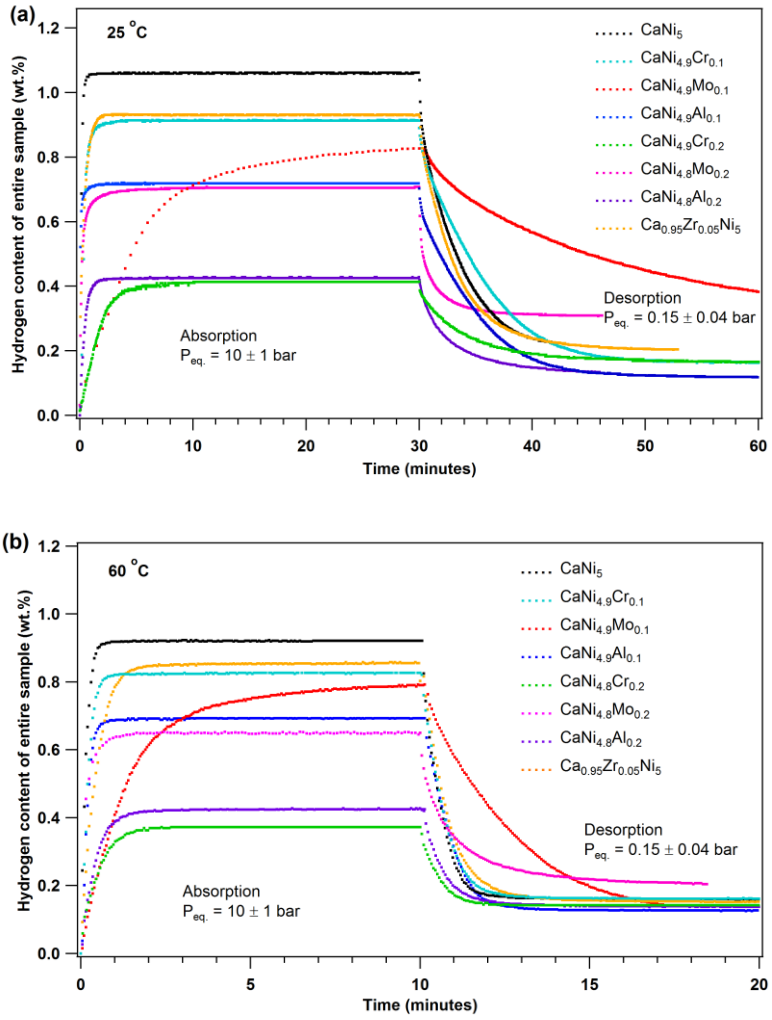

Figure 4-16: Absorption and desorption kinetics of selected alloys measured at (a) 25 ºC and (b) 60 ºC.

Full hydrogen absorption and desorption capacity at 25 ºC can be reached within 5 to 15 minutes for all compositions except $CaNi_{4.9}Mo_{0.1}$. As can be seen, the kinetics upon Mo addition in $CaNi_{4.9}Mo_{0.1}$ may take longer than 20 to 30 minutes for a complete absorption and desorption at 25 ºC. The kinetics at 60 ºC of this composition is still relatively slow. It should also be noted that the reaction between alloys and hydrogen can be enhanced by the presence of Ni clusters on the surface acting as a catalyst [194, 195]. Yeh et al. [170] indicated that Mo additives delay the formation of the hydrogen-rich β-phase of AB_5-type hydrides. As a result, the dissolution of Mo into this Ni phase (as confirmed by XRD and SEM results) could affect the catalytic property of the Ni clusters, which in turn could slow the sorption kinetics of $CaNi_5$-based alloys. In contrast to $CaNi_{4.9}Mo_{0.1}$, $CaNi_{4.8}Mo_{0.2}$ exhibits relatively fast kinetics. As discussed in section 4.4, the major phase of this alloy, ~ 63 wt.%, is Ca_2Ni_7. Thus, this kinetic data could be dominated by the kinetics of Ca_2Ni_7 instead of the $CaNi_5$ phase [184].

The presence of residual hydrogen absorbed in the alloys after desorption (approximately 0.2 – 0.3 wt.%) is due to the low pressure plateau region of $CaNi_5$ that appears at a hydrogen pressure of ~ 0.02 bar at 25 ºC [9, 85]. Thus, this amount of hydrogen cannot be released under this experimental condition with the hydrogen equilibrium pressure of 0.15 bar which is higher than this plateau pressure, i.e. 0.02 bar. The Mo substituted alloy, $CaNi_{4.8}Mo_{0.2,}$ has the poor reversibility even when performed at 60 ºC with higher residual hydrogen than the other alloys after desorption. As mentioned above, this alloy contains Ca_2Ni_7 as the major phase; therefore, the presence of this phase determines the hydrogen sorption properties of the sample. It was also reported that the hydride phase of Ca_2Ni_7 phase in $(Ca, Mg)_2Ni_7$ alloy has high stability and only desorbs 50% of its absorption capacity at 45 ºC under a hydrogen pressure of less than 0.1 bar [193].

4.6.3 Cyclic Stability

Cyclic stability of the alloys was evaluated as a series of absorption and desorption processes. This property was performed by a PCTPro-E&E (Hy-Energy) with the rate of 3 cycles h^{-1} at 85 ºC, which is the practical operating temperature of PEM fuel cells. It should be noted that in practice the waste heat of the PEM fuel cell operating at 85 ºC cannot be used to desorb the hydrogen from the alloys at this temperature.

The 85° C cycling temperature was chosen simply due to the fact that 85° C is the practical operating temperature of a PEM fuel cell. Each cycle of cyclic stability measurement included absorption (5 minutes), desorption (5 minutes) and evacuation and pressure preparation (10 minutes). Absorption was undertaken by applying 40 ± 2 bar of hydrogen pressure to a reservoir volume, which was then released into an evacuated sample volume. A stable final absorption pressure (~ 20 bar) was reached within ~ 5 minutes as shown in Figure 4-17, demonstrating that equilibrium was reached in each step.

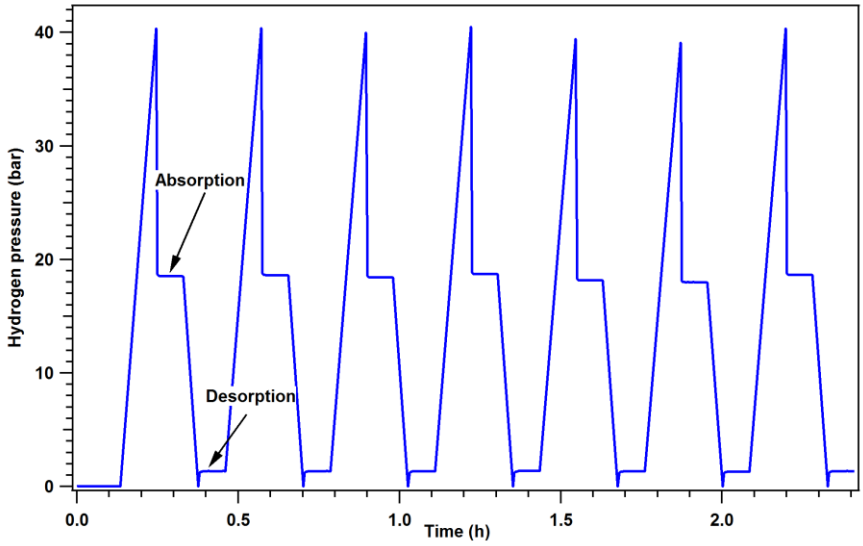

Figure 4-17: Sorption kinetics during cyclic stability measurement.

Figure 4-18 shows the absorption capacity of the alloys at the n^{th} cycle, C_n, compared to that of the first cycle, C_1. As can be seen, $CaNi_5$ maintains an absorption capacity of ~ 75% of initial capacity after 200 absorption-desorption cycles at 85 ºC. In significant contrast, less than 40% of initial capacity was left after the same number of cycles at 85 ºC for a $CaNi_5$ alloy prepared by air induction melting [8]. Further measurement of this alloy shows that the capacity decreases to approximately 65% of initial capacity after 350 cycles [163].

The absorption capacity of all substituted alloys decreases rapidly for the first 40 cycles, except for $CaNi_{4.9}Al_{0.1}$. Thus, $CaNi_{4.9}Al_{0.1}$ is shown to improve the stability of the $CaNi_5$ phase, where the initial capacity has been retained for 20 cycles as shown in Figure 4-18. Han and Lee [196] indicate that substitution of Al into $MmNi_5$- and $LaNi_5$-based alloys can improve the alloy stability due to the formation of Al_2O_3 at

the surface, which prevents further adsorption of oxygen and protects the hydrogen active phases. Another possibility is that the aluminium atom is significantly larger than nickel and could interfere with the chemical bond of Ca and its neighbour atoms. In addition, Al and Ni may form a very stable Ni_3Al cluster [8] leading to a more stable Ni sublattice in $CaNi_5$ causing retardation in Ni displacement. However, this experiment was stopped after 40 cycles due to the insufficient hydrogen pressure in the supply cylinder during the measurement. Thus, extended cycling needs to be investigated for this alloy. In contrast, the capacity of a higher Al-content alloy, i.e. $CaNi_{4.8}Al_{0.2}$ composition, decays with a faster rate, which is probably due to the inhomogeneity of the alloy [175].

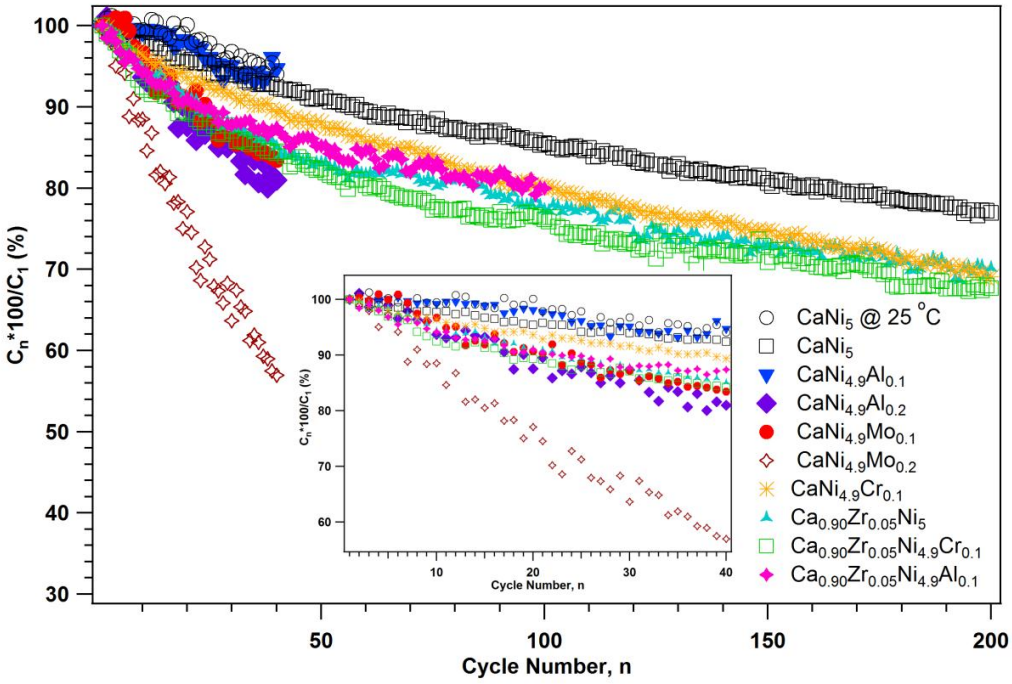

Figure 4-18: Hydrogen cycling behaviour of synthesised alloys performing at 85 °C; insertion shows the plot expansion up to 40 cycles.

$Ca_{0.95}Zr_{0.05}Ni_5$ and $Ca_{0.95}Zr_{0.05}Ni_{4.9}(Cr \text{ or } Al)_{0.1}$ rapidly lose their capacity over the first 50 cycles; however, the decay rate of capacity slows down comparing to $CaNi_{4.9}Cr_{0.1}$ for further cycles. This slow decay rate for Zr substituted alloys may result from the high strength of the Zr-Ni bond [177] that can retain the structure AB_5 units. The cyclic stability of the alloys has also been related to the unit cell volume [197], where a smaller unit cell volume leads to proportionally larger expansions and contractions during the hydrogen sorption process, and consequently the alloy

decrepitates at a higher rate. This effect is most likely the predominant influence on the alloy stability during the first few cycles. As can be seen from Figure 4-18, the substituted alloys with a larger unit cell volume, i.e. $CaNi_{4.9}Al_{0.1}$ and $CaNi_{4.9}Mo_{0.1}$ maintain a higher absorption capacity compared to that of the pure $CaNi_5$ alloy during the sorption measurements up to 10 cycles. The disproportion rate of $CaNi_{0.9}Mo_{0.1}$ increases after 10 cycles, which is probably caused by the inhomogeneity of the alloy. In contrast to the other compositions, the capacity of $CaNi_{4.8}Mo_{0.2}$ decays very quickly, with approximately 55% of its initial capacity left after 40 cycles, whilst the other compositions maintain more than 80% of their initial capacity. In fact, the main phase of this composition is Ca_2Ni_7 as discussed previously; therefore, the disproportion rate of the Ca_2Ni_7 phase appears much faster than that of the $CaNi_5$ phase under these experimental conditions.

A recent neutron diffraction study of deuterated $CaNi_5$ aged at 85 ºC suggests that the loss of capacity is actually associated with the leaching of Ni from specific crystallographic sites, resulting in Ni deficient $CaNi_5$ [198]. In life cycle measurements of metal hydrides, the applied H_2 pressure is normally significantly above the equilibrium pressure. Goodell et al. [8] point out that this overpressure of H_2 may lead to significant localized heating during the exothermic absorption process. In the cycling measurements herein, the applied H_2 pressure during absorption is ~20 bar while the equilibrium pressure for the samples is between 5 and 6 bar at 85 ºC. It is possible that samples could reach a temperature as high as 120 ºC during absorption (because their equilibrium pressure is ~ 20 bar at this temperature). This temperature increase could further promote segregation within $CaNi_5$ samples and contribute to their rapid capacity loss. During cycling the thermocouple did not measure a temperature increase during absorption. However, the large thermal mass and thermal conductivity of the stainless steel sample cell combined with the ~ 5 mm separation between the sample and the thermocouple does not exclude a temperature rise within the hydride bed. Life cycle measurements employing applied hydrogen pressures closer to the H_2 equilibrium pressure may yield slower degradation in the capacity.

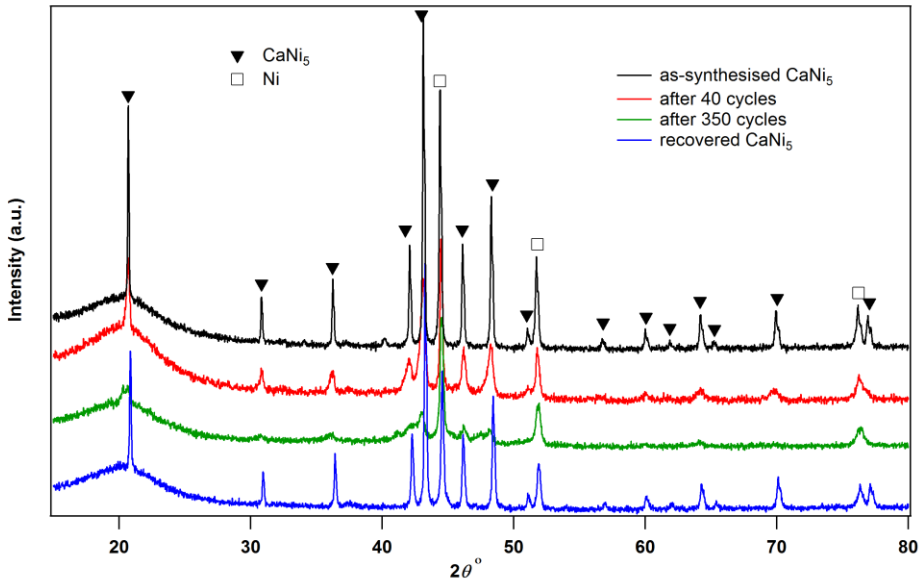

Figure 4-19: XRD spectra of $CaNi_5$ after cycling for 40 and 350 cycles, and the recovered alloy by further heat treatment at 800 ºC under vacuum for 3 h.

Figure 4-19 shows the XRD pattern of $CaNi_5$ after 40 and 350 absorption-desorption cycles. After cycling, the $CaNi_5$ peaks are broadened, indicating a reduction of crystallite size and disordering of the $CaNi_5$ crystal lattice, whilst the shape and position of Ni peaks have not changed significantly. The crystallite size of the cycled alloy, determined by Rietveld refinement, is significantly reduced from 190 nm in the as-synthesised $CaNi_5$ to 9.0 nm after 350 cycles. These results also confirm that the excess Ni does not react with hydrogen during sorption process. The XRD analysis does not detect CaH_2 as expected in other studies [9] for the following interaction of $CaNi_5$ with hydrogen:

$$CaNi_5 + H_2 \rightarrow CaH_2 + 5Ni \qquad (4.1)$$

Possible reasons for the lack of CaH_2 diffraction peaks could be their very fine crystallite size and the small quantity of this phase. Goodell [8] suggested that heat treatment at 500 ºC or higher, for longer than 4 h is required to recover the disproportionate alloys, which can approximately restore the initial hydrogen storage capacity.

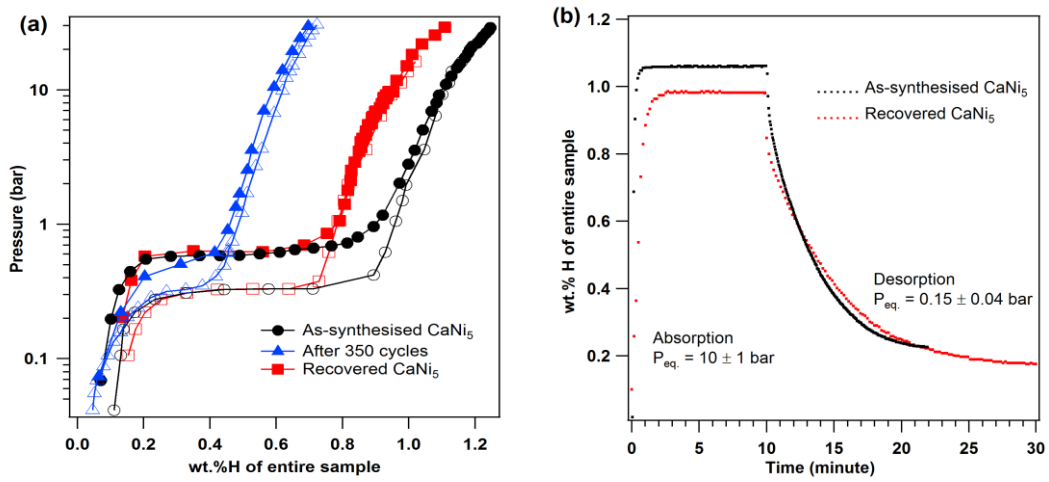

Figure 4-20: Hydrogen sorption properties; (a) PCIs and (b) Kinetics at 25 ºC of recovered $CaNi_5$ compared to an as-synthesised alloy.

After cycling for 350 cycles, the plateaux region of the alloy is significantly narrowed with a slightly lower absorption plateau pressure as shown in Figure 4-20 (a). Decrease of storage capacity is a result of the degradation of the $CaNi_5$ phase. The $CaNi_5$ phase that has been recovered by heat treatment at 800 ºC under vacuum for 3 h is also shown in Figure 4-19. The abundance of recovered $CaNi_5$ calculated by Rietveld refinement is approximately 67.23 wt.%, which is comparable to that for the as-synthesised alloy, 68.10 wt.%. The unit cell volume of recovered $CaNi_5$ is 83.708 $Å^3$, which is comparable to 83.700 $Å^3$ for the as-synthesised alloy. A fairly-flat absorption plateau of the recovered alloy is formed at 0.63 bar as shown in Figure 4-20 (a), which is slightly higher than that for the fresh alloy (0.59 bar). Goodell [8] mentioned that the increase of plateau pressure appears to be temporary, thus, the original plateau would be restored after a few additional cycles. However, their desorption plateaux are comparable at ~0.33 bar. The absorption capacity of the recovered alloy is approximately 10% lower than for fresh $CaNi_5$, demonstrating that there is still some irreversible degradation. Figure 4-20 (b) shows comparable hydrogen sorption kinetics at 25 ºC for the recovered and as-synthesised alloys.

4.7 CONCLUSIONS

Synthesis of $CaNi_5$-based alloys has been achieved by mechanical alloying followed by thermal treatment at 800 ºC under vacuum for 3 h. $CaNi_5$ yields a range of approximately 60 – 70 wt.% for binary alloy ($CaNi_5$) and ternary alloys ($Ca_{0.95}Zr_{0.05}Ni_5$ and $CaNi_{4.9}$(Cr, Al or Mo)$_{0.1}$. The abundance of the $CaNi_5$ phase decreases for the substituted alloys with higher contents of additive metals. The remaining secondary phase is predominantly Ni for all samples, probably existing as a Ni-rich solid solution with additives. Other secondary phases, $ZrNi_5$ and Ca_2Ni_7, are formed in Zr and Mo substituted alloys, respectively. It is interesting that the major phase of the $CaNi_{4.8}Mo_{0.2}$ composition is Ca_2Ni_7 (~63 wt.%) instead of $CaNi_5$. Thus, it is suggested that milling and annealing conditions need to be optimized for each composition to decrease segregation and secondary phase formation.

Incorporation of larger atomic size metals such as Al and Mo at the Ni site significantly increases the unit cell volume of $CaNi_5$ phase, whilst replacement of Zr at the Ca site leads to a decrease in the unit cell volume. At a low content of additive metal, the unit cell volumes of the $CaNi_5$ phase are determined to be: $CaNi_{4.9}Al_{0.1}$ > $CaNi_{4.9}Mo_{0.1}$ > $Ca_{0.95}Zr_{0.05}Ni_{4.9}Al_{0.1}$ > $CaNi_{4.9}Cr_{0.1}$ > $Ca_{0.95}Zr_{0.05}Ni_5$ > $Ca_{0.95}Zr_{0.05}Ni_{4.9}Cr_{0.1}$.

The hydrogen storage capacity of all substituted alloys is decreased and the plateau regions are narrowed compared to that of pure $CaNi_5$. Relatively flat plateau regions are retained for all compositions except $CaNi_{4.8}Mo_{0.2}$, which is dominated by the secondary phase, Ca_2Ni_7. Lower desorption plateau pressures exist for larger unit cell volumes of the $CaNi_5$ phase, i.e. Al and Mo substituted alloys, indicating high stability hydrides are formed in these alloys. On the other hand, higher plateau pressures and larger hysteresis were observed for the substitution of Ca with Zr, corresponding to the decrease of the unit cell volume of its $CaNi_5$ phase.

All substituted alloys, except $CaNi_{4.9}Mo_{0.1}$, show relatively fast and comparable kinetics to that of unsubstituted $CaNi_5$. Full absorption and desorption at 60 ºC with an equilibrium pressure ~10 bar can be achieved within 3 minutes. After 40 absorption-desorption cycles, most of the synthesised alloys retain approximately 80 – 95% of their initial hydrogen storage capacity. In contrast to the other compositions, the capacity of $CaNi_{4.8}Mo_{0.2}$ decays significantly fast to approximately

55% of its initial capacity by 40 cycles. Thus, this study confirms the unfavourable properties of Ca_2Ni_7 including the formation of a very stable hydride and a severe disproportionation rate. The hydrogen absorption capacity of substituted alloys with Zr at the Ca site rapidly decreases for the first 50 cycles and then the rate of capacity loss slows beyond 100 cycles. On the other hand, $CaNi_{4.9}Cr_{0.1}$ does not show a significant decrease in the rate of capacity loss beyond 100 cycles. $CaNi_{4.9}Al_{0.1}$ also shows improvement in the cyclic stability by retaining its initial capacity by 20 cycles before starts to lose its capacity gradually. It is likely that the addition of Al and Zr offer the possibility to improve cyclic stability of the $CaNi_5$-based alloy. After cycling, the $CaNi_5$ phase can be recovered by heat treatment with a comparable capacity and similar properties to that of the as-synthesised alloy.

In conclusion, $CaNi_5$-based alloy shows partially favorite hydrogen storage properties, e.g. fast kinetics and fairly flat plateau at low temperature. The cyclic stability measured at 85 ºC reveals the possibility to apply the alloy as low temperature hydride. The research shows that the $CaNi_5$ can maintain ~80% of initial capacity after 200 cycles. If the alloy operated at a lower temperature, its hydrogen storage capacity might decay slower. Therefore, the alloy is possibly operated at ~60 ºC to supply hydrogen, ~1 bar, to PEM fuel cell. Substitution method, at Ca and/or Ni sites, can alter the hydrogen sorption properties of the alloy. Particularly, Zr and Al additives show the possibility of cyclic stability enhancement. Mechanical alloying (ball milling) under this research conditions is not optimized where significant amount of Ni-rich phases have been formed. It is suggested that the synthesis conditions such as ball-milling and annealing conditions have to be improved to increase amount of $CaNi_5$ phase. At present, the ball-milling method may not meet the large-scale production but this technique offers opportunities to study and to alter the hydrogen storage properties of the intermetallic hydrides.

CHAPTER 5

HYDROGEN STORAGE PROPERTIES OF NANOCONFINED $NaAlH_4$

5.1 BACKGROUND

Complex metal hydrides have been studied since the mid-nineties as potential solid state hydrogen storage materials due to their very high hydrogen content [199-201]. Stable salt-like solids are formed between the least electropositive metals, such as Li and Na etc., and a negatively charged coordination complex. The complexes contain hydrogen covalently bonded to a more electronegative metal, e.g. $[AlH_4]^-$ or $[BH_4]^-$ as shown in Figure 5-1 for the crystal structure of $NaAlH_4$ and $LiBH_4$. Therefore, the anions ($[AlH_4]^-$ and $[BH_4]^-$) form the tetrahedral structure.

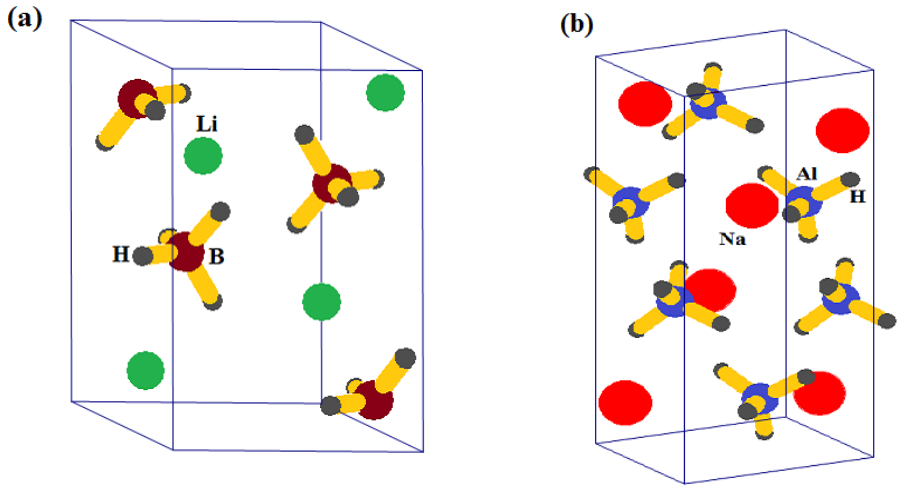

Figure 5-1: Crystal structure of (a) $LiBH_4$ and (b) $NaAlH_4$.

Generally, complex metal hydrides release hydrogen by thermolysis at temperatures higher than their melting points (m.p.) [10], see Figure 5-2. Of particular interest is $NaAlH_4$, which has a high gravimetric hydrogen capacity 7.4 wt.% H, and is known to decompose (without the addition of a catalyst) via a 3-step mechanism [202] as shown below

$$3NaAlH_4 \xleftrightarrow{>180\ ^\circ C} Na_3AlH_6 + 2Al + 3H_2 \quad ; 3.70\ \text{wt.\% H} \qquad (5.1)$$

$$Na_3AlH_6 \overset{>240\,^{\circ}C}{\longleftrightarrow} 3NaH + Al + 3/2H_2 \quad ; 1.85\ wt.\%\ H \qquad (5.2)$$

$$NaH \overset{>425\,^{\circ}C}{\longleftrightarrow} Na + 1/2H_2 \quad ; 1.85\ wt.\%\ H \qquad (5.3)$$

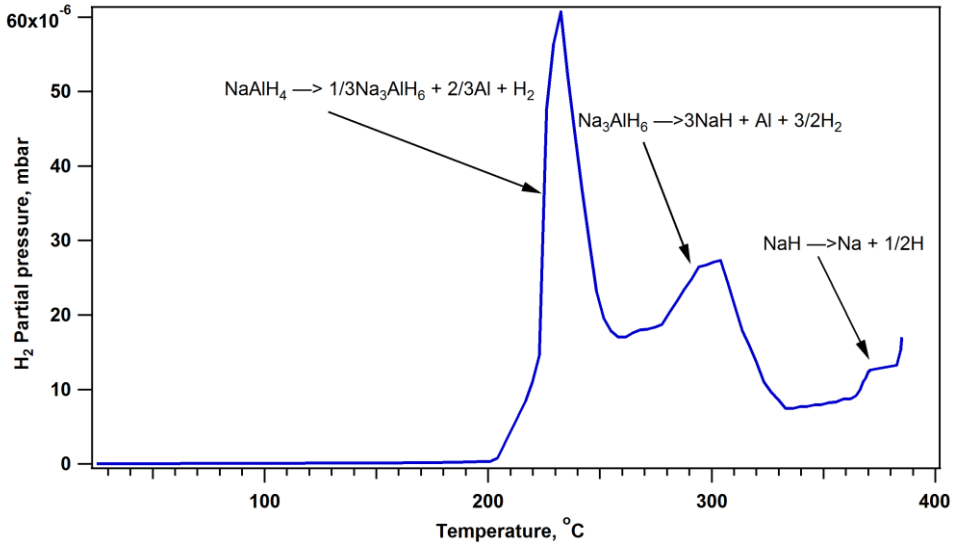

Figure 5-2: TPD-MS data of as-received $NaAlH_4$ using a heating rate of 2 ºC /min.

According to its decomposition temperature range, only the first and the second step are suitable for a moderate temperature application with a total reversible hydrogen storage capacity of ~5.6 wt.%, while approximately 5 wt.% can be achieved in practical application [14, 203]. Hydrogen desorption from pure $NaAlH_4$ at 200 ºC (above its m.p. of 181 ºC [12]) is only completed after ~20 h due to severe kinetic limitations [11]. However, the $NaAlH_4$ system has been investigated thoroughly over the last two decades and an extensive array of catalytic phases can enhance hydrogen release and uptake at lower temperature (120 – 140 ºC) [204]. Many transition metal catalysts are added to the $NaAlH_4$ system as halide salts, that are reduced to metal-Al surface-alloys that are catalytically active, with the generation of an inactive sodium halide salt by-product [205]. Although the list of catalytic phases for $NaAlH_4$ is extensive, recent focus on $CeCl_3$ [206] or Ti-based nanoparticles [207] show great promise, even when compared to the well-studied $TiCl_3$ doped $NaAlH_4$ system [204].

An alternative method to enhance the de- and rehydrogenation stability and kinetics of $NaAlH_4$ is by the reduction of particle size, e.g. mechanochemically [208-210]. Nanocrystalline Na_3AlH_6 and Na_2LiAlH_6 synthesised by high-energy milling show great improvement in performance compared to the bulk materials [142]. The

deposition of $NaAlH_4$ on to the surface of nanocrystalline titanium dioxide loaded carbon spheres (Ti-CSs) also shows improvement in hydrogen storage properties of the hydride on multiple absorption and desorption cycles [211]. Nanoconfinement is an emerging technique to provide improved kinetic and thermodynamic properties for hydrogen storage materials [212-215]. Evidence of the kinetic benefits of metal hydride particle size reduction are widespread [216] and a similar kinetic improvement exists when a metal hydride is nanoconfined [143], restricting its particle size to the pore size of the scaffold. There is also experimental proof for thermodynamic changes in metal hydrides with reductions in particle size, for example, small changes in enthalpy and entropy were observed for 7 nm MgH_2 particles [217]. Changes in the thermodynamic behaviour of MgH_2 confined within carbon aerogel have also been reported [218]. There were difficulties in interpreting some data in this previous study [218] due to the size distribution of the scaffold pores and hence the nanoconfined metal hydride. However, the problem with pore and particle polydispersity can be overcome through the implementation of ordered porous scaffolds with uniform pore networks (such as CMK-1).

A systematic study of the changes in properties of $NaAlH_4$ melt-infiltrated in carbon aerogels with different pore sizes has been conducted [219]. The temperature for the maximum hydrogen release rate, measured by TPD-MS, decreased from 252 ºC for bulk to 162 ºC for $NaAlH_4$ melt infiltrated in a macroporous aerogel (> 100 nm). This improvement is mainly assigned to the catalytic properties of the carbon aerogel surface, possibly with a small contribution from confinement in mesopores. An additional, but smaller, reducing the pore sizes in the range $7 \leq D_{max} \leq 39$ nm shows the kinetic improvement by lowering the temperature for maximum hydrogen release rate (T_{max}) measured by TPD-MS compared to bulk $NaAlH_4$, i.e. $\Delta T_{max} = -12$ to -16 ºC. The crystalline domain sizes of melt-infiltrated $NaAlH_4$ (determined from powder X-ray diffraction (PXD) data using the Scherrer formula) is larger than the pore sizes determined by nitrogen adsorption, possibly due to a thermodynamic preference for filling the larger pores of the aerogel [219, 220].

The melt infiltration of $NaAlH_4$ into carbon aerogels (17 nm pores) functionalized with a $TiCl_3$ catalyst improves the hydrogen desorption rate compared to $NaAlH_4$ ball-milled with the catalyst [221]. However, infiltration of molten $NaAlH_4$ in carbon aerogel scaffolds with smaller pore sizes (4 nm) shows that there is a lower pore size

limitation using this technique with carbon aerogels as pores remain unfilled [219]. In contrast to this study, $NaAlH_4$ has been reported to be infiltrated in 2 – 3 nm pores of high surface area porous graphite with desorption starting at 100 – 120 ºC, decomposing in a single step [202]. There can be a hydrogen capacity loss upon cycling hydrogen storage materials in a scaffold. In the case of $NaAlH_4$, Gao et al. [13] pointed out that the capacity loss was mainly caused by the loss of active Na(H) species. Therefore, it is assumed that Na(H) reacts with impurities such as oxygen containing groups or is dispersed on the surface of the carbon scaffold. In addition, they also reported that Al migrated out of the pores and formed large Al crystallites (> 100 nm) on the outer surface of the carbon scaffold after hydrogen desorption.

5.2 SYNTHESIS

5.2.1 Ordered Mesoporous Silica (MCM-48)

Porous materials can be classified depending on their predominant pore size, i.e. microporous (pore diameters less than 2 nm), mesoporous (pore diameters range of 2 – 50 nm), and macroporous (pore diameters exceeding 50 nm) [222]. Figure 5-3 shows a small angle X-ray scattering (SAXS) pattern of the synthesised ordered mesoporous silica MCM-48. The SAXS pattern contains Bragg peaks that can be indexed as (211), (220), (321), (400), (420), (611), and (543) corresponding to the reflections of the cubic *Ia3d* space group [223]. The large number of observed Bragg peaks in the SAXS pattern indicates a high pore order and long-range periodicity in this structure. The SAXS pattern of MCM-48 shows no peaks at high *q*, thus, the template is atomically disordered. The main peak presents at q = 0.178 $Å^{-1}$ corresponds to a repeating *d*-spacing of 3.53 nm. The structural information of calcined MCM-48 has been reported previously with an average pore size of 2.4 nm [93] and a silica wall thickness of 1.3 nm [224].

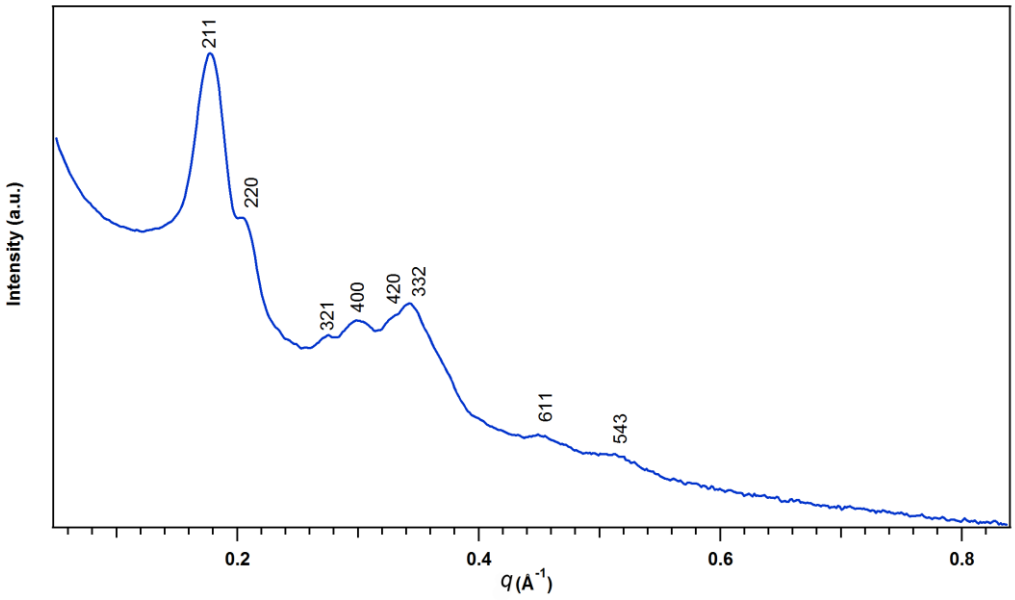

Figure 5-3: Small angle X-ray scattering (SAXS) of ordered mesoporous silica MCM-48.

5.2.2 Ordered Mesoporous Carbon (CMK-1)

An ordered mesoporous carbon (CMK-1) was synthesised by the carbon replication of a MCM-48 template as described in Chapter 2. The CMK-1 structure is confirmed by SAXS as shown in Figure 5-3. The insert in Figure 5-4 shows an SE-SEM image of synthesised CMK-1 powder with a typical particle size of ~10 μm.

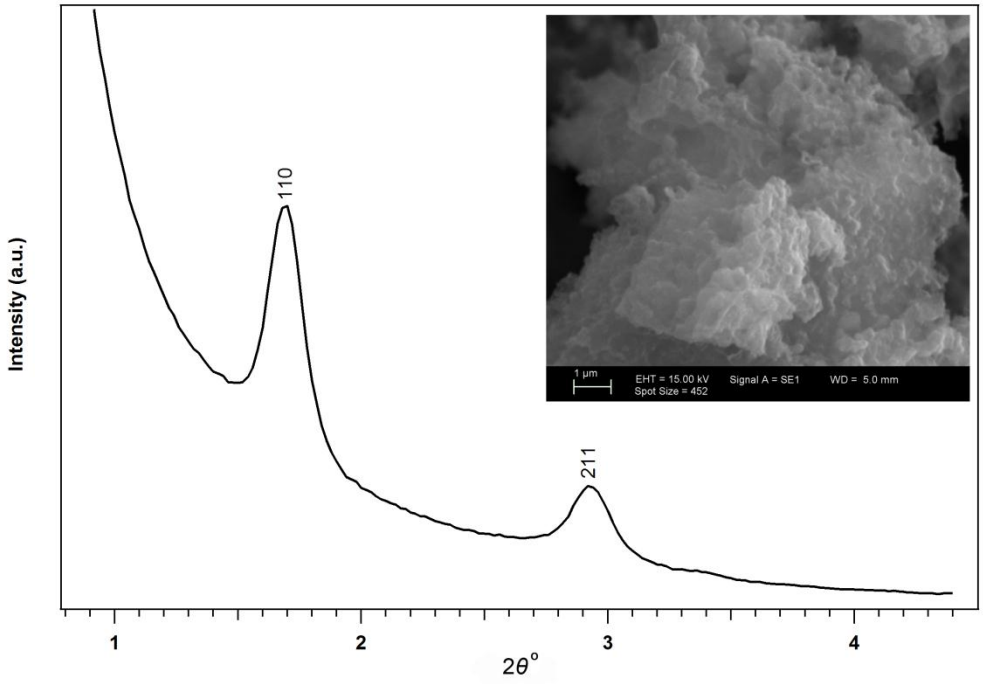

Figure 5-4: Small angle X-ray scattering (SAXS) pattern of synthesised CMK-1 with an SEM image insert.

The SAXS pattern for CMK-1 depicts low-angle diffraction peaks that originate from the relatively large ordering distance in the carbon framework. Peaks present at 1.7° and 2.9° 2θ correspond to repeating *d*-spacings of 5.2 and 3.0 nm, respectively. These peaks have been previously indexed to an I-1 (P-1 type) space group as (110) and (211) respectively [91]. The primary pore size of CMK-1 has also been reported as approximately 2 – 3 nm [91] but these are accompanied by a certain quantity of micropores ranging between 0.4 and 0.8 nm [94, 225]. These micropores are formed prior to the removal of the silica template, during carbonization of the sucrose, whilst the mesopores are formed upon the removal of the silica template [224]. The primary pore diameter should have been equal to the wall thickness of MCM-48 (~1.3 nm) if the carbon synthesis had followed a geometrical replication process. However, the average pore size of CMK-1 is approximately double that of the MCM-48 wall

thickness [91]. This can possibly be explained by the compaction of the reciprocated carbon after the high-temperature carbonisation process. The XRD pattern shows a broad peak at approximately 42º 2θ attributed to amorphous carbon as shown in Figure 5-5. In fact, another broad peak of amorphous carbon should be observed at ~25º 2θ [226] but this peak is difficult to resolve due to its overlap with the large hump from the PMMA XRD sample holder at ~21º 2θ.

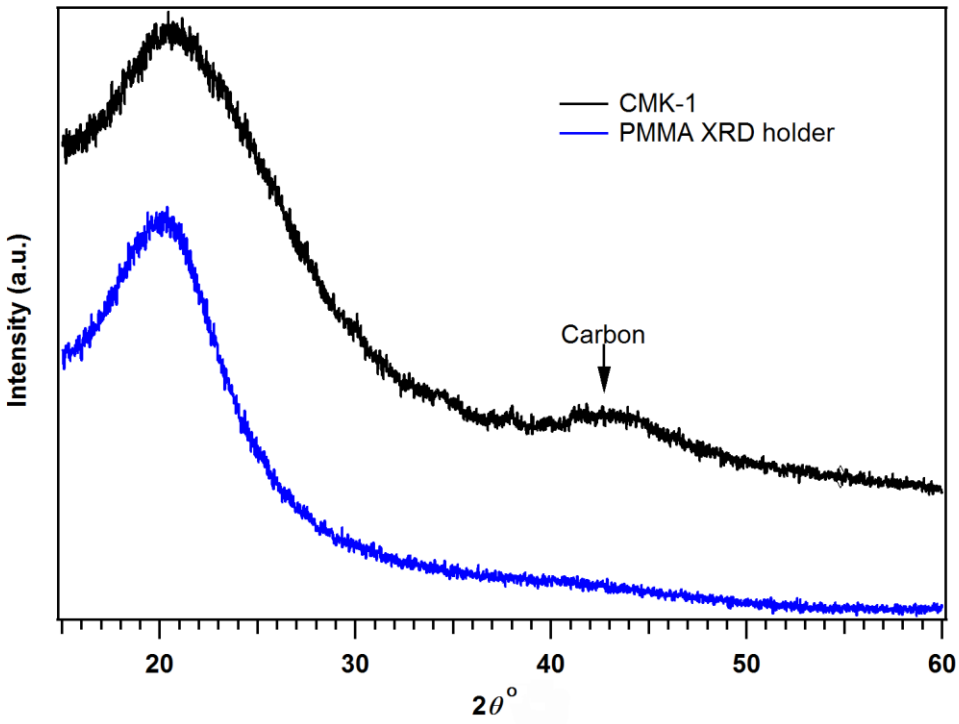

Figure 5-5: Powder X-ray diffraction (XRD) pattern of CMK-1.

5.2.3 Infiltration of $NaAlH_4$ into CMK-1 Scaffold

5.2.3.1 Solvent Infiltration

Figure 5-6 (a) shows the SAXS patterns of $NaAlH_4$ infiltrated CMK-1 scaffold with/without Ti dopant. The scattering length density difference (or contrast) is directly correlated to the resulting scattered intensity. The decrease in peak intensity of loaded CMK-1 is due to the fact that the infiltrated particles in the pores lead to a change in the electron density within the pores, and thus a reduction in the scattering length density difference (or contrast) between ordered features. In other words, the attenuation in SAXS intensity is a result of the scattering particles in the pores causing the phase cancellation between scattering from the scaffold and the pore

regions [227]. It is also of note that the primary diffraction peak (110) at 1.7° 2θ is greatly attenuated by $NaAlH_4$ infiltration, but the (211) peak at 2.9° 2θ peak is not attenuated as much. This may indicate that the $NaAlH_4$ is selectively infiltrating certain pores, which are more than likely the larger mesopores in the CMK-1 framework [228].

XRD patterns of infiltrated samples compared to that of pure CMK-1 are displayed in Figure 5-6 (b). Diffraction peaks are not obviously observable in the XRD patterns for the $NaAlH_4$ loaded CMK-1 by solution infiltration. This is a known phenomenon for nanoconfined materials and has previously been reported for other systems [229, 230]. Thus the sharpness and intensity of XRD peaks are decreased with reducing metal size. Accordingly, the characteristic peak of loaded metal is not present due to the metal being finely dispersed as nano-size particles [231]. It is still partially unclear why the XRD peaks for the metal hydride are not observable, though they may be severely broadened by either being nanocrystalline (same crystal structure in nanodomains) or amorphous (no long-range order).

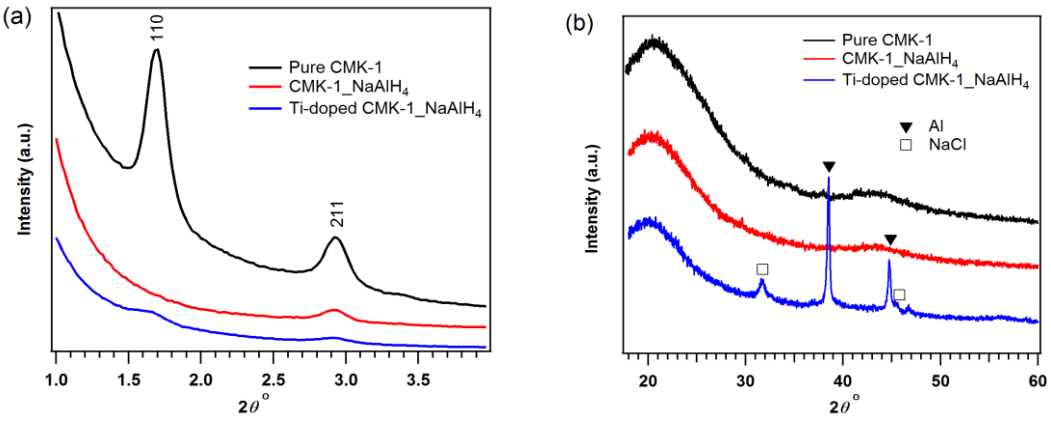

Figure 5-6: (a) SAXS pattern and (b) XRD pattern of solvent-infiltrated CMK-1.

For the Ti-doped sample, NaCl and Al peaks are observed due to the following reaction [232, 233].

$$3NaAlH_4 + TiCl_3 \rightarrow xAl + Al_{3-x}Ti + 3NaCl + 6H_2 \qquad (5.4)$$

Unfortunately, reaction (5.4) occurs quickly in solution, evolving hydrogen gas whilst crystallising Al/Al-Ti phases and sparingly soluble NaCl out of solution. Thus, Al/Al-Ti and NaCl are precipitated from THF before infiltration and are deposited

onto the outside of the CMK-1 scaffold. Because they are not nanoconfined the diffraction peaks are sharp and the compounds can be easily identified. In addition, aluminium titanium alloys form with very similar XRD pattern as compared to Al [234]. In general, Ti-doped $NaAlH_4$ can be prepared by a conventional method i.e., ball milling a mixture of $NaAlH_4$ and $TiCl_3$ [235]. However, for a nanoconfined system, the impregnated metals should firstly form amorphous or crystalline nanoparticles before being infiltrated into the scaffold nanopores [221, 236]. Thus, the solvent mediated infiltration is likely to be a suitable method, which has the capability of dissolving and forming homogeneous nanoparticles. Consequently, removal of the by-products on the scaffold surface and the solvent can be another challenge to the application of this technique.

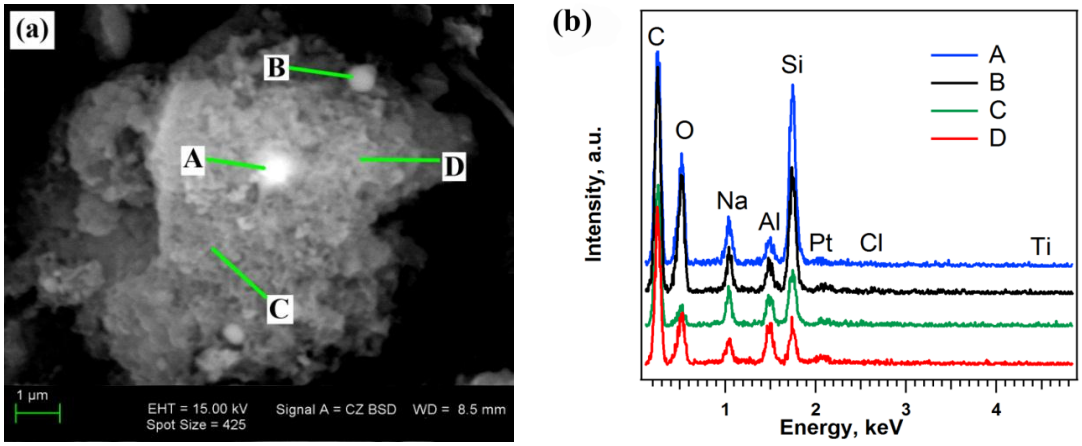

Figure 5-7: (a) Backscattered electron (BSE) SEM image and (b) EDS analysis at selected points of $NaAlH_4$-loaded CMK-1 with Ti dopant.

Figure 5-7 (a) and (b) show a backscattered electron SEM (BSE-SEM) image of $NaAlH_4$ loaded CMK-1 with Ti dopant and an energy dispersive X-ray spectroscopy (EDS) plot, respectively. The SEM (BSE-SEM) image detects a rather homogenous distribution of $NaAlH_4$ throughout the scaffold. Ti, from doping, is not clearly detected because of the very low quantity of the metal, whilst the presence of Pt is due to the sample coating process. The SEM and EDS also reveal the presence of a rather large quantity of Si, likely due to an incomplete removal of the MCM-48 silica template. However, from the SAXS measurements the MCM-48 structure is not observed. Residual SiO_2 is found as a spherical shape on the carbon scaffold surface as shown at point B of Figure 5-7 (a). This contamination is hard to remove from the

porous carbon scaffold even after washing with a hot NaOH deionized-water/ethanol solution several times.

5.2.3.2 Melt Infiltration

CMK-1 exhibits a high specific surface area (1500 – 1800 m^2 g^{-1}) with a total pore volume approximately 1.0 – 1.3 cm^3 g^{-1} [94, 225]. The density of $NaAlH_4$ is 0.91 g cm^{-3}, thus, the maximum possible amount of $NaAlH_4$ that can be loaded into pores of CMK-1 is approximately 50 wt.%. Figure 5-8 (a) shows SAXS data for the melt infiltration samples with different weight ratios of $NaAlH_4$ per CMK-1, i.e. 20, 33 and 50 wt.% of $NaAlH_4$/ CMK-1. For 20 and 33 wt.% $NaAlH_4$ loaded samples, their SAXS patterns show a clear reduction in the diffraction peak at lower 2θ (~ 1.7º) indicating a partial infiltration. In contrast, this peak disappears for the sample that was infiltrated with 50 wt.% of $NaAlH_4$. However, the peak at 2.9º 2θ still presents for all samples with a comparable intensity. In fact, the CMK-1 scaffold contains not only primary mesopores (~ 2 – 3 nm) but also micropores (with pore sizes < 1 nm) as discussed in section 5.2.2. This may indicate that the $NaAlH_4$ is selectively infiltrating certain pores, most likely the larger mesopores in the CMK-1 framework.

Figure 5-8 (b) shows the XRD data for the melt infiltrated samples. At 20 wt.% of $NaAlH_4$/CMK-1 loading, diffraction peaks for $NaAlH_4$ cannot be indexed by XRD indicating all $NaAlH_4$ particles are confined in the scaffold. For all samples, Al peaks are present as a result of partial decomposition of $NaAlH_4$ during melt infiltration, potentially due to the applied hydrogen pressure slightly below its equilibrium pressure. A small amount of excess $NaAlH_4$ is also observed for the 33 wt.% of $NaAlH_4$/CMK-1 sample whilst the sample with 50 wt.%-$NaAlH_4$/CMK-1 shows the highest content of crystalline $NaAlH_4$. Although the SAXS result shows a complete infiltration at 50 wt.% of $NaAlH_4$, some $NaAlH_4$ particles are on the scaffold surface as demonstrated by XRD result. Thus, the maximum amount of $NaAlH_4$ that is loaded into the CMK-1 scaffold is less than 50 wt.%. Previously, the maximum limit to $NaAlH_4$ loading into another porous carbon HSAG-500 (BET) has been approximated to 40 wt.% of the $NaAlH_4$/scaffold [202]. In fact, the micropores of CMK-1 (with pore size less than 1 nm) are approximately 21% of the total pore volume [224], which are likely inaccessible to the hydride melt.

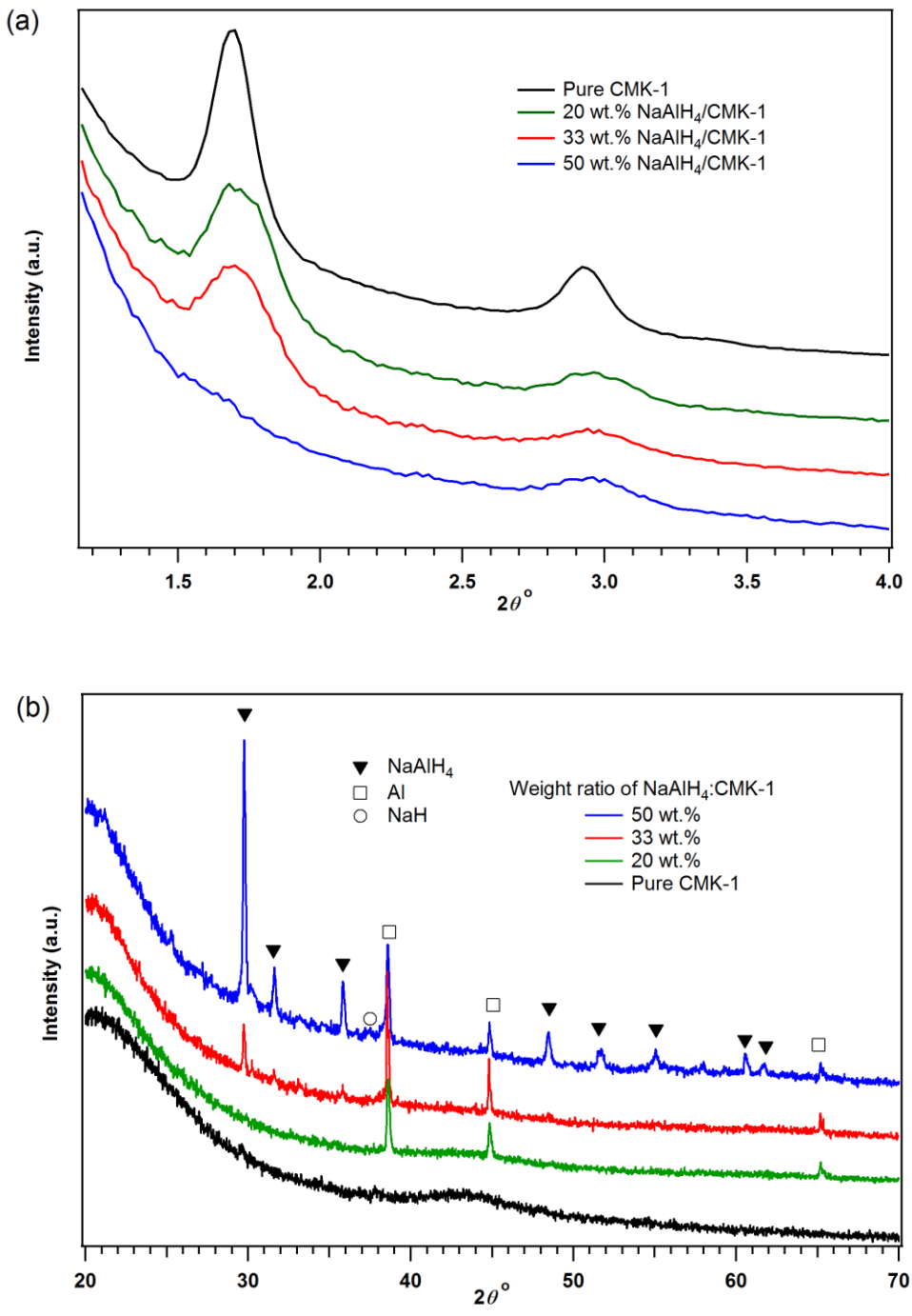

Figure 5-8: (a) SAXS patterns and (b) XRD spectra of $NaAlH_4$-loaded CMK-1 prepared by melt infiltration technique.

5.3 HYDROGEN STRORAGE PROPERTIES

5.3.1 Hydrogen Release Properties

Figure 5-9 shows the gas desorption profiles from the temperature programmed desorption mass spectrometry (TPD-MS) measurements for confined $NaAlH_4$ in CMK-1 prepared by the solvent infiltration method. The hydrogen desorption from the $NaAlH_4$-loaded scaffolds occurs below 100 ºC under a vacuum < 10^{-2} mbar. In contrast, bulk $NaAlH_4$ starts to release hydrogen beyond its melting point (181 ºC) at > 200 ºC with the first desorption peak maximum at ~ 230 ºC. The lower-temperature desorption peaks represent kinetically enhanced desorption behaviour of $NaAlH_4$ due to porous confinement. Accordingly, the first two decomposition steps, equations (5.1) and (5.2), are likely observed as a single hydrogen release peak, as has been reported previously for $NaAlH_4$ contained in carbon aerogels [237]. The existence of broad peaks at ~ 250 and 350 ºC is likely due to the decomposition of the excess $NaAlH_4$ that resides on the outside of the porous matrix.

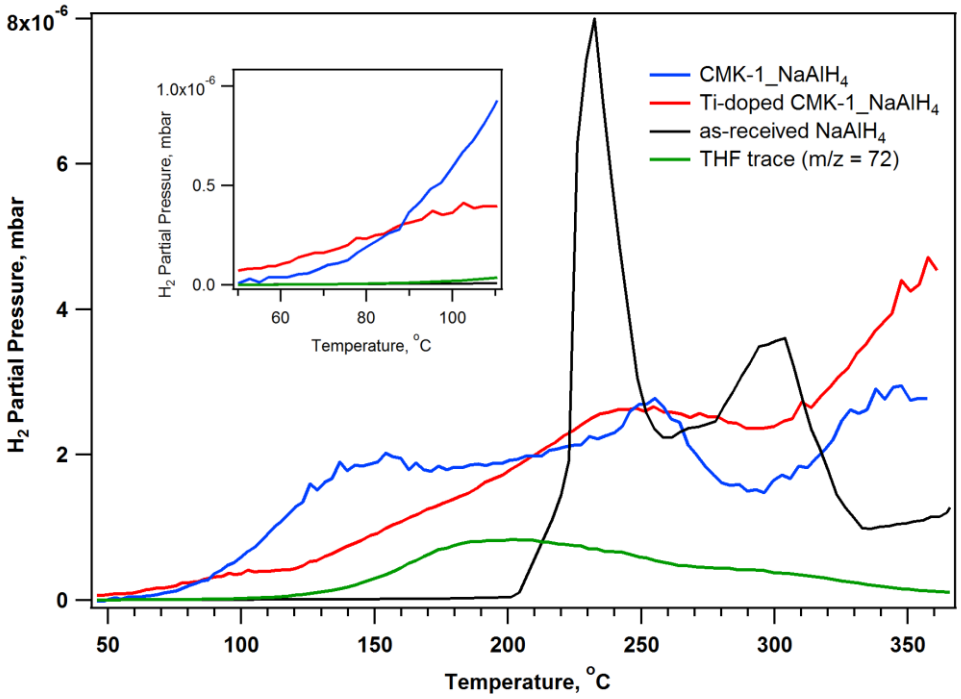

Figure 5-9: TPD-MS data of confined $NaAlH_4$ in CMK-1 prepared by solvent infiltration with and without Ti doping compared to bulk $NaAlH_4$ using a heating rate of 2 ºC /min. The THF trace was collected from the Ti-doped sample and the insert illustrates hydrogen evolution at lower temperatures.

Hydrogen desorption from solvent-infiltrated samples occurs with broad hydrogen release peaks, and despite being outgassed under vacuum for hours at room temperature they also generate a significant level of THF vapour, well above its boiling point (66 ºC). The oxygen in the THF molecule can likely form nano-clusters of Al_2O_3 [238] releasing hydrogen gas and other volatile material from a redox reaction between the solvent and infiltrated material. This illustrates that solvent infiltrated nanoconfined materials should be carefully outgassed to prevent the solvent from taking part in the decomposition pathway [228]. In this case the THF could not be adequately removed because the sample could not be taken to high enough temperatures without initiating hydrogen desorption from the nanoconfined $NaAlH_4$. It is also of interest that the Ti-doped $NaAlH_4$ sample displays an unusual decomposition profile. It appears as though the first hydrogen release event (at low temperature) is quite small and it is likely that hydrogen has been prematurely removed from the sample during the evacuation procedure at room temperature to remove excess THF from the scaffold.

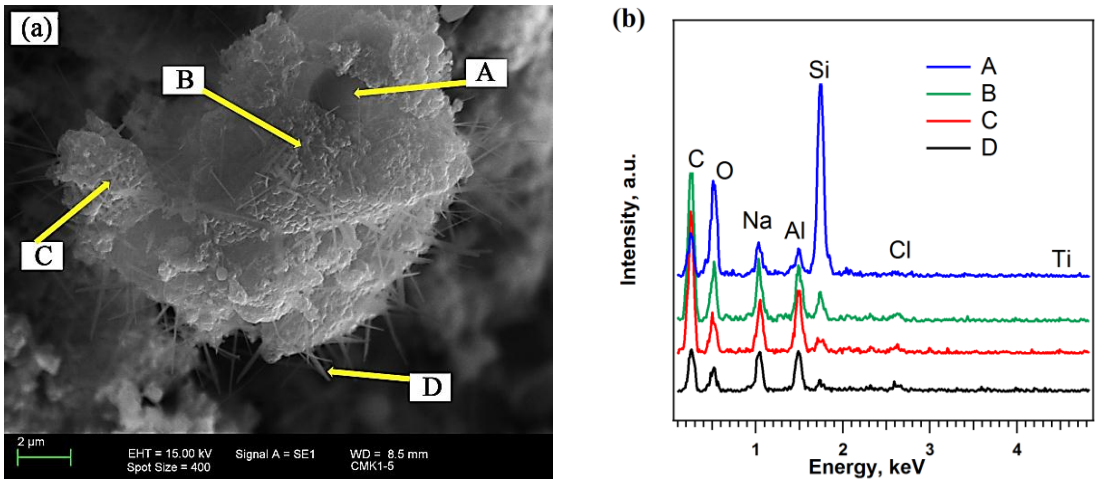

Figure 5-10: (a) SE-SEM image and (b) EDS measurement at the selected points of confined Ti-doped $NaAlH_4$ after TPD measurement.

After TPD measurements up to 375 ºC under vacuum, SEM images combined with the EDS measurements, Figure 5-10 (a) and (b), were undertaken to inspect the scaffold morphology. These images are very revealing, as they show the formation of needle-like filaments on the scaffold surface, which can be identified by EDS as Na(H) and Al. However, the EDS measurement has the effect of electron beam-spot size. Therefore, the result may associate with the signal generated from the

neighbouring area. The filaments are likely not single crystals and are not present in the undecomposed samples. The formation of these filaments outside the scaffold is caused by the heat treatment beyond the melting point of $NaAlH_4$ under vacuum during TPD measurement [228]. The previously infiltrated $NaAlH_4$ appears to have been extracted from the scaffold and then decomposed. This phenomenon has been reported previously, where large Al crystals (> 100 nm) were formed outside a porous carbon matrix after full dehydrogenation at 325 ºC [13]. The loss of Na has also been reported for nanoconfined $NaBH_4$ [239]. These results are of particular relevance for the nanoconfinement of complex hydrides, borohydrides in particular, as characterisation is often performed above their melting points [213, 229, 240]. Some borohydrides froth and foam [241] during hydrogen release above their melting point and this means that serious consideration needs to be given as to whether or not nanoconfined borohydrides actually stay confined during hydrogen release.

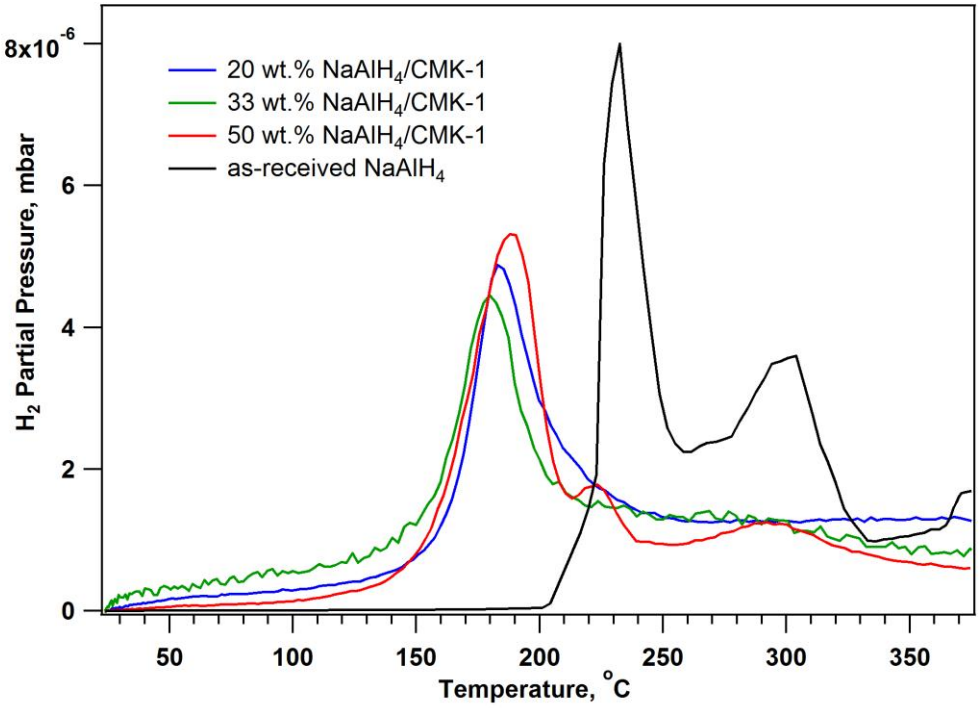

Figure 5-11: TPD-MS data of confined $NaAlH_4$ in CMK-1 prepared by melt infiltration compared to bulk $NaAlH_4$ using a heating rate of 2 ºC /min.

Figure 5-11 shows the hydrogen release for 20, 33 and 50 wt.% $NaAlH_4$/scaffold melt-infiltrated samples. For all confined $NaAlH_4$ samples, their main peak has

shifted to lower temperatures compared to that of bulk $NaAlH_4$. Therefore, the major peaks occur at ~180 – 190 ºC for the infiltrated $NaAlH_4$ and ~230 ºC for the bulk $NaAlH_4$. The 20 and 33 wt.% loaded $NaAlH_4$ samples show a single hydrogen release peak indicating that most $NaAlH_4$ particles are confined in the scaffold. This peak corresponds to a combination of the first two decomposition steps of $NaAlH_4$. At temperature > 250 ºC, small amount of hydrogen is still released from the samples indicating the decomposition of other high stability hydrides, e.g. the unconfined $NaAlH_4$ and NaH. Second and third minor peaks are clearly observed at ~220 and 300 ºC, respectively, for 50 wt.% $NaAlH_4$ loading as a result of bulk $NaAlH_4$ desorption behaviour [202]. This is in agreement with the large amount of excess $NaAlH_4$ that was detected by XRD for this sample as shown in Figure 5-8 (b).

After TPD measurements up to 375 °C under vacuum, TEM images combined with the EDS measurements, Figure 5-12, were undertaken on 33 wt.% $NaAlH_4$ melt infiltrated CMK-1 sample to inspect the scaffold morphology. The image reveals the formation of needle-like filaments that also found in the solvent infiltration sample. The needle-like filament can be identified by EDS as Al with diameter ~400 nm.

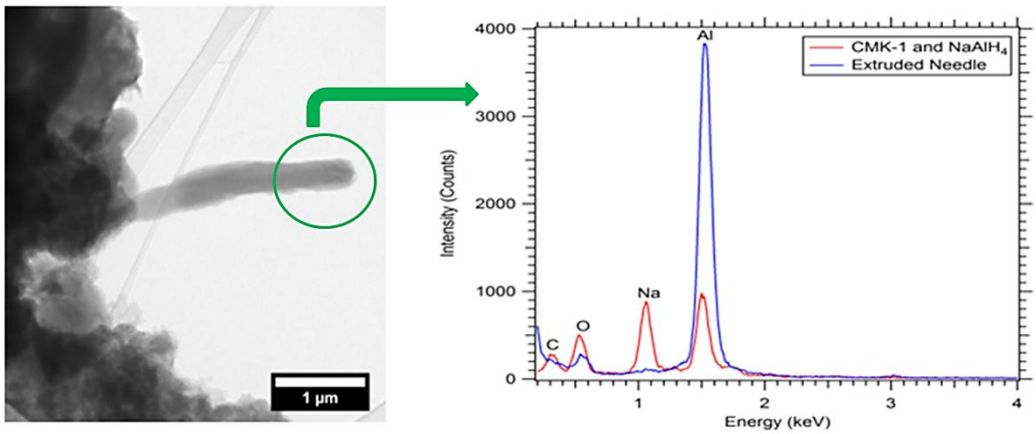

Figure 5-12: TEM micrograph of 33 wt.% $NaAlH_4$ melt infiltrated CMK-1 after TPD-MS to 375 °C and EDS measurements at selected region.

5.3.2 Kinetic Properties

Figure 5-13 shows the hydrogen evolution of the samples measured by residual gas analysis (RGA) with a final fixed temperature at 170 ºC. In this experiment, the samples were heated from 65 ºC until they reached the set temperature of 170 ºC. It should be noted that the total released hydrogen is an integrated H_2 partial pressure,

measured by RGA at a fixed temperature. Hence, the plot of integrated H_2 partial pressure versus time provides the hydrogen desorption kinetics of the sample. As can be seen, all confined $NaAlH_4$ samples show an improvement in desorption kinetics compared to bulk. Therefore, desorption at 170 ^oC of these samples has been completed within 10 h whilst the bulk $NaAlH_4$ continues decompose past 20 h.

All infiltrated samples show comparable isothermal desorption kinetics, i.e. the overall kinetics is likely dominated by a nanoconfinement effect instead of the Ti catalyst, that was not completely nanoconfined. However, the presence of Ti can reduce the onset hydrogen release temperature as discussed in section 5.3.1. In addition, Li et al. [230] suggested that the kinetics of complex hydride-confinement systems may also be enhanced by a catalytic effect of the carbon scaffold itself. The catalytic effect of the a porous carbon may be due to the fact that the electronegative carbon framework lowers the energy requirement for the Na atom to donate its charge to the AlH_4 cluster in a $NaAlH_4$ molecule and consequently reduces the strength of Al–H bond [242].

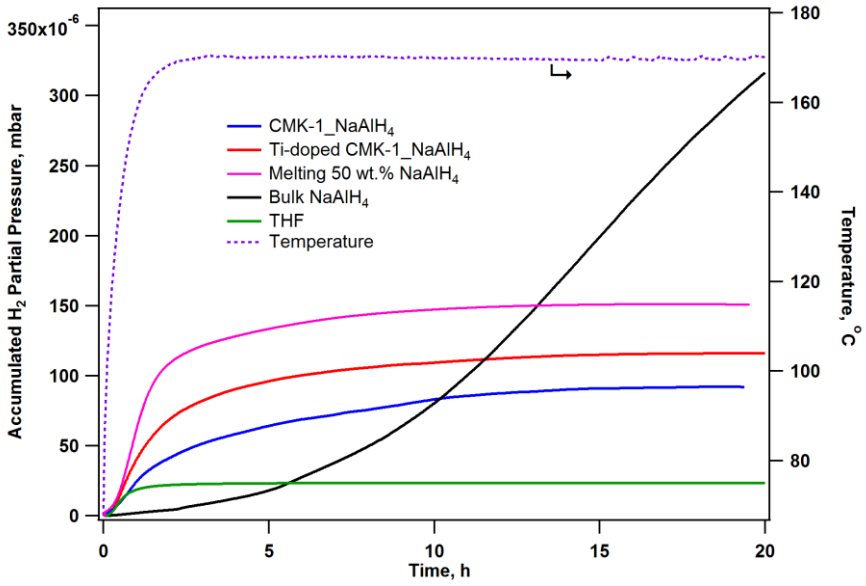

Figure 5-13: Hydrogen evolution of solution/melt infiltrated- and bulk $NaAlH_4$ measured by RGA technique under vacuum < 10^{-2} mbar.

5.4 CONCLUSIONS

Mesoporous silica (MCM-48) and ordered mesoporous carbon (CMK-1) are successfully synthesised and their structures are confirmed by small angle X-ray scattering (SAXS). However, the silica template is difficult to remove from the CMK-1 scaffold even after washing with a hot NaOH deionized-water/ethanol solution several times. This contamination is found as residual SiO_2 by energy dispersive X-ray spectroscopy (EDS) measurements.

$NaAlH_4$ was infiltrated into the pores of ordered mesoporous carbon, CMK-1, by both solvent- and melt infiltration methods, as demonstrated by SAXS. Significant issues have been identified relating to the nanoconfinement of hydrogen storage materials in porous scaffolds. For the solvent infiltration method, careful thought must be given to contamination from any solvents, e.g. THF in this study, that have been used to dissolve and then infiltrate the hydrogen storage materials. For the melt infiltration, it is suggested to apply the hydrogen pressure well above the equilibrium pressure during the impregnation process at the temperature just above the melting point of $NaAlH_4$ to prevent partial decomposition. It is likely that the CMK-1 scaffold contains very small pores (less than 1 nm) that are likely to be inaccessible to the $NaAlH_4$ particles. Accordingly, the maximum amount of $NaAlH_4$ that can be impregnated into CMK-1 is less than the theoretical maximum (~50 wt.% of $NaAlH_4$/CMK-1).

Single step hydrogen desorption occurs for confined $NaAlH_4$. The maximum release rate of this sample measured by TPD-MS is observed at a temperature lower than its melting point. The confined $NaAlH_4$ shows a significant improvement in the hydrogen decomposition temperature, with an onset below 100 ^oC, compared to bulk $NaAlH_4$ (~190 ^oC). The isothermal desorption kinetics of the $NaAlH_4$-CMK-1 system have also been improved compared to bulk $NaAlH_4$. Thus, the decrease in particle size and possible interactions with the scaffold play a significant role to improve the hydrogen sorption kinetics of $NaAlH_4$ and also other complex hydrides. Among the confined samples, the catalytic effect of the Ti additive on the isothermal desorption kinetics of confined $NaAlH_4$-CMK-1 system is unclear. However, the Ti-doped sample was not optimised due to the premature formation of Al-Ti compounds on the surface of the scaffold.

Of critical importance is the discovery of $NaAlH_4$ extraction from the scaffold after heating past its melting point. This leads to the formation of needle-like filaments with diameters ~400 nm on the scaffold surface, which can be identified as Al. This phenomenon has serious implications for reversibility studies and is relevant to other nanoconfined complex hydride systems such as borohydrides. Further research is clearly necessary to tackle some of these adverse issues that are often hard to detect.

This work has provided a basis for future research that will allow an identification of more advanced nanoconfined-hydride systems directed towards practical applications. The research shows that the nanoconfined system can enhance the hydrogen desorption property of $NaAlH_4$, i.e., the confined $NaAlH_4$ releases hydrogen more readily than unmodified $NaAlH_4$. The hydrogen desorption kinetics was also improved, and is comparable to the $Ti(OBu)_4$-doped $NaAlH_4$ [11]. The low onset temperature (~100 ºC) for hydrogen release implies the possibility of using the confined $NaAlH_4$ as a low temperature hydride. However, the kinetics are significantly slower when compared to the intermetallic hydrides, e.g., $LaNi_5$ and $CaNi_5$. Thus, further research is still required, especially on kinetic improvement and reversibility of this complex hydride [243].

CHAPTER 6

SUMMARY AND OUTLOOK

The research reveals the possibility of using $CaNi_5$-based alloys and nanoconfined $NaAlH_4$ as the low temperature metal hydrides for stationary power generation, e.g. remote-area power supply (RAPS) and concentrated solar thermal (CST) systems. The research findings and outlook will be summarized in the following sections.

6.1 $CaNi_5$-BASED ALLOYS

This study has achieved synthesis of $CaNi_5$-based alloys by mechanical milling followed by thermal treatment. The morphology, crystal structure and hydrogen sorption properties of the alloys are altered by substitution of a small amount of additive metals, e.g. Al, Cr, Mo, and Zr. It was found that the abundance of the $CaNi_5$ phase decreased with increasing additive content. The secondary phase of all synthesised alloys was predominantly Ni. Other secondary phases, $ZrNi_5$ and Ca_2Ni_7, are formed in Zr and Mo substituted alloys, respectively. With a high content of Mo, the major phase is Ca_2Ni_7 instead of the desired $CaNi_5$ phase. Additives Al, Cr and Mo are found to be incorporated at the Ni-atom site in the $CaNi_5$ lattice whilst Zr tends to be substituted at the Ca site. The incorporation of larger atomic size metals, e.g. Al and Mo, at the Ni site significantly increases the unit cell volume of the $CaNi_5$ phase, whilst replacement of Zr at the Ca site leads to a decrease in the unit cell volume.

The hydrogen storage capacity of all substituted alloys is decreased and the plateau regions are narrowed compared to that of pure $CaNi_5$. Substitution of Al and Mo results in a lowering of desorption plateau pressures, indicating higher stability hydrides are formed in these alloys. However, the $CaNi_{4.8}Mo_{0.2}$ alloy, which is dominated by a Ca_2Ni_7 phase, does not show a plateau region. The sorption kinetics of all substituted alloys, except $CaNi_{4.9}Mo_{0.1}$, are relatively fast and comparable to the kinetics of unsubstituted $CaNi_5$.

The hydrogen absorption capacity of substituted alloys with Zr at the Ca site rapidly decreases for the first 50 absorption/desorption cycles performed at 85 ºC, however,

the rate of capacity loss slows beyond 100 cycles. The Al additive shows improvement in the cyclic stability by retaining the initial capacity for 20 cycles and then the alloy capacity starts to decay gradually. Accordingly, the substitution of Al and Zr offers a possibility to improve the cyclic stability of the $CaNi_5$-based alloys. This study also found that the Ca_2Ni_7 phase shows unfavourable hydrogen storage properties including the formation of a very stable hydride with a severe disproportionation rate. The disproportionated $CaNi_5$ phase can be recovered by heat treatment with a comparable capacity and similar properties to that of the as-synthesised alloy.

Although the mechanical ball milling method results in homogeneity, the metallic mixture is generally formed as an amorphous phase. A thermal treatment (annealing) process is required to crystallise the product. Thus, it is strongly suggested that the milling and annealing conditions need to be optimized for each composition to promote the formation of the highest proportion of the $CaNi_5$ phase, and to decrease segregation and secondary phase formation.

6.2 NANOCONFINED $NaAlH_4$

$NaAlH_4$ was infiltrated into the pores (2 – 3 nm) of ordered mesoporous carbon, CMK-1, by both solvent- and melt-infiltration methods. Significant issues have been identified relating to the nanoconfinement of hydrogen storage materials in porous scaffolds. Infiltrated $NaAlH_4$ particles are mainly situated in the primary pores (2 – 3 nm pore size) of CMK-1 whilst the micropores with a pore size less than 1 nm are likely inaccessible to the loaded particles.

The research shows that the nanoconfined $NaAlH_4$ releases hydrogen more readily than bulk $NaAlH_4$. The hydrogen desorption kinetics of this system is comparable to the catalysis $NaAlH_4$ that reported previously. In contrast with the first two-step decomposition of the bulk $NaAlH_4$, the nanoconfined $NaAlH_4$ exhibits a single decomposition step with an onset temperature for hydrogen release lower than the melting point of $NaAlH_4$. Therefore, the onset temperature for hydrogen release of confined $NaAlH_4$ at ~100 ºC shows the possibility of its application as a low temperature hydride. Of primary importance is the extraction of $NaAlH_4$ from the scaffold after heating beyond its melting point as confirmed by EDS and TEM

measurements. This has serious implications for reversibility studies and is relevant to other nanoconfined complex hydrides. Thus, further research is clearly necessary to tackle some of these adverse issues that are often hard to detect. *In situ* XRD or SAXS analysis may reveal the mechanism of this phenomenon.

The major concern in the synthesis the CMK-1 scaffold is contamination from the silica template (MCM-48), which is difficult to remove completely from the templated carbon scaffold. For the solvent infiltration method, careful thought must be given to any solvents that can occupy and remain trapped in the pores. Thus, removal of solvents from the scaffold is another challenge for this technique.

REFERENCES

[1] U.S. Energy Information Administration, *Annual Energy Review 2011*, U.S. Department of Energy, Washington, DC, 2012, pp. 291.

[2] D.N. Harries, M. Paskevicius, D.A. Sheppard, T.E.C. Price, C.E. Buckley, Concentrating solar thermal heat storage using metal hydrides, *Proc IEEE*, 100 (2012) 539-549.

[3] C. Corgnale, B. Hardy, T. Motyka, R. Zidan, J. Teprovich, B. Peters, Screening analysis of metal hydride based thermal energy storage systems for concentrating solar power plants, *Renew Sust Energy Rev* 38 (2014) 821–833.

[4] Thomas Jefferson National Accelerator Facility Office of Science Education, The 10 Most Abundant Elements in the Earth's Crust, http://education.jlab.org/faq/index.html (accessed August 25, 2013).

[5] U.S. Geological Survey, Metal Prices in the United States through 1998, c2013, http://minerals.usgs.gov/minerals/pubs/metal_prices/ (accessed August 15, 2013)

[6] British Geological Survey, Rare Earth Elements, c2011, www.bgs.ac.uk/ (accessed August 25, 2013).

[7] M. Humphries, Rare Earth Elements: The Global Supply Chain, in: *Congressional Research Service*, Washington, DC, 2013.

[8] P.D. Goodell, Stability of rechargeable hydriding alloys during extended cycling, *J Less-Common Met* 99 (1984) 1–14.

[9] G.D. Sandrock, J.J. Murray, M.L. Post, J.B. Taylor, Hydrides and deuterides of $CaNi_5$, *Mater Res Bull*, 17 (1982) 887–894.

[10] A. Züttel, Materials for hydrogen storage, *Mater Today*, 6 (2003) 24–33.

[11] B. Bogdanović, M. Schwickardi, Ti-doped alkali metal aluminium hydrides as potential novel reversible hydrogen storage materials, *J Alloys Compds* 253–254 (1997) 1–9.

[12] P. Claudy, B. Bonnetot, G. Chahine, J.M. Letoffe, Etude du comportement thermique du tetrahydroaluminate de sodium $NaAlH_4$ et de l'hexahydroaluminate de sodium Na_3AlH_6 DE 298 A 600 K, *Thermochimica Acta* 38 (1980) 75–88.

[13] J. Gao, P. Ngene, I. Lindemann, O. Gutfleisch, K.P. de Jonga, P.E. de Jongh, Enhanced reversibility of H_2 sorption in nanoconfined complex metal hydrides by alkali metal addition, *J Mater Chem* 22 (2012) 13209–13215.

[14] I.P. Jain, P. Jain, A. Jain, Novel hydrogen storage materials: A review of lightweight complex hydrides, *J Alloys Compds* 503 (2010) 303–339.

[15] D.A.J. Rand, R.M. Dell, *Hydrogen Energy : Challenges and Prospects*, Royal Society of Chemistry, Cambridge, 2008.

[16] BP Statistical Review of World Energy, c2012, http://www.bp.com/ (accessed July 12, 2013).
[17] World Resources Institute, World Greenhouse Gas Emissions: 2005, c2009, http://www.wri.org/resources/charts-graphs/world-greenhouse-gas-emissions-2005 (accessed July 15, 2013).
[18] M. Fujita, The New Global Economic Order and East Asia -From the Viewpoint of Spatial Economics, in: *Plenary Session of the 2010 KEA Annual Meeting "East Asia in the Era of New Global Economic Order"*, c2012, http://www.rieti.go.jp/ (accessed July 15, 2013).
[19] R. Suppiah, B. Preston, P.H. Whetton, K.L. McInnes, R.N. Jones, I. Macadam, J. Bathols, D. Kirono, Climate change under enhanced greenhouse conditions in South Australia, in: *Assessment of climate change, impacts and risk management strategies relevant to South Australia*, CSIRO Marine and Atmospheric Research Aspendale, 2006.
[20] D.J. Wuebbles, A.K. Jain, Concerns about climate change and the role of fossil fuel use, *Fuel Proc Tech* 71 (2001) 99–119.
[21] European Commission, *EU action against climate change: Leading global action to 2020 and beyond* , European Communities, Luxembourg, 2008.
[22] European Renewable Energy Council, *Renewable energy Technology Roadmap 20% by 2020*, Renewable Energy House, Brussels
[23] European Commission, What is the EU doing about climate change?, http://ec.europa.eu/clima/policies/brief/eu/index_en.htm (accessed July 20, 2013).
[24] M. Momirlan, T.N. Veziroglu, The properties of hydrogen as fuel tomorrow in sustainable energy system for a cleaner planet, *Int J Hydrogen Energy* 30 (2005) 795–802.
[25] Fuel Cell and Hydrogen Energy Association, Fuel Cell and Hydrogen Energy: International Developments, in, c2013, http://www.fchea.org/ (accessed August 8, 2013).
[26] National Research Council and National Academy of Engineering, *The Hydrogen Economy: Opportunities, Costs, Barriers, and R&D Needs*, The national Academies Press, Washington, D.C., 2004.
[27] E. Chen, History, in: G. Hoogers (Ed.) *Fuel Cell Technology Handbook*, CRC Press, Boca Raton, 2003.
[28] F. Marscheider-Weidemann, E. Schirrmeister, A. Roser, Key role of fuel cells, in: M. Ball, M. Wietschel (Eds.) *The Hydrogen Economy: Opportunities and Challenges*, Cambridge University Press, New York, 2009, pp. 349.
[29] Fuel Cell Today, The Fuel Cell Today Industry Review, 2012, http://www.fuelcelltoday.com/ (accessed August 8, 2013).
[30] F. Barbir, *PEM Fuel Cell: Theoty and Practice*, 2nd ed., Elsevier/Academic Press, Boston, 2013.

[31] S. Giddey, S.P.S. Badwal, A. Kulkarni, C. Munnings, A comprehensive review of direct carbon fuel cell technology, *Prog Energy Combust Sci* 38 (2012) 360–399.
[32] G. Hoogers, Introduction, in: G. Hoogers (Ed.) *Fuel Cell Technology Handbook*, CRC Press, Boca Raton, 2003.
[33] K.K. Pant, R.B. Gupta, Fundamentals and Use of Hydrogen as a Fuel, in: R.B. Gupta (Ed.) *Hydrogen Fuel: Production, Transport, and Storage*, CRC Press, Boca Raton, 2009.
[34] SmartPlanet, Hands-on: Medis Power Pack fuel cell charger, c2008, http://crave.cnet.co.uk/ (accessed August 9, 2013).
[35] Horizon Fuel Cell Technologies, Portable Power, c2013, http://www.horizonfuelcell.com/ (accessed August 8, 2013).
[36] Hydrogen and Fuel Cells in Portable Applications, 2008, http://www.ika.rwth-aachen.de/r2h/index.php/ (accessed August 8, 2013).
[37] UltraCell, Mobile Power for Mobile Missions, c2007, http://www.powerstream.com/ (accessed August 12, 2013).
[38] R. Rose, Fuel Cells: Civilian and Military Applications, c2013, www.fuelcells.org/ (accessed August 12, 2013).
[39] Royal Society of Chemistry, Fuel cells head for mass market, 2006, http://www.rsc.org/ (accessed August 12, 2013).
[40] C.E. Thomas, Fuel cell and battery electric vehicles compared, *Int J Hydrogen Energy* 34 (2009) 6005-6020.
[41] J. Ernst, History of fuel cell development at Mercedes-Benz, c2007, http://www.daimler.com/ (accessed August 12, 2013).
[42] American Honda Motor Co., Inc., The History of the Honda FCX Clarity, Fuel Cell Electric Vehicle FCEV, c2013, http://corporate.honda.com/ (accessed August 16, 2013).
[43] J. Wing, Fuel Cell Electric Vehicles: Turns in the Road, 2013, http://www.cleantechinvestor.com/ (accessed August 16, 2013).
[44] D. King, Toyota forecasts tens of thousands of FCEVs by 2020s, 2012, http://green.autoblog.com/ (accessed August 18, 2013).
[45] Environmental Leader LLC., Hydrogen Fueling Stations Could Reach 5,200 by 2020, 2011, http://www.environmentalleader.com/ (accessed August 18, 2013).
[46] P. Hoffmann, *Tomorrow's Energy: hydrogen, fuel cells, and the prospects for a cleaner planet*, The MIT Press, Cambridge, 2012.
[47] Honda Motor Co., Ltd., FCX Clarity Specifications, http://world.honda.com/ (accessed August 18, 2013).
[48] FuelCell Energy, Inc., 2011 Annual Report: Meeting the World's Energy Needs Today, 2011, http://fcel.client.shareholder.com/annuals.cfm (accessed August 18, 2013).
[49] G. Huppmann, *High Temperature Fuel Cell Trigeneration for Commercial and Municipal Buildings: The MTU Carbonate Fuel Cell HotModule®*, CIBSE CHP Group and LHP London 2005.

[50] S. Samuelsen, *Fuel Cell/Gas Turbine Hybrid Systems*, ASME International Gas Turbine Institute, California, 2004.
[51] J. Larminie, A. Dicks, *Fuel Cell Systems Explained*, 2nd ed., John Wiley & Sons, West Sussex, 2003.
[52] Ceramic Fuel Cells, Gennex fuel cell module, c2013, http://www.cfcl.com.au/Gennex/ (accessed August 19, 2013).
[53] E.M. Gray, C.J. Webb, J. Andrews, B. Shabani, P.J. Tsai, S.L.I. Chan, Hydrogen storage for off-grid power supply, *Int J Hydrogen Energy* 36 (2011) 654–663.
[54] M. Fellet, Research on metal hydrides revived for next-generation solutions to renewable energy storage, *MRS Bulletin* 38 (2013) 1012–1013.
[55] M. Seitz, P. Cetin, M. Eck, Thermal Storage Concept for Solar Thermal Power Plants with Direct Steam Generation, *Energy Procedia* 49 (2014) 993–1002.
[56] A. Borgschulte, A. Züttel, U. Wittstadt, Hydrogen Production, in: A. Züttel, A. Borgschulte, L. Schlapbach (Eds.) *Hydrogen as a Future Energy Carrier*, Wiley-VCH Verlag GmbH & Co. KGaA, Weinheim, 2008.
[57] N.Z. Muradov, T.N. Veziroğlu, From hydrocarbon to hydrogen-carbon to hydrogen economy, *Int J Hydrogen Energy* 30 (2005) 225–237.
[58] B. Suresh, R. Gubler, Y. Yamaguchi, X. He, CEH product review: Hydrogen, in: SRI Consulting, *Chemical Economics Handbook*, 2001.
[59] K.B. Martin, W. Vaz, Hydrogen Infrastructure: Production, Storage, and Transportation, in: S.E. Grasman (Ed.) *Hydrogen Energy and Vehicle Systems*, CRC Press, Boca Raton, 2012.
[60] A. Züttel, M. Hirscher, B. Panella, K. Yvon, S.-i. Orimo, B. Bogdanović, M. Felderhoff, F. Schüth, A. Borgschulte, S. Goetze, S. Suda, M.T. Kelly, Hydrogen Storage, in: A. Züttel, A. Borgschulte, L. Schlapbach (Eds.) *Hydrogen as a Future Energy Carrier*, Wiley–VCH Verlag GmbH & Co. KGaA, Weinheim, 2008.
[61] US Department of Energy, Targets for Onboard Hydrogen Storage Systems for Light-Duty Vehicles, 2009, http://www1.eere.energy.gov/ (accessed August 19, 2013).
[62] J. Zheng, X. Liu, P. Xu, P. Liu, Y. Zhao, J. Yang, Development of high pressure gaseous hydrogen storage technologies, *Int J Hydrogen Energy* 37 (2012) 1048–1057.
[63] U. Bossel, Does a Hydrogen Economy Make Sense?, *Proc. IEEE* 94 (2006) 1826–1837.
[64] M. Fichtner, Hydrogen storage, in: M. Ball, M. Wietschel (Eds.) *The Hydrogen Economy: Opportunities and Challenges*, Cambridge University Press, New York, 2009.
[65] T. Koljonen, E. Pursiheimo, K. Gether, K. Jørgensen, System Analysis and Assessment of Technological Alternatives for Nordic H_2 Energy Foresight, in: *Nordic Hydrogen Energy Foresight*, Risø National Laboratory, 2004.

[66] U. Bosse, B. Eliasson, G. Taylor, The Future of The Hydrogen Economy: Bright or Bleak?, 2004, http://www.oilcrash.com/articles/h2_eco.htm (accessed August 22, 2013).
[67] L. Schlapbach, A. Züttel, Hydrogen-storage materials for mobile applications, *Nature* 414 (2001) 353-358.
[68] J. Garcia-Martinez, *Nanotechnology for the Energy Challenge*, WILEY–VCH Verlag, Weinheim, 2010.
[69] M. Bastos-Neto, C. Patzschke, M. Lange, J. Mollmer, A. Moller, S. Fichtner, C. Schrage, D. Lassig, J. Lincke, R. Staudt, H. Krautscheid, R. Glaser, Assessment of hydrogen storage by physisorption in porous materials, *Energy Envir Sci* 5 (2012) 8294–8303.
[70] H. Jin, Y.S. Lee, I. Hong, Hydrogen adsorption characteristics of activated carbon, *Catalysis Today* 120 (2007) 399–406.
[71] B. Panella, M. Hirscher, S. Roth, Hydrogen adsorption in different carbon nanostructures, *Carbon* 43 (2005) 2209-2214.
[72] H.W. Langmi, A. Walton, M.M. Al-Mamouri, S.R. Johnson, D. Book, J.D. Speight, P.P. Edwards, I. Gameson, P.A. Anderson, I.R. Harris, Hydrogen adsorption in zeolites A, X, Y and RHO, *J Alloys Compds* 356–357 (2003) 710–715.
[73] N.L. Rosi, J. Eckert, M. Eddaoudi, D.T. Vodak, J. Kim, M. O'Keeffe, O.M. Yaghi, Hydrogen Storage in Microporous Metal-Organic Frameworks, *Science* 300 (2003) 1127–1129
[74] H.Y. Tian, C.E. Buckley, D.A. Sheppard, M. Paskevicius, N. Hanna, A synthesis method for cobalt doped carbon aerogels with high surface area and their hydrogen storage properties, *Int J Hydrogen Energy* 35 (2010) 13242–13246.
[75] D. Chandra, Intermetallics for hydrogen storage, in: G. Walker (Ed.) *Solid-state hydrogen storage: Materials and Chemistry*, Woodhead Publishing Ltd., New Delhi, 2012.
[76] J.P. Blackledge, An Introduction to the Nature and Technology of Hydrides, in: W.M. Mueller, J.P. Blackledge, G.G. Libowitz (Eds.) *Metal Hydrides*, New York, New York, 1968.
[77] B. Bogdanović, R.A. Brand, A. Marjanović, M. Schwickardi, J. Tölle, Metal-doped sodium aluminium hydrides as potential new hydrogen storage materials, *J Alloys Compds* 302 (2000) 36–58.
[78] Y. Nakamori, S. Orimo, Borohydrides as hydrogen storage materials, in: G. Walker (Ed.) *Solid-state hydrogen storage: Materials and Chemistry*, Woodhead Publishing Ltd., New Delhi, 2012.
[79] J.S. Benjamin, Mechanical Alloying, *Sci Am* 234 (1976) 40-48.
[80] M.S. El-Eskandarany, K. Aoki, K. Suzuki, Rod milling for solid-state formation of $Al_{30}Ta_{70}$ amorphous alloy powder, *J Less-Common Met* 167 (1990) 113–118.
[81] C. Suryanarayana, *Mechanical Alloying and Milling*, Marcel Dekker, New York, 2004.

[82] G. Liang, R. Schulz, Phase structures and hydrogen storage properties of Ca–Mg–Ni alloys prepared by mechanical alloying, *J Alloys Compds* 356–357 (2003) 612–616.

[83] K.H.J. Buschow, Hydrogen absorption in intermetallic compounds, in: Karl A. Gschneidner, Jr., E. Leroy (Eds.) *Handbook on the Physics and Chemistry of Rare Earths*, Elsevier, Amsterdam, 1984.

[84] G.D. Sandrock, Development of Low Cost Nickel-Rare Earth Hydrides for Hydrogen Storage, in: T.N. Vezeroglu, W. Seifritz (Eds.) *The 2nd World Hydrogen Energy Conference*, Pergamon Press, Zuric, 1978.

[85] G. Liang, J. Huot, R. Schulz, Mechanical alloying and hydrogen storage properties of $CaNi_5$-based alloys, *J Alloys Compds* 321 (2001) 146–150.

[86] P.S. Gilman, J.S. Benjamin, Mechanical alloying, *Annu Rev Mater Sci* 13 (1983) 279–300.

[87] C.C. Koch, Materials synthesis by mechanical alloying, *Annu Rev Mater Sci* 19 (1989) 121–143.

[88] M. Paskevicius, *A Nanostructural Investigation of Mechanochemically Synthesised Hydrogen Storage Materials*, Imaging and Applied Physics, Curtin University, Perth, 2009.

[89] C. Suryanarayana, Mechanical alloying and milling, *Prog Mater Sci* 46 (2001) 1–184.

[90] E.J. Wheeler, D. Lewis, The Deformation and Annealing Characteristics of Germanium and Silicon, *J Electro Mater* 6 (1977) 597–606.

[91] L.A. Solovyov, V.I. Zaikovskii, A.N. Shmakov, O.V. Belousov, R. Ryoo, Framework Characterization of Mesostructured Carbon CMK-1 by X-ray Powder Diffraction and Electron Microscopy, *J Phys Chem B* 106 (2002) 12198–12202.

[92] M. Paskevicius, D.A. Sheppard, C.E. Buckley, Thermodynamic Changes in Mechanochemically Synthesized Magnesium Hydride Nanoparticles, *J Am Chem Soc* 132 (2010) 5077-5083.

[93] J. Xu, Z. Luan, H. He, W. Zhou, L. Kevan, A Reliable Synthesis of Cubic Mesoporous MCM-48 Molecular Sieve, *Chem Mater* 10 (1998) 3690–3698.

[94] R. Ryoo, S.H. Joo, M. Kruk, M. Jaroniec, Ordered Mesoporous Carbons, *Adv Mater* 13 (2001) 677–681.

[95] G. Hölzer, M. Fritsch, M. Deutsch, J. Härtwig, E. Förster, $K_{\alpha 1,2}$ and $K_{\beta 1,3}$ X-Ray Emission Lines of the 3*d* Transition Metals, *Phys Rev A* 56 (1997) 4554–4568.

[96] E.H. Kisi, Rietveld Analysis of Powder Diffraction Patterns, *Matter Forum* 18 (1994) 135-153.

[97] S. Pratapa, X-ray diffraction phase analyses for granukated and syntered ceramic materials, *Makara Sains* 11 (2007) 85–89.

[98] O. Kratky, A Survey, in: O. Glatter, O. Kratky (Eds.) *Small Angle X-ray Scattering*, Academic Press, London, 1982.

[99] B.D. Cullity, S.R. Stock, *Elements of X-ray Diffraction*, 3rd ed., Prentice Hall, New Jersey, 2001.

[100] P.W. Schmidt, A review of some recent applications of small-angle scattering in studies of polydisperse systems and porous materials, *Makromol Chem Makromol Symp* 15 (1988) 153–166.
[101] J.B. Kortright, A.C. Thompson, X-Ray Emission Energies, in: A.C. Thompson, D. Vaughan (Eds.) *X-ray Data Booklet*, Lawrence Berkeley National Laboratory, Berkeley, 2001.
[102] R.F. Egerton, *Physical Principles of Electron Microscopy: An Introduction to TEM, SEM, and AEM*, Springer Science+Business Media, New York, 2005.
[103] H. Hemmes, A. Driessen, R. Griessen, Thermodynamic properties of hydrogen at pressures up to 1 Mbar and temperatures between 100 and 1000 K, *J Phys C: Solid State Phys* 19 (1986) 3571–3585.
[104] K.G. McLennan, E.M. Gray, An equation of state for deuterium gas to 1000 bar, *Meas Sci Technol* 15 (2004) 211–215.
[105] K. Girgis, Structure of Intermetallic Compounds, in: R.W. Cahn, P. Haasen (Eds.) *Physical Metallurgy*, North-Holland Physics Publishing, Amsterdam, 1983.
[106] R.L. Fleischer, D.M. Dimiduk, H.A. Lipsitt, Intermetallic compounds for strong high-temperature materials: status and potential, *Annu Rev Mater Sci* 19 (1989) 234–263.
[107] M. Dornheim, Thermodynamics of Metal Hydrides: Tailoring Reaction Enthalpies of Hydrogen Storage Materials, in: J.C. Moreno-Pirajan (Ed.) *Thermodynamics - Interaction Studies - Solids, Liquids and Gases*, InTech, Rijeka, 2011.
[108] A. Züttel, Fuels – Hydrogen Storage | Hydrides, in: G. Jürgen (Ed.) *Encyclopedia of Electrochemical Power Sources*, Elsevier, Amsterdam, 2009, pp. 440–58.
[109] J.J. Reilly, G.D. Adzic, J.R. Johnson, T. Vogt, S. Mukerjee, J. McBreen, The correlation between composition and electrochemical properties of metal hydride electrodes, *J Alloys Compds* 293–295 (1999) 569–582.
[110] T. Sakai, K. Oguro, H. Miyamura, N. Kuriyama, A. Kato, H. Ishikawa, C. Iwakura, Some factors affecting the cycle lives of $LaNi_5$-based alloy electrodes of hydrogen batteries, *J Less-Common Met* 161 (1990) 193–202.
[111] A. Rodríguez Sánchez, H.-P. Klein, M. Groll, Expanded graphite as heat transfer matrix in metal hydride beds, *Int J Hydrogen Energy* 28 (2003) 515–527.
[112] W. Grochala, P.P. Edwards, Thermal Decomposition of the Non-Interstitial Hydrides for the Storage and Production of Hydrogen, *Chem Rev* 104 (2004) 1283−1315.
[113] B. Siegel, G.G. Libowitz, The covalent hydrides and hydrides of the group V and VIII transition metals, in: W.M. Mueller, J.P. Blackledge, G.G. Libowitz (Eds.) *Metal Hydrides*, Academic Press, New York, 1968.
[114] G. Sandrock, A panoramic overview of hydrogen storage alloys from a gas reaction point of view, *J Alloys Compds* 293–295 (1999) 877–888.

[115] E.H. Kisi, C.E. Buckley, E.M. Gray, The hydrogen activation of $LaNi_5$, *J Alloys Compds* 185 (1992) 369–384.
[116] T.I. Bratanich, S.M. Solonin, V.V. Skorokhod, Mechanical activation of hydrogen sorption with intermetallic compounds $LaNi_5$ and TiFe in powder systems, *Int J Hydrogen Energy* 20 (1995) 353–355.
[117] A. Pundt, R. Kircheim, Hydrogen in metals: Microstructural aspects, *Annu Rev Mater Res* 36 (2006) 555–608.
[118] E.L. Huston, G.D. Sandrock, Engineering properties of metal hydrides, *J Less-Common Met* 74 (1980) 435–443.
[119] J.J. Reilly, R.H. Wiswall, Hydrogen storage and purification systems III in: *Report BNL 21322*, Brookhaven National Laboratory, 1976.
[120] F.J. Castro, G. Meyer, Thermal desorption spectroscopy (TDS) method for hydrogen desorption characterization (I): theoretical aspects, *J Alloys Compds* 330–332 (2002) 59–63.
[121] P.S. Rudman, Hydriding and dehydriding kinetics, *J Less-Common Met*, 89 93–110.
[122] P.D. Goodell, P.S. Rudman, Hydriding and dehydriding rates of the $LaNi_5$-H system, *J Less-Common Met*, 89 (1983) 117–125.
[123] P.D. Goodell, G.D. Sandrock, E.L. Huston, Kinetic and dynamic aspects of rechargeable metal hydrides, *J Less-Common Met*, 73 (1980) 135–142.
[124] C. Read, G. Thomas, G. Ordaz, S. Satyapal, U.S. Department of Energy's System Targets for On-Board Vehicular Hydrogen Storage, *Mat Matter* 2 (2007) 3–4.
[125] J. Zhang, T.S. Fisher, P.V. Ramachandran, J.P. Gore, I. Mudawar, A Review of Heat Transfer Issues in Hydrogen Storage Technologies, *J Heat Transfer* 127 (2005) 1391–1399.
[126] L. Jörissen, Hydrogen and Fuel Cells. Fundamentals, Technologies and Applications, in: H. Detlev Stolten (Ed.) *Angew. Chem.*, Wiley-VCH, Weinheim, 2011.
[127] H.H. Van Mal, K.H.J. Buschow, A.R. Miedema, Hydrogen absorption in $LaNi_5$ and related compounds: Experimental observations and their explanation, *J Less-Common Met* 35 (1974) 65–76.
[128] D.G. Ivey, D.O. Northwood, Storing energy in metal hydrides: a review of the physical metallurgy, *J Mat Sci* 18 (1983) 321–347.
[129] S.N. Klyamkin, N.S. Zakharkina, Hysteresis and related irreversible phenomena in $CeNi_5$-based intermetallic hydrides: I. Peculiarities of the first hydrogenation, *J Alloys Compds* 361 (2003) 200–205.
[130] R. Griessen, T. Riesterer, Hydrogen in Intermetallic Compounds I in: L. Schlapbach (Ed.) *Topics in Applied Physics*, Springer-Verlag, Berlin, 1988.
[131] T. Gamo, Y. Moriwaki, N. Yanagihara, T. Yamashita, T. Iwaki, Formation and properties of titanium-manganese alloy hydrides, *Int J Hydrogen Energy* 10 (1985) 39–47.
[132] A. Andreasen, Predicting formation enthalpies of metal hydrides, in: *Risø-R-1484(EN)*, Risø National Laboratory, Roskilde, 2004.

[133] A.R. Miedema, K.H.J. Buschow, H.H. Van Mal, Which intermetallic compounds of transition metals form stable hydrides?, *J Less-Com Met* 49 (1976) 463–472.
[134] J.F. Herbst, On extending Miedema's model to predict hydrogen content in binary and ternary hydrides, *J Alloys Compds* 337 (2002) 99–107.
[135] B. Sakintuna, F. Lamari-Darkrim, M. Hirscher, Metal hydride materials for solid hydrogen storage: A review, *Int J Hydrogen Energy* 32 (2007) 1121–1140.
[136] L. Klebanoff, J. Keller, *Final Report for the DOE Metal Hydride Center of Excellence*, Sandia National Laboratories, Livermore, CA, 2012.
[137] G.J. Thomas, Reversible Hydrides for On-Board Hydrogen Storage, in: R.H. Jones, G.J. Thomas (Eds.) *Materials for the Hydrogen Economy*, CRC Press, Boca Raton, 2008.
[138] M. Felderhoff, Synthesis of Nanoscale Hydrogen StorageMaterials, in: A. Léon (Ed.) *Hydrogen Technology: Mobile and Portable Applications*, Springer, Berlin, 2008.
[139] M.U. Niemann, S.S. Srinivasan, A.R. Phani, A. Kumar, D.Y. Goswami, E.K. Stefanakos, Nanomaterials for Hydrogen Storage Applications: A Review, *J Nanomater* 2008 (2008).
[140] M.S. El-Eskandarany, *Mechanical alloying for fabrication of advanced engineering materials*, William Andrew Publishing, Norwich, 2001.
[141] C. Suryanarayana, C.C. Koch, Nanocrystalline materials – Current research and future directions, *Hyperfine Interact* 130 (2000) 5–44.
[142] J. Huot, G. Liang, S. Boily, A.V. Neste, R. Schulz, Structural study and hydrogen sorption kinetics of ball-milled magnesium hydride, *J Alloys Compds* 293–295 (1999) 495–500.
[143] T.K. Nielsen, K. Manickam, M. Hirscher, F. Besenbacher, T.R. Jensen, Confinement of MgH_2 Nanoclusters within Nanoporous Aerogel Scaffold Materials, *ACS Nano* 3 (2009) 3521–3528.
[144] H. Aoyagi, K. Aoki, T. Masumoto, Effect of ball milling on hydrogen absorption properties of FeTi, Mg_2Ni and $LaNi_5$, *J Alloys Compds* 231 (1995) 804–809.
[145] X.H. An, Y.B. Pan, Q. Luo, X. Zhang, J.Y. Zhang, Q. Li, Application of a new kinetic model for the hydriding kinetics of $LaNi_{5-x}Al_x$, *J Alloys Compds* 506 (2010) 63–69.
[146] A. Gasiorowski, W. Iwasieczko, D. Skoryna, H. Drulis, M. Jurczyk, Hydriding properties of nanocrystalline $Mg_{2-x}M_xNi$ alloys synthesized by mechanical alloying (M = Mn, Al), *J Alloys Compds* 364 (2004) 283–288.
[147] M.H. Mendelsohn, D.M. Gruen, A.E. Dwight, The effect of aluminum additions on the structural and hydrogen absorption properties of AB_5 alloys with particular reference to the $LaNi_{5-x}Al_x$ ternary alloy system, *J Less-Common Met* 63 (1979) 193–207.

[148] H. Yukawa, T. Matsumura, M. Morinaga, Chemical bond state and hydride stability of hydrogen storage alloys, *J Alloys Compds* 293–295 (1999) 227–230.

[149] G. Liang, J. Huot, R. Schulz, Hydrogen storage properties of the mechanically alloyed $LaNi_5$-based materials, *J Alloys Compds* 320 (2001) 133–139.

[150] A. Percheron-Guégan, C. Lartigue, J.C. Achard, P. Germi, F. Tasset, Neutron and X-ray diffraction profile analyses and structure of $LaNi_5$, $LaNi_{5-x}Al_x$ and $LaNi_{5-x}Mn_x$ intermetallics and their hydrides (deuterides), *J Less-Common Met* 74 (1980) 1–12.

[151] K. Nishimura, K. Sato, Y. Nakamura, C. Inazumi, K. Oguro, I. Uehara, S. Fujitani, I. Yonezu, Stability of $LaNi_{5-x}$ Al_x alloys (x = 0-0.5) during hydriding and dehydriding cycling in hydrogen containing O_2 and H_2O, *J Alloys Compds* 268 (1998) 207–210.

[152] C. Bossi, A. Del Corno, M. Scagliotti, C. Valli, Characterisation of a 3kW PEFC power system coupled with a metal hydride H_2 storage, *J Power Sources* 171 (2007) 122–129.

[153] E.C.E. Rönnebro, Technology and Manufacturing Readiness of Early Market Motive and Non-Motive Hydrogen Storage Technologies for Fuel Cell Applications, in: *Report for the U.S. Department of Energy*, Pacific Northwest National Laboratory, Washington, 2012.

[154] F.E. Lynch, Metal hydride practical applications, *J Less-Common Met* 172–4 (1991) 943–958.

[155] J.A. Murshidi, M. Paskevicius, D.A. Sheppard, C.E. Buckley, Structure, morphology and hydrogen storage properties of a $Ti_{0.97}Zr_{0.019}V_{0.439}Fe_{0.097}Cr_{0.045}Al_{0.026}Mn_{1.5}$ alloy, *Int J Hydrogen Energy* 36 (2011) 7587–7593.

[156] J.J. Murray, M.L. Post, J.B. Taylor, The thermodynamics of the system $CaNi_5$-H_2 using differential heat conduction calorimetry, *J Less-Common Met* 90 (1983) 65–73.

[157] L.D. Calvert, J.J. Murray, G.J. Gainsford, J.B. Taylor, Crystal structure of $CaNi_5H$ using x-ray diffraction with in situ hydriding, *Mater Res Bull* 19 (1984) 107–113.

[158] Y.K. Cho, R. Yamamoto, M. Doyama, The phase transfomations of $CaNi_5$ in a hydrogen atmosphere, *J Less-Common Met* 88 (1982) 125–131.

[159] Calcium metal powder, c2013, http://www.alibaba.com/ (accessed September 16, 2013).

[160] Metal-Pages, Metal Prices-Lanthanum, c2013, http://www.metal-pages.com/ (accessed September 16, 2013).

[161] InfoMine Inc., 6 Month Nickel Prices and Price Charts, c2013, http://www.infomine.com/, (accessed September 16, 2013).

[162] W.M. Morrison, R. Tang, *China's rare earth industry and export regime: economic and trade implications for the United States*, Congressional Research Service, 2012.

[163] S. Chumphongphan, M. Paskevicius, D.A. Sheppard, C.E. Buckley, Cycle life and hydrogen storage properties of mechanical alloyed $Ca_{1-x}Zr_xNi_{5-y}Cr_y$; (x = 0, 0.05 and y = 0, 0.1), *Int J Hydrogen Energy* 37 (2012) 7586–7593.
[164] M.S. Bawa, E.A. Ziem, Long-term testing and stability of $CaNi_5$ alloy for a hydrogen storage application, *Int J Hydrogen Energy* 7 (1982) 775–781.
[165] H. Oesterreicher, K. Ensslen, A. Kerlin, E. Bucher, Hydriding behavior in Ca-Mg-Ni-B, *Mater Res Bull* 15 (1980) 275–283.
[166] M.P. Sridhar Kumar, B. Viswanathan, C.S. Swamy, V. Srinivasan, High temperature interaction of hydrogen with intermetallic compound $CaNi_5$, *Mater Chem Phys* 20 (1988) 245–253.
[167] J.O. Jensen, N.J. Bjerrum, Systematic B-metal substitution in $CaNi_5$, *J Alloys Compds*, 293-5 (1999) 185–189.
[168] Z.P. Li, S. Suda, Effects of hydriding-dehydriding cycling on P-C-T and electrochemical properties of La-Ca-Ni-Al alloys, *J Alloys Compds* 231 (1995) 594–597.
[169] Z.P. Li, S. Suda, Electrochemical durability of Ca-based alloys, *Electrochem Acta* 40 (1995) 467–471.
[170] M.T. Yeh, V.M. Beibutian, S.E. Hsu, Effect of Mo additive on hydrogen absorption of rare- earth based hydrogen storage alloy, *J Alloys Compds* 293–295 (1999) 721–723.
[171] R.C. Bowman Jr, C.H. Luo, C.C. Ahn, C.K. Witham, B. Fultz, The effect of tin on the degradation of $LaNi_{5-y}Sn_y$ metal hydrides during thermal cycling, *J Alloys Compds* 217 (1995) 185–192.
[172] C. Iwakura, T. Oura, H. Inoue, M. Matsuoka, Effects of substitution with foreign metals on the crystallographic, thermodynamic and electrochemical properties of AB_5-type hydrogen storage alloys, *Electrochim Acta* 41 (1996) 117–121.
[173] T.Z. Si, G.P. Zhao, Q.A. Zhang, Phase structures and electrochemical properties of $Ca_{0.4}Mg_{0.6}(Ni_{0.9}Al_{0.05}M_{0.05})_2$ (M = Cu, Mn, Cr or Co) alloys, *Int J Hydrogen Energy* 32 (2007) 600–605.
[174] X.L. Wang, Y.H. Zhang, D.L. Zhaoa, X.P. Donga, S.H. Guoa, G.Q. Wang, Effects of Cr addition on the microstructures and electrochemical performances of La-Mg-Ni system ($PuNi_3$-type) hydrogen storage alloy, *J Alloys Compds* 446–7 (2007) 625–629.
[175] Z.P. Li, S. Suda, The annealing effect on the durabilities of La-substituted $CaNi_5$-type alloys, *J Alloys Compds* 231 (1995) 835–840.
[176] M. Anik, G. Ozdemir, N. Kucukdeveci, B. Baksan, Effect of Al, B,Ti and Zr additive elements on the electrochemical hydrogen storage performance of MgNi alloy, *Int J Hydrogen Energy* 36 (2011) 1568–1577.
[177] H. Yukawa, Y. Takahashi, M. Morinaga, Alloying effects on the electronic structures of $LaNi_5$ containing hydrogen atoms, *Intermetallics* 4 (1996) S215–224.
[178] L.M. Vrana, Calcium and Calcium Alloys, in: *Kirk-Othmer Encyclopedia of Chemical Technology*, John Wiley & Sons, 2011, pp. 1–10.

[179] K.H.J. Buschow, Calcium-nickel intermetallic compounds, *J Less-Common Met* 38 (1974) 95–98.
[180] A.A. Melas, Process for transition metal nitrides thin film deposition, in: IFI CLAIMS Patent Services, European Patent Office, 1986.
[181] K. Yasuda, Effects of the materials processing on the hydrogen absorption properties of $MmNi_5$ type alloys, *J Alloys Compds* 253–254 (1997) 621–625.
[182] Y. Xiong, J. Ba, W. Qing, W. Jing, Hydrogen Storage Properties of Nanocrystalline Mg_2Ni Based Alloys Prepared by Ball-Milling, *J Plasma Fusion Res* 10 (2013) 94–97.
[183] M. Notin, D. Belbacha, M. Rahmane, J. Hertz, G. Saindrenan, J.L. Jorda, Experimental diagram and numerical optimization of the calcium-nickel system, *J Less-Common Met* 162 (1990) 221–229.
[184] S. Chumphongphan, M. Paskevicius, D.A. Sheppard, C.E. Buckley, Effect of Al and Mo substitution on the structural and hydrogen storage properties of $CaNi_5$, *Int J Hydrogen Energy* 38 (2013) 2325–2331.
[185] S.-i. Towata, T. Noritake, A. Itoh, M. Aoki, K. Miwa, Cycle durability of Ti–Cr–V alloys partially substituted by Nb or Fe, *J Alloys Compds* 580 (2013) S226–S228.
[186] S.S. Batsanov, A.S. Batsanov, *Introduction to Structural Chemistry*, Springer, NewYork, 2012.
[187] E. Msika, M. Latroche, F. Cuevas, A. Percheron-Gue´gan, Zr-substitution in $LaNi_5$-type hydride compound by room temperature ball milling, Mater Sci Eng B, 108 (2004) 91–95.
[188] X.B. Yu, Z.X. Yang, S.L. Feng, Z. Wu, N.X. Xu, Influence of Fe addition on hydrogen storage characteristics of Ti–V-based alloy, *Int J Hydrogen Energy* 31 (2006) 1176–1181.
[189] J. Lamloumi, A. Percheron-Gue´gan, C. Lartigue, J.C. Achard, G. Jehanno, Thermodynamic, structural and magnetic properties of $LaNi_{5-x}Fe_x$ hydrides, J *Less-Common Met* 130 (1987) 111–122.
[190] S. Yang, S. Han, J. Song, Y. Li, Influences of molybdenum substitution for cobalt on the phase structure and electrochemical kinetic properties of AB_5-type hydrogen storage alloys, *J Rare Earths* 29 (2011) 692–697.
[191] A.J. Maeland, Hydrides for Hydrogen Storage, in: P. Maurizio, P. Rinaldo (Eds.) *Recent Advances in Hydride Chemistry*, Elsevier, Amsterdam, 2001, pp. 544.
[192] E.A. Kumar, M.P. Maiya, S.S. Murthy, B. Viswanathan, Structural, hydrogen storage and thermodynamic properties of some mischmetal-nickel alloys with partial substitutions for nickel, *J Alloys Compds* 476 (2009) 92–97.
[193] T.Z. Si, G. Pang, Q.A. Zhang, D.M. Liu, N. Liu, Solid solubility of Mg in Ca_2Ni_7 and hydrogen storage properties of $(Ca_{2-x}Mg_x)Ni_7$ alloys, *Int J Hydrogen Energy* 34 (2009) 4833–4837.
[194] J. Murray, H. Miller, P. Bird, A.J. Goudy, The effect of particle size and surface composition on the reaction rates of some hydrogen storage alloys, *J Alloys Compnds* 231 (1995) 841–845.

[195] S. Vivet, J.M. Jouberta, B. Knospa, A. Percheron-Gue´gan, Effects of cobalt replacement by nickel, manganese, aluminium and iron on the crystallographic and electrochemical properties of AB_5 -type alloys, *J Alloys Compds* 356–357 (2003) 779–783.

[196] J.I. Han, J.Y. Lee, Influence of oxygen impurity on the hydrogenation properties of $LaNi_5$, $LaNi_{4.7}Al_{0.3}$ and $MmNi_{4.5}Al_{0.5}$ during long-term pressure-induced hydridingedehydriding cycling., *J Less-Common Met* 152 (1989) 329–338.

[197] X.-z. Sun, H.-g. Pan, M.-x. Gao, R. Li, Y. Lin, S. Ma, Cycling stability of La-Mg-Ni-Co type hydride electrode with Al, *Trans Nonferrous Met Soc China* 16 (2006) s834–s838.

[198] M.P. Pitt, H.W. Brinks, J.O. Jensen, B.C. Hauback, An in-situ neutron diffraction study of the ageing of $CaNi_5D_x$ at 80 ^oC and 9 bar, *J Alloys Compds* 372 (2004) 190–196.

[199] S.i. Orimo, Y. Nakamori, J.R. Eliseo, A. Zuttel, C.M. Jensen, Complex Hydrides for Hydrogen Storage, *Chem Rev* 107 (2007) 4111–4132.

[200] B.C. Hauback, Structures of aluminium-based light weight hydrides, *Zeitschrift für Kristallographie - Crystal Mater* 223 (2008) 636–648.

[201] A. Züttel, S. Rentsch, P. Fischer, P. Wenger, P. Sudan, P. Mauron, C. Emmenegger, Hydrogen storage properties of $LiBH_4$, *J Alloys Compds* 356–357 (2003) 515–520.

[202] J. Gao, P. Adelhelm, M.H.W. Verkuijlen, C. Rongeat, M. Herrich, P.J.M. van Bentum, O. Gutfleisch, A.P.M. Kentgens, K.P. de Jong, P.E. de Jongh, Confinement of $NaAlH_4$ in Nanoporous Carbon: Impact on H_2 Release, Reversibility, and Thermodynamics, *J Phys Chem C* 114 (2010) 4675–4682.

[203] J.M. Bellosta von Colbe, M. Felderhoff, B. Bogdanovic, F. Schuth, C. Weidenthaler, One-step direct synthesis of a Ti-doped sodium alanate hydrogen storage material, *Chem Comm* (2005) 4732–4734.

[204] M.P. Pitt, P.E. Vullum, M.H. Sørby, H. Emerich, M. Paskevicius, C.E. Buckley, J.C. Walmsley, R. Holmestad, B.C. Hauback, Hydrogen Absorption Kinetics of the Transition-Metal-Chloride-Enhanced $NaAlH_4$ System, *J Phys Chem C* 116 (2012) 14205–14217.

[205] M.P. Pitt, P.E. Vullum, M.H. Sørby, H. Emerich, M. Paskevicius, C.E. Buckley, E.M. Gray, J.C. Walmsley, R. Holmestad, B.C. Hauback, A structural review of nanoscopic $Al_{1-x}TM_x$ phase formation in the $TMCl_n$ enhanced $NaAlH_4$ system, *J Alloys Compds* 527 (2012) 16–24.

[206] M.P. Pitt, M. Paskevicius, C.J. Webb, M.H. Sørby, S. Delleda, T.R. Jensen, B.C. Hauback, C.E. Buckley, E.M. Gray, Nanoscopic $Al_{1-x}Ce_x$ phases in the $NaH + Al + 0.02CeCl_3$ system, *Int J Hydrogen Energy* 36 (2011) 8403–8411.

[207] M.P. Pitt, P.E. Vullum, M.H. Sørby, H. Emerich, M. Paskevicius, C.J. Webb, E.M. Gray, C.E. Buckley, J.C. Walmsley, R. Holmestad, B.C. Hauback, Hydrogen absorption kinetics and structural features of $NaAlH_4$ enhanced with transition-metal and Ti-based nanoparticles, *Int J Hydrogen Energy* 37 (2012) 15175–15186.

[208] A.M. Seayad, D.M. Antonelli, Recent advances in hydrogen storage in metal-containing inorganic nanostructures and related materials, *Adv Mater* 16 (2004) 765–777.
[209] T. Vegge, Equilibrium structure and Ti-catalyzed H_2 desorption in $NaAlH_4$ nanoparticles from density functional theory, *Phys Chem Chem Phys* 8 (2006) 4853–4861.
[210] J. Huot, D.B. Ravnsbæk, J. Zhang, F. Cuevas, M. Latroche, T.R. Jensen, Mechanochemical synthesis of hydrogen storage materials, *Prog Mater Sci* 58 (2013) 30–75.
[211] R. Xiong, G. Sang, X. Yan, G. Zhang, X. Ye, C. Jiang, L. Luo, Improvement of the hydrogen storage kinetics of $NaAlH_4$ with nanocrystalline titanium dioxide loaded carbon spheres (Ti-CSs) by melt infiltration, *Int J Hydrogen Energy* 37 (2012) 10222–10228.
[212] T.K. Nielsen, F. Besenbacher, T.R. Jensen, Nanoconfined hydrides for energy storage, *Nanoscale* 3 (2011) 2086–2098.
[213] J.J. Vajo, Influence of nano-confinement on the thermodynamics and dehydrogenation kinetics of metal hydrides, *Curr Opin Solid State Mater Sci* 15 (2011) 52–61.
[214] M. Fichtner, Properties of nanoscale metal hydrides, *Nanotech* 20 (2009) 204009.
[215] P.E. de Jongh, P. Adelhelm, Nanosizing and Nanoconfinement: New Strategies Towards Meeting Hydrogen Storage Goals, *ChemSusChem* 3 (2010) 1332–1348.
[216] M.P. Pitt, M. Paskevicius, C.J. Webb, D.A. Sheppard, C.E. Buckley, E.M. Gray, The synthesis of nanoscopic Ti based alloys and their effects on the MgH2 system compared with the MgH_2 + $0.01Nb_2O_5$ benchmark, *Int J Hydrogen Energy* 37 (2012) 4227–4237.
[217] M. Paskevicius, D.A. Sheppard, C.E. Buckley, Thermodynamic Changes in Mechanochemically Synthesized Magnesium Hydride Nanoparticles, *J Am Chem Soc* 132 (2010) 5077–5083.
[218] M. Paskevicius, H.Y. Tian, D.A. Sheppard, C.J. Webb, M.P. Pitt, E.M. Gray, N.M. Kirby, C.E. Buckley, Magnesium Hydride Formation within Carbon Aerogel, *J Phys Chem C* 115 (2011) 1757–1766.
[219] T.K. Nielsen, P. Javadian, M. Polanski, F. Besenbacher, J. Bystrzycki, T.R. Jensen, Nanoconfined $NaAlH_4$: Determination of Distinct Prolific Effects from Pore Size, Crystallite Size, and Surface Interactions, *J Phys Chem C* 116 (2012) 21046−21051.
[220] M. Fichtner, Nanoconfinement effects in energy storage materials, *Phys Chem Chem Phys* 13 (2011) 21186–21195.
[221] T.K. Nielsen, M. Polanski, D. Zasada, P. Javadian, F. Besenbacher, J. Bystrzycki, J. Skibsted, T.R. Jensen, Improved Hydrogen Storage Kinetics of Nanoconfined $NaAlH_4$ Catalyzed with $TiCl_3$ Nanoparticles, *ACS Nano* 5 (2011) 4056–4064.

[222] B.D. Zdravkov, J.J. Cermak, M. Sefara, J. Janku, Pore classification in the characterization of porous materials: A perspective, *Cent Euro J Chem* 5 (2007) 385–395.
[223] G.S. Armatas, M.G. Kanatzidis, Mesostructured germanium with cubic pore symmetry, *Nature* 441 (2006) 1122–1125.
[224] R. Ryoo, S.H. Joo, S. Jun, Synthesis of Highly Ordered Carbon Molecular Sieves via Template-Mediated Structural Transformation, *J Phys Chem B* 103 (1999) 7743–7746.
[225] K. Xia, Q. Gao, S. Song, C. Wu, J. Jiang, J. Hu, L. Gao, CO_2 activation of ordered porous carbon CMK-1 for hydrogen storage, *Int J Hydrogen Energy* 33 (2008) 116–123.
[226] S. Shang, X. Yang, X.-m. Tao, Easy synthesis of carbon nanotubes with polypyrrole nanotubes as the carbon precursor, *Polymer* 50 (2009) 2815–2818.
[227] H. Huwe, M. Froba, Iron (III) oxide nanoparticles within the pore system of mesoporous carbon CMK-1: intra-pore synthesis and characterization, *Micro Meso Mater* 60 (2003) 151–158.
[228] S. Chumphongphan, U. Filsø, M. Paskevicius, D.A. Sheppard, T.R. Jensen, C.E. Buckley, Nanoconfinement degradation in $NaAlH_4$/CMK-1, I*nt J Hydrogen Energy* 39 (2014) 11103–11109.
[229] X. Liu, D. Peaslee, C.Z. Jost, E.H. Majzoub, Controlling the Decomposition Pathway of $LiBH_4$ via Confinement in Highly Ordered Nanoporous Carbon, *J Phys Chem C* 114 (2010) 14036–14041.
[230] Y. Li, G. Zhou, F. Fang, X. Yu, Q. Zhang, L. Ouyang, M. Zhu, D. Sun, De-/re-hydrogenation features of $NaAlH_4$ confined exclusively in nanopores, *Acta Mater* 52 (2011) 1829–1838.
[231] Xiaoping Dong, Weihua Shen, Jinlou Gu, Liangmin Xiong, Yufang Zhu, Hua Li, J. Shi, A structure of MnO_2 embedded in CMK-3 framework developed by a redox method, *Micro Meso Mater* 91 (2006) 120–127.
[232] A.G. Haiduc, H.A. Stil, M.A. Schwarz, P. Paulus, J.J.C. Geerlings, On the fate of the Ti catalyst during hydrogen cycling of sodium alanate, *J Alloys Compds* 393 (2005) 252–263.
[233] C.P. Balde, H.A. Stil, A.M.J.v.d. Eerden, K.P.d. Jong, J.H. Bitter, Active Ti Species in $TiCl_3$-Doped $NaAlH_4$. Mechanism for Catalyst Deactivation, *J Phys Chem C* 111 (2007) 2797–2802.
[234] M.P. Pitt, P.E. Vullum, M.H. Sørby, D. Blanchard, M. Sulic, H. Emerich, M. Paskevicius, C.E. Buckley, J. Walmsley, R. Holmestad, B.C. Hauback, The location of Ti containing phases after the completion of the $NaAlH_4 + x TiCl_3$ milling process, *J Alloys Compds* 513 (2012) 597–605.
[235] C.P. Balde, A.M.J.v.d. Eerden, H.A. Stil, F.M.F.d. Groot, K.P.d. Jong, J.H. Bitter, On the local structure of Ti during in situ desorption of Ti(OBu) and $TiCl_3$ doped $NaAlH_4$, *J Alloys Compds* 446–447 (2007) 232–236.
[236] L.H. Rude, T.K. Nielsen, D.B. Ravnsbæk, U. Bosenberg, M.B. Ley, B. Richter, L.M. Arnbjerg, M. Dornheim, Y. Filinchuk, F. Besenbacher, T.R.

Jensen, Tailoring properties of borohydrides for hydrogen storage: A review, *Phys Status Solidi* 208 (2011) 1754–1773.

[237] R.D. Stephens, A.F. Gross, S.L. Van Atta, J.J. Vajo, F.E. Pinkerton, The kinetic enhancement of hydrogen cycling in $NaAlH_4$ by melt infusion into nanoporous carbon aerogel, *Nanotech* 20 (2009) 204018

[238] E.H. Majzoub, J.L. Herberg, R. Stumpf, S. Spangler, R.S. Maxwell, XRD and NMR investigation of Ti-compound formation in solution-doping of sodium aluminum hydrides: solubility of Ti in $NaAlH_4$ crystals grown in THF, *J Alloys Compds* 394 (2005) 265–270.

[239] P. Ngene, R. van den Berg, M.H.W. Verkuijlen, K.P. de Jong, P.E. de Jongh, *Energy Envir Sci* 4 (2011) 4108–4115.

[240] C. Li, P. Peng, D.W. Zhou, L. Wan, Research progress in $LiBH_4$ for hydrogen storage: A review, *Int J Hydrogen Energy* 36 (2011) 14512–14526.

[241] M. Paskevicius, M.P. Pitt, C.J. Webb, D.A. Sheppard, U. Filsø, E.M. Gray, C.E. Buckley, In-Situ X-ray Diffraction Study of γ-$Mg(BH_4)_2$ Decomposition, *J Phys Chem C* 116 (2012) 15231–15240.

[242] P.A. Berseth, A.D. Harter, R. Zidan, A. Blomqvist, C.M. Araujo, R.H. Scheicher, R. Ahuja, P. Jena, Carbon Nanomaterials as Catalysts for Hydrogen Uptake and Release in $NaAlH_4$, *Nano Lett* (2009) 1501–1505.

[243] X. Xiao, L. Chen, X. Wang, S. Li, C. Chen, Q. Wang, Reversible hydrogen storage properties and favorable co-doping mechanism of the metallic Ti and Zr co-doped sodium aluminum hydride, *Int J Hydrogen Energy* 33 (2008) 64 –73.

APPENDIX: PEER REVIEWED PUBLICATIONS

The following peer reviewed publications are based on the work reported in this thesis. In all publications, I was the first author, i.e., I contributed the majority of the work on the papers such as sample synthesis, XRD, PCI, SEM, EDS, SAXS, and TPD measurements. Mark Paskevicius, Drew Sheppard and Craig Buckley assisted on data analysis, e.g. Rietveld refinement, XRD and SAXS data analysis. Mark Paskevicius also helped to collect and analyzed the TEM data. The carbon scaffold, CMK-1, was prepared with help from Uffe Filsø and Mark Paskevicius. Torben R. Jensen supported on data analysis of infiltrated-CMK-1system.

INTERNATIONAL JOURNAL OF HYDROGEN ENERGY 37 (2012) 7586–7593

Available online at www.sciencedirect.com

SciVerse ScienceDirect

journal homepage: www.elsevier.com/locate/he

Cycle life and hydrogen storage properties of mechanical alloyed $Ca_{1-x}Zr_xNi_{5-y}Cr_y$; ($x = 0$, 0.05 and $y = 0$, 0.1)

*Somwan Chumphongphan, Mark Paskevicius, Drew A. Sheppard, Craig E. Buckley**

Department of Imaging and Applied Physics, Fuels and Energy Technology Institute, Curtin University, GPO Box U 1987, Perth 6845, Australia

ARTICLE INFO

Article history:
Received 3 November 2011
Received in revised form
13 January 2012
Accepted 26 January 2012
Available online 25 February 2012

Keywords:
Hydrogen storage
Thermodynamics
Alloys
Cycling

ABSTRACT

$CaNi_5$–based alloys have been synthesized by mechanical alloying followed by isothermal annealing. The formation of the $CaNi_5$ structure occurred when the milled powders were heated at 800 °C under vacuum for 3 h. The abundance of $CaNi_5$ phase in the alloys ranges from 60 to 70 wt.%. Replacement of Zr into the Ca site reduces the unit cell volume of $CaNi_5$ whilst replacement of Cr into the Ni site slightly increases the unit cell volume. The hydrogen storage capacity of all substituted alloys is decreased and the hydrogen sorption plateau regions are narrowed compared to those of pure $CaNi_5$. Substitution of Zr into the Ca site extinguishes the flat plateau region unlike replacement of Cr into the Ni site where a flat plateau is maintained. The reaction enthalpy ΔH for both absorption and desorption are directly proportional to the unit cell volume of the alloys. The hydrogen storage capacity of all alloys rapidly decays for the first 50 cycles at 85 °C followed by a more gradual decline after 50 further cycles. The hydrogen storage capacity of the alloys after 200 cycles is in the range of 65–75% of the initial capacity.

1. Introduction

Although AB_5-type alloys cannot meet gravimetric hydrogen storage capacity targets for automotive application, they possess excellent properties for use as an energy carrier in the form of hydrogen for both stationary and distributed energy generation applications [1]. The AB_5-type alloys are also considered as one of the most suitable hydrogen storage materials for use in solar-hydrogen power generation systems, which are candidates for remote-area power supply (RAPS) applications [2]. These systems can operate as residential and/or industrial power supplies located in regions far from grid energy networks. As a prototype, it was shown that AB_5-type alloys have potential as the hydrogen storage material for a 3 kW polymer electrolyte membrane (PEM) fuel cell operating around 60–70 °C, which also successfully connected to the electrical grid network [3]. Commercial metal hydride storage systems have been successfully developed by several companies such as Ergenics, Inc., Wyckoff, NJ, U.S.A., Hydrogen Consultants, Inc. (HCI), Littleton CO, U.S.A., Hydrid-Wasserstofftechnik (HWT), Mulheim/Ruhr, F.R.G., and Japan Metals and Chemicals Co. Ltd., Tokyo, Japan [4].

$CaNi_5$, an AB_5-type alloy, has potential as a moderate-cost hydrogen storage material in many applications in comparison to other low hydrogen-to-metal atom ratio [H]/[M] materials that operate near room temperature, such as mischmetal (Mm) – or La-based alloys [5,6]. The current stock market price for Ca, La, battery-grade Mm and Ni in January 2012 is approximately 6, 25, 62 and 19 US$ per kg, respectively

* *Corresponding author*. Tel.: +61 8 92663532; fax: +61 8 92662377.
E-mail address: C.Buckley@curtin.edu.au (C.E. Buckley).
0360-3199/$ – see front matter
doi:10.1016/j.ijhydene.2012.01.131

[7,8]. Assuming the usable capacity of $LaNi_5$ and $CaNi_5$ is 1.4 and 1.05 wt.% of hydrogen, respectively, it means that to store 1 kg of hydrogen would cost around US$ 1500 for $LaNi_5$ and US$ 1600 for $CaNi_5$. Thus, it is expected that the cost of storing hydrogen in $CaNi_5$ is equivalent to $LaNi_5$. However, it should be noted that the world's major supplier of rare earth metals, China, imposes a 25% tariff on exports, a value that is not included in the stock market price. The market price for Freight On Board (FOB) rare earth metals, the full price including packaging and shipping, is typically 2–4 times higher than the stock market price. The wide range of high-tech applications for rare earth metals and the limited number high-concentration rare earth ore bodies suggests ongoing pressure for the cost of rare earth metals such as lanthanum and mischmetal. Wide scale deployment of lanthanum or mischmetal based hydrogen storage systems would further add to this price pressure. As such, $CaNi_5$ presents a potentially cheaper option for long-term, wide scale deployment as a hydrogen storage material.

$CaNi_5$ possesses favorable properties for practical applications with a low plateau pressure and fast kinetics at near ambient temperature [9] similar to other interstitial hydride alloys. Unfortunately, $CaNi_5$ has poor cyclic durability which is caused by the disproportionation of Ca from the alloy [10–12]. For instance, the hydrogen storage capacity of $CaNi_5$ decreased to less than 50% of the initial capacity in one study after absorption/desorption for 200 cycles at 85 °C [13]. However, the cyclic capacity degradation is not as severe at lower temperatures, where a capacity of 78% was maintained after 5000 cycles at 50 °C [5].

In the past decade much research has been undertaken to improve the hydrogen storage properties of $CaNi_5$ by partial substitution of rare earth or transition metals at Ca and Ni sites as shown in Fig. 1. Replacement of Ca by Ce and Ni by Zn changed the unit cell volume and consequently the plateau pressure and the thermodynamics properties were altered [14]. The hydrogen storage capacity of these substituted alloys was decreased and the plateau region was narrowed. It was concluded that the hydrogen storage capacity could be improved when the host metals of AB_5 alloys were replaced by larger metal atoms [15]. Another study showed that adding a small amount of Mg into $CaNi_5$ destroyed the AB_5 structure and formed AB_3 and Ni phases [6]. Although Sn and Al can improve the stability of $LaNi_5$- and $MmNi_5$-based alloys, they are not effective for $CaNi_5$-based alloys [13,16,17]. Furthermore, an attempt to replace Ni by Sn did not result in the $CaNi_5$ phase when subjected to mechanical alloying followed by annealing [14]. In other research, the cycling stability of Ca–Mg–Ni and La–Mg–Ni alloys as battery electrodes could be significantly improved by the substitution of Cr [18,19] but it led to a decrease in the discharge capacity.

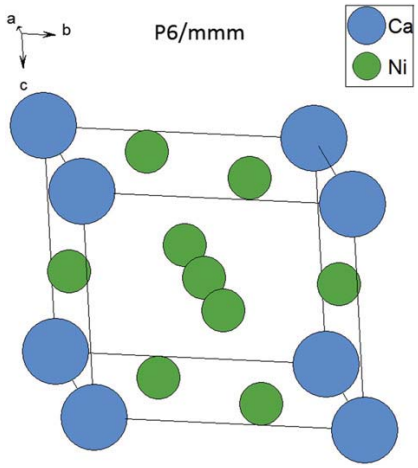

Fig. 1 – Schematic illustration of the $CaNi_5$ structure.

It was suggested that substitution for Ca in $CaNi_5$ is the likely option to improve cyclic stability [20]. Accordingly, substitution of the Ca site by rare earth or alkaline earth elements such as La and Ce can dramatically improve the cycle life of $CaNi_5$ based alloys during electrochemical charging and discharging [21]. In addition, La-substituted $CaNi_5$-type alloys annealed at a higher temperature and for a longer time show better electrochemical durability [22]. The incorporation of Zr in the Mg–Ni system causes a considerable increase in the stability of the alloy [23]. Furthermore, it was also reported that Zr formed a high strength metallic bond with Ni as found in substituted $LaNi_5$ [24]. Consequently, partial substitution of Zr at the Ca site may enhance the stability of the $CaNi_5$ alloy.

In this work, we synthesize and attempt to improve the hydrogen cycle life of $CaNi_5$ based alloys by substitution of Zr and Cr at the Ca and Ni sites, respectively. All alloys were synthesized by a mechanical alloying method followed by an annealing treatment. The effect of metal substitution at both the Ca and Ni sites were investigated by X-ray diffraction, PCIs (pressure-composition isotherms) and cycle life measurements of the alloys.

2. Experimental method

$CaNi_5$ alloys were synthesized by firstly mechanical milling elemental metals in a 316-stainless steel (SS) canister (650 cm^3 internal volume) attached to a Glen Mills Turbula T2C shaker mixer. Ca (1–2 mm, 99%), Ni, (<150 μm, 99.99%) and Cr (−325 mesh, 99+%) from Sigma–Aldrich, and Zr powder (Zr ≥ 97%, Hf ≤ 3%) from Riedel-de Haen were prepared for the desired composition under an argon atmosphere inside a glovebox (<1 ppm H_2O, <5 ppm O_2). Mechanical milling was performed at room temperature for 40 h with a ball to powder mass ratio of 12:1 using 12.7 mm and 7.938 mm 316 SS balls and 2 ml of hexane was added as a process control agent (PCA). The milled powders were then annealed for 3 h at 800 °C under vacuum better than 10^{-3} Torr (1.33×10^{-3} mbar).

X-ray diffraction (XRD) was performed using a Bruker D8 Advance diffractometer (CuK_α radiation) equipped with a LynxEye 3° linear position sensitive detector (192 pixels) with a 2θ range of 10–100° using 0.02° steps with 0.7 s of count time per step with operating conditions of 40 kV and 40 mA. The XRD samples were loaded into an XRD sample holder in an argon glovebox and sealed with a poly(methylmethacrylate) (PMMA) air-tight bubble to prevent oxygen/moisture contamination during data collection. Rietveld analysis in Topas (Bruker AXS) was used to calculate lattice parameters

and phase composition. Ultra-high purity hydrogen gas (BOC, 99.999%) was used for hydrogen sorption measurements. Pressure-Composition-Temperature data was collected using a custom-built Sieverts apparatus (details can be found elsewhere [25]). Typically a 0.5 g sample was contained within an 8 cm^3 sample volume where hydrogen was released to/from a 16 cm^3 reference volume equipped with a Rosemount 3051S_T Ultra pressure transducer (0.02% full scale accuracy). Kinetic sorption data was collected on a PCTPro-E&E (Hy-Energy) gas sorption analyzer isothermally from samples of ~0.5 g. Absorption was performed from a 12 cm^3 reference volume to a 10 cm^3 sample volume and desorption was performed into a large 165 cm^3 reference volume (to maintain isobaric conditions). The sample volume is comprised of ~1.2 kg of stainless steel with an internal diameter of 8 mm and a sheathed N-type thermocouple welded into the bottom end of the sample volume. The samples were placed within a filter-capped sample vial that sits within the sample volume. The sample is separated from the thermocouple by ~4 mm of stainless steel (2 mm from the thermocouple sheath and 2 mm from the sample vial). Cycle life was measured continuously with the rate of 3 cycles h^{-1} by a PCTPro-E&E at 85 °C up to 200 cycles for all alloys except pure $CaNi_5$, which was tested up to 350 cycles.

3. Results and discussion

3.1. Mechanical Alloying

Fig. 2 shows the XRD pattern of the powder obtained from mechanically milling Ca granules (12.015 wt.%) and Ni powder (87.985 wt.%) in the correct ratio to form a pure $CaNi_5$ alloy. The strong diffraction peaks for Ni are present, but the peaks from Ca are not observed due to its low weight fraction and small crystallite size. The $CaNi_5$ phase does not form directly at this stage, but the formation of a partially amorphous phase has probably taken place along with a nanocrystalline Ni phase [6]. However, different milling parameters including impact energy and milling time can possibly lead to the direct formation of the $CaNi_5$ phase as found in some substituted alloys [14].

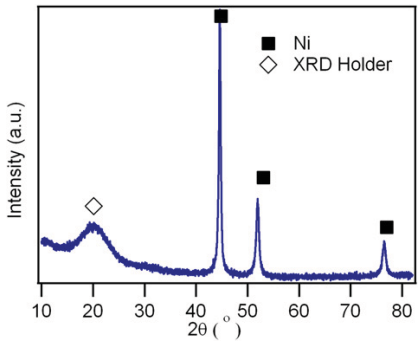

Fig. 2 – XRD pattern of the powder obtained from mechanical milling of Ca (12.015 wt.%) and Ni (87.985 wt.%) for 40 h.

After annealing at 800 °C for 3 h, the $CaNi_5$ phase ($CaCu_5$-type structure, P6/mmm) has been formed for all alloys as shown in Fig. 3. The abundance of the as-synthesized $CaNi_5$ phase in the alloys was calculated by the Rietveld method and varies in each composition ranging from 60 to 70 wt. % with the remaining proportion being predominantly Ni. This excess is likely present due to the annealing conditions [6] as the high vapor pressure of Ca can lead to its evaporation under high temperature annealing conditions. However we did not observe any large Ca deposits after annealing was complete. Moreover, calcium is a ductile metal which adheres easily to the surface of the milling canister and balls, causing losses of Ca metal during mechanical milling. At low hydrogen pressure Ni is inert to hydrogen gas, but the formation of nickel hydride can be observed under hydrogen pressures of 3000 bar [26]. The $ZrNi_5$ phase also presents in Zr-substituted alloys but it is difficult to accurately quantify because of its low abundance and the overlap of the strongest diffraction peak with Ni. A small hydrogen absorption of $ZrNi_5$, $H/M < 0.2$, was reported under approximately 100 bar of hydrogen pressure at 25 °C [27]. Therefore, it could be assumed that both the Ni and $ZrNi_5$ phases do not influence the hydrogen absorption/desorption process for this work. However, this will lower the wt.% of hydrogen content if the calculation is based on the total weight of the entire sample. The calculation of hydrogen sorption in the $CaNi_5$ phase has been corrected herein by using the weight fraction of the $CaNi_5$ phase from Rietveld analysis.

As shown in Table 1, the calculated lattice parameters of $CaNi_5$, *a* and *c*, are 4.9558 and 3.9354 Å, respectively, which are comparable to the literature [14]. Substitution of Zr into the Ca site to produce $Ca_{0.95}Zr_{0.05}Ni_5$ causes a decrease in the unit cell volume compared to $CaNi_5$. Similarly, substitution of smaller atoms at the A site of an AB_5-type alloy such as $LaNi_5$ leads to a decrease in the *a*-lattice parameter but an increase in *c* [27]. Substitution of Cr into the Ni site results in an increase in the *a*-lattice parameter and decrease in the *c*-

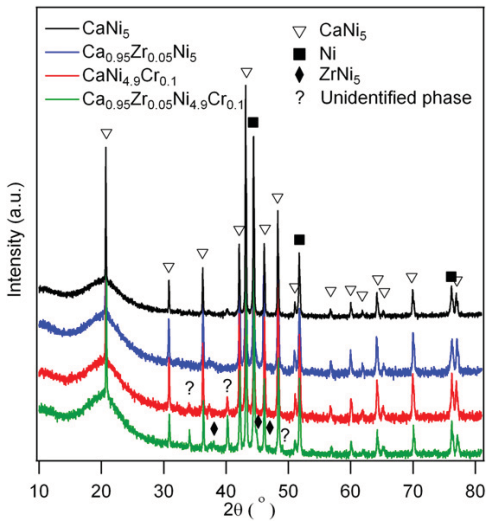

Fig. 3 – XRD patterns of the $CaNi_5$ based alloys after annealing at 800 °C for 3 h.

Table 1 – Lattice parameters and hydrogen storage properties of the synthesized alloys.

Alloys	a (Å)	c (Å)	V (Å^3)	[a]Plateau pressure (bar)		[b]Hydrogen content (wt.%)		[a]Plateau slope	[a]hysteresis
				Abs.	Des.	[1]wt.% H	[2]wt.% H		
$CaNi_5$	4.9558	3.9354	83.702	0.42	0.25	1.20	1.79	0.43	0.52
$Ca_{0.95}Zr_{0.05}Ni_5$	4.9486	3.9420	83.602	0.62	0.27	1.04	1.45	1.23	0.83
$CaNi_{4.9}Cr_{0.1}$	4.9563	3.9348	83.708	0.41	0.22	1.05	1.44	0.05	0.62
$Ca_{0.95}Zr_{0.05}Ni_{4.9}Cr_{0.1}$	4.9402	3.9416	83.572	0.72	0.33	0.85	1.32	1.58	0.78

a Determined from 25 °C plateau.
b Maximum absorption capacity measured at 25 °C and 40 bar of hydrogen pressure where [1] wt.% H and [2] wt.% H are calculated from the weight of the entire sample and only the $CaNi_5$ phase, respectively.

lattice parameter with an overall slight increase in the unit cell volume of $CaNi_5$. The unit cell volume is significantly decreased for the mixed $Ca_{0.95}Zr_{0.05}Ni_{4.9}Cr_{0.1}$ alloy. As a result, this non-linear variation of the unit cell volume of substituted alloys may be caused by the displacement of Ni atoms and the formation of an unidentified phase with its strongest diffraction peaks at $2\theta \sim 34.05°$ and 40.20°, respectively. This phase could not be indexed to any known Ca–Ni–Cr–Zr alloy. Neither could it be attributed to any known Ca–Ni–Cr–Zr oxide or carbide phase nor to any Fe phases that may be present due to contamination from the milling media. The possibility remains that it is an intermediate Ca–Ni, Cr–Ni or Zr–Ni alloy phase [6].

3.2. Hydrogen absorption/desorption properties

All alloys (after annealing) were activated three times under a hydrogen pressure of 60 bar at room temperature for 1 h before Pressure-Composition-Isotherms (PCI) measurements were undertaken. PCI's of all alloys at four temperatures near ambient are shown in Fig. 4. The desorption plateau pressure at 25 °C of the alloys ranges between 0.2 and 0.3 bar where $CaNi_{4.9}Cr_{0.1}$ has the lowest plateau pressure as shown in Table 1. The absorption plateau pressures of $Ca_{0.95}Zr_{0.05}Ni_5$ and $Ca_{0.95}Zr_{0.05}Ni_{4.9}Cr_{0.1}$ are clearly higher than those of the other two alloys. As a result, partial replacement of Cr at Ni site acts to lower the plateau pressure, but replacement of Zr at Ca results in a higher plateau pressure. This could be a function of the atomic radius (R) of the substituted metals i.e. $R_{Cr} > R_{Ni}$ and $R_{Zr} < R_{Ca}$, and will directly influence the unit cell volume of the substituted alloys. Therefore, the plateau pressure tends to be higher for the alloy with a smaller unit cell. The maximum hydrogen storage capacity of substituted alloys, at 25 °C, is lower than for pure $CaNi_5$, as shown in Table 1. It can be seen that the hydrogen content is 1.79 wt.% when normalized for the $CaNi_5$ content. This capacity is in agreement with other literature where 1.5–1.9 wt.% H capacities were obtained [10,14]. However, the wt.% H in the whole sample is actually lower than these values because of about 30 wt.% excess Ni.

The hydrogen pressure plateau regions of all substituted alloys are narrower than that of $CaNi_5$. Reasonably flat plateaux can be seen for replacement of Cr at the Ni site. This result contrasts with the results from $Ca_{0.95}Zr_{0.05}Ni_5$ and $Ca_{0.95}Zr_{0.05}Ni_{4.9}Cr_{0.1}$ alloys where sloping plateaux are observed. Thus, replacement of Zr at the Ca site does not exhibit a flat plateau as is found for pure $CaNi_5$. This could be due to the greater strength of the metallic bond of Zr–Ni [24] compared to Ca–Ni. The stronger bond of Zr–Ni leads to difficulties in expanding the crystal lattice during absorption, resulting in higher hydrogen pressures required to form the hydride phase especially at higher wt.% H content, thus causing a sloping plateau. In addition, the sorption hysteresis of Zr-substituted alloys increases indicating larger lattice expansion and contraction during the sorption cycle known as plastic deformation [28]. In practice, this change in property would be considered in the design and operation of the hydrogen storage system [29,30].

3.3. Kinetics and thermodynamics properties

Fig. 5 shows the absorption-desorption kinetics of $CaNi_5$ with the final pressure of 10 (applied pressure) and 0.16 bar for absorption and desorption, respectively. The alloy reaches 90% of full capacity within 20 s and reaches full absorption capacity within 1 min at both 25 °C and 60 °C. However, desorption at 25 °C displays much slower kinetics than at 60 °C. Therefore, the desorption equilibrium pressure can be reached within 2 min at 60 °C compared to >10 min at 25 °C.

The reaction enthalpy (ΔH) and entropy (ΔS) have been determined from the least-squares linear fit of van't Hoff plots as shown in Fig. 6 and these values are also given in Table 2. The ΔH of absorption of $CaNi_5$ is -35.1 ± 0.7 kJ/mol H_2, which is comparable to an earlier study, -33.5 kJ/mol H_2 [10]. The results provided in Table 2 for substituted alloys agree with an earlier report [31], which shows that the magnitude of ΔH for both absorption and desorption is directly proportional to the unit cell volume. Therefore, a larger unit cell could lead to increased metal-hydrogen (M-H) interactions reflected by more negative reaction enthalpies. The absolute value of the reaction entropy ($|\Delta S|$) is also dependent on unit cell volume and ranges between 100 and 120 J/(mol H_2 K).

3.4. Cycle life

Cycle life was measured as a series of absorption and desorption processes. This property was performed by a PCTPro-E&E (Hy-Energy) with the rate of 3 cycles h^{-1} at 85 °C as the practical operating temperature of PEM fuel cells. Each cycle included absorption (5 min), desorption (5 min) and evacuation and pressure preparation (10 min). Absorption was undertaken by applying 40 ± 2 bar of hydrogen pressure to the reservoir volume which was then released into the evacuated

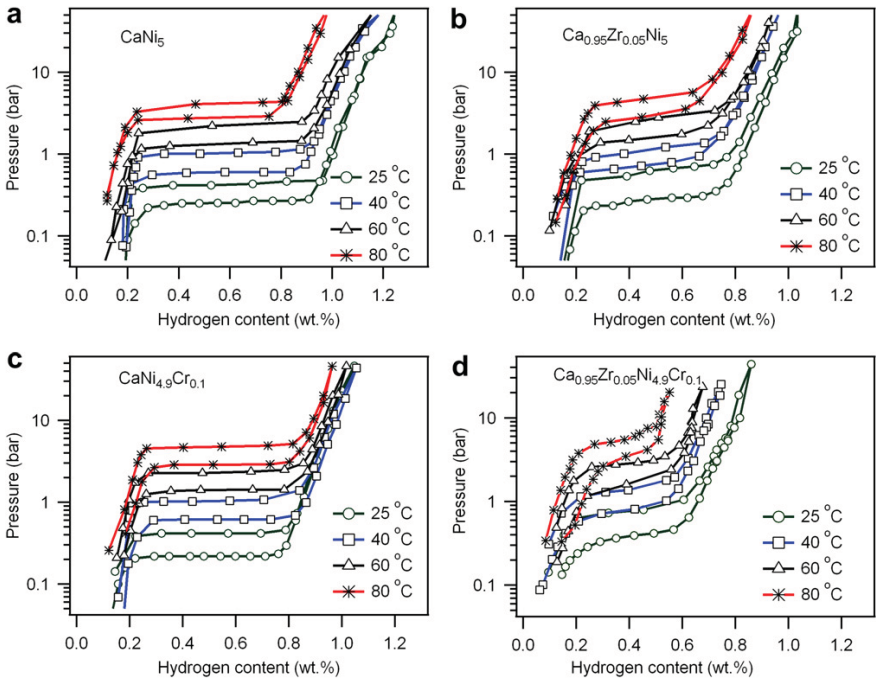

Fig. 4 – PCI's of (a) $CaNi_5$, (b) $Ca_{0.95}Zr_{0.05}Ni_5$, (c) $CaNi_{4.9}Cr_{0.1}$ and (d) $Ca_{0.95}Zr_{0.05}Ni_{4.9}Cr_{0.1}$ measured at 25 °C, 40 °C, 60 °C and 80 °C respectively.

sample volume. The absorption equilibrium pressure was reached within 5 min as shown in Fig. 7 demonstrating that equilibrium was reached in each step.

The cycle life hydrogen storage capacity for each alloy is given in Fig. 8. The absorption capacity of all alloys, which is not normalized to $CaNi_5$ phase content, decreases rapidly for the first 50 cycles, especially, $Ca_{0.95}Zr_{0.05}Ni_5$ and $Ca_{0.95}Zr_{0.05}Ni_{4.9}Cr_{0.1}$ where approximately 20% of their initial capacity is lost. This is probably caused by the larger expansion and contraction of the unit cell volume during the hydrogen sorption process and consequently the alloy decrepitates at a higher rate [32,33]. However, the rate of capacity decay of these alloys slows down after 100 cycles. On the other hand,

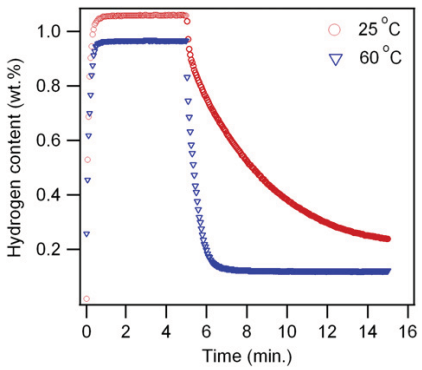

Fig. 5 – Absorption-desorption kinetics of $CaNi_5$ at 25 °C and 60 °C.

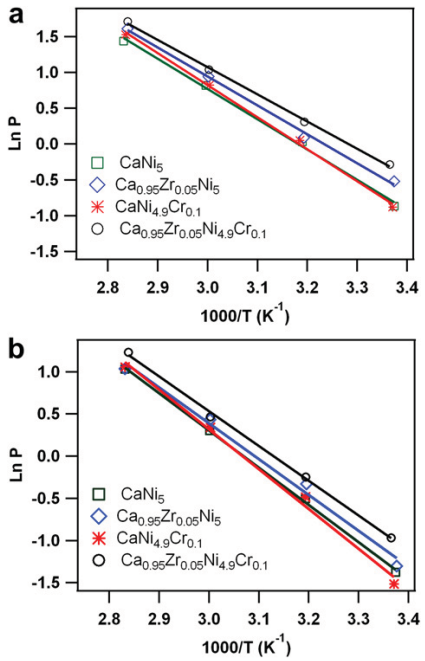

Fig. 6 – van't Hoff plots of hydrogen (a) absorption and (b) desorption of the synthesized alloys.

Table 2 – Thermodynamic data for synthesized alloys.

Alloys	Unit cell volume (Å^3)	ΔH (kJ/mol H_2)		ΔS (J/mol H_2 K)	
		$\Delta H_{abs.}$	$\Delta H_{des.}$	$\Delta S_{abs.}$	$\Delta S_{des.}$
$CaNi_5$	83.702	−35.1 ± 0.7	36.7 ± 1.1	−111.8 ± 1.9	112.5 ± 3.2
$Ca_{0.95}Zr_{0.05}Ni_5$	83.601	−33.5 ± 1.8	35.3 ± 2.6	−108.4 ± 5.3	109.2 ± 8.2
$CaNi_{4.9}Cr_{0.1}$	83.707	−37.2 ± 0.7	39.2 ± 1.8	−118.5 ± 1.9	120.3 ± 5.4
$Ca_{0.95}Zr_{0.05}Ni_{4.9}Cr_{0.1}$	83.568	−31.6 ± 0.4	34.2 ± 0.8	−109.8 ± 7.2	107.0 ± 2.4

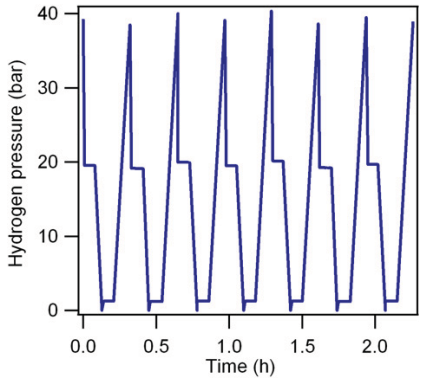

Fig. 7 – Sorption kinetics during cycle life measurement.

hydrogen absorption capacity of $CaNi_{4.9}Cr_{0.1}$ decays deeply after 100 cycles. It can be seen that $CaNi_5$ reported here maintains an absorption capacity of ~75% of initial capacity after 200 absorption-desorption cycles at 85 °C. In significant contrast, less than 40% of initial capacity was left at the same number of cycle during cycling at 85 °C for $CaNi_5$ alloy prepared by air induction melting [13].

A more recent neutron diffraction study of deuterated $CaNi_5$ aged at 85 °C suggests that the loss of capacity is actually associated with the leaching of Ni from specific crystallographic sites resulting in Ni deficient $CaNi_5$ [34]. In life cycle measurements of metal hydrides, the applied H_2 pressure is normally significantly above the equilibrium pressure.

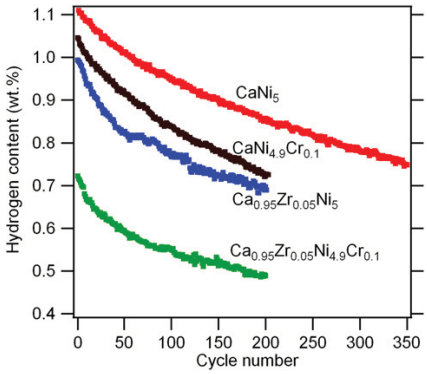

Fig. 8 – Cycling response of substituted $CaNi_5$ alloys at 85 °C.

Goodell et al. [13] point out that this overpressure of H_2 may lead to significant localized heating during the exothermic absorption. In the cycling measurements herein, the applied H_2 pressure during absorption is ~20 bar while the equilibrium pressure for the samples is between 5 and 6 bar at 85 °C. This infers that the samples could reach a temperature as high as 120 °C during absorption. This temperature increase could further promote segregation within $CaNi_5$ samples and contribute to their rapid capacity loss. During measurements the thermocouple did not measure a temperature increase during absorption. However, the large thermal mass and thermal conductivity of the stainless steel sample cell combined with the separation between the sample and the thermocouple does not exclude a temperature rise within the hydride bed. Life cycle measurements employing applied hydrogen pressures closer to the H_2 equilibrium pressure may yield slower degradation in the capacity.

Fig. 9 shows the XRD pattern of $CaNi_5$ after 350 absorption/desorption cycles. The $CaNi_5$ peaks are all broad indicating the reduction of crystallite size and disordering of the crystal lattice while the shape and position of Ni peaks have not changed significantly. As a result, the Lorentzian crystallite size of the cycled alloy, determined by Rietveld refinement, is reduced from 190.5 nm in the as-synthesized $CaNi_5$ to 9.0 nm. This also confirms that the excess Ni does not react with hydrogen during sorption process. The XRD analysis shows that CaH_2 phase is not clearly revealed as expected in other studies [10] for the following interaction of $CaNi_5$ with hydrogen:

$$CaNi_5 + H_2 \rightarrow CaH_2 + 5Ni \quad (1)$$

Possible reasons for no observation of CaH_2 peaks could be very fine particle and small quantity of this phase resulting in peaks too small to be identified in the X-ray diffraction patterns.

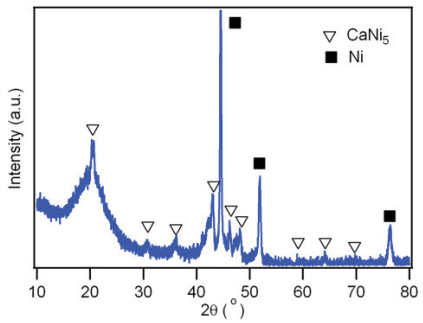

Fig. 9 – XRD pattern of $CaNi_5$ after cycling for 350 cycles.

4. Conclusions

Synthesis of $Ca_{1-x}Zr_xNi_{5-y}Cr_y$ ($x = 0$, 0.05 and $y = 0$, 0.1) has been achieved by mechanical alloying followed by thermal treatment. $CaNi_5$ yields were only 60–70% due to Ca loss during processing, suggesting that an alternate synthesis technique such as induction melting would retain Ca and provide higher $CaNi_5$ yields. Replacement of Zr at a Ca site leads to a decrease in the unit cell volume while replacement of Ni by Cr slightly increases this value. However, the unit cell volume of $Ca_{0.95}Zr_{0.05}Ni_{4.9}Cr_{0.1}$ is smaller than that of $Ca_{0.95}Zr_{0.05}Ni_5$. Flat plateaux can be seen for both $CaNi_5$ and $CaNi_{4.9}Cr_{0.1}$ alloys, and $CaNi_{4.9}Cr_{0.1}$ shows the lowest desorption plateau pressure at 25 °C. Hydrogen storage capacity of all substituted alloys is decreased and the plateau regions are narrowed compared to that of $CaNi_5$. The larger values of plateau pressure and hysteresis parameter of the alloys have been observed for substitution of Ca with Zr. The reaction enthalpy (ΔH) determined from van't Hoff plot results in the absolute value of ΔH being directly proportional to the unit cell volume.

The addition of Zr and Cr did not provide any benefit to the poor cycling properties of $CaNi_5$. The hydrogen absorption capacity of substituted alloys with Zr at a Ca site rapidly decreases for the first 50 cycles and then the rate of capacity loss slows beyond 100 cycles. In contrast, $CaNi_{4.9}Cr_{0.1}$ does not show a significant decrease in the rate of capacity loss beyond 100 cycles. After 200 absorption-desorption cycles, the synthesized alloys retain approximately 65–75% of their initial capacity. Further research into the cycling properties of other $CaNi_5$ alloys is required to determine if there is a suitable composition to improve cycling akin to Al in the $LaNi_5$ system. The cost of $CaNi_5$ and $LaNi_5$ is currently dominated by the price of Ni, making both compounds cost comparable. However the cost of La is likely to rise faster than the cost of Ca given it is a rare earth metal. We have significant interest in finding a $CaNi_5$ alloy with favorable cycling properties because $CaNi_5$ may be much cheaper than $LaNi_5$ in the near-future.

Acknowledgements

S. Chumphongphan would like to thank Ministry of Science and Technology, Thai Government, for full financial support during study the high degree research program. C.E.B. acknowledges the financial support of the Australian Research Council for ARC LIEF Grants LE0775551 and LE0989180, which enabled the XRD and hydrogen sorption studies to be undertaken.

REFERENCES

[1] Sakintuna B, Lamari-Darkrim F, Hirscher M. Metal hydride materials for solid hydrogen storage: a review. Int J Hydrogen Energy 2007;32:1121–40.
[2] Gray EM, Webb CJ, Andrews J, Shabani B, Tsai PJ, Chan SLI. Hydrogen storage for off-grid power supply. Int J Hydrogen Energy 2011;36:654–63.
[3] Bossi C, Del Corno A, Scagliotti M, Valli C. Characterisation of a 3kW PEFC power system coupled with a metal hydride H_2 storage. J Power Sources 2007;171:122–9.
[4] Lynch FE. Metal hydride practical applications. J Less Common Met 1991;172-4:943–58.
[5] Bawa MS, Ziem EA. Long-term testing and stability of $CaNi_5$ alloy for a hydrogen storage application. Int J Hydrogen Energy 1982;7:775–81.
[6] Liang G, Schulz R. Phase structures and hydrogen storage properties of Ca-Mg–Ni alloys prepared by mechanical alloying. J Alloys Compds 2003;356-7:612–6.
[7] Shanghai Metals Market [Internet]. China; c2012 [cited 2012 Jan 10]. Available from: http://en.smm.cn/.
[8] Nickel Historical Charts – Spot [Internet]. New York: Kitco Inc; c2011 [cited 2011 Sep 22]. Available from: http://www.kitcometals.com/charts/nickel_historical.html.
[9] Nahm KS, Jung WB, Lee WY. The reaction kinetics of hydrogen storage in $CaNi_5$. Int J Hydrogen Energy 1990;15:635–40.
[10] Sandrock GD, Murray JJ, Post ML, Taylor JB. Hydrides and deuterides of $CaNi_5$. Mater Res Bull 1982;17:887–94.
[11] Oesterreicher H, Ensslen K, Kerlin A, Bucher E. Hydriding behavior in Ca-Mg-Ni-B. Mater Res Bull 1980;15:275–83.
[12] Sridhar Kumar MP, Viswanathan B, Swamy CS, Srinivasan V. High temperature interaction of hydrogen with intermetallic compound $CaNi_5$. Mater Chem Phys 1988;20:245–53.
[13] Goodell PD. Stability of rechargeable hydriding alloys during extended cycling. J Less Common Met 1984;99:1–14.
[14] Liang G, Huot J, Schulz R. Mechanical alloying and hydrogen storage properties of $CaNi_5$-based alloys. J Alloys Compds 2001;321:146–50.
[15] Yeh MT, Beibutian VM, Hsu SE. Effect of Mo additive on hydrogen absorption of rare- earth based hydrogen storage alloy. J Alloys Compds 1999;293–295:721–3.
[16] Iwakura C, Oura T, Inoue H, Matsuoka M. Effects of substitution with foreign metals on the crystallographic, thermodynamic and electrochemical properties of AB_5-type hydrogen storage alloys. Electrochim Acta 1996;41:117–21.
[17] Bowman Jr RC, Luo CH, Ahn CC, Witham CK, Fultz B. The effect of tin on the degradation of $LaNi_{5-y}Sn_y$ metal hydrides during thermal cycling. J Alloys Compds 1995;217:185–92.
[18] Si TZ, Zhao GP, Zhang QA. Phase structures and electrochemical properties of $Ca_{0.4}Mg_{0.6}(Ni_{0.9}Al_{0.05}M_{0.05})_2$ (M=Cu, Mn, Cr or Co) alloys. Int J Hydrogen Energy 2007;32:600–5.
[19] Wang XL, Zhang YH, Zhaoa DL, Donga XP, Guoa SH, Wang GQ. Effects of Cr addition on the microstructures and electrochemical performances of La–Mg–Ni system ($PuNi_3$-type) hydrogen storage alloy. J Alloys Compds 2007;446-7:625–9.
[20] Jensen JO, Bjerrum NJ. Systematic B-metal substitution in $CaNi_5$. J Alloys Compds 1999;293-5:185–9.
[21] Li ZP, Suda S. Electrochemical durability of Ca-based alloys. Electrochim Acta 1995;40:467–71.
[22] Li ZP, Suda S. The annealing effect on the durabilities of La-substituted $CaNi_5$-type alloys. J Alloys Compds 1995;231:835–40.
[23] Anik M, Ozdemir G, Kucukdeveci N, Baksan B. Effect of Al, B, Ti and Zr additive elements on the electrochemical hydrogen storage performance of MgNi alloy. Int J Hydrogen Energy 2011;36:1568–77.
[24] Yukawa H, Takahashi Y, Morinaga M. Alloying effects on the electronic structures of $LaNi_5$ containing hydrogen atoms. Intermetallics 1996;4:S215–24.
[25] Paskevicius M, Sheppard DA, Buckley CE. Thermodynamic changes in mechanochemically synthesized magnesium hydride nanoparticles. J Am Chem Soc 2010;132:5077–83.

[26] Siegel B, Libowitz GG. The covalent hydrides and hydrides of the group V to VIII transition metals. In: Mueller WM, Blackledge JP, Libowitz GG, editors. Metal hydrides. New York: Academic Press; 1968. p. 631.
[27] Msika E, Latroche M, Cuevas F, Percheron-Guégan A. Zr-substitution in $LaNi_5$-type hydride compound by room temperature ball milling. Mater Sci Eng B 2004;108:91–5.
[28] Da Rosa AV. Fundamentals of renewable energy processes. Burlington: Academic Press; 2009.
[29] Huston EL, Sandrock GD. Engineering properties of metal hydrides. J Less Common Met 1980;74:435–43.
[30] Harries DN, Paskevicius M, Sheppard DA, Price T, Buckley CE. Concentrating solar thermal heat storage using metal hydrides. Proc IEEE; 2011. doi:10.1109/JPROC.2011.2158509.
[31] Kumar EA, Maiya MP, Murthy SS, Viswanathan B. Structural, hydrogen storage and thermodynamic properties of some mischmetal–nickel alloys with partial substitutions for nickel. J Alloys Compds 2009;476:92–7.
[32] Sun XZ, Pan HG, Gao MX, Li R, Lin Y, Ma S. Cycling stability of La–Mg–Ni–Co type hydride electrode with Al. Trans Nonferrous Met Soc China 2006;16:s834–8.
[33] Murshidi JA, Paskevicius M, Sheppard DA, Buckley CE. Structure, morphology and hydrogen storage properties of a $Ti_{0.97}Zr_{0.019}V_{0.439}Fe_{0.097}Cr_{0.045}Al_{0.026}Mn_{1.5}$ alloy. Int J Hydrogen Energy 2011;36:7587–93.
[34] Pitt MP, Brinks HW, Jensen JO, Hauback BC. An in-situ neutron diffraction study of the ageing of $CaNi_5D_x$ at 80 °C and 9 bar. J Alloys Compds 2004;372:190–6.

Available online at www.sciencedirect.com

SciVerse ScienceDirect

journal homepage: www.elsevier.com/locate/he

Effect of Al and Mo substitution on the structural and hydrogen storage properties of $CaNi_5$

*Somwan Chumphongphan, Mark Paskevicius, Drew A. Sheppard, Craig E. Buckley**

Department of Imaging and Applied Physics, Fuels and Energy Technology Institute, Curtin University, GPO Box U1987, Perth 6845, Australia

ARTICLE INFO

Article history:
Received 28 September 2012
Received in revised form
20 November 2012
Accepted 21 November 2012
Available online 23 December 2012

Keywords:
Hydrogen storage materials
Mechanical alloying
Cyclic stability

ABSTRACT

A simple mechanical milling and annealing process has been used to synthesize $CaNi_5$-based hydrogen storage alloys. Heat treatment at 800 °C under vacuum results in the formation of a crystalline $CaNi_5$ phase. Secondary phases, including Ca_2Ni_7 and Mo–Ni, are formed when substituting Mo for Ni. Replacement of Ni by Al or Mo leads to an increase in the unit cell volume of the $CaNi_5$ phase. The hydrogen storage capacity of all substituted alloys is reduced and the plateau pressures are lower than those of pure $CaNi_5$. Fairly flat plateau regions are retained for all compositions except the $CaNi_{4.8}Mo_{0.2}$ composition where a Ca_2Ni_7 phase is dominant. The incorporation of Mo also causes slow sorption kinetics for the $CaNi_{4.9}Mo_{0.1}$ alloy. $CaNi_{4.9}Al_{0.1}$ maintains its initial hydrogen absorption capacity for 20 cycles performed at 85 °C but the other substituted alloys lose their capacity rapidly, especially the $CaNi_{4.8}Mo_{0.2}$ composition.

1. Introduction

Hydrogen is one of the most promising alternative fuels offering clean energy which reduces the emissions of both greenhouse gas (GHG) and air pollutants [1]. Kim and Moon [2] show that the proportion of hydrogen-based road transportation in Korea would reach 76% in 2044 by using a scenarios-based energy economic model. Hydrogen-based energy storage also has a potential for stationary applications with the possibility of power generation, telecommunications, road signs, and remote-area power supply (RAPS) [3–7]. However, the major obstacles of this promising technology are safety concerns and the challenges of bulk hydrogen storage [8].

$CaNi_5$, an AB_5-type alloy, has potential as a moderate-cost hydrogen storage material with a hydrogen content up to 1.9 wt.% [9] which comparable with a promising AB_2 alloys [10]. Although its hydrogen storage capacity cannot meet the target for automotive application, it possesses excellent properties for both stationary and distributed energy generation applications [11]. The alloy shows favorable properties for practical applications with fast kinetics and relatively flat plateau pressure at near ambient temperature, approximately 1 bar at 60 °C for hydrogen desorption [12]. However, its poor cycle-life property is the most serious barrier for its implementation as a hydrogen storage material. Accordingly, many studies have been attempted to improve the hydrogen storage properties of this alloy including its capacity and stability [13–16], but to date these studies have only met limited success.

The hydrogen storage properties of $CaNi_5$ can be altered by the inclusion of minor additives including transition, rare earth and alkaline earth elements, which can substitute into either the Ca or Ni atomic site to form a ternary alloy.

* *Corresponding author*. Tel.: +61 411597043.
E-mail addresses: somwan_ch@hotmail.com (S. Chumphongphan), C.Buckley@curtin.edu.au (C.E. Buckley).
0360-3199/$ – see front matter
http://dx.doi.org/10.1016/j.ijhydene.2012.11.107

Substitution into the Ca site by rare earth or alkaline earth metals such as La and Ce is possible and shows improvement of the electrochemical durability during electrochemical charging and discharging [14,15]. Moreover, substitution of Zr into the Ca site leads to a gradual decay of hydrogen storage capacity after 100 cycles with more than 70% of the initial capacity maintained [12]. Bawa and Ziem [17] pointed out that the $CaNi_5$ alloy benefits from performing in a low temperature range where greater than 75% of its initial capacity is maintained after 5000 cycles over a temperature range of approximately 20–50 °C. However, higher temperatures are required if higher equilibrium pressures are sought for practical applications. It was reported that Mo and Al additives can improve both the hydrogen storage capacity and cyclic stability of La–Ni based alloys [18–20]. Replacement of Ni by Al to form $LaNi_{4.7}Al_{0.3}$ greatly improves the cycling capacity where 75% of initial capacity was retained after 1500 cycles [21]. In a similar way, improvement of the hydrogen storage properties of $CeNi_5$ has been found when 10–20% Ni is replaced by Al [22]. Accordingly, partial substitution of Ni by Mo and Al may improve the hydrogen storage property of $CaNi_5$-based alloys. To synthesize the alloys, mechanical milling has been used instead of the traditional casting procedure in order to assess the viability of the milling method. This was undertaken because there can be problems with the traditional casting method in forming substituted $CaNi_5$ with transition metals [15].

2. Experimental

All $CaNi_5$-based alloys were synthesized by first mechanical milling elemental metals in a 316-stainless steel (SS) canister (650 cm^3 internal volume) attached to a Glen Mills Turbula T2C shaker mixer. Ca (1–2 mm, 99%), Ni, (<150 μm, 99.99%), Al flakes (1 mm, 99.99%) and Mo (1–2 μm, >99.9%) from Sigma–Aldrich were prepared for the desired composition $CaNi_{5-x}(Al, Mo)_x$ where $x = 0$, 0.1 and 0.2. The mixture preparation was processed under an argon atmosphere inside a glovebox (<1 ppm H_2O, <1 ppm O_2). Mechanical milling was performed at room temperature for 40 h with a ball to powder mass ratio of 12:1 using equal numbers of 12.7 mm and 7.938 mm 316 SS balls. The milled powders were then annealed for 3 h at 800 °C under vacuum $< 10^{-3}$ Torr (1.33×10^{-3} mbar).

X-ray diffraction (XRD) was performed using a Bruker D8 Advance diffractometer (CuK_α radiation) equipped with a LynxEye 3° linear position sensitive detector (192 pixels) with a 2θ range of 10–100° using 0.02° steps with 0.7 s of count time per step with operating conditions of 40 kV and 40 mA. The XRD samples were prepared in an argon glovebox and sealed with a poly(methylmethacrylate) (PMMA) air-tight bubble to prevent oxygen/moisture contamination during data collection. Rietveld analysis in Topas (Bruker AXS) was used to calculate lattice parameters and phase composition. Scanning Electron Microscopy (SEM) was performed on a Zeiss Evo 40XVPan using a backscatter electron (BSE) detector operating at 20 keV. The microscope was coupled with an Oxford Instruments energy dispersive X-Ray spectrometer (EDS) for quantitative elemental analysis. To activate the alloys, three cycles (hydrogen absorption/desorption) at 25 °C under 40 ± 2 bar of H_2 pressure and then vacuum were performed. Kinetics and Pressure–Composition-Isotherms (PCI's) measurements were evaluated by a PCTPro-E&E (Hy-Energy) gas sorption analyzer using ultra-high purity hydrogen gas (BOC, 99.999%). Finally, the cycling stability of all alloys was measured at 85 °C up to 40 cycles by using a custom-built Sieverts apparatus.

3. Results and discussion

3.1. Mechanical alloying and structure analysis

The XRD pattern of the metal precursors after milling, 12.016 wt.% Ca and 87.984 wt.% Ni, was dominated by Ni, whilst Ca was not clearly observable, as shown in Fig. 1. This result is likely due to either Ca becoming amorphous or nanocrystalline during milling i.e., Ni peaks are broad but clearly crystalline whereas the Ca peaks and/or its intermediate phases with Ni are masked by the background [15]. The $CaNi_5$ structure does not form directly under these milling conditions and the metal mixture must be annealed at high temperature for alloys to form. After annealing at 800 °C for 3 h under vacuum a $CaNi_5$ phase ($CaCu_5$-type structure, P6/mmm) was identified for all alloys except $CaNi_{4.8}Mo_{0.2}$, which primarily formed a Ca_2Ni_7 phase, Er_2Co_7 structure, space group *R-3m*. Secondary phases of Ca–Ni compounds such as $CaNi_2$, $CaNi_3$ and Ca_2Ni_7 have been formed previously instead of $CaNi_5$ when using a high content of Cr, Mn, Fe and Co as additives [13]. It was reported that the A_2B_7 phase usually formed coexisting with the AB_5 phase for $Ca_{1-x}La_xNi_{4.7}Al_{0.3}$ alloys, however, the appropriate annealing conditions can reduce this A_2B_7 phase [23]. These results in other similar systems reveal that each composition is probably not completely optimized due to a strong dependence on the

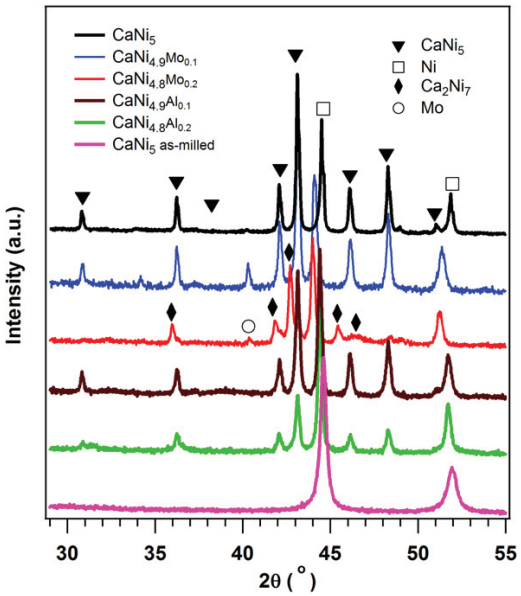

Fig. 1 – XRD spectra of as-milled and annealed alloys (800 °C for 3 h).

conditions of annealing. Pure elemental Ni is still present after annealing with strong diffraction peaks, and it is probably due to the evaporation or loss of Ca during the milling and annealing processes. Excessive Ni is also observed as an effect of Ca evaporation while annealing under Ar atmosphere [23]. The Ca-poor system leads to the incomplete formation of the desired $CaNi_5$ alloy system and excess Ni metal persists in the powder. Interestingly, the excessive Ni phase in the annealed $CaNi_{5-x}(Al\ or\ Mo)_x$ systems displays Ni peak positions that are shifted to lower angle (higher *d*-spacing). This is likely a result of Al and Mo dissolving into the pure Ni and forming nickel-rich solid solutions of Ni–Al and Ni–Mo, respectively [13]. This phenomenon results in the expansion of the Ni unit cell because the atomic radii of Al and Mo are larger than that of Ni.

Backscatter electron SEM micrographs of $CaNi_5$ and $CaNi_{4.8}Mo_{0.2}$ are shown in Fig. 2(a) and (c), respectively. The $CaNi_5$ alloy shows relative homogeneity of the formed phases with the average particle size approximately 10 μm. In contrast, a clearly segregated phase exists in $CaNi_{4.8}Mo_{0.2}$. The EDS spectra at four selected areas for each alloy are shown in Fig. 2(b) and (d), respectively. All initially milled elements are present including a small quantity of Pt due to the SEM sample coating process. The quantitative EDS analysis results are shown in Table 1. The Ca-rich $CaNi_5$ alloy is observed in larger particles (area A of Fig. 2(a)), whilst Ca-poor regions appear in a smaller particles (area B of Fig. 2(a)). Particles with average sizes such as those in regions C and D of Fig. 2(a) show Ca and Ni ratios close to those expected from a pure $CaNi_5$ phase. The minor inhomogeneity appears to be due to an artifact of milling large Ca granules (1–2 mm) and small Ni powder (<150 μm), which leaves some powder grains with excess Ca. Accordingly, this also leads to the presence of the excess Ni in other regions of the sample. It is possible that the inhomogeneity could be avoided by adequate compaction of the milled powder into a firm pellet before annealing at high temperature, thus providing adequate diffusion paths for the elements. In addition, optimization of milling and annealing conditions can also improve the homogeneity of the alloys [24]. A Ni–Mo phase is observed in Ni-rich regions of $CaNi_{4.8}Mo_{0.2}$ shown in areas C and D of Fig. 2(c) that confirms the expansion of the Ni unit cell by Mo incorporation observed by XRD. Other regions of this sample resemble a pure Ca_2Ni_7phase i.e. area B of Fig. 2(c).

The calculated lattice parameters of pure $CaNi_5$ from XRD are $a = 4.956$ and $c = 3.935$ Å, with a unit cell volume of 83.70 Å^3. The unit cell volume of $CaNi_5$ increases for all substituted alloys, as shown in Table 2. However, the non-linear variation of unit cell volume with respect to an atomic radius and content of the additives is possibly the effect of their occupied position within the crystal lattice, and the unit cell deformation [25,26]. Due to segregation, the abundance of

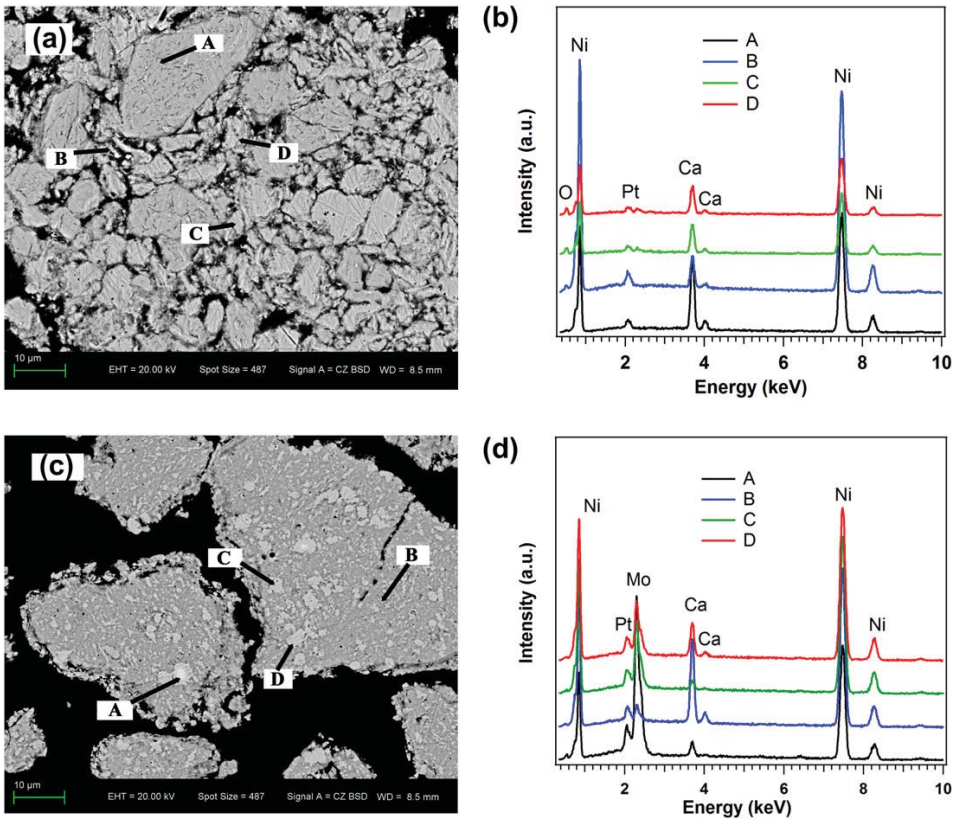

Fig. 2 – Backscatter electron (BSE) micrographs and EDS spectra at selected areas of (a–b) $CaNi_5$ and (c–d) $CaNi_{4.8}Mo_{0.2}$, respectively.

Table 1 – Quantitative EDS analysis of the elemental composition of $CaNi_5$ and $CaNi_{4.8}Mo_{0.2}$.

Alloy	Element	Composition at selected area[a], wt.%				Calculation
		A	B	C	D	
$CaNi_5$	Ca	18.46	5.76	11.37	13.87	12.02
	Ni	81.54	94.24	88.63	86.13	87.98
$CaNi_{4.8}Mo_{0.2}$	Ca	2.15	15.47	1.51	5.97	11.75
	Ni	42.30	76.10	67.16	68.61	82.62
	Mo	55.55	8.43	31.33	25.42	5.63

a Areas A, B, C and D are related to Fig. 2(a) and (c).

the $CaNi_5$ phase in substituted alloys, $CaNi_{5-x}(Al \text{ or } Mo)_x$, has been reduced with increasing of x, except for the $CaNi_{4.9}Mo_{0.1}$ composition. It is of interest that the Ca_2Ni_7 phase is observed for the $CaNi_{4.8}Mo_{0.2}$ composition, however a solid solution phase between Ni and Al/Mo is observed in all substituted systems. Liang and Schulz [24] pointed out that some intermediate phases of Ni with additives may be present when using low temperature annealing for short time periods. This unwanted solid solution with free Ni results in the reduction of the ideal Ni/Ca ratio and supports the formation of the Ca_2Ni_7 phase instead of the desired $CaNi_5$ phase. The unit cell volume of the Mo-substituted Ni increases to 45.044–45.572 $Å^3$ compared to 44.115 $Å^3$ for pure Ni. Nickel and its solid solutions are considered inactive phases for hydrogen sorption under these experimental conditions [27].

3.2. *Hydrogen storage properties*

Fig. 3 shows the hydrogen absorption and desorption kinetics of all synthesized alloys, performed at (a) 25 and (b) 60 °C with the final equilibrium pressures (P_{eq}) of 10 ± 1 and 0.15 ± 0.03 bar for absorption and desorption, respectively. Full hydrogen absorption capacity can be reached within 3 min for all compositions at both temperatures, except $CaNi_{4.9}Mo_{0.1}$. The Al-substituted alloys show an improvement in desorption kinetics, i.e. full desorption at 25 °C can be reached within 2 min, while other alloys require longer times, see Fig. 3(a). The sorption kinetics at 60 °C of pure $CaNi_5$ are comparable to those of Al-substituted alloys as shown in Fig. 3(b). The presence of residual hydrogen during desorption, approximately 0.2–0.3 wt.%, is due to the lower pressure plateau region which appears at the hydrogen pressure of ~0.02 bar at 25 °C [9,15]. Thus, this plateau cannot be reached according to this experiment condition, i.e. the final equilibrium pressure is ~0.15 bar. $CaNi_{4.8}Mo_{0.2}$ shows poor reversibility of hydrogen absorption–desorption with a high wt.% of residual hydrogen upon desorption. As mentioned above, this alloy contains Ca_2Ni_7 as the major phase; therefore, the presence of this phase results determines the hydrogen sorption properties of the sample. It was also reported that the hydride phase of Ca_2Ni_7 phase in $(Ca, Mg)_2Ni_7$ alloy has high stability and only desorbs 50% of its absorption capacity, which desorbed at 45 °C under a hydrogen pressure of less than 0.1 bar [28].

There are clearly much slower kinetics upon the addition of Mo in $CaNi_{4.9}Mo_{0.1}$ as shown in Fig. 3. As can be seen, it may take longer than 20 and 30 min for a complete absorption and desorption at 25 °C, respectively. It should also be noted that the reaction between alloys and hydrogen can be enhanced by the presence of Ni clusters on the surface acting as a catalyst [29,30]. Yeh et al. [19] indicated that Mo additives delay the formation of the hydrogen-rich β-phase of AB_5-type hydrides. As a result, the dissolution of Mo into this Ni phase (as shown above by XRD) could affect the catalytic property of the Ni clusters, which in turn could slow the sorption kinetics of $CaNi_5$-based alloys.

Table 2 – Phase composition, lattice parameters and hydrogen absorption properties of synthesized alloys.

Alloy	Phase	Phase abundance (wt.%)	a (Å)	c (Å)	V ($Å^3$)	Absorption capacity[a] (wt.% H)
$CaNi_5$	$CaNi_5$	68.10	4.9557	3.9354	83.700	1.76
	Ni	31.90	3.5334		44.115	
$CaNi_{4.9}Mo_{0.1}$	$CaNi_5$	69.88	4.9587	3.9364	83.822	1.41
	Ca_2Ni_7	7.77	4.9600	36.0933	768.994	
	Ni	21.32	3.5580		45.044	
	Mo	1.04	3.1661		31.738	
$CaNi_{4.8}Mo_{0.2}$	$CaNi_5$	3.70	4.9596	3.9416	83.963	1.24
	Ca_2Ni_7	63.31	5.0046	35.9980	780.808	
	Ni	32.61	3.5719		45.572	
	Mo	0.38	3.1649		31.701	
$CaNi_{4.9}Al_{0.1}$	$CaNi_5$	62.72	4.9604	3.9377	83.907	1.49
	Ni	37.28	3.5365		44.231	
$CaNi_{4.8}Al_{0.2}$	$CaNi_5$	41.43	4.9602	3.9363	83.872	1.16
	Ni	58.57	3.5360		44.213	

a Measured at 25 °C and ~30 bar of H_2 equilibrium pressure with respect to H_2 active phases.

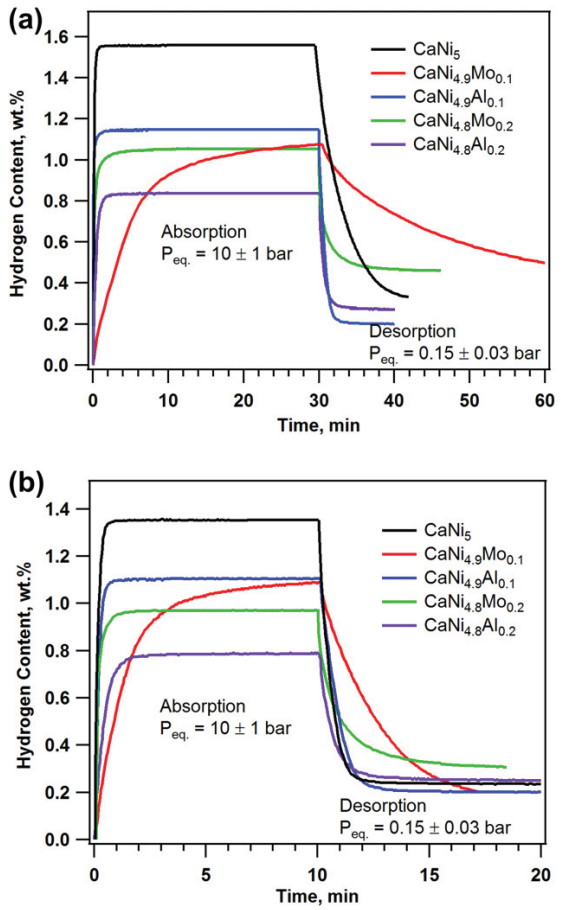

Fig. 3 – Absorption and desorption kinetics of synthesized alloys measured at (a) 25 °C and (b) 60 °C.

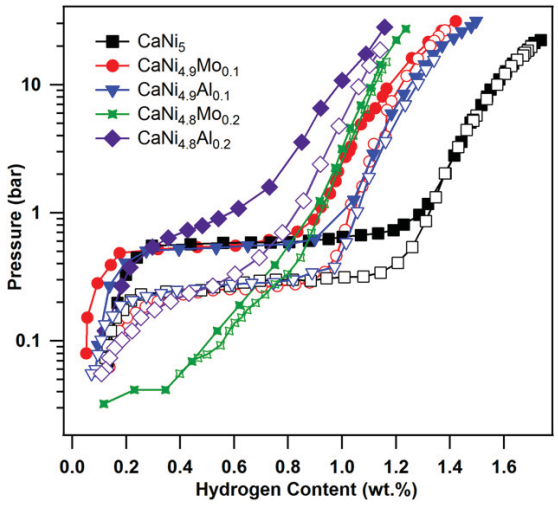

Fig. 4 – PCI's of synthesized alloys at 25 °C; closed and opened makers represent hydrogen absorption and desorption, respectively.

Pressure–Composition-Isotherms (PCI's) of all alloys measured at 25 °C are shown in Fig. 4. The hydrogen storage capacity is reduced for the substituted alloys, especially the $CaNi_{4.8}Al_{0.2}$ composition. The hydrogen storage capacity is likely decreased due to a reduction of sites in the lattice that may be occupied by hydrogen, as observed in the $LaNi_{5-x}Fe_x$ system [31]. The measured hydrogen capacity is correlated to the abundance of the active hydrogen storage phase, $CaNi_5$ or Ca_2Ni_7, whereas the Ni phase is not active to hydrogen, and can be considered as dead-weight. Therefore, the wt.% of H will be lower than reported when the inactive Ni-rich phases are included in the calculation. For instance, the hydrogen content for the entire sample of $CaNi_5$, $CaNi_{4.9}Mo_{0.1}$ and $CaNi_{4.9}Al_{0.1}$ will be about 1.20, 1.10 and 0.94 wt.%, respectively. It should be noted that the substitution of Mo and Al does not significantly increase the hydrogen storage capacity as found in another AB_5-type alloy, $Lm(Ni, Mn, Co, Al)_{5-x}$ Mo_x, where Lm is La-rich mischmetal [19,32]. Accordingly, a certain content of Al and Mo in the alloy needs to be studied to optimize the hydrogen storage capacity [18]. In addition, these three compositions also show relatively flat plateaux with minimal hysteresis indicated by the absorption and desorption pressures of 0.5 and 0.3 bar, respectively at 25 °C.

The Al and Mo additives do result in slightly lower plateau pressures where desorption plateau pressures for $CaNi_5$, $CaNi_{4.9}Al_{0.1}$ and $CaNi_{4.9}Mo_{0.1}$ are 0.29, 0.27 and 0.25 bar, respectively. In contrast to other alloys the plateau does not exist for the $CaNi_{4.8}Mo_{0.2}$ composition due to the presence of Ca_2Ni_7 as the main phase. Ca_2Ni_7 forms a very stable hydride and full desorption can only be undertaken at a very low pressure. A similar result is found by Si et al. [28] where a $(Ca,Mg)_2Ni_7$ alloy was found to have no plateau for hydrogen pressures above 0.1 bar.

3.3. *Cyclic stability*

The cyclic stability data for each of the synthesized alloys were collected after the activation process was complete. Each cycle included an absorption (10 min) at 85 °C with 20 ± 1 bar of H_2 pressure followed by a dynamic system evacuation (10 min). Fig. 5(a) shows the absorption capacity of the alloys at the *n*th cycle, C_n, compared to that of the first cycle, C_1. The addition of Al to form $CaNi_{4.9}Al_{0.1}$ is shown to improve the stability of the $CaNi_5$ phase where the initial capacity has been retained up to 20 cycles. Han and Lee [33] indicate that substitution of Al into $MmNi_5$- and $LaNi_5$-based alloys can improve the alloy stability due to the formation of Al_2O_3 at the surface, which prevents further adsorption of oxygen and protects the hydrogen active phases. However, the capacity of a higher Al-content alloy, i.e. $CaNi_{4.8}Al_{0.2}$ composition, decays with a faster rate which is probably due to the inhomogeneity of the alloy [23].

The cyclic stability of the alloys has also been related to the unit cell volume [20], where a smaller unit cell volume leads to larger expansion and contraction during the hydrogen sorption process, and consequently the alloy degrades at a higher

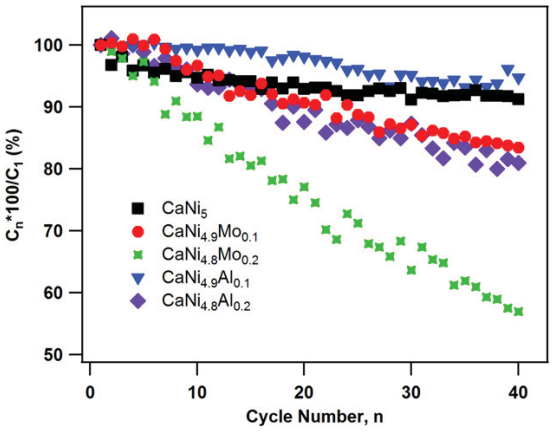

Fig. 5 – Hydrogen cycling behavior of synthesized alloys at 85 °C.

rate. This effect is most likely the predominant influence on the alloy stability during the first few cycles. As can be seen from Fig. 5, the substituted alloys with a larger unit cell volume, i.e. $CaNi_{4.9}Al_{0.1}$ and $CaNi_{4.9}Mo_{0.1}$ maintain a higher absorption capacity compared to that of pure $CaNi_5$ alloy during the sorption measurements up to 10 cycles. In contrast to the other compositions, the capacity of $CaNi_{4.8}Mo_{0.2}$ decays significantly with approximately 55% of initial capacity at 40 cycles while the other compositions maintain more than 80% of their initial capacity. In fact, the main phase of this composition is Ca_2Ni_7 as discussed above; therefore, the disproportion rate of the Ca_2Ni_7 phase appears much faster than that of the $CaNi_5$ phase under these experimental conditions. The reduction of crystallite size and disordering of the crystal lattice of $CaNi_5$ after cycling has been reported previously [12]. Goodell [21] suggested that heat treatment at 500 °C or higher is required to recover the disproportionate alloys, which can restore initial hydrogen storage capacity.

4. Conclusions

Synthesis of $CaNi_{5-x}$(Al or Mo)$_x$ (x = 0, 0.1 and 0.2) has been achieved by mechanical alloying followed by thermal treatment. Secondary phases of additives and Ni are formed as Ni-rich solid solutions. It is suggested that appropriate milling and annealing conditions need to be optimized for each composition to decrease segregation and secondary phase formation. Furthermore, compaction of the milled powder into a firm pellet before annealing may support the development of the $CaNi_5$ phase with uniform composition. Relatively flat plateau regions are retained for all compositions except $CaNi_{4.8}Mo_{0.2}$ which is dominated by the secondary phase, Ca_2Ni_7. Hydrogen desorption kinetics are improved by the addition of Al, whilst the slowest kinetics are observed for the $CaNi_{4.9}Mo_{0.1}$ alloy. Among the synthesized alloys, $CaNi_{4.9}Al_{0.1}$ shows improvement in the cyclic stability, retaining its initial capacity up to 20 cycles. The addition of Al offers the possibility to improve both kinetics and cyclic stability of the $CaNi_5$-based alloy. This study also confirms that Ca_2Ni_7 forms a stable hydride with a sloped plateau, which is unfavorable for technological applications. Moreover, a severe decay rate of hydrogen storage capacity is another problem for Ca_2Ni_7.

Acknowledgments

S. C. would like to thank Thai Government, Ministry of Science and Technology, and Mae Fah Luang University for full financial support during a higher degree research program. C.E.B, M.P and D.A.S acknowledges the financial support of the Australian Research Council (ARC) for ARC Linkage grant LP120101848 and C.E.B. also acknowledges ARC LIEF grants LE0989180 and LE0775551, which enabled the XRD and gas sorption studies to be done. The authors also acknowledge the facilities, scientific and technical assistance of the Curtin University Electron Microscope Laboratories, a facility partially funded by the University, State and Commonwealth Governments.

REFERENCES

[1] Ball M, Wietschel M. The future of hydrogen – opportunities and challenges. Int J Hydrogen Energy 2009;34:615–27.
[2] Kim J, Moon I. The role of hydrogen in the road transportation sector for a sustainable energy system: a case study of Korea. Int J Hydrogen Energy 2008;33:7326–37.
[3] Gray EM, Webb CJ, Andrews J, Shabani B, Tsai PJ, Chan SLI. Hydrogen storage for off-grid power supply. Int J Hydrogen Energy 2011;36:654–63.
[4] Dunn S. Hydrogen futures: toward a sustainable energy system. Int J Hydrogen Energy 2002;27:235–64.
[5] Shabani B, Andrews J. An experimental investigation of a PEM fuel cell to supply both heat and power in a solar-hydrogen RAPS system. Int J Hydrogen Energy 2011;36:5442–52.
[6] Sheppard DA, Paskevicius M, Buckley CE. The thermodynamics of hydrogen desorption from $NaMgH_3$ and its application as a solar heat storage medium. Chem Mater 2011;23:4298–300.
[7] Harries DN, Paskevicius M, Sheppard DA, Price T, Buckley CE. Concentrating solar thermal heat storage using metal hydrides. Proc IEEE 2012;100:539–49.
[8] Ogden JM. Prospects for building a hydrogen energy infrastructure. Annu Rev Energy Environ 1999;24:227–79.
[9] Sandrock GD, Murray JJ, Post ML, Taylor JB. Hydrides and deuterides of $CaNi_5$. Mater Res Bull 1982;17:887–94.
[10] Murshidi JA, Paskevicius M, Sheppard DA, Buckley CE. Structure, morphology and hydrogen storage properties of a $Ti_{0.97}Zr_{0.019}V_{0.439}Fe_{0.097}Cr_{0.045}Al_{0.026}Mn_{1.5}$ alloy. Int J Hydrogen Energy 2011;36:7587–93.
[11] Sakintuna B, Lamari-Darkrim F, Hirscher M. Metal hydride materials for solid hydrogen storage: a review. Int J Hydrogen Energy 2007;32:1121–40.
[12] Chumphongphan S, Paskevicius M, Sheppard DA, Buckley CE. Cycle life and hydrogen storage properties of mechanical alloyed $Ca_{1-x}Zr_xNi_{5-y}Cr_y$; (x = 0, 0.05 and y = 0, 0.1). Int J Hydrogen Energy 2012;37:7586–93.
[13] Jensen JO, Bjerrum NJ. Systematic B-metal substitution in $CaNi_5$. J Alloys Compds 1999;293–295:185–9.

[14] Li ZP, Suda S. Effects of hydriding–dehydriding cycling on P–C–T and electrochemical properties of La–Ca–Ni–Al alloys. J Alloys Compds 1995;231:594–7.
[15] Liang G, Huot J, Schulz R. Mechanical alloying and hydrogen storage properties of $CaNi_5$-based alloys. J Alloys Compds 2001;321:146–50.
[16] Li ZP, Suda S. Electrochemical durability of Ca-based alloys. Electrochem Acta 1995;40:467–71.
[17] Bawa MS, Ziem EA. Long-term testing and stability of $CaNi_5$ alloy for a hydrogen storage application. Int J Hydrogen Energy 1982;7:775–81.
[18] Zhang X, Sun D, Yin W, Chai Y, Zhao M. Crystallographic and electrochemical characteristics of $La_{0.7}Mg_{0.3}Ni_{3.5-x}(Al_{0.5}Mo_{0.5})_x$ ($x = 0$–0.8) hydrogen storage alloys. J Power Sources 2006;154:290–7.
[19] Yeh MT, Beibutian VM, Hsu SE. Effect of Mo additive on hydrogen absorption of rare-earth based hydrogen storage alloy. J Alloys Compds 1999;293–295:721–3.
[20] Sun X-z, Pan H-g, Gao M-x, Li R, Lin Y, Ma S. Cycling stability of La–Mg–Ni–Co type hydride electrode with Al. Trans Nonferrous Met Soc China 2006;16:s834–8.
[21] Goodell PD. Stability of rechargeable hydriding alloys during extended cycling. J Less Common Met 1984;99:1–14.
[22] Sinha VK, Wallace WE. Hydrogen storage properties of $CeNi_{5-x}Al_x$ alloys. J Phys Chem 1984;88:102–5.
[23] Li ZP, Suda S. The annealing effect on the durabilities of La-substituted $CaNi_5$-type alloys. J Alloys Compds 1995;231: 835–40.
[24] Liang G, Schulz R. Phase structures and hydrogen storage properties of Ca–Mg–Ni alloys prepared by mechanical alloying. J Alloys Compds 2003;356–357:612–6.
[25] Percheron-Guégan A, Lartigue C, Achard JC. Correlations between the structural properties, the stability and the hydrogen content of substituted $LaNi_5$ compounds. J Less Common Met 1985;109:287–309.
[26] Notten PHL, Einerhand REF, Daams JLC. On the nature of the electrochemical cycling stability of non-stoichiometric $LaNi_5$-based hydride-forming compounds Part I. crystallography and electrochemistry. J Alloys Compds 1994;210:221–32.
[27] Siegel B, Libowitz GG. The covalent hydrides and hydrides of the group V to VIII transition metals. In: Mueller WM, Blackledge JP, Libowitz GG, editors. Metal hydrides. New York: Academic Press; 1968. p. 631.
[28] Si TZ, Pang G, Zhang QA, Liu DM, Liu N. Solid solubility of Mg in Ca_2Ni_7 and hydrogen storage properties of $(Ca_{2-x}Mg_x)Ni_7$ alloys. Int J Hydrogen Energy 2009;34:4833–7.
[29] Murray J, Miller H, Bird P, Goudy AJ. The effect of particle size and surface composition on the reaction rates of some hydrogen storage alloys. J Alloys Compnds 1995;231:841–5.
[30] Vivet S, Joubert JM, Knosp B, Percheron- Guégan A. Effects of cobalt replacement by nickel, manganese, aluminium and iron on the crystallographic and electrochemical properties of AB_5-type alloys. J Alloys Compds 2003;356–357:779–83.
[31] Lamloumi J, Percheron-Guégan A, Lartigue C, Achard JC, Jehanno G. Thermodynamic, structural and magnetic properties of $LaNi_{5-x}Fe_x$ hydrides. J Less Common Met 1987; 130:111–22.
[32] Yang S, Han S, Song J, Li Y. Influences of molybdenum substitution for cobalt on the phase structure and electrochemical kinetic properties of AB_5-type hydrogen storage alloys. J Rare Earths 2011;29:692–7.
[33] Han JI, Lee JY. Influence of oxygen impurity on the hydrogenation properties of $LaNi_5$, $LaNi_{4.7}Al_{0.3}$ and $MmNi_{4.5}Al_{0.5}$ during long-term pressure-induced hydriding–dehydriding cycling. J Less Common Met 1989; 152:329–38.

Available online at www.sciencedirect.com

ScienceDirect

journal homepage: www.elsevier.com/locate/he

Nanoconfinement degradation in $NaAlH_4$/CMK-1

Somwan Chumphongphan [a], Uffe Filsø [a,b], Mark Paskevicius [a,*], Drew A. Sheppard [a], Torben R. Jensen [b], Craig E. Buckley [a]

[a] Department of Imaging and Applied Physics, Fuels and Energy Technology Institute, Curtin University, GPO Box U1987, Perth, WA 6845, Australia

[b] Interdisciplinary Nanoscience Center (iNANO) and Department of Chemistry, University of Aarhus, DK-800 Aarhus, Denmark

ARTICLE INFO

Article history:
Received 8 May 2014
Accepted 13 May 2014
Available online 12 June 2014

Keywords:
Nanoconfinement
CMK-1
$NaAlH_4$
Scaffold
Hydrogen storage
Infiltration

ABSTRACT

An ordered mesoporous carbon scaffold (CMK-1) has been synthesized and infiltrated with $NaAlH_4$ nanoparticles by solvent- and melt-infiltration techniques. Small angle X-ray scattering (SAXS), powder X-ray diffraction (XRD), scanning electron microscopy (SEM), Transmission Electron Microscopy (TEM) and energy dispersive spectroscopy (EDS) are used to characterize the structure, composition and morphology before and after thermal treatment. This study illuminates some of the problems that can be associated with nanoconfinement of hydrogen storage materials including scaffold contamination, residual solvent contamination, sample morphology changes after heating, and other factors that can be detrimental to the application of these systems. Of particular interest is the expulsion of $NaAlH_4$ decomposition products from the scaffold after heating beyond its melting point under vacuum. This results in the surface of mesoporous carbon particles having arrays of multi-micron-long Al filaments that are >100 nm in diameter.

Introduction

Complex metal hydrides have been studied since the mid-1990's as potential solid state hydrogen storage materials due to their very high hydrogen content [1–3]. Stable salt-like solids are formed between the least electropositive metals, such as Li and Na etc., and a negatively charged coordination complex with hydrogen covalently bonded to a more electronegative metal, e.g. $[AlH_4]^-$ or $[BH_4]^-$. These metal hydrides release hydrogen by thermolysis at temperatures higher than their melting points (m.p.) [4]. Of particular interest is $NaAlH_4$, which has a high gravimetric hydrogen capacity, 7.4 wt.% H, and is well known to decompose via a 3-step mechanism [5]:

$$3NaAlH_4 \leftrightarrow Na_3AlH_6 + 2Al + 3H_2 \quad ; 3.70 \text{ wt.\% H} \tag{1}$$

$$Na_3AlH_6 \leftrightarrow 3NaH + Al + 3/2H_2 \quad ; 1.85 \text{ wt.\% H} \tag{2}$$

$$NaH \leftrightarrow Na + 1/2H_2 \quad ; 1.85 \text{ wt.\% H} \tag{3}$$

Without the addition of a catalyst the hydrogen release temperatures for these reactions are greater than 180, 240 and 425 °C, respectively. Accordingly, only the first and the second step are suitable for a moderate temperature application with a total reversible hydrogen storage capacity of 5.6 wt.%, whilst 5 wt.% can be achieved in practical application [6,7]. Hydrogen desorption from pure $NaAlH_4$ at 200 °C (above its m.p. of 181 °C

* Corresponding author. Tel.: +61 892661381.
E-mail address: mark.paskevicius@gmail.com (M. Paskevicius).
http://dx.doi.org/10.1016/j.ijhydene.2014.05.087

[8]) is only completed after ~20 h due to severe kinetic limitations [9]. However, the $NaAlH_4$ system has been investigated thoroughly over the last >20 years and an extensive array of catalytic phases can allow low temperature (120–140 °C) hydrogen release and uptake [10]. Many of these transition metal catalysts are added to the $NaAlH_4$ system as halide salts, that are reduced to metal-Al surface-alloys that are catalytically active, with the generation of an inactive sodium halide salt by-product [11]. Although the list of catalytic phases for $NaAlH_4$ is extensive, recent focus on $CeCl_3$ [12] or Ti-based nanoparticles [13] show great promise, even when compared to the well-studied $TiCl_3$ doped $NaAlH_4$ system [10].

An alternative method to enhance the de- and rehydrogenation stability and kinetics of $NaAlH_4$ is by the reduction of particle size, e.g. mechanochemically [14–16]. Nanocrystalline Na_3AlH_6 and Na_2LiAlH_6 synthesized by high-energy milling show great improvement in performance compared to the bulk materials [17]. The deposition of $NaAlH_4$ on to the surface of nanocrystalline titanium dioxide loaded carbon spheres (Ti-CSs) also shows improvement in hydrogen storage properties of the hydride after multiple cycles [18]. Nanoconfinement is an emerging technique to provide improved kinetic and thermodynamic properties for hydrogen storage materials [19–22]. Evidence of the kinetic benefits of metal hydride particle size reduction are widespread [23] and a similar kinetic improvement exists when a metal hydride is nanoconfined [24], restricting its particle size to the pore size of the scaffold. There is also experimental proof for thermodynamic changes in metal hydrides with reductions in particle size, for example, small changes in enthalpy and entropy were observed for 7 nm MgH_2 particles [25]. Changes in the thermodynamic behaviour of MgH_2 confined within carbon aerogel have also been reported [26]. There were difficulties in interpreting some data in this previous study [26] due to the size distribution of the scaffold pores and hence the nanoconfined metal hydride. However, the problem with pore and particle polydispersity can be overcome through the implementation of ordered porous scaffolds with uniform pore networks (such as CMK-1).

A systematic study of $NaAlH_4$ melt-infiltrated into carbon aerogels with different pore sizes has been conducted [27,28]. The temperature for the maximum hydrogen release rate, measured by temperature programmed desorption mass spectroscopy (TPD-MS), decreased from 252 °C for bulk to 162 °C for $NaAlH_4$ melt infiltrated in macroporous aerogel (>100 nm). This improvement is assigned mainly to the catalytic properties of the carbon aerogel surface, possibly with a small contribution from confinement in mesopores. An additional, but smaller, improvement is induced by reducing the pore sizes in the range $7 \leq D_{max} \leq 39$ nm for $\Delta T_{max} = -12$ to -16 °C. The size distribution maxima for $NaAlH_4$ crystallites is larger than the pore sizes determined by nitrogen adsorption, possibly due to a thermodynamic preference for filling the larger pores [27,29]. The melt infiltration of $NaAlH_4$ into carbon aerogels (17 nm pores) functionalized with a $TiCl_3$ catalyst may improve the hydrogen desorption rate compared to $NaAlH_4$ ball-milled with the catalyst [30]. However, attempting to infiltrate molten $NaAlH_4$ in carbon aerogel scaffolds with smaller pore sizes (4 nm) shows that there is a lower pore size limitation using this technique with carbon aerogels [27]. In contrast to this study, $NaAlH_4$ has been reported to be infiltrated in 2–3 nm pores of high surface area porous graphite with desorption starting at 100–120 °C, decomposing in a single step [5]. There can be a hydrogen capacity loss upon cycling of hydrogen storage materials in a scaffold. In the case of $NaAlH_4$, Gao et al. [31] pointed out that the capacity loss was mainly caused by the loss of active Na(H) species. Therefore, it is assumed that Na(H) reacts with impurities such as oxygen containing groups or is dispersed on the surface of the carbon scaffold. In addition, they also reported that Al migrated out of the pores and formed large Al crystallites (>100 nm) on the outer surface of the carbon scaffold after hydrogen desorption.

Material and methods

Synthesis

An ordered mesoporous silica, MCM-48, was synthesized according to [32] by dissolving 10 g of cetyltrimethylammonium bromide (CTAB, Sigma–Aldrich) and 1.1 g of sodium hydroxide (NaOH, ≥99%, Merck) in 56.6 g of deionized water at 35 °C, and then 11.9 g of tetraethylorthosilicate (TEOS, ≥99.0%, Fluka Chemika) was added dropwise. The mixture was heated in a water bath at 100 °C for 24 h. After cooling to room temperature, the pH of the mixture was adjusted to 7 using 1 M HCl solution, followed by heating at 100 °C for 24 h. The product was filtrated, rinsed with distilled water, and dried in air at 100 °C. The product was then calcined by thermal treatment in air at 550 °C for 6 h.

Ordered mesoporous carbon CMK-1 was synthesized according to [33] by adding 1.25 g of sucrose (≥99.5%, Sigma–Aldrich) into a solution of 0.14 g of sulphuric acid (H_2SO_4) and 5 g of deionized water. Then 1 g of MCM-48 was added into the above solution. The mixture was then heated in air at 100 °C for 6 h, and subsequently at 150 °C for 6 h in air. The mixture was reheated at 100 and 150 °C for 6 h, respectively, after a second batch of 0.80 g of sucrose, 0.09 g of H_2SO_4 and 5.0 g deionized water was added. The product was treated at 900 °C for 6 h under vacuum for carbonization of the scaffold. To remove the silica template, the product was washed, at 100 °C, with excess 1 M NaOH solution in deionized water (50 vol%) and ethanol (50 vol%). It was then filtered and rinsed with ethanol, and rewashed with deionized water (50 vol%) - ethanol (50 vol%) solution three times just below its boiling point. Finally, the product was dried at 100 °C for 2 h in air and, consequently, 250 °C for 3 h under vacuum to remove the possible moisture and gases before transferring the carbon scaffold into a glovebox under an Ar atmosphere.

$NaAlH_4$ was infiltrated into the pores of the CMK-1 scaffold either by a solvent or melt infiltration method. For solvent infiltration, the precursor solutions were prepared under an Ar atmosphere by using 1.2 g of $NaAlH_4$ (95% purity, Sigma–Aldrich) and 23.1 ml of anhydrous tetrahydrofuran (THF, ≥99.9%, Sigma–Aldrich) to make a 1 M $NaAlH_4$ solution. CMK-1 (1 g) was added to this solution, magnetically stirred for 15 h and then centrifuged for 30 min to separate the loaded scaffold from excess solvent. This was followed by decanting the excess solvent off. Surface deposits were removed by rinsing the CMK-1 surface with pure THF followed by centrifuging for 20 min and

then decanting once more. Finally, the samples were dried in a glovebox under an argon atmosphere for several days followed by 2 h under vacuum at room temperature before hydrogen desorption measurements were conducted.

For the melt infiltration, $NaAlH_4$ (50 wt.%) and CMK-1 (50 wt.%) was mixed manually by hand-grinding using an agate mortar in an Ar-filled glovebox and loaded into a stainless steel cell. The sealed cell was evacuated and filled with hydrogen to 110 bar at room temperature. It was then heated to 185 °C, which is just above the melting point of $NaAlH_4$, and kept at this temperature for 15 min with the final hydrogen pressure of 125 bar before cooling to room temperature.

Analysis

Small-angle X-ray scattering (SAXS) patterns were recorded with a Bruker Nanostar SAXS instrument at 40 kV and 35 mA using a wavelength of, $\lambda = 1.5418$ Å (CuK_α) with a 2D multiwire detector. Samples were sealed within glass capillaries and raw data were radially averaged and background subtracted. Powder X-ray diffraction (XRD) was performed using a Bruker D8 Advance diffractometer (CuK_α) equipped with a LynxEye 3° linear position sensitive detector (192 pixels) with a 2θ range of 15–70° using 0.02° steps with 0.7 s of count time per step with operating conditions of 40 kV and 40 mA. The XRD samples were prepared in an argon glovebox and sealed with a poly(-methylmethacrylate) (PMMA) air-tight bubble holder to prevent oxygen/moisture contamination during data collection.

Scanning Electron Microscopy (SEM) was performed on a Zeiss Evo 40XVPan operating at 15 keV and a TESCAN MIRA3 operating at 3 keV. SEM samples were briefly air-exposed to be coated with Pt before imaging could be undertaken. Transmission Electron Microscopy (TEM) was performed on a JEOL 3000F FEG TEM at an operating voltage of 300 keV. Elemental analysis was conducted using an Oxford Instruments INCA EDS system. Samples were loaded onto TEM grids by suspension in toluene before briefly (up to a minute) being exposed to air before being inserted into the TEM column.

The hydrogen release measurements were undertaken by temperature programmed desorption mass spectroscopy (TPD-MS) using a Stanford Research Systems (SRS) Residual Gas Analyzer (RGA 300) Quadrupole Mass Spectrometer. Samples were connected to a turbo molecular pump and evacuated at room temperature to a pressure below 10^{-4} mbar for 3 h. The samples were then heated to 375 °C with a heating rate of 2 °C/minute.

Results and discussion

CMK-1 synthesis and $NaAlH_4$ infiltration

CMK-1 was synthesized and loaded with $NaAlH_4$ by solvent and melt infiltration as described in the experimental section. Small angle X-ray scattering (SAXS) patterns of CMK-1 and $NaAlH_4$ infiltrated CMK-1 are displayed in Fig. 1(A). The SAXS pattern from pure CMK-1 depicts low-angle diffraction peaks that originate from the relatively large ordering distance in the carbon framework. Peaks present at 1.7° and 2.9° 2θ correspond to repeating d-spacings of 5.2 and 3.0 nm, respectively. These peaks have been previously indexed to an I-1 (P-1 type) space group as (110) and (211) respectively [34]. The primary pore size of CMK-1 has also been reported as approximately 2–3 nm [34] but these are accompanied by a certain quantity of micropores ranging between 0.4 and 0.8 nm [33,35]. These micropores are formed prior to the removal of silica template, during carbonization of the sucrose, whilst the mesopores are formed upon the removal of the silica template [36]. The micropores are likely not infiltrated with $NaAlH_4$, because they may be too small [27,35] and/or isolated as closed pores. Formation of larger nanoparticles in the mesopores are thermodynamically preferred and lead to minimisation of the surface

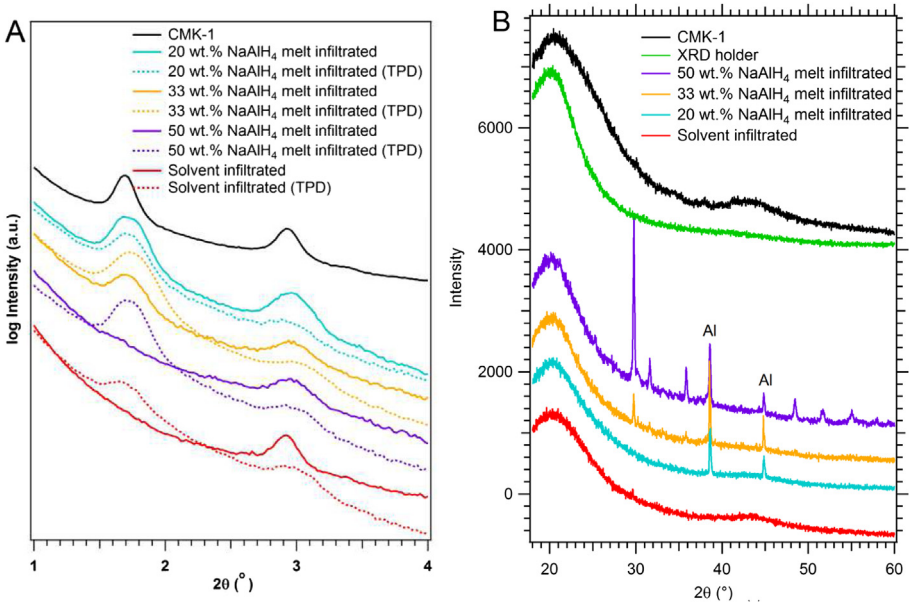

Fig. 1 – (A) Small-angle X-ray scattering (SAXS) and (B) Powder X-ray diffraction (XRD) patterns of CMK-1 and $NaAlH_4$-infiltrated CMK-1. Unlabelled XRD peaks are $NaAlH_4$.

energy [27]. It is known that changes in the wall thickness (or reduction of the pore size) in CMK materials leads to great changes in the diffraction profile, with certain lattice reflections becoming reduced or absent [37]. The X-ray diffraction from these pore networks can be described in a similar manner to that from small angle scattering theory, where the scattering length density difference (or contrast) is directly correlated to the resulting scattered intensity [38]. In this case, the electron density difference of the ordered features causes diffraction peaks to present at low angle (high d-spacing). Therefore, the decrease in peak intensity of loaded CMK-1 is due to the fact that the infiltrated material in the pores leads to a change in the electron density within the pores, and thus a reduction in the scattering contrast between ordered features. It is notable that the primary diffraction peak (110) at 1.7° 2θ is greatly affected by $NaAlH_4$ infiltration but the (211) 2.9° 2θ peak is not. This may indicate that the $NaAlH_4$ is selectively infiltrating certain pores, likely the larger mesopores in the CMK-1 framework.

XRD patterns of infiltrated samples compared to that of pure CMK-1 are displayed in Fig. 1(B). Diffraction peaks are not observable in the XRD patterns for the $NaAlH_4$ loaded CMK-1 by solution infiltration. This is a known phenomenon for nanoconfined materials and has previously been reported for other systems [39,40]. It is still not completely clear why the diffraction peaks for the metal hydride are not observable, though they may be severely broadened by either being nanocrystalline (same crystal structure in nanodomains) or amorphous (no long-range order). The XRD pattern of the melt infiltrated sample of 50 wt.%-$NaAlH_4$/CMK-1 shows the existence of large quantities of crystalline $NaAlH_4$, which indicates a limitation of loaded capacity (the ratio of hydride to scaffold). Previously, the maximum limit for $NaAlH_4$ loading into porous carbon HSAG-500 (BET) has been approximated to 40 wt.% $NaAlH_4$ [5]. In fact, the micropores of CMK-1 (with pore size less than 1 nm) are approximately 17% of the total pore volume [35], which are likely inaccessible to the hydride melt. There is also some Al present due to partial decomposition of $NaAlH_4$ during melt infiltration, potentially due to the applied hydrogen pressure slightly below its equilibrium pressure. It may also be possible that some $NaAlH_4$ has reacted with impurities in the scaffold during infiltration, causing Al formation.

Fig. 2(A) and (B) show secondary electron SEM images of as-synthesized CMK-1 and $NaAlH_4$ loaded CMK-1, respectively. The particle size of the scaffold is approximately 10 μm. After infiltration, backscattered electron SEM (BSE-SEM) images and EDS measurements (Figs. S1 and S2) detect a rather homogenous distribution of the $NaAlH_4$, throughout the scaffold. The SEM and EDS also reveal the presence of a rather large quantity of Si, likely due to an incomplete removal of the MCM-48 silica template. However, from the SAXS measurements, the MCM-48 structure is not observed. The silica contamination is hard to remove from the porous carbon scaffold even after washing with sodium hydroxide solutions several times. Silica can adversely react with metal hydrides and lower the reversible hydrogen capacity due to oxidation.

Hydrogen release properties

Fig. 3 shows the hydrogen desorption profiles from TPD-MS measurements. The hydrogen desorption from $NaAlH_4$-loaded scaffolds occurs below 100 °C under a vacuum $<10^{-2}$ mbar. In contrast, bulk $NaAlH_4$ starts to release hydrogen beyond its melting point (181 °C) at > 200 °C with the first desorption peak maximum at ~230 °C. The lower-temperature desorption peaks from nanoconfined samples represent kinetically enhanced desorption behaviour of $NaAlH_4$ due to porous confinement. Accordingly, the first two decomposition steps, Eqs. (1) and (2), are likely observed as a single hydrogen release peak, as has been reported before for $NaAlH_4$ contained in carbon aerogels [41]. The existence of some bulk $NaAlH_4$ is likely due to the high loading ratio of $NaAlH_4$ per scaffold, consequently, it leaves the excess $NaAlH_4$ outside the pores.

Hydrogen desorption from solvent-infiltrated samples display broad hydrogen release peaks and despite being outgassed under vacuum for several hours at room temperature they also generate a significant level of THF vapour well above its boiling point (66 °C). The oxygen in the THF molecule can likely form nano-clusters of Al_2O_3 [42] releasing hydrogen gas and other volatiles from a redox reaction between the solvent and infiltrated material. This illustrates that solvent infiltrated nanoconfined materials should be carefully outgassed to prevent the solvent taking part in the decomposition pathway. In this case, the THF could not be adequately removed because

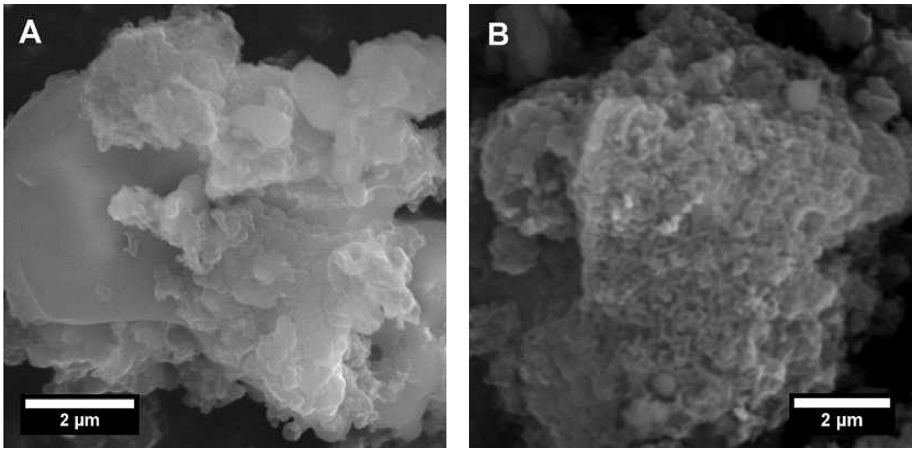

Fig. 2 – (A) SE–SEM image of pure CMK-1 (B) and SE–SEM image of 33 wt.% $NaAlH_4$ melt infiltrated CMK-1.

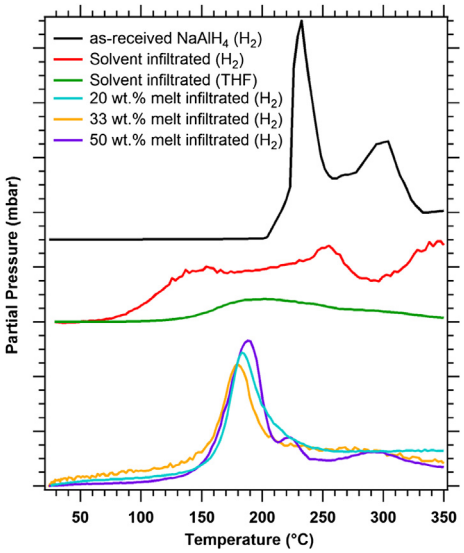

Fig. 3 – TPD-MS data of $NaAlH_4$ infiltrated in CMK-1 compared to bulk $NaAlH_4$ measured with a heating rate of 2 °C/min. Patterns are offset for clarity.

the sample could not be taken to high enough temperatures without initiating hydrogen desorption from the nanoconfined $NaAlH_4$.

After TPD measurements up to 375 °C under vacuum, SEM and TEM images combined with the EDS measurements, Fig. 4, were undertaken to inspect the scaffold morphology. These images are revealing, as they show the formation of needle-like filaments with diameters >100 nm on the scaffold surface, which can be identified by EDS as Al (Fig. 4(B)). The filaments are not present in undecomposed samples. The formation of these filaments outside the scaffold is likely caused by the heat treatment beyond the melting point of $NaAlH_4$ under vacuum during TPD measurement. The previously infiltrated $NaAlH_4$ appears to have been extracted from the scaffold and then decomposed. This phenomenon has been reported before where large Al crystals (>100 nm) were formed outside a porous carbon after full dehydrogenation at 325 °C [31]. However, Al filaments were not identified in this study. We did have more difficulty seeing these filaments in TEM when ultrasonication was used to prepare the sample, suggesting that sample preparation may break or disrupt the delicate filaments. The loss of Na has also been reported for nanoconfined $NaBH_4$ [43]. These results are of particular relevance for the nanoconfinement of complex hydrides, borohydrides in particular, as characterisation is often performed above their melting points [20,39,44]. Some borohydrides froth and foam [45,46] during hydrogen release above their melting point and this means that serious consideration needs to be given as to whether or not nanoconfined borohydrides actually stay confined during hydrogen release.

SAXS measurements (Fig. 1(A)) also reveal a change in the structure of the $NaAlH_4$/CMK-1 composites after TPD. The first diffraction peak from the CMK-1 scaffold was originally quenched upon $NaAlH_4$ loading, more so with higher levels of loading. After TPD the first peak typically reappears, indicating that the CMK-1 pores are less filled and more similar to an unloaded CMK-1 scaffold. Interestingly, there is also mild quenching of the second diffraction peak after TPD. This may indicate either a disruption to the CMK-1 structure itself or permeation of $NaAlH_4$ decomposition products into different (and possibly smaller) pores in the scaffold. The low 20 wt.% loaded sample behaves differently, presenting a smaller primary diffraction peak after TPD. This sample was only partially loaded, keeping some open porosity in the scaffold. It is reasonable to assume that the decomposition products after TPD will occupy different parts of each pore, especially since the density changes upon decomposition. The crystallographic density of $NaAlH_4$ ($\rho = 1.25$ gcm^{-3}) is lower than the decomposition products NaH ($\rho = 1.396$ gcm^{-3}) and Al ($\rho = 2.70$ gcm^{-3}), meaning that even less pore space needs to be occupied after TPD. However it is expected that the decomposition products may migrate throughout the pore network, indicated by the quenching of the second diffraction peak after TPD. This reduction in the second diffraction peak may also infer that the CMK-1 nanostructure undergoes damage during decomposition, a reasonable possibility given the high level of gas release and the evidence of Al structure growth after heating. These issues obviously present problems with the reversibility of nanoconfined complex hydrides.

Conclusion

$NaAlH_4$ was infiltrated into the pores of ordered mesoporous carbon, CMK-1, by both solvent- and melt infiltration methods, as demonstrated by SAXS. Significant issues have been identified relating to the nanoconfinement of hydrogen storage materials in porous scaffolds. Careful thought must be given to contamination from the scaffold itself, its precursor (i.e. SiO_2), and any solvents that have been used to dissolve and then infiltrate the hydrogen storage materials. It is likely that scaffolds with very small pores, such as CMK-1, are more susceptible to some of these problems due to the increased surface areas and tighter confinement of contaminants. Of primary importance is the discovery of the extraction of decomposition products from the scaffold. This has serious implications for reversibility studies and is relevant to other nanoconfined complex hydride systems such as borohydrides. Thermal decomposition under hydrogen backpressure may limit the expulsion of decomposition products from scaffolds. Further research is clearly necessary to tackle some of these adverse issues that are often hard to detect.

Acknowledgements

S.C. would like to thank Thai Government, Ministry of Science and Technology, and Mae Fah Luang University for full financial support during a higher degree research program. C.E.B, M.P. and D.A.S acknowledges the financial support of the Australian Research Council (ARC) for ARC Linkage grant LP120101848. C.E.B. also acknowledges ARC LIEF grants LE0989180 and LE0775551, and ARC RIEF grant R00107962 which enabled the XRD, gas sorption and SAXS studies to be

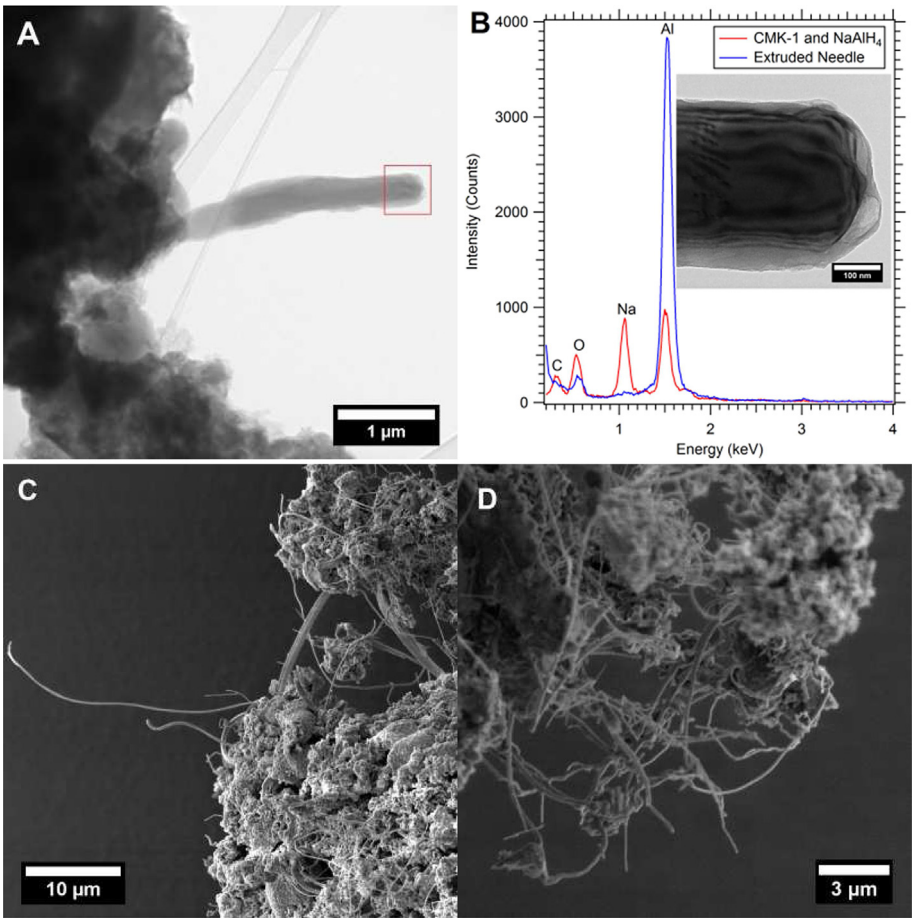

Fig. 4 – A) TEM micrograph of 33 wt.% $NaAlH_4$ melt infiltrated CMK-1 after TPD-MS to 375 °C. B) Needle-like extrusions of Al from the CMK-1 scaffold as shown by EDS measurements of the loaded scaffold and needle. The inset is the same region indicated by the red square in A. C & D) SE–SEM image after TPD measurement on 33 wt.% $NaAlH_4$ melt infiltrated CMK-1. (For interpretation of the references to colour in this figure legend, the reader is referred to the web version of this article.)

conducted. The authors also acknowledge the facilities, scientific and technical assistance of the Curtin University Electron Microscope Laboratories and the Australian Microscopy & Microanalysis Research Facility at the Centre for Microscopy, Characterization & Analysis, The University of Western Australia, facilities partially funded by the University, State and Commonwealth Governments. The work was partly supported by the Danish National Research Foundation, Center for Materials Crystallography (DNRF93), the Danish Strategic Research Council (the research project HyFillFast), and by the Carlsberg Foundation.

Appendix A. Supplementary data

Supplementary data related to this article can be found at http://dx.doi.org/10.1016/j.ijhydene.2014.05.087.

REFERENCES

[1] Orimo SI, Nakamori Y, Eliseo JR, Zuttel A, Jensen CM. Complex hydrides for hydrogen storage. Chem Rev 2007;107:4111–32.

[2] Hauback BC. Structures of aluminium-based light weight hydrides. Z Krist 2008;223:636–48.

[3] Züttel A, Rentsch S, Fischer P, Wenger P, Sudan P, Mauron P, Emmenegger C. Hydrogen storage properties of $LiBH_4$. J Alloys Compd; 2003:356–7. 515–20.

[4] Züttel A. Materials for hydrogen storage. Mater Today 2003;6:24–33.

[5] Gao J, Adelhelm P, Verkuijlen MHW, Rongeat C, Herrich M, van Bentum PJM, Gutfleisch O, Kentgens APM, de Jong KP, de Jongh PE. Confinement of $NaAlH_4$ in nanoporous carbon: impact on H_2 release, reversibility, and thermodynamics. J Phys Chem C 2010;114:4675–82.

[6] Jain IP, Jain P, Jain A. Novel hydrogen storage materials: a review of lightweight complex hydrides. J Alloys Compd 2010;503:303–39.

[7] Bellosta von Colbe JM, Felderhoff M, Bogdanovic B, Schuth F, Weidenthaler C. One-step direct synthesis of a Ti-doped sodium alanate hydrogen storage material. Chem Comm; 2005:4732–4.

[8] Claudy P, Bonnetot B, Chahine G, Letoffe JM. Etude du comportement thermique du tetrahydroaluminate de sodium $NaAlH_4$ et de l'hexahydroaluminate de sodium Na_3AlH_6. Thermochim Acta 1980;38:75–88.

[9] Bogdanović B, Schwickardi M. Ti-doped alkali metal aluminium hydrides as potential novel reversible hydrogen storage materials. J Alloys Compd; 1997:253–4. 1–9.

[10] Pitt MP, Vullum PE, Sørby MH, Emerich H, Paskevicius M, Buckley CE, Walmsley JC, Holmestad R, Hauback BC.

Hydrogen absorption kinetics of the transition-metal-chloride-enhanced $NaAlH_4$ system. J Phys Chem C 2012;116:14205–17.
[11] Pitt MP, Vullum PE, Sørby MH, Emerich H, Paskevicius M, Buckley CE, Gray EM, Walmsley JC, Holmestad R, Hauback BC. A structural review of nanoscopic Al_1-xTM_x phase formation in the TMCln enhanced $NaAlH_4$ system. J Alloys Compd 2012;527:16–24.
[12] Pitt MP, Paskevicius M, Webb CJ, Sørby MH, Delleda S, Jensen TR, Hauback BC, Buckley CE, Gray EM. Nanoscopic Al_1-xCex phases in the NaH^+ Al^+ $0.02CeCl_3$ system. Int J Hydrogen Energy 2011;36:8403–11.
[13] Pitt MP, Vullum PE, Sørby MH, Emerich H, Paskevicius M, Webb CJ, Gray EM, Buckley CE, Walmsley JC, Holmestad R, Hauback BC. Hydrogen absorption kinetics and structural features of $NaAlH_4$ enhanced with transition-metal and Ti-based nanoparticles. Int J Hydrogen Energy 2012;37:15175–86.
[14] Seayad AM, Antonelli DM. Recent advances in hydrogen storage in metal-containing inorganic nanostructures and related materials. Adv Mater 2004;16:765–77.
[15] Vegge T. Equilibrium structure and Ti-catalyzed H_2 desorption in $NaAlH_4$ nanoparticles from density functional theory. Phys Chem Chem Phys 2006;8:4853–61.
[16] Huot J, Ravnsbæk DB, Zhang J, Cuevas F, Latroche M, Jensen TR. Mechanochemical synthesis of hydrogen storage materials. Progr Mater Sci 2013;58:30–75.
[17] Huot J, Liang G, Boily S, Van Neste A, Schulz R. Structural study and hydrogen sorption kinetics of ball-milled magnesium hydride. J Alloys Compd 1999;293–295:495–500.
[18] Xiong R, Sang G, Yan X, Zhang G, Ye X, Jiang C, Luo L. Improvement of the hydrogen storage kinetics of $NaAlH_4$ with nanocrystalline titanium dioxide loaded carbon spheres (Ti-CSs) by melt infiltration. Int J Hydrogen Energy 2012;37:10222–8.
[19] Nielsen TK, Besenbacher F, Jensen TR. Nanoconfined hydrides for energy storage. Nanoscale 2011;3:2086–98.
[20] Vajo JJ. Influence of nano-confinement on the thermodynamics and dehydrogenation kinetics of metal hydrides. Curr Op Sol Stat Mater Sci 2011;15:52–61.
[21] Fichtner M. Properties of nanoscale metal hydrides. Nanotechnol 2009;20:204009.
[22] de Jongh PE, Adelhelm P. Nanosizing and nanoconfinement: new strategies towards meeting hydrogen storage goals. ChemSusChem 2010;3:1332–48.
[23] Pitt MP, Paskevicius M, Webb CJ, Sheppard DA, Buckley CE, Gray EM. The synthesis of nanoscopic Ti based alloys and their effects on the MgH_2 system compared with the MgH_2+$0.01Nb_2O_5$ benchmark. Int J Hydrogen Energy 2012;37:4227–37.
[24] Nielsen TK, Manickam K, Hirscher M, Besenbacher F, Jensen TR. Confinement of MgH_2 nanoclusters within nanoporous aerogel scaffold materials. ACS Nano 2009;3:3521–8.
[25] Paskevicius M, Sheppard DA, Buckley CE. Thermodynamic changes in mechanochemically synthesized magnesium hydride nanoparticles. J Am Chem Soc 2010;132:5077–83.
[26] Paskevicius M, Tian HY, Sheppard DA, Webb CJ, Pitt MP, Gray EM, Kirby NM, Buckley CE. Magnesium hydride formation within carbon aerogel. J Phys Chem C 2011;115:1757–66.
[27] Nielsen TK, Javadian P, Polanski M, Besenbacher F, Bystrzycki J, Jensen TR. Nanoconfined $NaAlH_4$: determination of distinct prolific effects from pore size, crystallite size, and surface interactions. J Phys Chem C 2012;116:21046–51.
[28] Nielsen TK, Javadian P, Polanski M, Besenbacher F, Bystrzycki J, Skibsted J, Jensen TR. Nanoconfined $NaAlH_4$: prolific effects from increased surface area and pore volume. Nanoscale 2014;6:599–607.
[29] Fichtner M. Nanoconfinement effects in energy storage materials. Phys Chem Chem Phys 2011;13:21186–95.
[30] Nielsen TK, Polanski M, Zasada D, Javadian P, Besenbacher F, Bystrzycki J, Skibsted J, Jensen TR. Improved hydrogen storage kinetics of nanoconfined $NaAlH_4$ catalyzed with $TiCl_3$ nanoparticles. ACS Nano 2011;5:4056–64.
[31] Gao J, Ngene P, Lindemann I, Gutfleisch O, de Jonga KP, de Jongh PE. Enhanced reversibility of H_2 sorption in nanoconfined complex metal hydrides by alkali metal addition. J Mater Chem 2012;22:13209–15.
[32] Xu J, Luan Z, He H, Zhou W, Kevan L. A reliable synthesis of cubic mesoporous MCM-48 molecular sieve. Chem Mater 1998;10:3690–8.
[33] Ryoo R, Joo SH, Kruk M, Jaroniec M. Ordered mesoporous carbons. Adv Mater 2001;13:677–81.
[34] Solovyov LA, Zaikovskii VI, Shmakov AN, Belousov OV, Ryoo R. Framework characterization of mesostructured carbon CMK-1 by X-ray powder diffraction and electron microscopy. J Phys Chem B 2002;106:12198–202.
[35] Xia K, Gao Q, Song S, Wu C, Jiang J, Hu J, Gao L. CO_2 activation of ordered porous carbon CMK-1 for hydrogen storage. Int J Hydrogen Energy 2008;33:116–23.
[36] Ryoo R, Joo SH, Jun S. Synthesis of highly ordered carbon molecular sieves via template-mediated structural transformation. J Phys Chem B 1999;103:7743–6.
[37] Schmidt W. Calculation of XRD patterns of simulated FDU-15, CMK-5, and CMK-3 carbon structures. Micro Meso Mater 2009;117:372–9.
[38] Paskevicius M, Buckley CE. Analysis of polydisperse bubbles in the aluminium-hydrogen system using a size-dependent contrast. J Appl Cryst 2006;39:676–82.
[39] Liu X, Peaslee D, Jost CZ, Majzoub EH. Controlling the decomposition pathway of $LiBH_4$ via confinement in highly ordered nanoporous carbon. J Phys Chem C 2010;114:14036–41.
[40] Li Y, Zhou G, Fang F, Yu X, Zhang Q, Ouyang L, Zhu M, Sun D. De-/re-hydrogenation features of $NaAlH_4$ confined exclusively in nanopores. Acta Mater 2011;52:1829–38.
[41] Stephens RD, Gross AF, Van Atta SL, Vajo JJ, Pinkerton FE. The kinetic enhancement of hydrogen cycling in $NaAlH_4$ by melt infusion into nanoporous carbon aerogel. Nanotechnol 2009;20:204018.
[42] Majzoub EH, Herberg JL, Stumpf R, Spangler S, Maxwell RS. XRD and NMR investigation of Ti-compound formation in solution-doping of sodium aluminum hydrides: solubility of Ti in $NaAlH_4$ crystals grown in THF. J Alloys Compd 2005;394:265–70.
[43] Ngene P, van den Berg R, Verkuijlen MHW, de Jong KP, de Jongh PE. Energy Env Sci 2011;4:4108–15.
[44] Li C, Peng P, Zhou DW, Wan L. Research progress in $LiBH_4$ for hydrogen storage: a review. Int J Hydrogen Energy 2011;36:14512–26.
[45] Paskevicius M, Pitt MP, Webb CJ, Sheppard DA, Filsø U, Gray EM, Buckley CE. *In-situ* X-ray diffraction study of γ-$Mg(BH_4)_2$ decomposition. J Phys Chem C 2012;116:15231–40.
[46] Paskevicius M, Ley MB, Sheppard DA, Jensen TR, Buckley CE. Eutectic melting in metal borohydrides. Phys Chem Chem Phys 2013;15:19774–89.